Numerical Study of Natural Convection Coupled to Gas Radiation in a Cavity Containing an Active Obstacle

Xuan Bach Nguyen Le

THESE

Pour l'obtention du Grade de

DOCTEUR DE L'ECOLE NATIONALE SUPERIEURE DE MECANIQUE ET D'AEROTECHNIQUE

(Diplôme National - Arrêté du 25 mai 2016)

Ecole Doctorale: Sciences et Ingénierie en Matériaux, Mécanique, Énergétique

Secteur de Recherche: Énergétique, Thermique et Combustion

Présentée par:
Xuan Bach NGUYEN

****

Numerical study of natural convection coupled to gas radiation in a cavity containing an active obstacle

****

Directeur de thèse: Denis LEMONNIER

****

Soutenue le 24 Novembre 2020

devant la Commission d'Examen

****

JURY

Président:

Didier SAURY, Professeur à l'ISAE-ENSMA, Poitiers.

Rapporteurs:

Abderramane BAIRI, Professeur à l'université de Paris X.

Patrice JOUBERT, Professeur à l'université de La Rochelle.

Examinateurs:

Vladimir P. SOLOVJOV, Professeur à l'université Brigham Young, Provo, Utah, USA.

Siham LAOUAR-MEFTAH, Maitre de Conférences à l'université de Boumerdes, Algérie.

Yann BILLAUD, Maitre de Conférences à l'université de Poitiers.

Denis LEMONNIER, Directeur de Recherches au CNRS, Poitiers.

Acknowledgements

This dissertation is the result of our work during the PhD between 10/2016 and 11/2020 at Institute Pprime - ISAE-ENSMA under the direction of M. Denis LEMONNIER, research director at CNRS.

To accomplish this thesis, I have experienced a lot of whole new things. It was fun to deal with the problems that I had never met before. However, it was absolutely not easy. I would haven't achieved this results without the the help and the encouragement of a lot of people.

I would like to express my sincere thank in the first place to my advisor, who has given me an interesting subject. Thanks to his guidance, encouragement and patience during nearly four years.

I would like to send my thanks to M. Abderramane BAIRI, M. Patrice JOUBERT, M. Vladimir P. SOLOVJOV, Mme. Siham MEFTAH-LAOUAR, M. Didier SAURY and M. Yann BILLAUD for accepting to judge this thesis work.

I also send my thank to M. Didier SAURY, Professor at ISAE-ENSMA, for all his technical support and great ideas for my questions during the works.

My life in laboratory would be so boring without my friendly colleagues: Yang, Elissa, Paul, Alexandre, Pièrre, ... Thank you all for the joyful moments that we have shared together.

I would like to express my thanks to all my Vietnamese friends who have shared a period of their lives with me during my thesis. Thank you for all supports, delicious meals, badminton matches and over all, for our brotherhood in a whole new and strange country.

I would like to give my last thanks to my beloved family and girl friend who have been always by my side. You are the motivation for me to continue over this long way.

Once a gain, I would like to spend my deepest thanks to all you guys for being a part of my life during this not easy period. An old road seems to be closed and I am now ready to discovery new journeys.

Résumé

Introduction

L'étude de la convection naturelle en milieu confiné fait encore l'objet de nombreuses recherches, tant numériques qu'expérimentales. Dans ce type de problème, les différents modes de transfert de chaleur (convection, conduction, rayonnement) peuvent intervenir de manière couplée. Cependant, lorsque le transport radiatif est considéré, un problème particulier se pose lorsque le fluide absorbe et émet un rayonnement infrarouge. Il est alors nécessaire de prendre en compte une source de chaleur interne au milieu, résultant de la différence entre l'énergie rayonnante absorbée et émise par chaque élément de volume. De nombreuses études ont étudié ce phénomène dans une cavité différentiellement chauffée (Yücel, Acharya, and Williams [1], Tan and Howell [2], Colomer et al. [3], Colomer, Consul, and Oliva [4], Soucasse et al. [5], Billaud, Saury, and Lemonnier [6]). Le problème d'un apport de chaleur placé dans un environnement confiné a également retenu l'attention de nombreux chercheurs, soit avec une source ponctuelle (Tetsu, Itsuki, and Haruo [7], Urakawa, Morioka, and Kiyota [8], Xin et al. [9], Hernandez [10], etc.) ou avec obstacles solides de taille finie (Kuznetsov and Sheremet [11], Kuznetsov and Sheremet [12], Paroncini and Corvaro [13], Kuznetsov, Maksimov, and Sheremet [14], Souayeh et al. [15], Gibanov and Sheremet [16],Iyi, Hasan, and Penlington [17], Rahmati and Tahery [18] etc.), mais dans la plupart des cas, la source de chaleur est placée dans le fluide, sans aucun contact avec les murs. Ici, nous abordons le cas d'un obstacle chauffant placé au fond de la cavité. Cela constitue une nouvelle configuration intéressante.

Tout d'abord, concernant la convection naturelle à l'intérieur d'une cavité contenant un obstacle opaque, Kuznetsov and Sheremet [12] ont étudié les effets du nombre de Grasshof ($10^5 - 10^7$) sur le mouvement du fluide et ont conclu à l'influence de ce paramètre sur le champ thermique dans l'enceinte. Kuznetsov and Sheremet [11] ont étudié la même configuration, mais avec une plage différente du nombre de Grasshof ($10^7 - 10^9$) et ont souligné que, lorsque ce nombre augmente, l'écoulement et le processus de transfert de chaleur sont stabilisés. Paroncini and Corvaro [13], Kuznetsov, Maksimov, and Sheremet [14], Souayeh et al. [15], Gibanov and Sheremet [16], Iyi, Hasan, and Penlington [17],Rahmati and Tahery [18] ont étudié différents écoulements convectifs de manière numérique et expérimentale avec l'influence de la numéro de Rayleigh. Ils ont rapporté que l'augmentation de ce paramètre intensifie le mouvement du fluide et augmente le transfert de chaleur par processus convectif. De plus, l'étude sur la taille de l'obstacle chaud de Paroncini and Corvaro [13] a souligné que, lorsque la hauteur de l'obstacle est la moitié de la cavité, le transfert de chaleur convectif est le pire parmi les cas analysés. En outre, Bouafia and Daube [19] ont examiné les comportements instables dans cette configuration à différents rapports d'aspect de l'enceinte et ont conclu que le mécanisme de l'instabilité était dû au cisaillement lorsque ce paramètre vaut 1 et 2. Pour un rapport d'aspect plus élevé (4) , le principal mécanisme était les instabilités de flottabilité. Hernandez [10] a étudié une cavité carrée avec une source de chaleur attachée au sol. Ses résultats indiquent que le comportement instable était dû à la vitesse horizontale élevée juste au-dessus de l'obstacle.

Ensuite, le problème de la convection naturelle combinée au rayonnement de surface a été étudié par Sun, Chénier, and Lauriat [20], Martyushev and Sheremet [21], Saravanan and Sivaraj [22], Patil, Sharma, and Velusamy [23], Miroshnichenko, Sheremet, and Chamkha [24]. Ils ont conclu que l'augmentation de l'émissivité renforce le mouvement du fluide près de la paroi, intensifie le transfert radiatif mais réduit le transport convectif. Sun, Chénier, and Lauriat [20] ont également signalé que le rayonnement de surface ralentit la transition vers l'instabilité à l'intérieur de la cavité.

Jusqu'à présent, une revue détaillée de littérature a montré que la convection naturelle couplée au rayonnement volumique n'étaient pas encore prise en compte dans la configuration d'une cavité contenant un obstacle. De plus, le coefficient d'absorption qui varie avec le nombre d'ondes, la fraction molaire du composant absorbant et la température du milieu pose également un problème remarquable. Notre objectif est donc d'étudier ce couplage (à la fois en convection thermique pure et double convection) à l'intérieur d'une cavité cubique dont les parois horizontales sont adiabatiques et les parois verticales isothermes. Un obstacle cubique est situé au centre de plancher. Il est opaque et sa surface est uniformément maintenue à une température supérieure à celle des parois de la cavité. L'étude comprend, dans un premier temps, une analyse des phénomènes en gaz transparent (convection thermique et panache confiné en double diffusion: cas aidant et cas opposant). Une première approche des gaz participants est ensuite effectuée en supposant que le mélange absorbant est gris. La dernière approche - et la plus importante - est la simulation en gaz réel. Concrètement, on considère les mélanges $air - H_2O$ et $air - CO_2$ avec une concentration prescrite d'espèces absorbantes à la surface de l'obstacle et une concentration nulle sur les parois verticales de la cavité. Nous analysons les résultats par comparaison avec les cas transparents, mais aussi en examinant dans quelle mesure les observations faites avec le modèle des gaz gris restent pertinentes.

Ce manuscrit est divisé en six chapitres. Premièrement, le présent chapitre présente la motivation de la thèse, ses objectifs et une revue de bibliographie sur certaines recherches connexes des dernières décennies. Ensuite, dans le deuxième chapitre, nous fournissons plus de détails sur les modèles mathématiques ainsi que sur les méthodes numériques utilisées dans cette étude. Ensuite, le chapitre trois présentera Code Saturne, l'outil de simulation CFD utilisé tout au long de notre travail et la mise en œuvre de notre propre modèle SLW dans le module radiatif intégré de ce code. Nous présentons également quelques tests de validation pour évaluer la précision de nos calculs dans des configurations de plus en plus complexes. Le quatrième chapitre contient les résultats et l'analyse de la convection thermique combinée au rayonnement dans un gaz gris ainsi que dans un mélange gazeux réel. Ensuite, le chapitre cinq se concentrera sur les effets du rayonnement dans de nombreuses situations typiques de convection de double diffusion, coopérante ou opposée, dans un mélange de gaz gris ou réels. Pour terminer, le chapitre de conclusion synthétisera les principaux résultats de cette étude et fournira des perspectives pour les travaux futurs.

Methodologie

Modèle mathématique

Les hypothèses utilisées dans ce travail sont les suivantes :

- L'écoulement dans la cavité est tridimensionnel et laminaire.
- Le fluide est considéré comme newtonien et incompressible.
- Les surfaces actives (parois verticales de l'enceinte et surfaces extérieures de l'obstacle) sont noires par rapport au rayonnement tandis que les surfaces adiabatiques (plafond et plancher de l'enceinte) sont purement réfléchissantes.
- Les variations de température et de concentration à l'intérieur de la cavité sont suffisamment faibles pour permettre l'approximation de Boussinesq. Par conséquent, les variations des propriétés du fluide sont ignorées, sauf pour la densité dans l'expression de la pousée d'Archimède.
- La dissipation visqueuse et le travail de pression sont négligées.
- Les effets de Soret et de Dufour sont négligés.

Équations de la dynamique des fluides

Plusieurs équations de conservation régissent les mouvements d'écoulement et les processus de transfert dans l'enceinte. Elles expriment un équilibre local en termes de masse, de quantité de mouvement, d'énergie et de composition au sein du fluide.

- Équation de continuité

$$\boldsymbol{\nabla} \cdot \mathbf{u} = 0 \tag{1}$$

- Équation de quantité de mouvement

$$\rho_0 \frac{\partial \mathbf{u}}{\partial t} + \rho_0 \mathbf{u} \cdot \boldsymbol{\nabla} \mathbf{u} = -\boldsymbol{\nabla} p + \rho_0(\beta_T(T_0 - T) + \beta_C(C_0 - C))\mathbf{g} + \mu \boldsymbol{\nabla}^2 \mathbf{u} \tag{2}$$

  Le terme source $\rho_0(\beta_T(T_0 - T) + \beta_C(C_0 - C))\mathbf{g}$ représente la force de flottabilité qui met le fluide en mouvement (exprimée ici sous l'approximation de Boussinesq).

- Équation dénergie

$$\rho_0 C_p \frac{\partial T}{\partial t} + \rho_0 C_p \mathbf{u} \cdot \boldsymbol{\nabla} T = \lambda \boldsymbol{\nabla}^2 T - \boldsymbol{\nabla} \cdot \mathbf{q} \tag{3}$$

- Équation de conservation de la concentration

$$\frac{\partial C}{\partial t} + \mathbf{u} \cdot \boldsymbol{\nabla} C = D \boldsymbol{\nabla}^2 C \tag{4}$$

Toutes les équations de conservation sont couplées : le champ dynamique influence le transport des quantités scalaires (T et C) qui, à leur tour, entraînent l'écoulement par les effets de la flottabilité. De plus, dans le cas du mélange binaire, la concentration a un effet direct sur le champ thermique puisqu'elle modifie les propriétés d'absorption-émission du milieu. Par conséquent, la source radiative dans le bilan énergétique est impactée.

Équation de transfert radiatif

La cavité est remplie d'un milieu gazeux semi-transparent à l'équilibre thermodynamique local, qui absorbe et émet le rayonnement en tout point de l'espace. La luminance $I_\eta(\mathbf{s}, \mathbf{\Omega})$[1] représente le flux radiatif (par unité d'angle solide et par unité de nombre d'onde) qui se propage au point $\mathbf{s}$ dans la direction $\mathbf{\Omega}$ au nombre d'onde η. Dans un milieu non diffusant, le changement local de luminance est décrit par l'équation de transfert radiatif.

$$\mathbf{\Omega} \cdot \mathbf{\nabla} I_\eta(\mathbf{s}, \mathbf{\Omega}) = -\kappa_\eta(s) I_\eta(\mathbf{s}, \mathbf{\Omega}) + \kappa_\eta(\mathbf{s}) I_{b\eta}(T(\mathbf{s})) \tag{5}$$

La solution dépend de trois coordonnées de position, de deux variables de direction (deux angles polaires ou deux cosinus de direction) et du nombre d'ondes. La luminance totale peut être trouvée par intégration sur l'ensemble du spectre.

$$I(\mathbf{s}, \mathbf{\Omega}) = \int_0^\infty I_\eta(\mathbf{s}, \mathbf{\Omega}) d\eta \tag{6}$$

Le terme $-\mathbf{\nabla} \cdot \mathbf{q}$ qui apparaît dans l'équation d'énergie est la divergence totale du flux radiatif. Ce flux peut être calculé à partir de la luminance totale par l'expression :

$$\boldsymbol{q}(\mathbf{s}) = \int_0^{4\pi} I(\mathbf{s}, \mathbf{\Omega}) \mathbf{\Omega} d\Omega = \int_0^{4\pi} \int_0^\infty I_\eta(\mathbf{s}, \mathbf{\Omega}) \mathbf{\Omega} d\eta d\Omega \tag{7}$$

Conditions aux limites

Toutes les surfaces de l'obstacle[2] sont portées à une température et une concentration constantes et uniformes :
En ce qui concerne la cavité, les parois verticales sont uniformément maintenues à une température et une concentration constantes. Les parois horizontales sont adiabatiques, imperméables et supposées se comporter comme des surfaces entièrement réfléchissantes.

Modèle de rayonnement

Méthode des ordonnées discrètes

Dans les problèmes couplés impliquant le rayonnement, nous devons résoudre le problème du transfert radiatif en plus des équations de conservation. Historiquement, plusieurs méthodes ont été développées pour atteindre cet objectif.
Dans la présente étude, nous avons utilisé la méthode des ordonnées discrètes pour nos calculs radiatifs en raison de son bon compromis entre la précision et le coût de calcul et de sa facilité d'implantation dans de nombreux codes CFD. En particulier, Code Saturne, un code CFD open-source développé par EDF, offre un module DOM

[1] $\mathbf{s}$ est la vecteur de position le long du chemin optique
[2] excepté la surface en contact avec le sol de la cavité

radiatif déjà intégré.

Méthode SLW

Chaque fois que l'on considère le rayonnement gazeux, il faut tenir compte du comportement spectral réel des propriétés d'absorption des fluides. À cette fin, divers modèles de gaz ont été introduits avec différents niveaux de complexité, d'exigences de calcul et de précision. Ces modèles peuvent être classés en trois groupes principaux comme suit :

- Modèle raie par raie
- Modèles de bandes
- Modèles globales

Dans le modèle raie par raie et les modèles de bande, les propriétés radiatives sont évaluées sur chaque raies ou sur un intervalle donnée de nombres d'onde. D'autre part, les modèles globaux déterminent les caractéristiques radiatives sur l'ensemble du spectre.

Mise en œuvre du modèle de gaz SLW
Le modèle SLW (un modèle global) implique un nombre fini de gaz gris (N_g) et un gaz transparent. Le coefficient d'absorption du gaz j^{th} est calculé comme suit

$$\kappa_j = N \cdot Y \cdot C_j \tag{8}$$

où C_j est la section efficace d'absorption. Connaissant N et Y, le problème restant est de déterminer C_j.

Calculs de la fonction de distribution du corps noir de la ligne d'absorption et des poids des gaz gris

Les poids associés à chaque gaz gris sont calculés à partir de la fonction de distribution globale du coefficient d'absorption pondéré par la fonction de Planck (ALBDF). Cette fonction est évaluée comme l'intégrale de la fonction de Planck calculée à une température de source T_b sur les intervalles de nombres d'onde de telle que la section efficace d'absorption $C_\eta(\phi_g)$ à un état thermodynamique du gaz ϕ_g est inférieure à une valeur spécifiée de C.

Le poids du gaz gris j^{th} a_j correspond à la différence de l'ALBDF aux deux sections d'absorption supplémentaires qui définissent le j^{me} intervalle $[\tilde{C}_{j-1},\tilde{C}_j]$

Code Saturne et Calcul du Rayonnement

Code Saturne

Toutes les équations de notre problème ont été résolues en utilisant Code Saturne version 5.0.4 (Archambeau, Méchitoua, and Sakiz [25]), un logiciel open source de calcul CFD développé par EDF. Un module radiatif intégré est disponible, dans lequel nous avons implémenté nos propres données pour l'intégration directionnelle et un module spécifique pour le rayonnement gazeux selon le modèle SLW.

Mécanique des fluides

Code Saturne utilise une méthode de volumes finis pour résoudre les équations régissant le mouvement des fluides et le transfert de chaleur et de masse. Pour l'équation de quantité de mouvement, le logiciel recourt à l'algorithme SIMPLEC. Différentes discrétisations dans l'espace et dans le temps sont disponibles.

Discrétisation temporelle
Le schéma temporel est implémenté dans Code Saturne est un schéma θ avec:

$$\begin{cases} \theta = 1 & \text{pour un schéma d'Euler implicite de premier ordre,} \\ \theta = \frac{1}{2} & \text{pour le schéma Crank-Nicolson de second ordre.} \end{cases} \tag{9}$$

Il existe deux options pour définir le pas temporel: constant ou variable. Dans ce dernier cas, le code calcule automatiquement après chaque itération le pas de temps qui satisfait au critère CFL.

Discrétisation spatiale
Code Saturne propose différents schémas de premier ordre (Upwind) et de second ordre (Centré ou Second-Order-Linear-Upwind (SOLU)) pour la discrétisation spatiale et. Dans cette étude, nous avons sélectionné le schéma de second ordre centré.

Méthode des ordonnées discrètes

La méthode des ordonnées discrètes (DOM) a été utilisée pour résoudre l'équation de transfert radiatif correspondant à chaque gaz gris du modèle SLW. Cette méthode consiste à remplacer les intégrales angulaires par une sommation sur un ensemble de directions discrètes telles que:

$$\int_0^{4\pi} f(\boldsymbol{\Omega}) d\Omega \approx \sum_{m=1}^{M} \omega_m f(\Omega_m) \tag{10}$$

où M désigne le nombre de directions et ω_m est le poids attribué à l'élément m. Par conséquent, la distribution du rayonnement incident et du flux radiatif est approximée par:

$$G_\eta^P = \int_0^{4\pi} I_\eta^P(\boldsymbol{\Omega}) d\Omega \approx \sum_{m=1}^{M} \omega_m I_{\eta,m}^P(\boldsymbol{\Omega}) \tag{11}$$

$$\boldsymbol{q}_m^P = \int_0^{4\pi} I_\eta^P(\boldsymbol{\Omega}) \boldsymbol{\Omega} d\Omega \approx \sum_{m=1}^{M} \omega_m I_{\eta,m}^P(\boldsymbol{\Omega}) \boldsymbol{\Omega}_m \tag{12}$$

où P désigne ici le centre d'un volume de contrôle.
Il existe plusieurs façons de définir les ensembles de directions discrètes. Un aperçu plus général de ce problème se trouve dans [26]. Nous avons sélectionné ici la quadrature symétrique de niveau S_N en utilisant l'ensemble de données amélioré

suggéré par [27].

Critères de convergence

Code Saturne n'a pas de critère intégré pour déterminer la convergence de la solution. Au lieu de cela, il est conseillé de surveiller l'évolution temporelle des variables considérées à différentes positions dans le champ d'écoulement pour décider si le calcul atteint un état stationnaire (EDF [28]). L'utilisateur peut arrêter le calcul chaque fois qu'il trouve les résultats acceptables ou le code s'exécutera jusqu'à atteindre le nombre maximal de pas de temps déclaré. De plus, les conservations du flux de chaleur et de masse peuvent être un critère pour tester l'atteinte d'un régime stationaire car les flux totaux qui arrivent aux parois actives de la cavité (à faible valeur de température et de concentration) doivent être les mêmes que ceux qui sortent des surfaces de l'obstacle (à des valeurs élevées de température et de concentration).

Validation du Code

Dans cette section, Code Saturne et son modèle radiatif amélioré sont validés en convection thermique pure et en convection de double diffusion couplée au rayonnement. les comparaisons avec les travaux de De Vahl Davis [29], Colomer et al. [30] et Fusegi and Hyun [31], Yücel, Acharya, and Williams [1] et Laouar-Meftah [32], Billaud, Saury, and Lemonnier [6] et Soucasse, Rivière, and Soufiani [33], Sezai and Mohamad [34], Cherifi [35], Sun, Chénier, and Lauriat [20] Paroncini and Corvaro [13] donnent un bon accord entre les résultats.

Couplage convection naturelle-rayonnement

Un premier ensemble de résultats concerne la convection thermique pure. Dans cette configuration, le fluide est de composition homogène et l'écoulement n'est régi que par les gradients de température.

Dans cette partie, nous analysons tout d'abord l'effet du rayonnement sur la structure de l'écoulement et le transfert de chaleur de manière simple, en supposant que le milieu remplissant la cavité est gris et possède des propriétés radiatives uniformes. Différentes valeurs du coefficient d'absorption κ sont considérées et l'opacité du milieu est caractérisée par l'épaisseur optique $\tau = \kappa L$ liée à la taille de la cavité, L. Tous les calculs ont été effectués à $Ra = 5 \cdot 10^6$, $Pr = 0,71$ et $\theta_0 = 11,1$. Les parois chaude et froide sont noires et les parois adiabatiques sont purement réfléchissantes. De ce fait, il n'y a pas de couplage radiatif-convectif lorsque $\tau = 0$ (milieu transparent). Ce cas limite sert de référence pour déterminer les effets du rayonnement sur l'écoulement.Nous avons réalisé des calculs avec plusieurs valeurs de l'opacité: $\tau = 0.1; 0.2; 0.5; 1; 2$.

Ensuite, nous considérons la présence d'un composant absorbant-émettant (H_2O) dilué à différentes concentrations dans un gaz transparent (air sec). Le spectre d'absorption réel de la vapeur d'eau doit être pris en compte pour permettre des simulations réalistes. À cette fin, et suite à la discussion présentée au chapitre 2, nous avons recours au modèle SLW associé à l'approche de "Rank correlattion". Concernant les conditions limites, les surfaces de l'obstacle sont fixées à $T_h = 580K$ [3], les parois verticales sont uniformément maintenues à $T_c = 530K$ tandis que le plafond et le sol sont supposés parfaitement réfléchissants ($\epsilon = 0$) et adiabatiques.

Les comparaisons entre les résultats obtenus et la référence transparente ont mis en évidence les phénomènes suivant :

- Le rayonnement a tendance à accélérer de manière non uniforme les couches limites de la cavité et de l'obstacle intérieur. Il fait met en mouvement certaines parties du fluide qui étaient stagnantes dans le cas transparent. L'écoulement du panache et sa recirculation interfèrent et créent les modèles d'écoulement de cisaillement.
- Le rayonnement modifie partiellement le gradient thermique près des parois de la cavité : les valeurs du nombre de Nusselt convectif sont augmentées dans la moitié supérieure et diminuées dans la moitié inférieure. Cependant, à la surface horizontale de l'obstacle, le gradient thermique est renforcé.
- Le rayonnement modifie la stratification thermique à l'extérieur du panache et uniformise légèrement la température moyenne.
- le rayonnement réduit le transfert thermique total, en particulier la partie convective sur les parois verticales et l'échange radiatif entre la surface supérieure de l'obstacle et les murs de la cavité.
- Tous ces effets augmentent lorsque le milieu devient plus opaque (dans la gamme étudiée des épaisseurs optiques et de la fraction molaire).
- En outre, dans le cas du gaz gris, lorsque l'épaisseur optique du milieu est unitaire, le rayonnement mène à un écoulement périodique. Ce mécanisme est dû à l'instabilité de cisaillement créée par l'interférence du panache ascendant et des couches limites s'écoulant vers le bas. Enfin, à $\tau = 2$, l'écoulement devient totalement turbulent à $Ra = 5 \cdot 10^6$.

Couplage convection de double diffusion-rayonnement

En convection de double diffusion, il existe deux gradients qui pilotent l'écoumenent : le gradient thermique et le gradient de concentration. L'ampleur relative des effets de ces deux gradients est définie par le rapport de flottabilité de masse/thermique N : son signe caractérise la coopération (> 0) ou l'opposition (< 0) de la conduite induite.

Dans le cadre de ce travail, nous avons effectué des calculs en convection de double diffusion, y compris des cas où le rayonnement gazeux est pris en compte. Des prédictions sans rayonnement (fluide transparent) sont également fournies pour différents rapports de masse/flottabilité thermique et servent de valeurs de référence mettant en évidence l'influence du transfert radiatf sur la structure d'écoulement et le transfert de chaleur et de masse. Tous les calculs sont effectués à $Ra = 5.10^6$, $Le = 1$, pour un recouvrement parfait des couches limites thermiques et de concentration, $Pl = 4.43 \cdot 10^{-3}$ et $\theta_0 = 11.1$. Concernant les conditions limites, une

[3] Sauf celle du fond qui est en contact avec le sol de la cavité

forte concentration de l'espèce absorbante est appliquée sur toutes les surfaces de l'obstacle (C_h), et une concentration nulle ($C_l = 0$) le long des parois verticales de la cavité. L'émissivité des surfaces limites (y compris l'obstacle) est fixée à l'unité, sauf le plafond et le plancher, qui sont considérés comme parfaitement réfléchissants. Pour chaque rapport de force, des calculs sont réalisés à différent opacités: τ =0.1; 0.2; 0.5; 1 et 2.

- Écoulement aidant

  A $N = 1$, l'introduction de rayonnement gazeux n'affecte pas beaucoup le champ de concentration. Il accélère légèrement les couches limites mais réduit la vitesse maximale à l'intérieur du panache. Concernant le champ thermique, le rayonnement volumique tend à homogénéiser le milieu. Il diminue la température dans la moitié supérieure de la cavité et redistribue les isothèmes (passant d'une stratification presque verticale à une stratification horizontale). L'augmentation de l'opacité du milieu renforce ces effets.
  A $N = 2$, les mêmes tendances sont observées mais leur amplitude est réduite.

- Écoulement opposant

  A $N = -1$, pour un milieu transparent, aucun écoulement ne se produit à l'intérieur de la cavité en raison de la symétrie parfaite des gradients thermique et de concentration. Mais, avec le rayonnement, cet équilibre est rompu et de nouveaux mouvements de fluides s'établissent. L'écoulement dans la partie inférieure de la cavité est dominé par le gradient de masse pour toutes les épaisseurs optiques considérées. Plus haut, le gradient thermique régit le flux. Pour des valeurs de 0 à 1, le rayonnement intensifie le panache thermique. Cependant, à $\tau = 1$, l'augmentation de la concentration dans l'axe du panache limite le mouvement vertical et provoque son étalement. À $\tau = 2$, ces changements se renforcent, entraînant la séparation entre le panache et une zone de fluide presque immobile au centre de la cavité. En ce qui concerne le champ thermique, la prise en compte du rayonnement gazeux a réduit la température dans les régions proches des parois verticales de l'obstacle. Au-dessus du niveau de l'obstacle, la température est généralement réduite par rapport au cas transparent. Cependant, elle augmente avec l'opacité, sauf une légère diminution au centre de la cavité lorsque $\tau = 2$. En ce qui concerne le champ de concentration, les tendances d'altération sont les mêmes que pour le champ thermique à l'exception d'une légère augmentation de cette quantité près des parois verticales froides dans la partie inférieure de l'enceinte.

  A $N = -2$, la domination du gradient de masse sur le thermique, le rayonnement gazeux affecte la dynamique, la thermique et le champ de concentration de la même manière que pour $N = -1$ mais avec une amplitude plus faible.

Un autre cas considéré est le couplage entre la convection de double diffusion et le rayonnement du mélange de gas réél ($air - H_2O$ et $air - CO_2$). L'obstacle étant à la fois source de chaleur et de polluant, selon le mélange appliqué, nous avons deux types d'écoulements : opposant et aidant. La vapeur d'eau, dont on sait qu'elle est plus légère que l'air, crée un gradient de masse qui a la même direction que le gradient de température. Ces deux gradients provoquent donc des écoulements de même sens (cas aidant). Dans le cas du mélange $air - CO_2$, nous avons des écoulements opposant provoqués par deux gradients agissant en directions opposés car la densité molaire de CO_2 est plus grande que celle de l'air sec. Les parois verticales de la cavité sont maintenues à $T_c = 530K$, $C_l = 0$ et pour l'obstacle, elles sont $T_h = 580K$ et C_h[4]. Toutes les parois actives sont supposées noires alors que les parois adiabatiques sont totalement réfléchissantes. Les principales conclusions issues de résultats de simulations sont :

- Mélange $air - H_2O$

  Lorsque le rayonnement est pris en compte, aucun changement significatif n'est constaté par rapport au cas transparent, sauf dans le champ thermique. Le rayonnement tend à réduire la température du fluide dans la moitié supérieure de la cavité (où l'émission domine sur l'absorption). Cet effet augmente avec la fraction molaire de vapeur d'eau dans le mélange. Le rayonnement diminue également le transfert thermique total à l'intérieur de la cavité en raison de la diminution du transport convectif près des parois verticales et de l'atténuation du transfert radiatif par l'effet d'absorption. Le transfert de masse semble être inchangé en raison de la structure dynamique préservée.

- Mélange $air - CO_2$

  Le rayonnement tend à ralentir les couches limites (parois verticales de la cavité, surfaces latérales de l'obstacle) dans la partie inférieure de l'enceinte. Plus haut, il renforce le gradient thermique, crée un panache qui remplace le flux descendant dans l'enceinte observé dans le cas transparent. En outre, le rayonnement réduit la température dans la région proche de la paroi verticale dans la partie basse de la cavité. En revanche, il augmente le niveau de température dans la partie supérieure. Il renforce le panache thermique qui amène plus de fluide fortement chargé vers les régions élevées de la cavité, augmentant ainsi la concentration à ces niveaux. La présence de rayonnement réduit le transfert thermique total (par convectif près des parois verticales et transport radiatif le long de la surface supérieure de l'obstacle). De plus, elle diminue légèrement le transfert de masse.

[4] C_h dépend de la fraction molaire de référence fixée dans le milieu.

Contents

List of Figures

List of Tables

List of Symbols

A	area of the considered surface	m^2
a_j	weight of j^{th} gray gas	
c_p	specific heat	$\mathrm{J \cdot kg^{-1} \cdot K^{-1}}$
C	concentration	$\mathrm{mol \cdot m^{-3}}$
C_h	high concentration	$\mathrm{mol \cdot m^{-3}}$
C_l	low concentration	$\mathrm{mol \cdot m^{-3}}$
C_j	j^{th} absorption cross section	$\mathrm{m^2 \cdot mol^{-1}}$
D	mass diffusivity	$\mathrm{m^2 \cdot s^{-1}}$
$\boldsymbol{g}$	gravitional acceleration vector: 9.81	$\mathrm{m \cdot s^{-2}}$
G	incident radiation	$\mathrm{W \cdot m^{-2}}$
I	radiative intensity	$\mathrm{W \cdot m^{-2} \cdot sr^{-1}}$
l	obstacle size	m
L	cavity size	m
Le	Lewis number $Le = \frac{\alpha}{D}$	
$\boldsymbol{n}$	unit normal vector	
N	mass to thermal buoyancy ratio $N = \frac{\beta_C(C_h - C_l)}{\beta_T(T_h - T_c)}$	
N_g	number of gray gases	
Nu_c	convective Nusselt number $Nu_c = \frac{L}{\Delta T}\frac{\partial T}{\partial x}$	
Nu_r	radiative Nusselt number $Nu_r = \frac{Lq^{net}}{\lambda \Delta T}$	
Nu_t	total Nusselt number $Nu_t = Nu_c + Nu_r$	
P	absolute pressure	Pa
Pl	Planck number $Pl = \frac{\lambda}{4\sigma T_{ref}^3 L}$	
Pr	Prandlt number $Pr = \frac{\nu}{\alpha}$	
$\boldsymbol{q_r}$	radiative flux vector	$\mathrm{W \cdot m^{-2}}$
q^{inc}	incident radiative flux	$\mathrm{W \cdot m^{-2}}$
$\boldsymbol{s}$	unit vector on a propagation direction of radiation	
t	time	s

t_{ref}	reference time $t_{ref} = \frac{L^2}{\alpha\sqrt{Ra}}$	
T_c	absolute temperature at cold surfaces	K
T_h	absolute temperature at hot surfaces	K
T_{ref}	reference temperature $T_{ref} = (T_h + T_c)/2$	K
Ra	Rayleigh number $Ra = \frac{g\beta_T \Delta T L^3}{\alpha\nu}$	
u, v, w	velocity component	$\mathrm{m \cdot s^{-1}}$
U_{ref}	reference velocity $U_{ref} = \alpha\frac{\sqrt{Ra}}{L}$	$\mathrm{m \cdot s^{-1}}$
U_x	normalized velocity component $U_x = \frac{u}{U_{ref}}$	
U_y	normalized velocity component $U_y = \frac{v}{U_{ref}}$	
U_z	normalized velocity component $U_z = \frac{w}{U_{ref}}$	
R	ideal gas constant: 8.3144621	$\mathrm{J \cdot K^{-1} \cdot mol^{-1}}$
x, y, z	Cartersian coordinate	m
X, Y, Z	normalized coordinate $X = \frac{x}{L}, Y = \frac{y}{L}, Z = \frac{z}{L}$	
x_{CO_2}, x_{H_2O}	molar fraction of $C0_2$ and H_2O in the mixture	
ΔC	concentration difference	$\mathrm{mol \cdot m^{-3}}$
ΔT	temperature difference	K
α	thermal diffusivity	$\mathrm{m^2 \cdot s^{-1}}$
β_C	mass expansion coefficient	$\mathrm{m^3 \cdot mol^{-1}}$
β_T	thermal expansion coefficient	$\mathrm{K^{-1}}$
ϵ	emissivity	
κ	absorption coefficient	$\mathrm{m^{-1}}$
λ	thermal conductivity	$\mathrm{W \cdot m^{-1} \cdot K^{-1}}$
μ	dynamic viscosity	$\mathrm{m^2 \cdot s}$
η	wavenumber	$\mathrm{cm^{-1}}$
ν	kinematic viscosity	$\mathrm{Pa \cdot s^{-1}}$
ρ	density	$\mathrm{kg \cdot m^{-3}}$
τ	optical thickness	
Ω	solid angle	sr
Ω_m	m^{th} discrete direction	
σ	Stefan Boltzmann constant: 5.670367×10^{-8}	$\mathrm{W \cdot m^{-2} \cdot K^{-4}}$

Chapter 1

Introduction

1.1 Context and Configuration

Natural convection flows are sensitive to the effects of volume radiation in the presence of infrared active gases. This is appearent in particular in mixtures where an absorbing component diffuses into a transparent gas. While several studies have investigated this phenomenon in differentially heated cavities, in single and double diffusion, the case of a heating and diffusing obstacle placed on the floor constitutes a new worthy configuration of interest. Very schematically, it mimics the combustion of an object in the center of a room. The release of heat and the injection of polluting infrared active gases generate a confined buoyant plume due to the combined effects of thermal and concentration gradients. Moreover, radiative absorption and emission within the fluid depends on the gas composition, strongly influences the temperature distribution and, in turn, alters the flow motion.

The configuration under consideration in this thesis is illustrated in figure 1.1. It deals with a cubical cavity of size $L = 0.25m$ having adiabatic horizontal walls, while the vertical ones are maintained at a constant and uniform temperature (T_c). A small solid cube of size $l = 0.05m$ is located at the center of the bottom wall. It creates an opaque obstacle whose surfaces are set uniformly at a higher temperature than the walls ($T_h > T_c$).

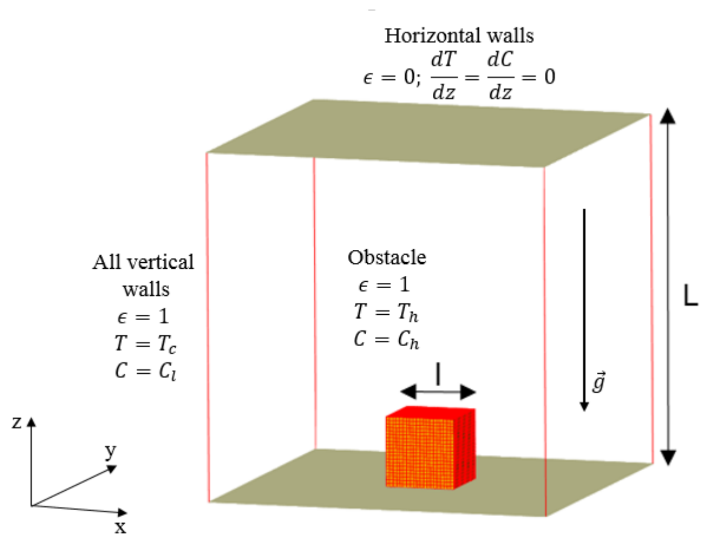

Figure 1.1: Problem configuration

The enclosure is filled with either dry air or a binary mixture involving an absorbing component, depending on the case study. In pure thermal convection, the medium is homogeneous in composition and the temperature difference between the obstacle and the cavity walls generates a natural convection flow. In double-diffusive cases, a concentration gradient is prescribed within the enclosure: it creates additional buoyancy forces that may either cooperate or oppose to those of thermal origin, depending on the molar weight of the injected species. The highest value C_h of this component is uniformly fixed at the obstacle surfaces and the lowest concentration C_l is prescribed along the active (cold) walls of the enclosure.

1.2 Objective of the thesis

Our goal is to study the natural convection flows generated in the configuration described above in the presence of volume radiation within the gas. These flows are, by nature, complex, especially in double diffusion where the cooperating/opposing configurations can generate original structures, and this even in the absence of radiative participation.

Transparent medium

The study will therefore include, firstly, an analysis of the phenomena in a transparent gas (confined double diffusion plume: co-operating and opposite case). This first approach can be carried out using a dimensionless formulation: this will highlight the characteristic parameters of the configuration (in particular, the definition of the Rayleigh number). The results will concern the dynamic, thermal and mass fields in laminar regime and at steady state, for different values of the mass-to-thermal buoyancy ratio. Steady state solutions are mainly considered, but unsteady behaviors can be reached in some typical cases. This series of calculations will provide reference results when dealing with cases involving radiative effects.

Gray gas

A first approach to participating gases can be carried out by assuming that the absorbing mixture is gray. This amounts to working with a hypothetical medium whose opacity can be freely varied, which is advantageous for a parametric study. It is also possible, at this stage, to maintain a formulation in non-dimensional quantities. The idea is to reproduce some simulations, already carried out without radiation, with a gas whose reference optical thickness varies from 0 (transparent case) to a few units (2, in general). This approach is expected to reveal major trends in the influence of radiation on the flow behavior and on heat and mass transfers.

Real gases

The last - and the most important - part is the simulation of real gas flows. Concretely, we will consider $air - H_2O$ and $air - CO_2$ mixtures with a prescribed concentration of absorbing species at the surfaces of the obstacle and a zero concentration on the vertical walls of the cavity. Cases with water vapor will give rise to cooperating flows, those with CO_2 to opposing flows. Concentrations will be varied in situations where thermal diffusion dominates, mass diffusion dominates, or both phenomenons are equivalent.

We will analyse the results by comparison with the cases involving a transparent gas.

1.3 Bibliography review

1.3.1 Natural convection with the consideration of radiation

The first work about the coupling of natural convection and radiation was performed by Goody [36] with the gray gas assumption in the framework of Rayleigh-Bernard configuration in the stellar atmospheres. The authors concluded that the fluid radiation delays the trigger of the instability by decreasing the thermal stratification and damping the temperature fluctuations. Bdéoui and Soufiani [37] have extended this problem to the real gas mixture using a rigorous linearisation of the radiative source term and the same conclusion was found.

In recent decades, many researchers have given more attention to the configuration of the differentially heated enclosure. They considered the effects of surface radiation (transparent gas) as well as volume radiation from a participating fluid.

Concerning surface radiation, the coupling of convection with radiative transport is indirectly created through the boundary conditions of a prescribed flux on the bounding surfaces. In this framework, Behnia, Reizes, and De Vahl Davis [38] have investigated the coupled process within a rectangular cavity. The horizontal walls were assumed to be adiabatic, a vertical wall was opaque and maintained at high temperature (150°C) while the other was semi-transparent and was exchanging with the outer environment (kept at 20°C) by convection and radiation. The results obtained in the range of Rayleigh number $[10^4 - 3 \cdot 10^5]$ showed that surface radiation accelerates the fluid motion and this effect increases with this parameter.

Wang, Xin, and Le Quéré [39] considered the natural convection-radiation coupling inside a rectangular cavity filled with air. All the walls had the same emissivity. The results showed that the radiation of adiabatic wall lowers the average temperature of top wall while increasing the temperature of the bottom wall. This reduces the thermal stratification of the fluid inside the cavity and the influence of the radiation was still found significant at low temperature and with weak emissivities. It was also observed that the radiative coupling lower the critical Rayleigh number beyond which the unsteady solutions occur.

Regarding the volume radiation effects within the fluid, Lauriat [40] has investigated the coupled transfer in a vertical tall cavity (whose height to width ratio was varied between 5 and 20) filled with a gray gas. The computations were performed at different opacities and Rayleigh numbers. The predictions of the radiant field was achieved using the P_1 method. The results showed that, in convective regime, the radiation of gray gas increases the velocities in boundary layers and decreases the vertical thermal stratification.

The same observations were reported by Yücel, Acharya, and Williams [1] while considering a square cavity whose walls are black and with the optical thickness varying between 0.2 and 5. The Rayleigh number was $5 \cdot 10^6$. In addition, the authors concluded that volume radiation warms up the center of the cavity and, through that, alters the thermal field.

Similarly, Tan and Howell [2] have addressed the effects of volume radiation on natural convection inside a 2D cavity at different Ra in the range of $[10^3 - 10^5]$ and $Pr = 0.72$. The sensitivity to the parameters that characterize radiation (wall emissivity, optical thickness, Planck number and albedo) has been analyzed and it was found that all of them, except the albedo, significantly affect the heat transfer.

Other works by Han and Baek [41] and Lari et al. [42] in the same framework provided similar conclusions.

Colomer et al. [3] have extended the calculation of coupled natural convection and radiation of a gray gas from a bi-dimensional enclosure to a cubical cavity. The results showed that the radiation increases the 3-D effects at the intermediate optical thickness. In addition, with a constant Rayleigh number, the heat flux at the hot wall decreases as the optical thickness increases.

Later, Colomer, Consul, and Oliva [4] as well as Lari et al. [43] have studied the coupled natural convection and radiation using different approaches for modeling the real gas mixtures. The authors concluded that the use of the gray gas approximation overestimates the radiative transfer and the fluid circulation of real gas mixtures.

Regarding real gas mixtures, Soucasse et al. [5] have studied natural convection in a cubical cavity filled with an $air/H_2O/CO_2$ mixture. The results showed that radiative transfer homogenizes the thermal field and accelerates the vertical boundary layer. This steady state problem was later extended to the weakly turbulent and unsteady regime in Soucasse et al. [44]. The authors reported a transition to the unsteadiness at $Ra = 3 \cdot 10^8$ and, beyond this value, volume radiation intensifies the turbulent fluctuations and decreases the thermal stratification in the center of the cavity.

Recently, Billaud, Saury, and Lemonnier [6] have considered the case of a differentially heated cubical enclosure filled with humid air and have varied the cavity size. They used the Discrete Ordinates Method associated with the SLW model for the calculation of radiative source term within the fluid. All the simulations were performed at $Ra = 10^6$ and $Pr = 0.71$. The results showed that the thermal field and velocities field depend on the cavity length even when keeping the Ra-value constant. More generally, radiation was found to accelerate the global circulation in the enclosure to limit the stagnant core region of the cavity.

Beside the numerical works, there exist a few experimental studies by Fusegi and Farouk [45] and Clergent [46], for instance, for the coupled natural convection and radiation in a differentially heated cavity. In order to prevent the condensation of water vapor, the gas used in these experiments is usually carbon dioxide or ammonia. An interferometry method has been used for the measurement of temperature. Because of the difficulty of setting the boundary conditions and fluid characteristics as precisely as in the numerical calculations, the comparisons between numerical and experimental results are delicate.

1.3.2 Combined double diffusive convection and radiation

Several studies dealing with the coupling of double diffusive convection and the radiation have been performed. Borjini et al. [47] have investigated the case of a square cavity filled with a gray gas whose absorption coefficient was assumed independent of the concentration of the absorbing component. The calculations have been performed at $Ra = 10^5$, $Le = 2$ and $Pr = 13.6$. Different optical thicknesses have been considered. The results showed that the radiation alters the flow structure inside the cavity.

Rafieivand [48] and Mezrhab et al. [49] were the first to report results in a more realistic case for a differentially heated square cavity filled with a binary gas mixture, still considered as a gray gas, whose radiative properties were depending on the local concentration of the absorbing component. The calculations were performed at $Ra = 5 \cdot 10^6$, $Pr = 0.71$ and different values of the mass-to-thermal buoyancy ratio. They showed that radiation could either alter or eliminate the vertical stratification of density, which may drive the oscillatory behavior in unsteady state.

Meftah et al. [50], Laouar-Meftah et al. [51] extended the previous study to real gas mixtures such as $air - H_2O$ and $air - CO_2$ at different mole fraction. They used the SLW model to determine the fluid radiative properties as function of the local thermodynamic state. Their results show that radiation breaks the centro-symmetry of the thermal field, concentration field and flow structure compared to the transparent cases. It was also pointed out that the fluid is accelerated in both the vertical and horizontal boundary layers when thermal and concentration gradients cooperate. On the other hand, gas radiation has little influence on mass transfer, but due to the homogenization of the temperature field, the vertical thermal stratification decreases and thus reduces the convective transfer. Moreover, the radiative transfer between the two active walls also decreases because of the absorption by the participating gas. For these two reasons, the global heat transfer is lowered.

Ibrahim and Lemonnier [52] studied the transient processes in 2D-configurations filled with a $N_2 - CO_2$ mixture with the Rayleigh number up to $1.5 \cdot 10^9$. They reported that radiation, for cooperating flows, stabilizes the fluid motion and slightly accelerates the transition to the steady state. Conversely, for opposing flows, it delays the achievement of the steady state and may even promote the development of thermalsolutal instabilities.

The work of Cherifi et al. [53] is an extension to a 3-D configuration of the study by Laouar-Meftah et al. [51]. The authors investigated only the cooperating flow. The results showed that radiation slightly affects the fluid motion near the transverse walls. The radiation also breaks the symmetry of thermal and concentration field as well as flow structure compared to a transparent medium. The total heat transfer is reduced while the influence of radiation on mass transfer is not sensible.

1.3.3 Enclosures with an obstacle or a heat source

First of all, concerning the natural convection inside a cavity containing and opaque obstacle within it, Paroncini and Corvaro [13] published a study based on numerical calculations and experiments inside a square cavity with an obstacle located on its floor. Regarding the experimental approach, the authors used the PIV (Particle Image Velocimetry) method for the detection of flow structures (velocity field, stream function and velocity vector distribution) and an interferometry technique to evaluate heat transfer, and especially the local and mean Nusselt numbers. The investigation were performed for Rayleigh numbers ranging from $3 \cdot 10^4$ to $3.5 \cdot 10^5$. The results showed that the Nusselt number increases with this parameter. Besides it was found that among the three considered heights of the hot source: 0, 0.25 and 0.5 (compared to the cavity size), when the size of the heated obstacle reaches one half of the cavity, the convective heat transfer is the worst while the height of one fourth the cavity length gives the best performance.

Gibanov and Sheremet [16] have investigated the natural convection in a 3-D enclosure with a heat source of triangular cross section on its floor. The authors performed the numerical simulations for the Rayleigh number in the interval $[10^4 - 10^6]$. They observed that the increase in Rayleigh number leads to the decrease of the thermal boundary layer while intensifying the convective flow.

Mousa [54] has modeled the natural convection inside a differentially heated square cavity containing an adiabatic obstacle. The calculations have been run for $Pr = 0.71$ and the Rayleigh number ranging in $[10^2 : 10^7]$. The results have been considered with respect to the aspect ratio between the obstacle and cavity size. It is reported that as the aspect ratio increases, the heat transfer rate decreases at Rayleigh number in $[10^2 : 10^4]$, augments for the Ra values in $[10^5 : 10^6]$ and seems to be maintained at $Ra = 10^7$.

Raji et al. [55] have considered the effect of the subdivision of an obstacle on the natural convection in a square cavity. The investigation was performed for different values of Rayleigh number in $[10^3 - 10^8]$ with different numbers of sub-obstacles. The results showed that the increase in the number of blocks reduced the heat transfer and fluid motion.

Kuznetsov and Sheremet [11] have investigated the natural convection inside a rectangular cavity with a local heating on a vertical wall. The calculations were performed at $Pr = 0.71$, $Gr = 10^7 - 10^9$. The results showed that the heat transfer was increased with greater Grashof numbers. The authors have also considered the problem of conjugate heat transfer in a closed domain with a locally lumped heat-release source at $Pr = 0.71$ and $Gr = 10^5 - 10^7$. The results reported in the work by Kuznetsov and Sheremet [12] pointed out that as the Grashof number increases, the structure of central vortex, which drives the formation of the temperature profile inside the room, changes in the manner that its center shifts toward the right part of calculation domain. An experimental research on convective heat transfer has been conducted by Kuznetsov, Maksimov, and Sheremet [14] in the configuration of a closed parallelepiped containing a local energy source.

Kuznetsov and Sheremet [56] have simulated a typical element of electronic equipment by a 3-D gas filled cavity surrounded by thick solid walls that contains a local heat source located on its floor. This configuration has one vertical wall with variable thermal physical properties, which is in contact with outer environment. The others are insulated. The authors have investigated the convective process inside the cavity with respect to the variation in intensity of the heat source and to the environment conditions. It was shown a destabilizing role of the heat source on the flow structure and a significant effect of external conditions on the hydrodynamic and heat transfer in the system.

Souayeh et al. [15] have studied the unsteady natural convection within a square cavity containing an obstacle at Rayleigh number in the range $[5 \cdot 10^5 - 10^7]$. The authors observed the slight decrease in the extreme values of the stream function, which was explained by the appearance of a small are of re-circulation occurring at the horizontal wall of the obstacle.

Bouafia and Daube [19] have studied the natural convection for large temperature gradients within a rectangular cavity with an inner square solid body. The effects of the aspect ratio as well as of the Rayleigh numbers have been investigated. The results showed that, for any considered values of the aspect ratio, the steady flow can be obtained at a low enough Rayleigh number; for sufficiently large values of Rayleigh number, a periodical flow always appears, but the transition to unsteadiness occurs in different manners depending on the aspect ratio.

Hernandez [10] has studied the natural convection generated by a heat source placed at the center of the bottom of a rectangular cavity. The computation were carried out at different values of Rayleigh number : 10^4, $5 \cdot 10^4$, 10^5. The author concluded that the unsteadiness of the flow in high aspect ratio cavity at high Rayleigh number and low Prandlt number come from the shear instability of the interaction between ascending and descending fluid layers.

Concerning the coupled natural convection and surface radiation, Sun, Chénier, and Lauriat [20] have studied the coupling of natural convection and surface radiation inside a square cavity with an obstacle at its center. The results showed that surface radiation stabilizes the fluid motion inside the cavity. The range of Rayleigh number in which the transition between steady and oscillatory flows appears was shifted from $Ra_{c1} = 2 \cdot 10^5$ and $1.7 \cdot 10^5 < Ra_{c2} < 1.75 \cdot 10^5$ for pure natural convection to $Ra_{c1} = 3.15 \cdot 10^5$ and $2.85 \cdot 10^5 < Ra_{c2} < 2.9 \cdot 10^5$. The authors have also investigated the effects of the inner body size and pointed out that at the aspect ratio between the obstacle and the cavity of $A = 0.8$, the conduction dominates the heat transfer process in the enclosure.

Patil, Sharma, and Velusamy [23] have investigated the combined natural convection and surface radiation in an enclosure containing a protrusion. The studies on the protrusion shape and position and surface emissivity have been performed for Rayleigh numbers in range of 10^3-10^6 with surface emissivity values varying in $[0;1]$. The results showed that the surface radiation did not much alter the velocity field but it changes noticeably the wall temperature: it partially increases this quantity at the bottom wall and decreases this parameter at the top temperature.

Martyushev and Sheremet [21] have investigated the effect of surface radiation on the natural convection in an enclosure with a local energy source. In their works, different sizes of the hot obstacle and different positions have been considered. The calculations have been performed at $Ra = 10^6$ and $Pr = 0.7$ while the emissivities of the active surfaces are set to $0 \leq \epsilon < 1$. The results pointed out that the increase in the emissivity leads to intensify the radiative transfer but reduce the convective Nusselt number. Besides, the increase in the length of the energy source induces the slow down of the arrival at a steady state.

Very recently, Ying Wang [57] has considered a confined thermal plume inside an air-filled cubical cavity containing a line heat source. The simulations have been performed at Ra in the interval $[10^6 - 10^9]$. The impacts of gas radiation on the flow have been taken into account using a gray gas assumption and the SLW model (for predicting the radiative properties of an $air - H_2O$ mixture). The results have reported that volume radiation stabilizes the plume, delays the transition to the instability. It also homogenizes the thermal field.

1.4 Thesis organization

This manuscript is divided into six main chapters. Firstly, the present chapter introduces the motivation of the thesis, its objectives and a bibliography review about some related researches in the recent decades. Then, in the second chapter, we provide more details about the mathematical models as well as the numerical methods used in this study. Chapter three will introduce Code Saturne, the CFD simulation tool used all along our work and the implementation of our own SLW model into the built-in radiative module of this code. We also present some validation tests for assessing the accuracy of our calculations in configurations with an increasing degree of complexity. The fourth chapter contains the results and analysis about the combined thermal convection and radiation in a gray gas as well as in a real gas mixture. Then, chapter five will focus on the radiation effects in many typical situations of double diffusive convection, either cooperating or opposing, in gray or real gas mixture. To end with, the concluding chapter will synthesize the main results of this study and provide perspectives for future works.

Chapter 2

Methodology

In this chapter, we present the mathematical model of the double diffusive convection and the method for solving the radiative transfer equation. We recall that the studied configuration is illustrated in figure 1.1. It deals with a cubical cavity containing an obstacle (diffusion source of heat and pollutant) located on its floor. The enclosure is filled with dry air or a binary mixture involving an absorbing-emitting component.

2.1 Mathematical model

2.1.1 Main assumptions

- The flow in the cavity is three-dimensional, laminar.
- The fluid is considered as Newtonian and incompressible.
- The active surfaces (vertical walls of the enclosure and outer surfaces of the obstacle) are black with respect to radiation while the adiabatic surfaces (ceiling and floor of enclosure) are purely reflective.
- The variations in temperature and concentration within the cavity are weak enough to allow the Boussinesq approximation. Consequently, the variations of the fluid properties are ignored, except for density in the buoyancy force expression, which is written as:

$$\rho(T, C) = \rho_0[1 - \beta_T(T - T_0) - \beta_C(C - C_0)] \tag{2.1}$$

  Here, ρ_0 is the density of the mixture in an average state (T_0, C_0) and β_T, β_C denote, respectively, the thermal and concentration expansion coefficients:

$$\beta_T = -\frac{1}{\rho}(\frac{\partial \rho}{\partial T})_{P,C} \tag{2.2}$$

$$\beta_C = -\frac{1}{\rho}(\frac{\partial \rho}{\partial C})_{P,T} \tag{2.3}$$

- The viscous dissipation and pressure work are negligible.
- Soret and Dufour effects are negligible.

2.1.2 Fluid Dynamics Equations

Several conservation equations govern the flow motions and the transfer processes in the enclosure. They express a local balance in mass, momentum, energy and composition within the fluid:

- Continuity equation
  Since density variations are neglected, the total mass conservation reads:

$$\nabla \cdot \mathbf{u} = 0 \tag{2.4}$$

- Momentum equation

$$\rho_0 \frac{\partial \mathbf{u}}{\partial t} + \rho_0 \mathbf{u} \cdot \nabla \mathbf{u} = -\nabla p + \rho_0(\beta_T(T_0 - T) + \beta_C(C_0 - C))\mathbf{g} + \mu \nabla^2 \mathbf{u} \tag{2.5}$$

  The source term $\rho_0(\beta_T(T_0 - T) + \beta_C(C_0 - C))\mathbf{g}$ accounts for the buoyancy force that sets the fluid into motion (here expressed under the Boussinesq approximation).

- Energy equation

$$\rho_0 C_p \frac{\partial T}{\partial t} + \rho_0 C_p \mathbf{u} \cdot \nabla T = \lambda \nabla^2 T - \nabla \cdot \mathbf{q} \tag{2.6}$$

  The divergence term $-\nabla \cdot \mathbf{q}$ is the internal radiative source resulting from the difference between the absorbed and emitted radiant energy in each elementary volume of fluid.

- Concentration equation
  In this study, we only consider binary mixtures. A component (which absorbs and emits radiation) diffuses into a transparent gas. Its concentration obeys a conservation equation that, under the Boussinesq approximation, is expressed as :

$$\frac{\partial C}{\partial t} + \mathbf{u} \cdot \nabla C = D \nabla^2 C \tag{2.7}$$

All the conservation equations are coupled: the dynamic field influences the transport of scalar quantities (T and C) which, in turn, drive the flow through the buoyancy effects. Moreover, the concentration has a direct effect on the thermal field since it changes the absorption-emission properties of the medium. Therefore, the radiative source in the energy balance is impacted.

2.1.3 Radiative transfer equation

The cavity is filled with a semi-transparent gaseous medium at local thermodynamic equilibrium, which absorbs and emits radiation at any point in space. The spectral radiation intensity $I_\eta(\mathbf{s}, \mathbf{\Omega})$[1] represents the radiant flux (per unit solid angle and per unit wavenumber) that propagates at point $\mathbf{s} = (x, y, z)$ in the direction $\mathbf{\Omega}$ at the

[1] s is the position vector

wavenumber η. In a non-scattering medium, the local change of intensity is described by the radiative transfer equation:

$$\mathbf{\Omega} \cdot \mathbf{\nabla} I_\eta(\mathbf{s}, \mathbf{\Omega}) = -\kappa_\eta(s) I_\eta(\mathbf{s}, \mathbf{\Omega}) + \kappa_\eta(\mathbf{s}) I_{b\eta}(T(\mathbf{s})) \tag{2.8}$$

where $\kappa_\eta(\mathbf{s})$ is the local spectral absorption coefficient defined as $\kappa_\eta(\mathbf{s}) = N(\mathbf{s})\ X(\mathbf{s})\ C_\eta(\phi(\mathbf{s}))$. In this expression, $C_\eta(\phi(\mathbf{s}))$ is the spectral absorption cross section, which depends on the local thermodynamic state, $\phi(T, P, C)$, $X(\mathbf{s})$ the mole fraction and $N(\mathbf{s})$ the molar density of the absorbing species (Denison and Webb [58]). The radiative intensity depends on three position coordinates, two direction variables (either two polar angles or two direction cosines) and the wavenumber. The total intensity can be found by integration over the whole spectrum as:

$$I(\mathbf{s}, \mathbf{\Omega}) = \int_0^\infty I_\eta(\mathbf{s}, \mathbf{\Omega}) d\eta \tag{2.9}$$

The term $-\mathbf{\nabla} \cdot \mathbf{q}$ which appears in the energy equation is the total divergence of the radiative flux. This flux can be calculated from the total intensity by the expression:

$$\boldsymbol{q}(\mathbf{s}) = \int_0^{4\pi} I(\mathbf{s}, \mathbf{\Omega}) \mathbf{\Omega} d\Omega = \int_0^{4\pi} \int_0^\infty I_\eta(\mathbf{s}, \mathbf{\Omega}) \mathbf{\Omega} d\eta d\Omega \tag{2.10}$$

and, as a result:

$$\begin{aligned} -\mathbf{\nabla} \cdot \boldsymbol{q}(\mathbf{s}) &= \int_0^\infty \int_0^{4\pi} (\mathbf{\Omega} \cdot \mathbf{\nabla} I_\eta(\mathbf{s}, \mathbf{\Omega})) d\Omega d\eta \\ &= \int_0^\infty \int_0^{4\pi} \Big(\kappa_\eta(\mathbf{s}) I_\eta(\mathbf{s}, \mathbf{\Omega}) - \kappa_\eta(\mathbf{s}) I_{b\eta}(T(\mathbf{s})) \Big) d\Omega d\eta \\ &= \int_0^\infty \int_0^{4\pi} \kappa_\eta(\mathbf{s}) I_\eta(\mathbf{s}, \mathbf{\Omega}) d\Omega d\eta - 4\pi \int_0^\infty \kappa_\eta(\mathbf{s}) I_{b\eta}(T(\mathbf{s})) d\eta \end{aligned} \tag{2.11}$$

2.1.4 Boundary conditions

Conservation equations

All the surfaces of the obstacle[2] are set at constant and uniform temperature and concentration:

$$\begin{aligned} T &= T_h \\ C &= C_h \end{aligned} \tag{2.12}$$

Regarding the cavity:

- Vertical walls are uniformly maintained at constant temperature and concentration:

$$\begin{aligned} T &= T_c \\ C &= C_l \end{aligned} \tag{2.13}$$

- Horizontal walls are adiabatic, impermeable and assumed to behave as fully reflective surfaces:

$$\frac{\partial T}{\partial z} = 0 \quad \text{at} \quad z = 0, L \tag{2.14}$$

[2]Except the surface in contact with the floor of the cavity

$$\frac{\partial C}{\partial z} = 0 \quad \text{at} \quad z = 0, L \tag{2.15}$$

Zero velocities are applied to all the walls of the cavity and all the surfaces of the obstacle.

Radiative Transfer Equation

To solve the radiative transfer equation, we need to input the intensity coming from the bounding walls towards the fluid. This intensity is prescribed for all direction $\mathbf{\Omega}$ pointing inward to the cavity such that $\mathbf{\Omega} \cdot \boldsymbol{n} > 0$ where $\boldsymbol{n}$ is the local unit vector[3] on the boundary limit. Assuming gray diffuse surfaces, the boundary condition reads:

$$I_\eta(\mathbf{s}, \underset{(\mathbf{\Omega}\cdot\boldsymbol{n}>0)}{\mathbf{\Omega}}) = \epsilon I_{b\eta}(T(\mathbf{s})) + (1-\epsilon) q_\eta^{inc} \tag{2.16}$$

where:

$$q_\eta^{inc} = \int_{\mathbf{\Omega}\cdot\boldsymbol{n}<0} I_\eta(\mathbf{s}, \mathbf{\Omega}) |\mathbf{\Omega} \cdot \boldsymbol{n}| d\Omega \tag{2.17}$$

In this study, the surfaces of the obstacle and the vertical walls of the cavity are black ($\epsilon = 1$) and the horizontal walls of the enclosure are purely reflective ($\epsilon = 0$).

2.1.5 Heat and Mass Transfer

To investigate the thermal and mass wall fluxes, we calculate the Nusselt and Sherwood numbers[4]. Their local values are defined as follows:

- The local convective Nusselt number refers to the ratio of convective to conductive heat transfer at a boundary in a fluid:

$$Nu_C = \frac{L}{\Delta T} \left| \frac{\partial T}{\partial x} \right|_{x=0,L} \tag{2.18}$$[5]

- The local radiative Nusselt number represents the ratio of radiative to conductive heat transfer at a bounding wall of the enclosure:

$$Nu_R = \frac{L}{\lambda \Delta T} |q_{r,x}^{net}|_{x=0,L} \tag{2.19}$$

  where $q_{r,x}^{net} = \epsilon(\sigma T_(\mathbf{s})^4 - q^{inc}(\mathbf{s}))$ at $x = 0, L$

- The local total Nusselt number adds up the contribution of convective and radiative transfer:

$$Nu_T = Nu_C + Nu_R \tag{2.20}$$

[3] $\boldsymbol{n}$ is the vector pointing into the medium that it is the inner vector for the cavity walls and the outer vector at the surface of the obstacle.

[4] This quantities are considered only at the active surfaces which consist of: the lateral walls of the cavity, the vertical and top walls of the obstacle.

[5] This expression holds for the walls that are normal to the x-direction of the cavity. For the other bounding surfaces of the enclosure and the obstacle, it needs to be changed to adapt the normal vector and the positions of the walls.

- The local Sherwood number refers to the ratio of convective mass transfer to diffusive mass transport:

$$Sh = \frac{L}{\Delta C} \mid \frac{\partial C}{\partial x} \mid_{x=0,L} \tag{2.21}$$

Integrating these quantities over the bounding walls yields the following mean values:

- Mean convective Nusselt number:

$$\overline{Nu}_C = \frac{L}{A \cdot \Delta T} \int_A \mid \frac{\partial T}{\partial x} \mid dA \tag{2.22}$$

  where A is area of the considered surface.

- Mean radiative Nusselt number:

$$\overline{Nu}_R = \frac{L}{A \cdot \Delta T} \int_A \mid q_r^{net} \mid dA \tag{2.23}$$

- Mean total Nusselt number:

$$\overline{Nu}_T = \overline{Nu}_C + \overline{Nu}_R \tag{2.24}$$

- Mean Sherwood number:

$$\overline{Sh} = \frac{L}{A \cdot \Delta C} \int_A \mid \frac{\partial C}{\partial x} \mid dA \tag{2.25}$$

2.2 Gas Radiation Model

2.2.1 Resolution Methods of Radiative Transfer Equation

In coupled problems involving radiation transport, we have to solve the radiative transfer problem in addition to the conservation equations. Historically, several methods have been developed to achieve this goal. We just present here a short overview of the most popular approaches, and we refer the reader to the main textbooks in this domain for a complete survey (Modest [59], Lewis and Miller [60] for instance):

- Multiflux models.
  This method was first introduced in the pioneering works of Schuster [61] and Schwarzschild [62]. It is based on a division of the angular space, where the radiation intensity is considered as uniform in each discrete solid angles. The most popular approach remains the two-flux method for 1-D problems, in which the direction space is splitted into only two solid angles (one in each coordinate direction) over which the radiant intensities are assumed constant. The RTE is thus reduced to two differential equations. Recently, Dombrovsky, Randrianalisoa, and Baillis [63],[64] have applied this approach for the identification of the radiative properties of absorbing and scattering media and radiative properties of highly scattering dispersed materials in combination with a Monte Carlo method. This two-flux approximation was in the past extended

to four-flux (Vargas [65], Maheu, Letoulouzan, and Gouesbet [66], Maheu and Gouesbet [67]) and six-flux models (Brucato et al. [68], Puma and Brucato [69]) models for solving multi-dimensional problems.

- Spherical Harmonics Approximation : P_N
The P_N method was first proposed by Jeans [70] in the domain of the astrophysics and was further developed in the field of neutronics. It consists in developing the radiative intensity on a basis of orthogonal functions truncated at the order N: the spherical harmonics associated with the Legendre polynomials P_N (Shen [71], Weisstein [72]). High order P_N approximations for radiative transfer in arbitrary geometries were introduced by Bayazitoilu and Higenyi [73], Mengüç and Viskanta [74]. Practice shows that order 1 can give good results in certain configurations and that moving to higher orders increases considerably the computational cost for a moderate gain in accuracy. This method (P_1 or differential approximation, Modest [59]) has the advantage of the simplicity and the compatibility with standard methods for the solution of the energy equation. But in the optical thin limit, errors appear while treating the radiative flux coming from the bounding surfaces. A modification has been proposed by Olfe [75] to eliminate this error. Radiation coming from walls is calculated separately with an accurate method and the P_1-approximation only applies to radiation originating from medium emission. Modest [76] has extended this modified version to three-dimensional and linear-anisotropically scattering media with reflecting boundaries.

- Discrete Ordinate Method : DOM
The method was introduced by Chandrasekhar [77] in the field of astrophysics. Then, Lee [78], Lathrop [79] and Carlson [80] used the DOM to solve neutron transport problem. After that, Fiveland [81], Fiveland [82], Fiveland [83], Truelove [84], Truelove [85] have adapted the method to the solution of radiative heat transfer. Jamaluddin and Smith [86] applied the DOM for the heat transfer problem in an axisymmetric cylindrical enclosures, while Kim and Baek [87] used this approach in analysis of combined conductive and radiative transfer in a two-dimensional rectangular enclosure. Colomer et al. [3] have investigated the combined radiation and natural convection in a three dimensional cavity working with the DOM. Overall, the principle of the discrete-ordinate method is to replace the angular integrals by a numerical quadrature formula:

$$\int_0^{4\pi} f(\mathbf{\Omega}) d\Omega \approx \sum_{m=1}^{M} \omega_m f(\mathbf{\Omega}_m) \tag{2.26}$$

The selections of set of directions and weights is in general constrained by the need of preserving the symmetry of radiant propagation. Different quadratures have been introduced by Lee [78], Lathrop and Carlson [88], Truelove [84], Fiveland [81], Thurgood [89], Koch et al. [90] and Balsara [27], among others.

The solutions from the DOM are affected by two types of inaccuracies: false scattering and ray effect, which are caused by the spatial and angular discretization errors respectively. The false scattering is similar to the 'numerical diffusion' in CFD calculations. It is related to the interpolation schemes that are involved by the method. The first order upwind scheme (STEP) creates false diffusion (however, this problem can be reduced by using a fine spatial discretization), while the second order DIAMOND scheme may produce negative intensities and thus fluctuations in radiative flux. A solution for this problem is to use high order bounded schemes such as the CLAM scheme (Coelho [91]). In order to reduce the 'ray effect', Ramankutty and Crosbie [92], Ramankutty and Crosbie [93] introduced a modified version of the DOM for treating separately the radiation coming from surfaces and medium in two and three dimensional problem respectively. In a recent past, this approach has also been considered for the radiative transfer problems with irregular geometries by Amiri, Mansouri, and Coelho [94].

Besides, for treating complex configurations, different structured and unstructured grid procedures such as block off, embedded boundaries, body-fitted structure, body-fitted unstructured, multi-block, local grid refinement have been proposed and then reported by Coelho [95]. Recently, different spatial schemes in discrete ordinates method using 3D unstructured mesh have been compared by Joseph et al. [96], while, the block-off and embedded boundary procedure have been used to mesh the irregular enclosures with Cartesian grid by Aghanajafi and Abjadpour [97]. In addition, Le Hardy et al. [98] have developopped specific numerical algorithms for handling specular reflection when solving 3D radiative transfer equation using DOM.

- Finite Volume Method : FVM
  Raithby and Chui [99] first introduced this method for predicting the radiant heat transfer in enclosures with participating media. Other researches in the same frame work were introduced by Chui, Raithby, and Hughes [100] for radiative problems in cylindrical enclosures. In this method, the RTE is integrated over the space and the solid angle like in Discrete ordinates method. The main difference between these two methods regards the angular discretization (Coelho [95]). In the DOM, integrals over solid angles are replaced by the quadratures while, in the FVM, the RTE is integrated over a solid angle, often referred to as a control angle, $\Delta\Omega$ which arises from the discretization of the entire spherical solid angle. Hunter and Guo [101] have compared these two methods over the problems of radiative transfer problem in cylindrical geometries and concluded that with the same grid size and number of discrete direction, the DOM is more efficient than the FVM (less memory used and faster calculation).

- Zonal Method : ZM
  Zonal method was first introduced in radiative heat transfer by Hottel and Cohen [102]. In this method, the surface and the volume of an enclosure are divided into a number of zones, each assumed to have a uniform distribution of temperature and radiative properties. The direct exchange areas (factors) between the surface and volume elements are evaluated and the total exchange areas are determined using matrix inversion techniques (Viskanta and Mengüç [103]). Since this method was first introduced for an absorbing, emitting and non-scattering gray gas with constant absorption coefficient, Hottel and Sarofim [104] improved it to relax this last restriction. Recently, Ebrahimi et al. [105] have used the zonal method to calculate radiative heat transfer in

industrial furnaces using a simplified numerical integration to evaluate the exchange areas. The advantage of Zonal Method is its simplicity for the adaptation of different sets of boundary conditions but it is difficult to apply it to complex geometries. Moreover, the calculation of the direct exchange area may require a high computational cost.

- Monte Carlo Method : MCM
  The method was initially developed in the context of nuclear transport. Its first application to the thermal radiation problems is due to Fleck Jr [106] and Howell and Perlmutter [107]. In this approach, the method consists in simulating a finite number of photon histories through the use of random number generator (Lewis and Miller [60]). In its standard form, photo bundles are traced in a forward direction but, in case radiation comes to a small area, it may become inefficient. Collins et al. [108] have introduced a new approach called 'Backward Monte Carlo' based on the review of Case [109]. Modest [110] recently published his research about Backward Monte Carlo in a scattering media and show that this backward method become inefficient when the scattering coefficient increases. The Monte Carlo method can easily handle anisotropically scattering media, complex geometries and spectral aspects. Its accuracy regularly serves as reference for other calculation tools. Its main drawback is the large computational time needed to achieve the results.

  Recently, Fournier et al. [111] have presented the problem of combined heat transfer using a single Monte Carlo algorithm. It is then applied in complex geometry problems by Ibarrart et al. [112] and Caliot et al. [113].

- Discrete Transfer Method: DTM
  This method was first introduced in the work by Lockwood and Shah [114]. It is similar to the ray tracing method in choosing a set of directions along which the propagation of radiation is computed. The ray from each point of a surface is traced in a given direction through the medium until it meets another surface. Henson and Malalasekera [115] have compared the DTM and Monte Carlo for radiative heat transfer in three-dimensional, non homogeneous, scattering media and pointed out the good agreement between the two methods. Selçuk and Kayakol [116] have compared the DTM and DOM for radiative transfer calculation in rectangular furnaces and the results showed that S_4-approximation and DT64 (64 rays per wall node) give good predictions of flux density and radiative energy source term compared to the exact solutions, but DOM consumes about 3 orders of magnitude less CPU times than the DTM. This method, however, carries the advantage of easily treating the irregular geometries but, like the DOM, it may suffer from 'ray effect', an error linked to the angular discretization. Cumber [117] and Cumber [118] have proposed some modifications for this method while Coelho and Carvalho [119] have developed a conservative formulation of DTM. Heugang, Kamdem Tagne, and Pelap [120] have performed the calculations of radiative heat transfer through anisotropically scattering media and showed that DTM can correctly deal with this problem, but a finer angular discretization is necessary when the scattering anisotropy is strong.

  Some years ago, Feldheim and Lybaert [121] have developped a DTM approach for the radiative transfer equation in a gray medium on unstructured triangular meshes. It was validated and found to perform well on pure radiative as well as combined heat transfer problems.

Coelho et al. [122] solved the radiation problem in 2-D enclosures with an obstacle using DTM, DOM, FVM, MC, ZM. They found that DOM and FVM are the most efficient in terms combined accuracy and computational cost.

In the present study, we have used the Discrete Ordinate Method for our radiative calculations because of its good compromise between the accuracy and computational cost and its easy implantation in many CFD codes. In particular, Code Saturne, an open-source CFD code developed by EDF (Archambeau, Méchitoua, and Sakiz [123]), offers an already integrated radiative DOM module. More details about the Discrete Ordinate Method are provided in the next chapter along with the description of its implementation in the Code Saturne code.

2.2.2 Gas models

Whenever gas radiation is considered, the actual spectral behavior of the fluid absorption must be accounted for. To that end, various gas models have been introduced with different levels of complexity, computational requirements and accuracy. These models can be classified into three main groups as:

- Line by Line model
- Band models
- Global models

2.2.2.1 Line by Line model

The Line by line model is considered as the most accurate. It is constructed by discretizing the absorption spectrum into discrete values (up to one million) so that the full spectral dynamics of the gas mixture can be recovered. As a result, the radiative transfer equation must be solved as many times as there are discrete κ-values. It therefore requires a huge computational time. This is why it remains in practice not affordable in coupled problems (where radiation is calculated iteratively at each time step), but this method serves as a reference for assessing the accuracy of simplified models.

2.2.2.2 Band models

In the band models, the spectral domain is divided into intervals of a given size and the radiative properties of the gas are evaluated over each of them. There are mainly two groups of band models depending on the width of the spectral band: the narrow band and wide band models.

The Narrow Band Models are constructed by selecting a band size, which is narrow enough to keep the Planck function constant. There still are two main approaches: Statistical Narrow Band (SNB) and k-distribution. The SNB model was first introduced by Goody [124] and Godson [125]. In this method, the radiative properties of the gas (transmissivity or emissivity) are calculated by adopting a statistical model to describe the distribution of line intensities, widths and spacing. Therefore, this approach is not compatible with some methods of solution of the

RTE, such as P_1 or DOM, which requires explicit values of the absorption coefficients (Taine and Soufiani [126]). The k-distribution model was first reported in Kondratyev [127]. It is based on the observation that the absorption coefficients κ attains the same value k over a narrow spectral range. These identical quantities are, therefore, reordered as an increasing function of k with respect to the reordered artificial wave number g[6] to reduce the repetition of computations with the same values of κ (Modest [59]). To deal with nonhomogeneous gases, the correlated-k distributions has been introduced by Goody et al. [128] Lacis and Oinas [129] and Fu and Liou [130]. The term 'correlated' indicates a hypothesis that the heterogeneities of the medium (temperature, in particular) are treated by assuming that the spectra between different state are correlated. The k-distribution differs from the SNB by the fact that it directly provides a (reordered) absorption coefficient representation and, therefore, can be used with any arbitrary RTE solver (including P_1, DOM, FVM,...).

The Wide Band Models consider the bands whose spectral range is adjusted to the width of the physical absorption bands of the component. In principle, wide band correlations are found by integrating narrow band results across an entire band Modest [59]. The most popular model is the exponential wide band, which was initially presented by Edwards [131] and its applications to radiative transfer problems have been discussed by Ströhle and Coelho [132]. This method is less accurate than the narrow band ones, but it allows significant reductions in calculation time.

2.2.2.3 Global models

In the line by line model and the band models, one considered the radiative properties over each line of the spectral representation or a specified interval of wavenumbers. On the other hand, the global models find the radiative characteristic over the entire gas spectrum.

The simplest model of this group is the gray gas model in which the absorption coefficient is assumed to be constant over the whole spectrum. With only one value of local absorption coefficient κ_a, the radiative transfer equation can be directly expressed in total quantities and no further spectral integration is needed.

Another model of this group is the weighted-sum-of-gray-gases (WSGG). This model was first introduced by Hottel and Sarofim [104] in the frame of the zonal method. Its principle is to replace the continuous spectral absorption coefficient by a finite set of values (each of them being related to a gray gas) with their associated weights. Modest [133] applied this method for the solution of the radiative transfer equation with the assumption of spatially constant absorption coefficients for all gray gases, but letting their weights vary with temperature. The radiative parameters (absorption coefficients and their associated weights) were originally identified by making the total emissivity $\epsilon \approx \sum_{j=1}^{n} a_j \cdot (1 - e^{-\kappa_j L})$ fit the experimental data.

Based on the same idea as the WSSG model, Denison and Webb [58] have presented the Spectral Line-Based Weighted-sum-of-gray-gases models (SLW). The weights of the gray gases are now determined by using the global distribution function of the absorption coefficient weighted by the Planck function. This distribution function was calculated directly from high resolution spectral databases. Similar to SLW,

[6] g indicates the fraction of spectrum where $\kappa_\eta \leq k$

the Absorption Distribution Function model (ADF) (Pierrot et al. [134]) and Full Spectrum K-distribution model (FSK) (Modest and Zhang [135], Modest and Mehta [136]) have been reported. These three methods have differences in the way of calculating the gas radiative properties, but their relationship has been brought out in the article of Solovjov and Webb [137]. Recently, Solovjov, Lemonnier, and Webb [138] introduced the SLW-1 model such that the calculations is now performed by using only one gray (optimized) gas and one transparent component.

Goutiere, Liu, and Charette [139] and Goutière, Charette, and Kiss [140] through their works about the comparisons of the different gas models, showed that the SLW provides the best compromise between the accuracy and the computational cost. The SLW model is therefore, chosen for the calculations of radiative properties of the gas mixtures in all the simulations presented in this thesis.

Recently, the SLW model in non uniform media has been developped using different novel approaches: the Rank Correlated (RC) ([141]), Scaled (SC) (Solovjov et al. [142]) and Locally Correlated (LC) (Solovjov et al. [143]) models.

2.2.3 The SLW gas model

In this section, the SLW model will be described in more details for isothermal, homogeneous as well as non-isothermal, non-uniform media.

2.2.3.1 Calculation of the absorption coefficients

The SLW model involves a set of finite number (N_g) gray gases and one clear (transparent) gas. The absorption coefficient of j^{th} gas is calculated as:

$$\kappa_j = N \cdot X \cdot C_j \tag{2.27}$$

where C_j is the absorption cross section, N is molar density and X the mole fraction. Knowing N and X, the remaining problem is to determine C_j.

The wavenumber range under consideration prescribes an overall absorption cross section interval [C_{min},C_{max}]. The N_g gray gases discretize this range into several intervals Δ_j such that, for the j^{th} gray gas:

$$\begin{aligned} \Delta_j &= \eta : \tilde{C}_{j-1} < C_\eta(\phi_g) < \tilde{C}_j : \text{gray gas intervals} \\ \Delta_0 &= \eta : C_\eta(\phi_g) \leq \tilde{C}_0 = C_{min} : \text{clear gas intervals} \end{aligned} \tag{2.28}$$

where $\tilde{C}_{j-1}$ and $\tilde{C}_j$ are discrete values of C defined over [C_{min},C_{max}]. They are termed the supplemental cross sections.

The value of C_j can be arbitrarily chosen in the interval [$\tilde{C}_{j-1}$,$\tilde{C}_j$] for calculating the absorption coefficient κ_j.
In all our simulations, and following the classical approach, the supplemental values were defined as:

$$\tilde{C}_j = C_{min}(C_{max}/C_{min})^{j/N_g} \tag{2.29}$$

$$C_j = \sqrt{\tilde{C}_{j-1}\tilde{C}_j} \tag{2.30}$$

The resulting set of local absorption coefficients, was therefore obtained as:

$$\begin{aligned} &\kappa_j = NXC_j = NX\sqrt{\tilde{C}_{j-1}\tilde{C}_j} : \text{with j=1,...,}N_g \\ &\kappa_0 = 0 \text{ for the clear gas} \end{aligned} \tag{2.31}$$

2.2.3.2 Calculations of Absorption line black body distribution function and the weights of gray gases

The weights associated with each gray gas are calculated from the global distribution function of the absorption coefficient weighted by the Planck function: it is named the absorption line black body distribution function (ALBDF) in the seminal work by Denison and Webb [144]. This function is evaluated as the integral of the Planck function calculated at a source temperature T_b over the wavenumber intervals such that the absorption cross section $C_\eta(\phi_g)$ at a gas thermodynamic state ϕ_g[7] is below a prescribed value of C, namely:

$$\begin{aligned} F(C,\phi_g,T_b) &= \frac{1}{E_b(T_b)} \int_{\eta:C_\eta(\phi_g)<C} E_{b\eta}(T_b)d\eta \\ &= \frac{\pi}{\sigma T_b^4} \int_{\eta:C_\eta(\phi_g)<C} I_{b\eta}(T_b)d\eta \end{aligned} \tag{2.32}$$

where $E_{b\eta}(T_b)$ is the Planck spectral emissive power emitted by a blackbody at temperature T_b and E_b is the total blackbody emissive power given by the Stefan-Boltzmann Law.

The ALBDF is determined by performing integrations over the whole spectrum at high resolution (line by line) at different pressures, temperatures and compositions. The resulting data are made available for the main participating species (H_2O, CO_2, CO) either as mathematical correlations or in look-up tables. The most recent contribution is reported in Pearson et al. [145] based on HITEMP-2010 spectral database. The main features of two methods are shortly introduced below:

Mathematical correlations

- For $air - H_2O$ mixtures:

$$F_w(C,T_g,T_b,X_w) = \frac{1}{2}\tanh[P_w(T_g,T_b,\xi-\xi_p)] + \frac{1}{2} \tag{2.33}$$

[7] $\phi_g = (X,P,T_g)$ where T_g is the gas temperature, Y the molar fraction, and P the total pressure.

where :

$$
\begin{aligned}
P_w(T_g, T_b, \xi - \xi_p) &= \sum_{l=0}^{3}\sum_{m=0}^{3}\sum_{n=0}^{3} b_{lmn}\left(\frac{T_g}{2500}\right)^n\left(\frac{T_b}{2500}\right)^m(\xi - \xi_p)^l \\
\xi_p &= \sum_{l=0}^{3}\sum_{m=0}^{3}\sum_{n=0}^{3} u_{lmn}\left(\frac{T_g T_b}{2500^2}\right)^n \xi^m \psi_w^{l+1} \\
\psi_w &= \frac{1}{10}\ln(100 p_e) \\
p_e &= (1 + 8.17 X_w) p \\
\xi &= \ln(C) \text{ with } 1 \cdot 10^{-4} \leq C \leq 60 \left[\frac{m^2}{mol}\right]
\end{aligned}
$$

Here, F_w denotes the approximation of the ALBDF when considered participating species is water vapor and P_w is a temporary variable.

- For $air - CO_2$ mixtures:

$$
F_c(C, T_g, T_b) = \frac{1}{2}\tanh[P_c(T_g, T_b, \xi - \xi_p)] + \frac{1}{2} \tag{2.34}
$$

where :

$$
\begin{aligned}
P_c(T_g, T_b, \xi - \xi_p) &= \sum_{l=0}^{3}\sum_{m=0}^{3}\sum_{n=0}^{3} d_{lmn}\left(\frac{T_g}{2500}\right)^n\left(\frac{T_b}{2500}\right)^m(\xi - \xi_p)^l \\
\xi_p &= \sum_{l=0}^{3}\sum_{m=0}^{3}\sum_{n=0}^{3} v_{lmn}\left(\frac{T_g T_b}{2500^2}\right)^n \xi^m \psi_c^{l+1} \\
\psi_w &= \frac{1}{10}\ln(100 p) \\
\xi &= \ln(C) \text{ with } 1 \cdot 10^{-4} \leq C \leq 600 \left[\frac{m^2}{mol}\right]
\end{aligned}
$$

Here, F_c denotes the approximation of the ALBDF when considered participating species is CO_2 and P_c is a temporary variable.
The parameters $b_{lmn}, u_{lmn}, d_{lmn}, v_{lmn}$ are tabulated in the work by Pearson et al. [145].

Look-up table
The tabulated approach consists in storing the ALBDF values obtained discrete value of the cross sections C, temperature T, pressure P and composition X. In more details, these tabulations are made: every 100K for T between 300 and 3000K; for 70 values of C between 10^{-4} and 10^3 m^2/mol; for 10 values of P in the range of $[0.1 - 50]$ atm and in the case of $air - H_2O$ mixture, for 9 discrete values of molar fraction between 0 and 1. All this tabulated data were assembled by V.P. Solovjov and are available at `http://albdf.byu.edu`. Then, through the interpolations over P, X (for $air - H_2O$ mixture only), C, T_b and T_g, the value of F at local conditions $(\phi_g = (X, P, T_g))$ and for a given black body temperature T_b are determined.

The weight of the j^{th} gray gas a_j corresponds to the difference in the ALBDF at the two supplemental absorption cross sections that define the j^{th} interval [$\tilde{C}_{j-1}$,$\tilde{C}_j$]:

$$\begin{aligned} a_j &= F(\tilde{C}_j, \phi_g, T_b) - F(\tilde{C}_{j-1}, \phi_g, T_b) : \text{for j = 1,...,}N_g \\ a_0 &= F(\tilde{C}_0, \phi_g, Tb) \end{aligned} \tag{2.35}$$

where T_b = T_g, the gas temperature, in a uniform medium and $T_b = T_w$ at the boundaries (T_w, is the wall temperature). The determination of these quantities for non-uniform gases will be described in the following section.

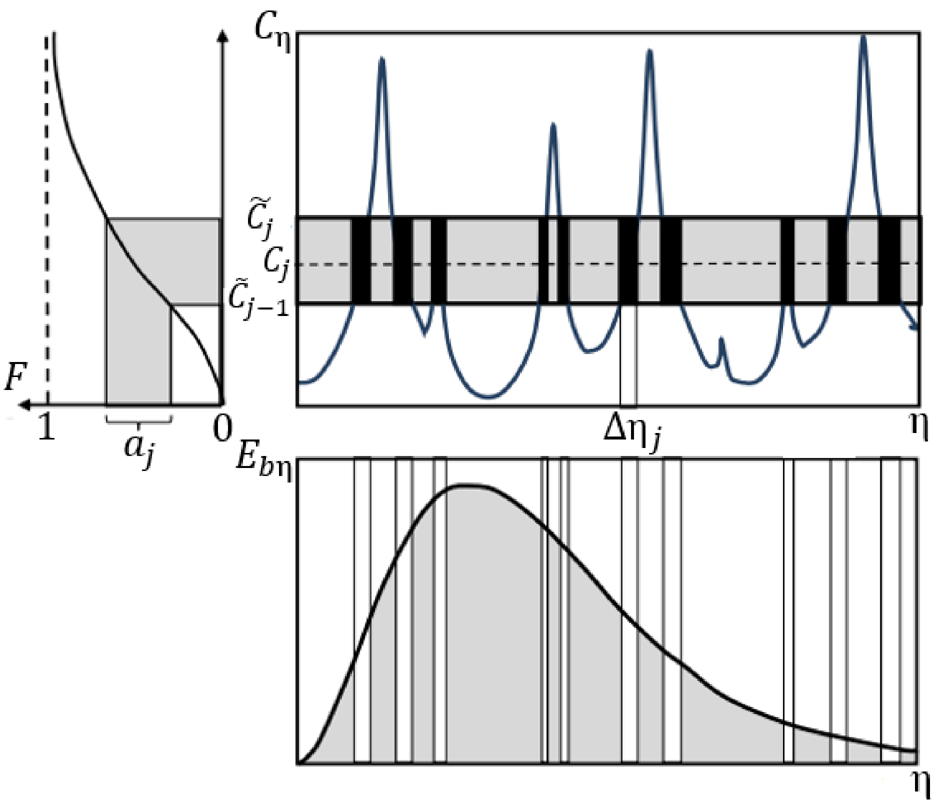

Figure 2.1: SLW calculation diagram for j^{th} gray gas (from Solovjov, Webb, and André [146])

2.2.4 Implementation of SLW model in the radiative transfer equation

We consider the spectral integration of the monochromatic RTE over the wavenumber ranges corresponding to the j^{th} gray gas:

$$\int_{\Delta_j} \mathbf{\Omega} \cdot \nabla I_\eta(\mathbf{s}) d\eta = \int_{\Delta_j} (-\kappa_j I_\eta(\mathbf{s}) + a_j \kappa_j I_{b\eta}) d\eta \tag{2.36}$$

$\Delta_j = [a_{i,j}(s); b_{i,j}(s)]$ is the wavenumber intervals also defined in (2.28). Applying the Leibnitz formula to the left hand side term in the equation (2.36), yields:

$$\begin{aligned}
&\mathbf{\Omega} \cdot \nabla \int_{\Delta_j(\mathbf{s})} I_\eta(\mathbf{s}, \mathbf{\Omega}) d\eta \\
&= \int_{\Delta_j(\mathbf{s})} \mathbf{\Omega} \cdot \nabla I_\eta(\mathbf{s}, \mathbf{\Omega}) d\eta \\
&\underbrace{+ \sum_i \{ I_\eta[\mathbf{s}, \eta = b_{i,j}(\mathbf{s}), \mathbf{\Omega}] \mathbf{\Omega} \cdot \nabla b_{i,j}(\mathbf{s}) - I_\eta[\mathbf{s}, \eta = a_{i,j}(\mathbf{s}), \mathbf{\Omega}] \mathbf{\Omega} \cdot \nabla a_{i,j}(\mathbf{s}) \}}_{\text{Leibnitz terms}}
\end{aligned} \tag{2.37}$$

For an isothermal, homogenous medium, the Leibnitz terms in the equation (2.37) are null because all the wavenumber intervals Δ_j are identical (therefore, $\mathbf{\Omega} \cdot \nabla a_{i,j}(\mathbf{s}) = 0$ and $\mathbf{\Omega} \cdot \nabla b_{i,j}(\mathbf{s}) = 0$).

For non-isothermal and/or non-homogeneous media, the Leibnitz terms are no longer null and vary with the position $\mathbf{s}$. Their evaluation at each point of the domain and for each gray gas would require a huge calculation effort.

A first option is to simply neglect these terms when solving the RTE. But it leads to significant errors in predicting the radiative quantities when large temperature and concentration gradients are present (like in combustion problems, for instance).

Another approach is to select the wavenumber intervals such that they do not depend on the locations: $\Delta_j(\mathbf{s}) = \Delta_j = const$. This idea is related to the assumption of an "ideal spectrum behavior" proposed in Denison and Webb [144]. The main hypothesis can be summarized as follows: consider a reference state ϕ_{ref} = $(P_{ref}, T_g = T_{ref}, X_{ref})$ and a local state ϕ_{loc} = $(P_{loc}, T_g = T_{loc}, X_{loc})$. The interval over which $C_\eta(\phi_{ref})$ remains below a fixed value C^{ref} is the same as the interval over which the cross section $C_\eta(\phi_{loc})$, at local state, remains below a value C^{loc} when the black body temperature is the same. In other words:

$$\eta : C_\eta(\phi_{ref}) < C^{ref} = \eta : C_\eta(\phi_{loc}) < C^{loc} \tag{2.38}$$

This equality assumes that the gas spectrum of the related species is *correlated*, in the sense that there exist some relation linking the spectra at different conditions. This approximation leads to the equality of the values of the ALBDF calculated for a fixed source temperature T_b=T_{ref}

$$F(C^{loc}, \phi_{loc}, T_b = T_{ref}) = F(C^{ref}, \phi_{ref}, T_b = T_{ref}) \tag{2.39}$$

The cross section valid in the local state C_{loc} can therefore be deduced from the reference value C_{ref} by inverting the equation (2.39): $C^{loc} = C(F^{ref}, \phi_{loc}, T_b = T_{ref})$ where $C(F, \phi, T_b)$ is the distribution function of cross section with respect to F, that is the reciprocal function of F and where $F^{ref} = F(C^{ref}, \phi_{ref}, T_b = T_{ref})$.

The above assumption is referred to as the Reference Approach (RA). More recent implementations of the SLW model include the Rank Correlated (RC) ([141]), Locally Correlated (LC) (Solovjov et al. [143]) and Scaled approaches (SC) (Solovjov et al. [142]). We will here focus on the RA-SLW and RC-SLW taking advantage of the explanations given by Solovjov et al. [141] and Solovjov, Webb, and André [147]:

Reference Approach
This approach involves different steps that may be summarized as follow:

1. Choose a reference state: $\phi^{ref} = T_{ref}, X_{ref}, p_{ref}$
2. At reference state, chose the set of the reference supplemental cross sections $\tilde{C}_j^{ref}$ using (2.29).
3. Solve the following implicit equation to determine the local supplemental cross sections $\tilde{C}_j^{loc}$

$$F(\tilde{C}_j^{ref}, \phi_{ref}, T_b = T_{ref}) = F(\tilde{C}_j^{loc}, \phi_{loc}, T_b = T_{ref}) \tag{2.40}$$

4. Use equation (2.30) with the determined supplemental cross section for the calculation the local gray gas absorption coefficients:

$$\kappa_j(s) = N_{loc} X_{loc} C_j^{loc} = N(s) X(s) \sqrt{\tilde{C}_j^{loc} \tilde{C}_{j-1}^{loc}} \tag{2.41}$$

5. Calculate the local weights attributed to the j^{th} gray gas:

$$a_j(s) = a_j^{loc} = F(\tilde{C}_j^{ref}, \phi_{ref}, T_b = T_{loc}) - F(\tilde{C}_{j-1}^{ref}, \phi_{ref}, T_b = T_{loc}) \tag{2.42}$$

In case of boundaries emitting at the temperature T_w, it is advised to set the black body temperature equal to these wall temperature (Solovjov, Webb, and André [146])

$$a_j(T_w) = F(\tilde{C}_j^{ref}, \phi_{ref}, T_b = T_w) - F(\tilde{C}_{j-1}^{ref}, \phi_{ref}, T_b = T_w) \tag{2.43}$$

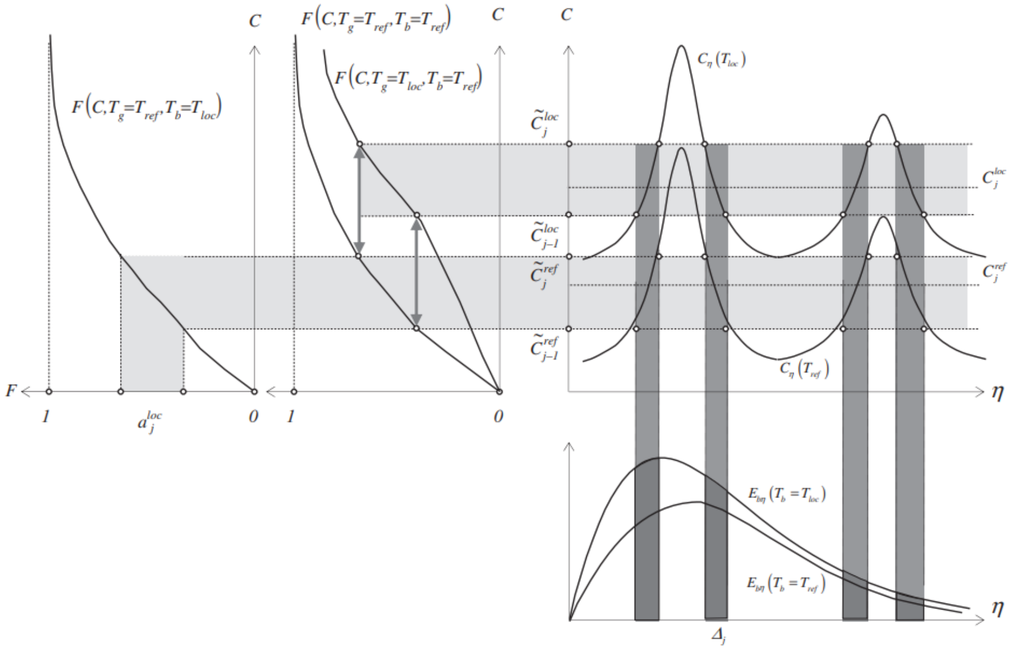

Figure 2.2: Schematic representation of the Reference Approach (from Solovjov, Webb, and André [147])

Rank Correlated Approach

In this approach, Solovjov et al. [141] suggest a modification of the assumption of "ideal spectrum" or "correlated spectrum" discussed above. They consider a less restrictive assumption of rank correlation regarding the relationship between absorption spectra at different thermodynamic states. The main hypothesis underlying this approach can be summarized as follows. Consider a fixed value of the ALBDF at a fixed black body temperature T_b: the wavenumber intervals $\Delta_1 = \eta : C_\eta(\phi_1) < C(F, \phi_1, T_b)$ and $\Delta_2 = \eta : C_\eta(\phi_2) < C(F, \phi_2, T_b)$ are the same. This expression is assumed to be correct for any two thermodynamic states, thus, $\Delta_1 = \Delta_2 =$ *constant* (see figure 2.3) for a given value of F at a fixed T_b. It ensures the elimination of the Leibnitz term in equation (2.37). It can be observed that we no longer need to specify any reference state, but only a black body source temperature T_b. Moreover, the process involves a discretization of the ALBDF in the interval of $[F_{min}, F_{max}]$ rather than of the absorption cross section. The following algorithm can therefore be used:

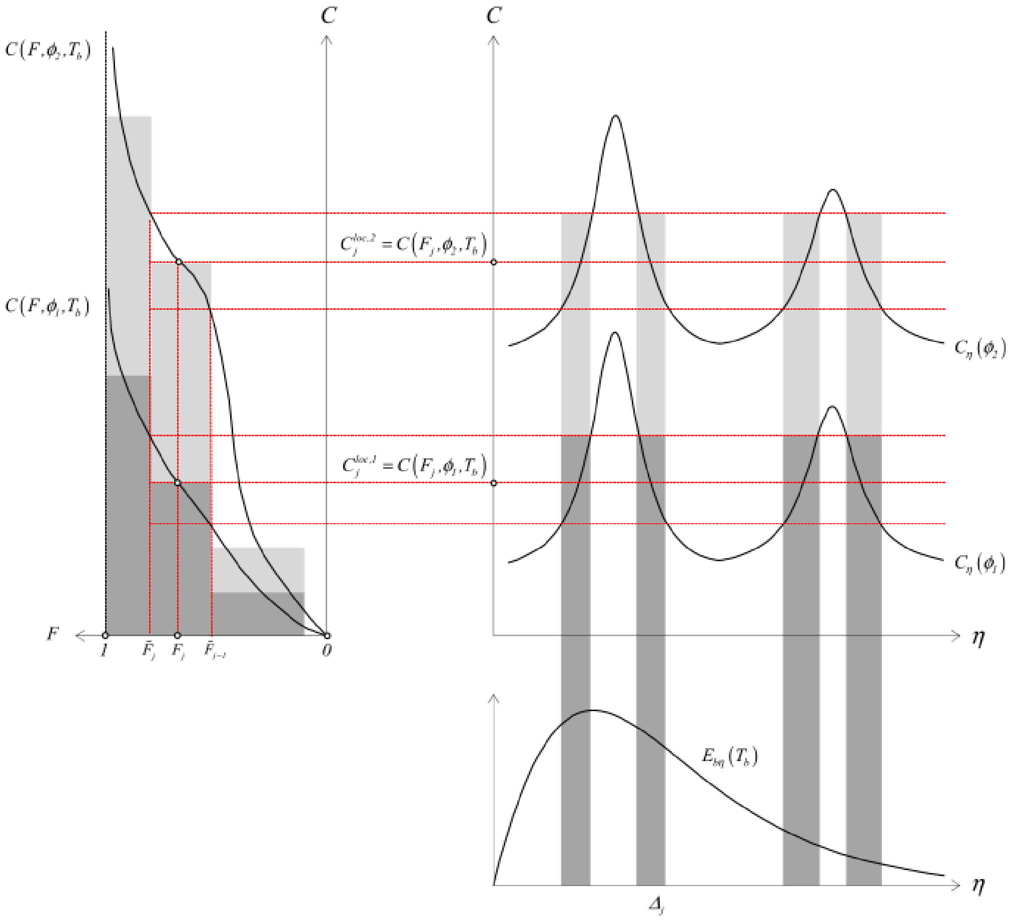

Figure 2.3: Schematic representation of the Rank Correlated (from Solovjov et al. [141])

1. Arbitrarily subdivide the ALBDF in the range $[F_{min}, F_{max}]$ into the discrete values: F_j^{ref} and the supplemental values $\tilde{F}_j^{ref}$ such that $F_{min} \leq \tilde{F}_j^{ref} \leq F_{max}$ for $j = 0, 1, ..., n$ and $\tilde{F}_{j-1}^{ref} \leq F_j^{ref} \leq \tilde{F}_j^{ref}$ with $j = 1, 2, ..., n$. With a large number of gray gases N, even simple uniform subdivision is likely satisfactory for accurate results (Webb, Solovjov, and André [148]). However, for a small number of gray gases, a more efficient discretization can be achieved by using the Gauss-Legendre quadrature nodes and weights. Firstly, the positive abscissas $x_j > 0$ and the corresponding weights w_j, $j = 1, 2, ..., n$ of Gauss-Legendre quadrature for integration over the interval [-1,1] are calculated. And then, we can determine the reference values of ALBDF F_j^{ref} and supplemental reference values $\tilde{F}_j^{ref}$ in interval $[F_{min}, F_{max}]$ (Solovjov, Webb, and André [147]) such that:

$$
\begin{aligned}
F_j^{ref} &= F_{min} + x_j(F_{max} - F_{min}) \\
\tilde{F}_j^{ref} &= F_{min} + (F_{max} - F_{min}) \sum_{k=1}^{j} w_k \\
\tilde{F}_0^{ref} &= F_{min}
\end{aligned}
\tag{2.44}
$$

with $j = 1, 2, ..., N_g$

2. Use the inverse ALBDF to find the values of local absorption cross sections and also local supplemental absorption cross sections:

$$\begin{aligned} C_j^{loc} &= C(F_j^{ref}, \phi_{loc}, T_{ref}) \\ \tilde{C}_j^{loc} &= C(\tilde{F}_j^{ref}, \phi_{loc}, T_{ref}) \end{aligned} \tag{2.45}$$

3. Calculate the local gray gas absorption coefficients:

$$\begin{aligned} \kappa_j^{loc} &= N^{loc} X_{loc} C_j^{loc} \\ \kappa_0^{loc} &= 0 \end{aligned} \tag{2.46}$$

4. Calculate the local corresponding weights of local gray gas absorption coefficients with the help of the ALBDF at local cross sections $\tilde{C}_j^{loc}$:

$$\begin{aligned} a_j^{loc} &= F(\tilde{C}_j^{loc}, \phi^{loc}, T^{loc}) - F(\tilde{C}_{j-1}^{loc}, \phi^{loc}, T^{loc}) : \text{with j = 1,2,...,}N_g \\ a_0^{loc} &= F(\tilde{C}_0^{loc}, \phi^{loc}, T^{loc}) \end{aligned} \tag{2.47}$$

Applying the newly calculated radiative properties to eq. (2.36) yields the radiative transfer equations for j^{th} gray gas written as :

$$\mathbf{\Omega} \cdot \mathbf{\nabla} I_j(\mathbf{s}) = -\kappa_j I_j(\mathbf{s}) + a_j \kappa_j I_b(\mathbf{s}) \tag{2.48}$$

where $\int_{\Delta_j} \mathbf{\Omega} \cdot \mathbf{\nabla} I_\eta d\eta = \mathbf{\Omega} \cdot \mathbf{\nabla} I_j$

Consequently, the total intensity and radiative source term are given by the following expressions:

$$I(\mathbf{s}, \mathbf{\Omega}) = \sum_{j=1}^{N_g} I_j(\mathbf{s}, \mathbf{\Omega}) \tag{2.49}$$

$$\mathbf{\nabla} \cdot \boldsymbol{q} = \sum_{j=1}^{N_g} (4\pi a_j \kappa_j I_b(\mathbf{s}) - \kappa_j G_j(\mathbf{s})) \tag{2.50}$$

where $G_j(\mathbf{s}) = \int_0^{4\pi} I_j(\mathbf{s}, \mathbf{\Omega}) d\Omega$ is the incident radiation in the case of j^{th} gray gas.

2.3 Conclusion

In this chapter, the mathematical basis of the study was presented. Besides, we have shortly described the methods of resolution for the RTE and the Discrete Ordinates Method (DOM) has been selected as the solver for our simulations. Finally, we have mentioned some existed gas models and focused on the formation of the SLW method with the center of interest was the Reference Approach and the Rank Correlated for the treatment of non-isothermal, non-homogeneous medium.

Chapter 3

Code Saturne and Radiative Calculation

3.1 Code Saturne

In this section, we introduce the resolution of the governing equations of our problem. For this purpose, we have used Code Saturne version 5.0.4 [123], an open source software for CFD calculation developed by EDF. A built-in radiative module is available, in which we have implemented our own data for directional integration and gas radiation modeling.

3.1.1 Computational Fluid Dynamic

Code Saturne uses a finite volume method to solve the governing equations of fluid motion and heat and mass transfer. For the momentum equations, Code Saturne uses an algorithm of type prediction-correction called SIMPLEC, which stands for Semi-Implicit Methods for Pressure Linked Equations Consistent. Different discretizations in space and in time are also available.

Time stepping

The time scheme is used in Code Saturne is a $\theta - scheme$ with:

$$\begin{cases} \theta = 1 & \text{for an implicit first order Euler scheme,} \\ \theta = \frac{1}{2} & \text{for second order Crank-Nicolson scheme.} \end{cases} \tag{3.1}$$

In our study, we have used the implicit first order backward Euler scheme[1] [2]. Code Saturne provides two options for the temporal step: constant or variable (where the code automatically calculates the time step after each iteration that satisfy the CFL criterion).

Spatial discretization

In the finite volume approach, the equations are integrated over each cell. Using the Green Theorem, the volume integrations become surface integrations. We, therefore, need only to calculate the face gradients of each variables. Code Saturne proposes different schemes of first order (Upwind) and second order (Centered or Second-Order-Linear-Upwind (SOLU)) for spatial discretization. In this study, we have selected the centered second order.

[1]This is the default scheme in Code Saturne and it was validated to be suitable for our calculations.

[2]This choice can be questioned when unsteady behaviors are addressed. In that case, a specific convergence steady was conducted to ensure that the selected time step was appropriate.

3.1.2 Discrete Ordinate Method in Code Saturne

A set of discrete directions with associated weights has to be specified. For each of these directions, the radiative transfer equation (2.8) is solved over the entire spatial domain. Integrating this equation on a control volume centered at the grid node P, yields :

$$\int_{CV} \mathbf{\Omega} \cdot \nabla I_\eta^P(\mathbf{\Omega}) dV = -\int_{CV} \kappa_\eta^P I_\eta^P(\mathbf{\Omega}) dV + \int_{CV} \kappa_\eta^P I_{b\eta}^P dV \tag{3.2}$$

Applying the Green theorem to the left hand side of this expression with the assumption that the variables on the right hand side remains constant within the control volume, gives:

$$\int_A \mathbf{\Omega} \cdot \boldsymbol{n} I_\eta^P(\mathbf{\Omega}) = -V\kappa_\eta^P I_\eta^P(\mathbf{\Omega}) + V\kappa_\eta^P I_{b\eta}^P \tag{3.3}$$

where A and V denote, respectively, the surface and the volume of the elementary cell while $\boldsymbol{n}$ is the outer unit vector normal to a cell face.

Approximating the integral over the boundaries of the control volume by a discrete sum, yields:

$$\sum_{f=1}^{F} \mathbf{\Omega} \cdot \boldsymbol{n}_f I_\eta^f(\mathbf{\Omega}) A_f = -V\kappa_\eta^P I_\eta^P(\mathbf{\Omega}) + V\kappa_\eta^P I_{b\eta}^P \tag{3.4}$$

Here, f denotes a cell face with its area A_f, F is the total number of cell faces of the control volume and $I_\eta^f(\mathbf{\Omega})$ is the mean monochromatic radiation intensity in a cell face f along the direction $\mathbf{\Omega}$.

An interpolation is needed to relate $I_\eta^f(\mathbf{\Omega})$ to the unknown $I_\eta^P(\mathbf{\Omega})$. Different schemes may be applied but the implemented radiative module of Code Saturne resorts to the first order step scheme. It approximates the face value $I_\eta^f(\mathbf{\Omega})$ by the center value of the upstream control volume. For instance, for a face f_1 where the outer unit normal vector $\boldsymbol{n_1}$ is such as $\mathbf{\Omega} \cdot \boldsymbol{n_1} < 0$, the scheme prescribes $I_\eta^{f_1}(\mathbf{\Omega}) = I_\eta^U(\mathbf{\Omega})$. Conversely, for the face f_2 where $\mathbf{\Omega} \cdot \boldsymbol{n_2} > 0$, the $I_\eta^{f_2}(\mathbf{\Omega})$ is set to $I_\eta^P(\mathbf{\Omega})$ (see figure 3.1).

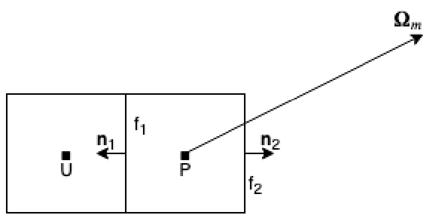

Figure 3.1: Presentation of step scheme for calculation of intensity at one face

Inserting this interpolation into equation (3.4) gives:

$$\left(\sum_{\substack{f=1 \\ (\boldsymbol{\Omega}\cdot\boldsymbol{n}_f>0)}}^{F} \boldsymbol{\Omega}\cdot\boldsymbol{n}_f A_f + \kappa_\eta^P V \right) I_\eta^P(\boldsymbol{\Omega}) = \sum_{\substack{f=1 \\ (\boldsymbol{\Omega}\cdot\boldsymbol{n}_f<0)}}^{F} |\boldsymbol{\Omega}\cdot\boldsymbol{n}_f| I_\eta^U A_f + V\kappa_\eta^P I_{b\eta}^P \tag{3.5}$$

and solving this equation makes the whole intensity field - attached to one given direction - available at all the grid points. To further obtain the discrete values of incident radiation and radiative flux, each nodal intensity must be integrated over all the directions in space ($4\pi\ sr$). The DOM, in this situation, replaces the angular integrals by a summation over a set of discrete directions such as:

$$\int_0^{4\pi} f(\boldsymbol{\Omega})d\Omega \approx \sum_{m=1}^{M} \omega_m f(\Omega_m) \tag{3.6}$$

where M denotes the number of directions in the set and ω_m is the weight attributed to the m^{th} element. Consequently, the distribution of incident radiation and radiative flux are approximated by:

$$\begin{aligned} G_\eta^P &= \int_0^{4\pi} I_\eta^P(\boldsymbol{\Omega})d\Omega \\ &\approx \sum_{m=1}^{M} \omega_m I_\eta^P(\boldsymbol{\Omega}_m) \end{aligned} \tag{3.7}$$

$$\begin{aligned} \boldsymbol{q}_m^P &= \int_0^{4\pi} I_\eta^P(\boldsymbol{\Omega})\boldsymbol{\Omega}d\Omega \\ &\approx \sum_{m=1}^{M} \omega_m I_\eta^P(\boldsymbol{\Omega}_m)\boldsymbol{\Omega}_m \end{aligned} \tag{3.8}$$

There are several ways to define the discrete direction sets. We will here focus on the quadrature available in Code Saturne and the ones we have introduced to improve this part of the code. A more general overview on this problem can be found in Koch and Becker [26].

- The first (and more classic) set is the Level Symmetric quadrature S_N. It was introduced for radiative transfer by Lee [149]. Different sets of directions and weights were later introduced, for example, by Lathrop and Carlson [88] and Fiveland [150]. The principle of this quadrature scheme is to apply strict rules of symmetry in order to equally treat all the directions of propagation. These rules prescribe that, if $\boldsymbol{\Omega}_m$, characterized by the direction cosines value (μ_m,η_m,ξ_m) is in the quadrature:

  i. all the direction $(\pm\mu_m,\pm\eta_m,\pm\xi_m)$ are also in the discrete ordinates set and have the same weight.

  ii. all the directions coming from a permutation of (μ_m,η_m,ξ_m) are also in the quadrature and are assigned the same weight.

  However, the customary choice of discrete ordinates has to preserve the zeroth, first and second moments of integration of the intensity over the whole direction range (Modest [59]). Fiveland [82] and Truelove [84] have studied different direction sets and they pointed out the requirement of satisfying, in addition, the first moments over a half range of direction to avoid biasing the evaluation of wall fluxes.

- The T_N quadrature set is due to Thurgood [89]. The basic idea of this scheme is to divide the unit sphere into spherical triangles. For each triangle, an associated direction is defined from the center of the sphere to the center of the triangle region. The quadrature weight are calculated according to the spherical triangle areas. The order N refers to the number of subdivisions of the edges of the principal triangle.
- The $LC-11$ quadrature set. Based on the fundamentals of Sobolev [151], Lebedev [152] proposed quadrature schemes which are rotational invariant to the group of regular polyhedrons and are capable to exactly integrate the spherical harmonics functions $Y_n(\mathbf{\Omega})$ up to the order of N on the unit sphere ($N = 11$ for the LC-11 quadrature). Quadratures of that type are developed so that the spherical harmonics of order $N = 11, 15$ can be integrated exactly. All the weights are identical while the directions can be adjusted.
- The $DCT-020-2468$ quadrature set is one of the DCT (Double Cyclic Triangles) quadrature schemes. It has been designed to provide as many degrees of freedom as possible for satisfying additional moment conditions (Koch et al. [90]), (Koch and Becker [26]). The naming convention of these quadrature schemes is DCT$xyz - abcd...$ where x, y, z denote respectively the number of non-degenerated tuples [3], the number of single degenerated tuples and the number of double degenerated tuples; $abcd...$ denotes the moment conditions that are satisfied by the quadrature.

3.1.3 Encountered Difficulties and Applied Modifications

The S_N quadrature set implemented in the version 5.0.4 of Code Saturne comes from the selection of Lathrop and Carlson [88] and Fiveland [81]. We have assessed the accuracy of these implementations by comparisons in a test case where the exact (analytical) solution is available. We have also input in the code more recent values of the S_8 and S_{12} sets based on the modifications proposed by Balsara [27].

As a benchmark, we have considered the radiative equilibrium in a 2-D square cavity of size $1m \times 1m$ (see Figure 3.2). The walls are black, one of them (hot wall) is heated up to $1000K$ while the others are uniformly set at $500K$ (cold walls). The medium inside the cavity is homogeneous and gray. The evaluation criterion used here is the distribution of the radiative net flux on the cold wall facing the hot wall. It is known to be the most sensitive result. We have also checked the integral value of this flux over the entire wall. The reference solution is taken from Crosbie and Schrenker [153] who have provided a semi-analytical solution to this problem. The calculations are run with Code Saturne and, for sake of comparison, with a home-made code using the discrete ordinates in 2-D geometries. Two different values of the gray absorption coefficient were considered $\kappa = 0.25m^{-1}$ and $\kappa = 1.0m^{-1}$. The results and comparisons are illustrated in the figures below (3.3 and 3.4).

It appears that the S_8 quadrature implemented in Code Saturne leads to erroneous results (at least, in the version we have used). Indeed, none of the calculations

[3] A tuple is the arrangement of six nodal points on an octant

returns the correct reference distribution, but this is a well-known bias of the DOM named "ray-effect". It is due to the discrete representation of the direction space, and these errors are attached to the choice of the quadrature set. However, it is known that the integrated flux (over the entire wall) is preserved when using the S_N data: therefore, our results must match the exact (reference) value. This is true for our S_N set (based on Balsara data), both for the homemade code or after implementation in Code Saturne (see table 3.1 and 3.2). Conversely, the built-in S_8 quadrature in Code Saturne returns erroneous values. This is probably due to some inaccuracies when inputting the related data in the code. Note that:

- The other quadrature (S_4, S_6, ...) implemented in Code Saturne give satisfactory results.
- The correct S_8 set (based of Fiveland data) returns results close to what is obtained with the Balsara set.

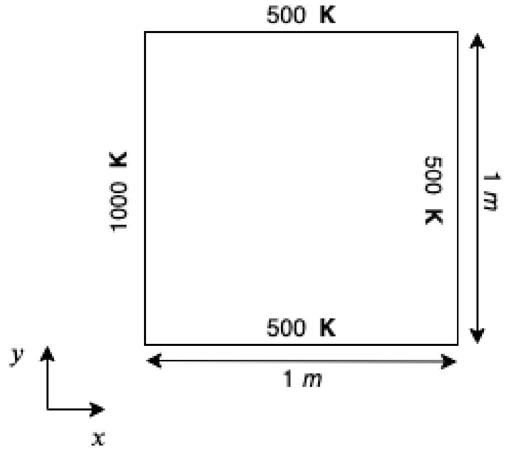

Figure 3.2: 2D - Square Cavity

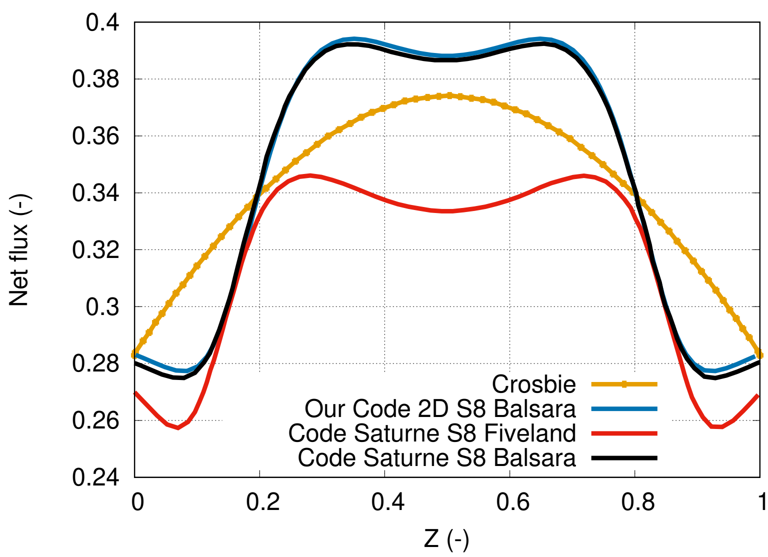

Figure 3.3: 2D - Radiant flux at the cold wall, opposed to the hot wall with $\kappa = 0.25$

	$\kappa = 0.25$	
	Integration	Relative difference (%)
Crosbie	0.342532207	
Code 2D	0.343785469	0.3658
Code Saturne Fiveland	0.315125699	8.001
Code Saturne Balsara	0.345137495	0.7606

Table 3.1: Integrated wall flux, $\kappa = 0.25$, quadrature S_8

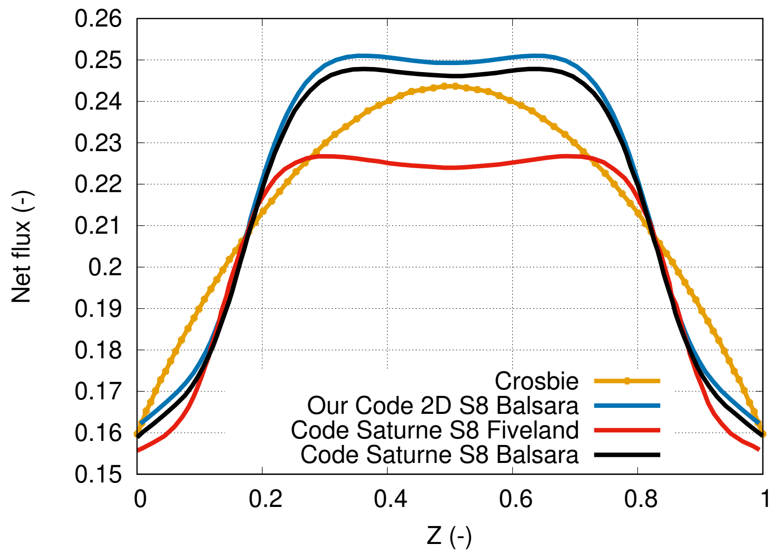

Figure 3.4: 2D - Radiant flux at the cold wall, opposed to the hot wall with $\kappa = 1$

	$\kappa = 1$	
	Integration	Relative difference (%)
Crosbie	0.215529801	
Code 2D	0.21866138	1.4529
Code Saturne Fiveland	0.205275837	4.7575
Code Saturne Balsara	0.217682182	0.9986

Table 3.2: Integrated wall flux, $\kappa = 1$, quadrature S_8

These comparisons led us to choose the quadratures of Balsara [27] in all our calculations (mainly S_8).

3.1.4 Implementation of SLW model

Dealing with a non-gray gas mixture requires a spectral model to account for the variation of the absorption coefficient in the medium. To that end, we have implanted the SLW model, which is described in the previous chapter, in the radiative module of Code Saturne. This implementation is presented in the diagram below:

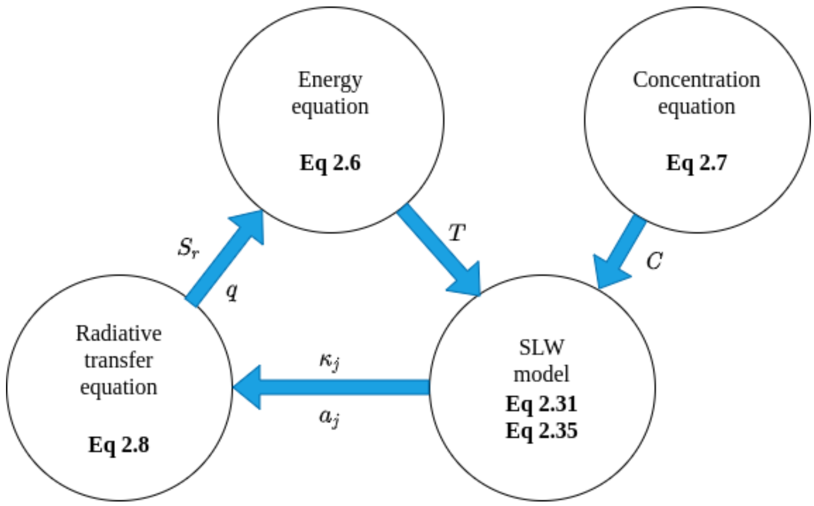

Figure 3.5: Implantation of SLW model in the Code Saturne

This general diagram describes how SLW model interacts with other components of Code Saturne. All these processes can be summarized as:

1. The values of concentration and temperature coming from the conservation of species equation and the energy equation are input for the SLW model.
2. The choice of the number of gray gases N_g (user input) and the tabulated data of the ALBDF are then used for determining the local radiative properties: the absorption coefficient and the corresponding weights for each gray gas.
3. The radiative properties are transferred to the module solving the radiative transfer equation using the Discrete Ordinate method. The solution is repeated for each gray gas and the integrations are performed over all directions to get the incident radiation and radiant flux. Then, these quantities are summed up over all the gray gases and are assembled to get the radiative source (divergence of the total radiative flux).
4. This radiative source is then injected into the right hand side of the energy equation.

In more details, for implanting SLW model into the built-in radiative module of Code Saturne (which contains tens of source files and hundreds of subroutines), we firstly had to find out the data-flow between these files for determining the location where our own model can be inserted. Next, the extraction of the inputs (from the conservation equations) had to be performed. Besides, a new library was created to store all the new variables and information related to SLW model. Finally, the subroutines for calculating the radiative properties had to be added. The highest difficulty of this implantation was to insert our own data without breaking the coherence of the built-in module. More details on the implementation are given in appendix B .

3.1.5 Convergence criteria

Code Saturne has no criteria to determine the convergence of the solution in term of variable residuals. Instead, it is advised to monitor the time evolution of the considered variables at different positions in the flow field to decide whether the calculation reaches a steady state (EDF [28]). The user can stop the computation whenever he finds the results stable enough or the code will run until it attains the declared number of time-steps. Besides, the conservations of the heat and mass flux can be a criterion for the consideration of a steady solution where the total fluxes arriving at the cavity walls have to be the same as those coming from the obstacle surfaces.

In our study, the convergence of the solution is qualitatively monitored by observing the temporal evolutions of the variables (temperature, concentration, velocity components) at different points inside the cavity. Quantitatively, the convergence is evaluated by the balance of the heat exchange between the hot source and the cavity active walls, which is written as:

$$\frac{|\sum_{f\in F_1} Nu_f^t S_f - \sum_{f\in F_2} Nu_f^t S_f|}{\sum_{f\in F_2} Nu_f^t S_f} \leq 10^{-3} \tag{3.9}$$

where F_1 and F_2 are the active walls of the enclosure and the hot source respectively, S_f being the surface area.

3.2 Code Validation

3.2.1 Differentially heated cavity

In this section, Code Saturne and its improved radiative model is validated by the simulations of both pure thermal convection and double diffusive convection coupled with radiation in a differentially heated cavity (see figure 3.6).

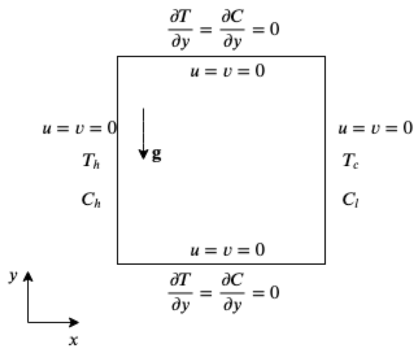

(a) 2D

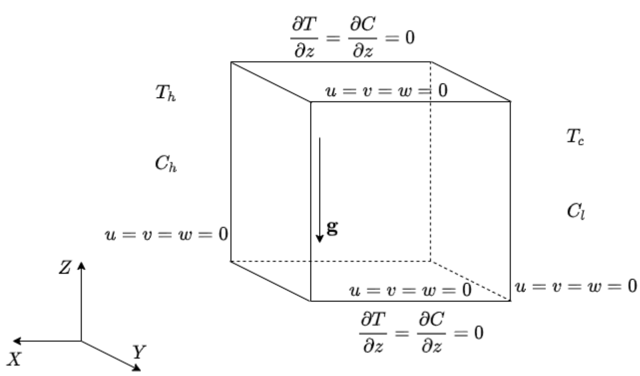

(b) 3D

Figure 3.6: Differentially heated cavity

3.2.1.1 Pure Thermal Convection

First, we have performed the calculation of natural convection at different Rayleigh numbers while keeping the Prandlt number at 0.71. There is no radiation (transparent medium, non-emitting walls). Our calculations are run using an uniform grid of 80 × 80 cells. Many reference results are available (Le Quéré [154], Tric, Labrosse, and Betrouni [155],...). Here, the solutions are compared to the data provided by De Vahl Davis [29] and are presented below. A good agreement is found between our works and this reference.

Ra	Our work	De Vahl Davis [29] (Relative Difference %))
10^3	1.113	1.117 (0.36)
10^4	2.235	2.238 (0.13)
10^5	4.507	4.509 (0.04)
10^6	8.816	8.817 (0.01)

Table 3.3: Mean Nusselt number on the hot wall

Regarding 3-D cases, we have performed calculations in the configurations studied by Colomer et al. [30] and Fusegi and Hyun [31]. An uniform 81^3 grid has been used. The computations have been run at $Pr = 0.71$. A good agreement is observed between our results and these references (see table 3.4).

Ra	Our work	Colomer[30]	Fusegi[31]
10^4	2.059	2.030 (1.42%)	2.100 (1.95 %)
10^5	4.365	4.334 (0.71 %)	4.361 (0.09%)
10^6	8.717	8.862 (1.63%)	8.770 (0.60 %)

Table 3.4: Mean Nusselt Number on the hot wall (Pr = 0.71)

3.2.1.2 Pure Thermal Convection coupled with radiation

We now present the comparisons between our computations and those of Yücel, Acharya, and Williams [1] and Laouar-Meftah [32] for coupled thermal convection and radiation in a gray gas inside a 2D differentially heated square cavity. In [1], the authors have used a non-uniform 50^2 grid (but they did not specify which type) and performed the calculations at different values of the overall optical thickness $\tau = \kappa \cdot L$ (L is the cavity size and κ the gray absorption coefficient). The Rayleigh number was fixed at $5 \cdot 10^6$ with $Pr = 0.72$ and the Planck number defined as $Pl = \frac{\lambda}{4\sigma L T_0^3}$ is set to $Pl = 0.02$. The dimensionless temperature θ_0 defined as $T_0/\Delta T$ was 1.5 while the emissivities (ϵ_i) of the bounding walls were set at 1. In our work, a non-uniform 81^2 grid like in reference [32] but with a different function for nodal distribution has been used: it is a tangent hyperbolic function in [32] while we used a cosine hyperbolic one. The results are listed in table 3.5. They show that the difference between our calculations and the reference does not exceed 4 %. This difference may come from the different interpolation schemes used in the DOM (Lathrop scheme in [32], STEP scheme in our study)

τ	S_N	Convective Nusselt			Total Nusselt		
		Our work	Ref.[1]	Ref.[32]	Our work	Ref.[1]	Ref.[32]
0.2	S_4	36.01	37.40	37.40	46.50	46.11	46.05
1	S_8	31.88	31.25	31.25	39.38	38.93	38.81
5	S_4	24.58	23.64	23.57	31.47	31.76	31.59

Table 3.5: Mean Nusselt number on the hot wall ($Pr = 0.71$, $Pl = 0.02$, $\theta_0 = 1.5$, $\epsilon_i = 1$)

For coupling thermal convection and radiation in a real gas (that is, accounting for the real absorption spectrum of the medium), we have performed different validation tests in a 3-D differentially heated cavity. We have re-produced the works of Billaud, Saury, and Lemonnier [6] by considering a cubic enclosure filled with humid air ($air - H_2O$ mixture). Different case studies based on the radiative behavior of the bounding walls and the medium are performed. They are described in the table 3.6. Our calculations have been carried out using a non-uniform 91^3 grid like in reference [6]. Our results are also compared with the data obtained by Soucasse, Rivière, and Soufiani [33] and presented in table 3.7. The comparisons show a fairly good agreement between our predictions and the two references.

Case	A	B	C	D
Isothermal walls	$\epsilon = 1$	$\epsilon = 1$	$\epsilon = 1$	$\epsilon = 1$
Adiabatic walls	$\epsilon = 0$	$\epsilon = 0$	$\epsilon = 1$	$\epsilon = 1$
Gas nature	Transparent	Participating	Transparent	Participating

Table 3.6: Radiative boundary conditions and radiative properties of the medium

Case	Our work	Billaud[6]	Soucasse[33]
A	8.64	8.65 (0.11 %)	8.64 (0.0 %)
B	7.24	7.42 (2.42 %)	7.55 (4.10 %)
C	7.93	8.10 (2.09 %)	8.47 (6.37 %)
D	8.48	8.01 (5.86 %)	8.48 (0.0 %)

Table 3.7: Mean convective Nusselt number on the hot wall ($air - H_2O$ mixture, $Ra = 10^6$, $Pr = 0.707$)

3.2.1.3 Double diffusive convection without radiation

We now simulate a double diffusive convection flow in a cubic enclosure with opposing temperature and concentration gradients. The calculations are performed at $Ra = 10^7$, $Le = 1$, $Pr = 0.71$ and different mass-to-thermal buoyancy ratios. No radiation is included at this stage, neither from the fluid (transparent), nor from the surfaces. The results are compared to the works of Sezai and Mohamad [34].

N	Our work	Sezai and Mohamad [34]	Relative difference (%)
-0.01	16.35	16.27	0.5
-0.5	13.57	13.53	0.3
-0.9	8.64	8.64	0.0
-1.5	13.58	13.54	0.3

Table 3.8: Mean Nusselt number on the hot wall ($Ra = 10^7$, $Le = 1$ and $Pr = 0.71$)

Calculations were performed over a grid of 80^3 uniform cells. The comparisons in table 3.8 shows a good agreement with the results of the reference [34]: the maximum difference in Nusselt number is less than 0.5%.

3.2.1.4 Double diffusive convection coupled with radiation

We now address the coupling of double diffusive convection and radiation in a real gas whose radiative properties are evaluated by SLW model. The comparisons of the Nusselt and Sherwood numbers between our results and the work by Cherifi [35] are performed and reported below for $air - CO_2$ and $air - H_2O$ mixtures at different concentration x. A non-uniform grid generated from a cosine function was used in the calculations of the reference [35]. In our computations, the mesh is $81 \times 81 \times 81$ with a nonuniform distribution along each edge whose density is given by a hyperbolic tangent function.

x_{CO_2}	Our work	Cherifi [35]	Relative difference (%)
0.05	14.66	14.60	0.41
0.11	15.66	15.65	0.06
0.20	17.11	17.16	0.29

Table 3.9: Mean convective Nusselt number on the hot wall for an $air - CO_2$ mixture

x_{CO_2}	Our work	Cherifi [35]	Relative difference (%)
0.05	19.53	19.38	0.77
0.11	21.65	21.44	0.98
0.20	23.96	23.77	0.80

Table 3.10: Mean Sherwood number on the hot wall for an $air - CO_2$ mixture

x_{H_2O}	Our work	Cherifi [35]	Relative difference (%)
0.05	15.65	15.78	0.82
0.11	16.51	16.75	1.43
0.20	18.17	18.03	0.77

Table 3.11: Mean convective Nusselt number on the hot wall for an $air - H_2O$ mixture

x_{H_2O}	Our work	Cherifi [35]	Relative difference (%)
0.05	15.82	15.74	0.5
0.11	16.85	16.79	0.35
0.20	19.15	19.02	0.68

Table 3.12: Mean Sherwood number on the hot wall for an $air - H_2O$ mixture

In all cases, our results coincide with the reference within a tolerance of 1.5%.

3.2.2 Cavity with a hot obstacle located inside

Our purpose is now to test the ability of our simulation code to handle geometries involving obstacles. The first validation test considers a 2-D square cavity with a heat source located at the center of the bottom wall (see figure 3.7). The enclosure has the dimension of $0.05 \times 0.05\ m^2$. The heat source is $0.01m$ wide and $0.025m$ high. The enclosure is filled by dry air (transparent) and the Prandtl number is set to 0.71. The heat source is maintained at $T_h = 301.16K$ while two lateral walls of cavity are prescribed at $T_c = 291.16K$. The remaining surfaces of the enclosure are adiabatic. The tests are performed with different Rayleigh numbers, using a 100^3 uniform grid and the results are compared to the experiments and the simulations of Paroncini and Corvaro [13].

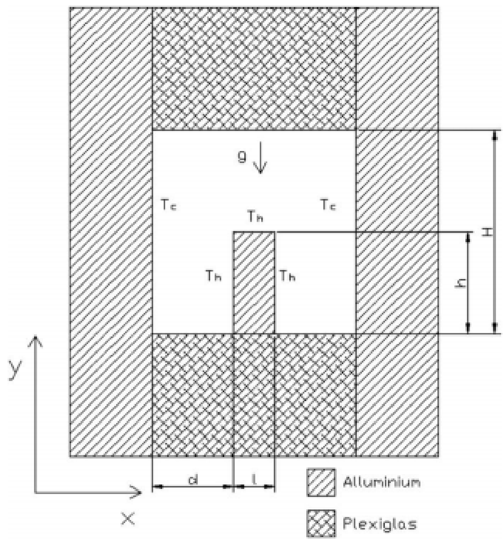

Figure 3.7: Calculation domain (Paroncini and Corvaro [13])

Ra	Reference[13] (exp)	Reference[13] (num)	Our work
$1.02 \cdot 10^5$	10.49	10.46	10.42
$1.21 \cdot 10^5$	10.96	10.96	10.96
$1.48 \cdot 10^5$	11.46	11.58	11.61
$1.68 \cdot 10^5$	11.89	11.99	12.04
$1.93 \cdot 10^5$	12.34	12.45	12.52
$2.11 \cdot 10^5$	12.71	12.76	12.84

Table 3.13: Mean Nusselt number on the lateral wall of the heated obstacle

The comparisons show a good agreement with the reference, the maximum difference being less than 1% when comparing the two numerical simulations. Difference are larger with respect to measured quantities (but this is also true in the reference work). Some thermal leakage through the plexiglas plates (imperfect insulation) may explain these variations.

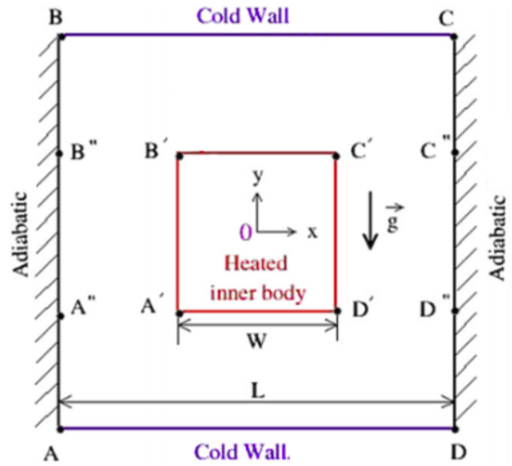

Figure 3.8: Domain of calculation ($Ra = 2 \cdot 10^5$, $Pr = 0.71$)

The second validation test considers a hot obstacle located at the center of a 2-D square cavity (see figure 3.8). Now, two vertical walls of the cavity are kept adiabatic while the horizontal one are maintained at a constant lower temperature compared to the isothermal heated obstacle. The enclosure is filled with dry air. The simulation is run at a Rayleigh number of $Ra = 2 \cdot 10^5$ and a Prandlt number of $Pr = 0.71$. The comparisons with the results of Sun, Chénier, and Lauriat [20] reported in table 3.14 point out that our code can efficiently handle this type of configuration, both for the flow description and thermal transport (the maximum difference is less than 0.5%).

	Our work	Reference [20]	Relative difference (%)
Side A′B′ or C′D′	3.7129	3.7174	0.121
Side A′D′ (bottom)	5.6527	5.6347	0.319
Side B′C′ (top)	9.4989	9.4614	0.396
Bottom wall	2.5342	2.5346	0.015
Top Wall	6.4966	6.4778	0.290

Table 3.14: Mean Nusselt number on different walls ($Ra = 2 \cdot 10^5$, $Pr = 0.71$)

3.3 Conclusion

In this section, we have described the Discrete Ordinates Method and the improvements we have brought to its implementation in Code Saturne. We have also detailed the introduction of the SLW model in this code.

Different validation tests in differentially heated cavity (thermal or double diffusive convection with/without radiation) as well as the configuration of the cavity with an obstacle located inside have been performed. The comparisons between our predictions and different references point out that:

- Code Saturne can accurately handle the calculation of thermal convection or double diffusive convection.
- The built-in radiative module of Code Saturne is reliable after the correction of some flaws that are present in version 5.0.4.

- Our implemented SLW model is able to predict the radiation effects with a satisfactory accuracy in configuration involving real gases.

Chapter 4

Coupling between Pure Thermal Convection and Radiation

A first set of results concerns pure thermal convection. In this configuration, the fluid is homogeneous in composition and the flow is only governed by the temperature gradients.

4.1 Introduction

We firstly present the cross section planes and the crosslines used to display the results. The dimensionless temperature, concentration and velocity fields are plotted in the median vertical plane of the cavity ($Y = 0.5$ or $y = 0.125m$) (see figure 4.1). We also consider the profiles of these quantities along different crosslines in the plane $Y = 0.5$:

- Z-lines: $Z = 0.1$, $Z = 0.5$, $Z = 0.8$
- X-lines: $X = 0.2$, $X = 0.5$, $X = 0.8$

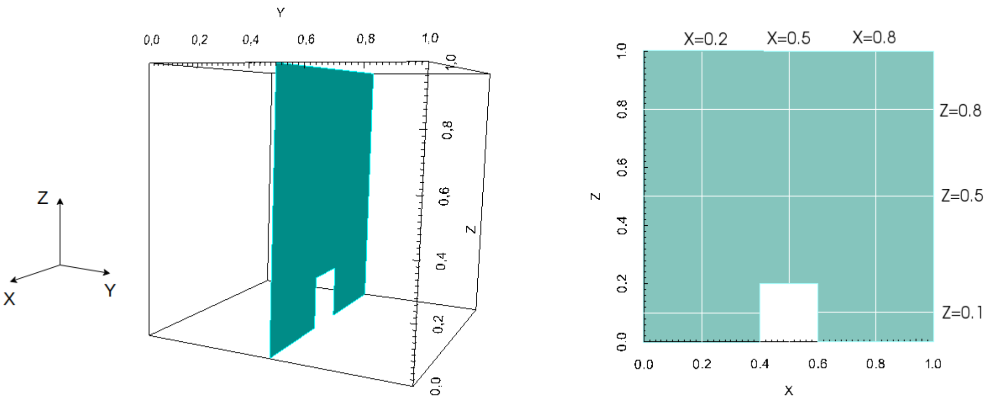

(a) Plane under consideration ($Y = 0.5$)

(b) Crosslines in the plane $Y = 0.5$

Figure 4.1: Median plane ($Y = 0.5$) and crosslines used for the results display

All the results presented hereafter are normalized using the reference temperature $T_{ref} = \frac{T_h+T_c}{2}$, the reference length L, the reference velocity $U_{ref} = \alpha\frac{\sqrt{Ra}}{L}$ and the reference time $\frac{L^2}{\alpha\sqrt{Ra}}$ (where $\alpha = \frac{\lambda}{\rho_0 C_p}$ is the thermal diffusivity).

4.1.1 Convergence on spatial grid

Before conducting original simulations, we have analyzed the convergence of results with respect to the spatial meshing, the angular discretization and the number of gray gases (spectral divisions) in the SLW model. We have run different tests, but we only present here those concerning a case of natural convection at $Ra = 5 \cdot 10^6$, $Pr = 0.71$, $T_0 = 555K$ and $\Delta T = 50K$ with black active walls and purely reflective adiabatic walls. Three uniform grids of different size have been considered: $80 \times 80 \times 80$ (80^3), $100 \times 100 \times 100$ (100^3) and $120 \times 120 \times 120$ (120^3).

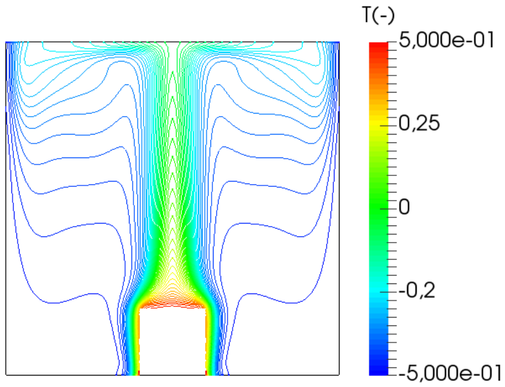

(a) 80^3

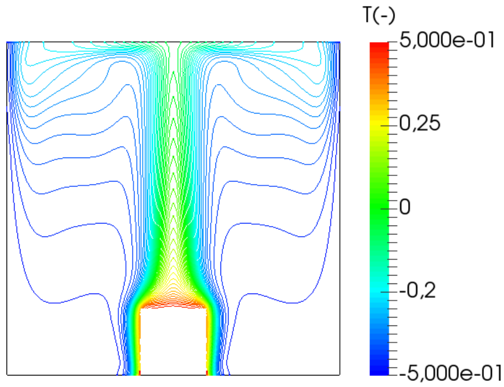

(b) 100^3

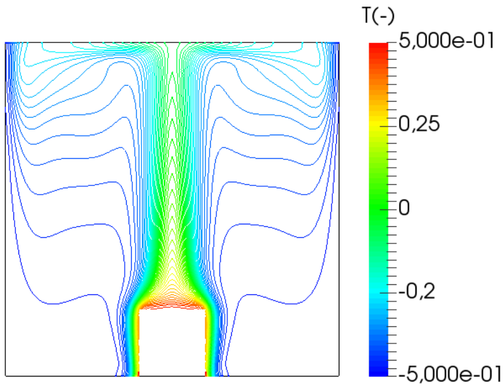

(c) 120^3

Figure 4.2: Temperature $\frac{T-T_{ref}}{T_h-T_c}$ distribution in the median plane ($Y = 0.5$) with different mesh sizes: transparent medium.

Mesh	u_{max} (m/s)	w_{max} (m/s)
80^3	0.191	0.339
100^3	0.191	0.342
120^3	0.191	0.342

Table 4.1: Maximum horizontal and vertical velocities for different mesh sizes.

Mesh	Front wall	Back wall	Left wall	Right wall
80^3	1.690	1.690	1.690	1.690
100^3	1.682	1.682	1.682	1.682
120^3	1.681	1.681	1.681	1.681

Table 4.2: Mean Nusselt numbers at the bounding surfaces of the enclosure.

Mesh	Front wall	Back wall	Left wall	Right wall	Top wall
80^3	38.664	38.664	38.664	38.664	14.343
100^3	38.508	38.508	38.508	38.508	14.166
120^3	38.492	38.492	38.492	38.492	14.132

Table 4.3: Mean Nusselt numbers at the bounding surfaces of the hot source.

From the result displayed above, we consider that the simulations are converged with respect to the spatial meshing when using a $100 \times 100 \times 100$ grid. Therefore, we have selected this mesh for our subsequent calculations.

4.1.2 Convergence on angular discretization

When radiation is present, the sensitivity of the results to the angular discretization needs to be assessed. To that end, we consider the coupling of natural convection and radiation in a gray gas at $Ra = 5 \cdot 10^6$, $Pr = 0.71$ and θ_0[1] = 11.1 with an optical thickness of $\tau = 0.5$. Different orders of the level symmetric quadrature S_N are tested: S_6, S_8, S_{12}. The corresponding results in terms of temperature and velocity are displayed in figures. 4.3-4.4 and in table 4.2.

[1] θ_0 is defined as $\frac{T_0}{T_h - T_c}$. This dimensionless parameter relates the absolute temperature T_0 (which governs the radiation problem) to the temperature difference (which drives the convection motion)

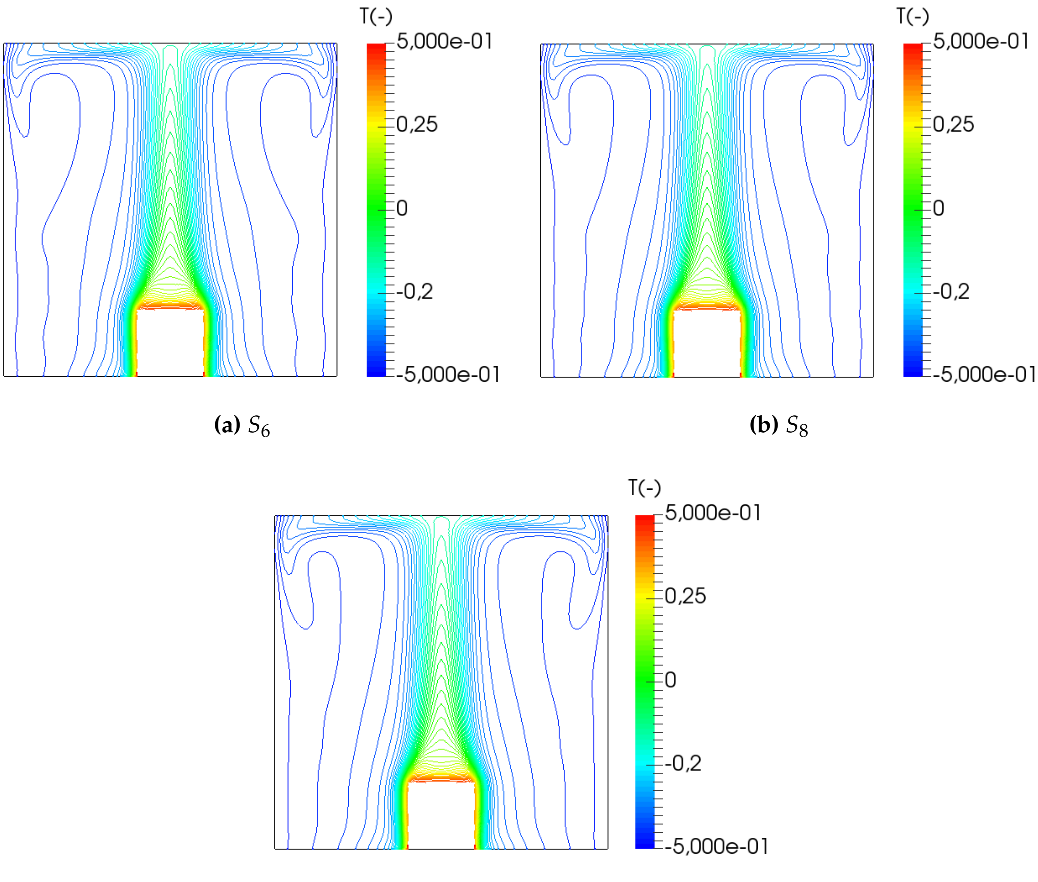

(a) S_6 **(b)** S_8 **(c)** S_{12}

Figure 4.3: Temperature $\frac{T-T_{ref}}{T_h-T_c}$ distribution in the median plane ($Y = 0.5$) for the gray medium at $\tau = 0.5$.

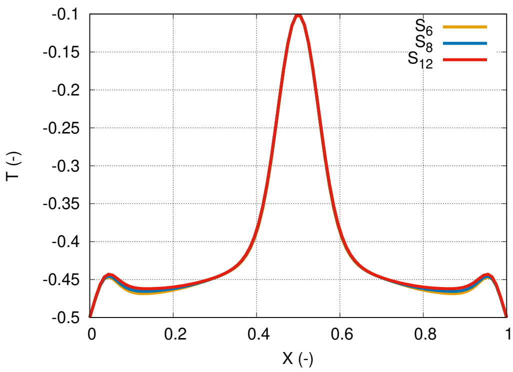

(a) Temperature profile along the line at $Z = 0.8$

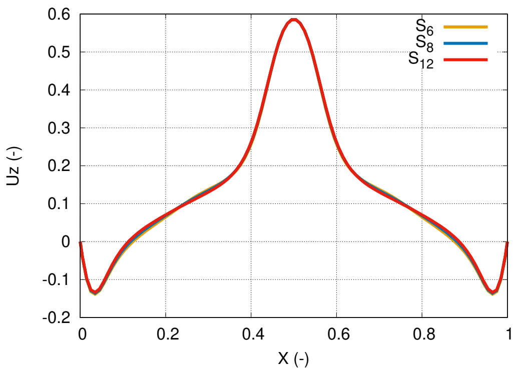

(b) Vertical velocity profile along the line at $Z = 0.8$

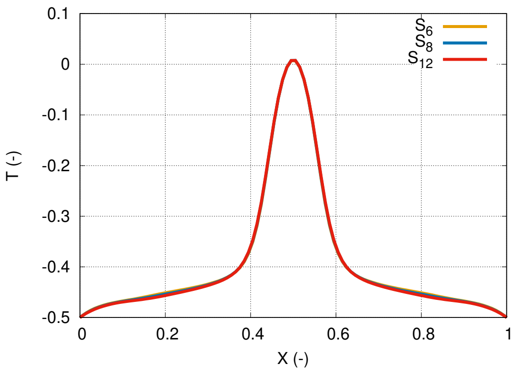

(c) Temperature profile along the line at $Z = 0.5$

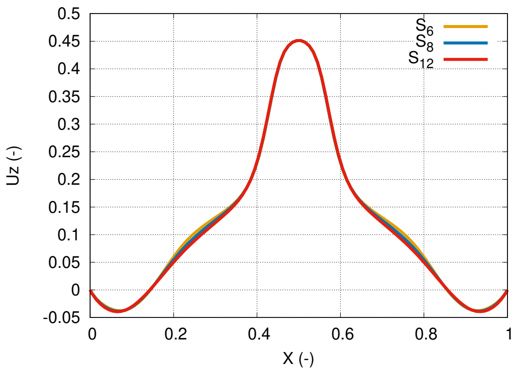

(d) Vertical velocity profile along the line at $Z = 0.5$

Figure 4.4: Profiles of temperature $\frac{T-T_{ref}}{T_h-T_c}$ and vertical velocities $\frac{w}{U_{ref}}$ at different crosslines in the median plane ($Y = 0.5$).

S_N	Convective Nusselt number	Radiative Nusselt number
S_6	0.976	11.073
S_8	0.989	11.055
S_{12}	0.995	11.053

Table 4.4: Mean convective and radiative Nusselt numbers over the vertical surfaces of the enclosure.

The comparisons presented above confirm that, with a S_8 quadrature set only (80 directions), we can obtain the results with a good accuracy. This was confirmed for other optical thicknesses ranging from 0.1 to 2. Consequently, we have selected this discrete directions set for our following calculations.

4.1.3 Convergence on the number of gray gases for the SLW model

The tests are performed for the case of coupling natural convection and radiation in a real (non gray) gas mixture $air - H_2O$ at concentration $x_{H_2O} = 0.20$. For the radiative calculations, we have used the rank-correlated approach, as described in Chapter 2. The results are displayed below (figure 4.5 and table 4.5):

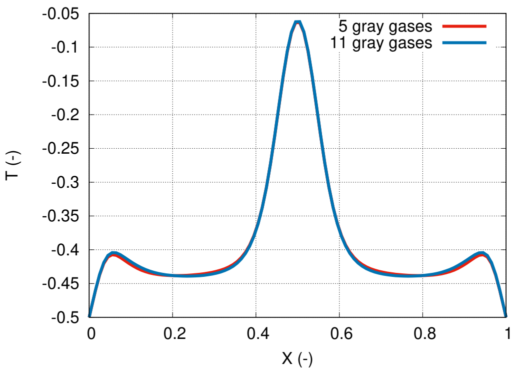

(a) Temperature profile along the line at $Z = 0.8$

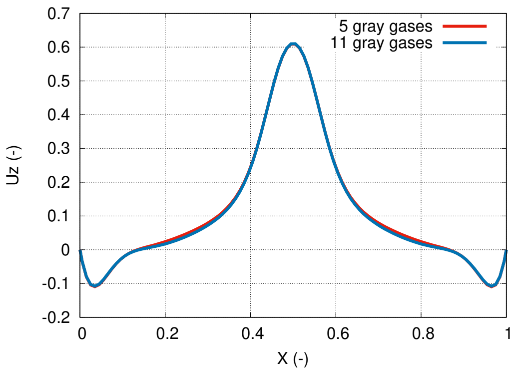

(b) Vertical velocity profile along the line at $Z = 0.8$

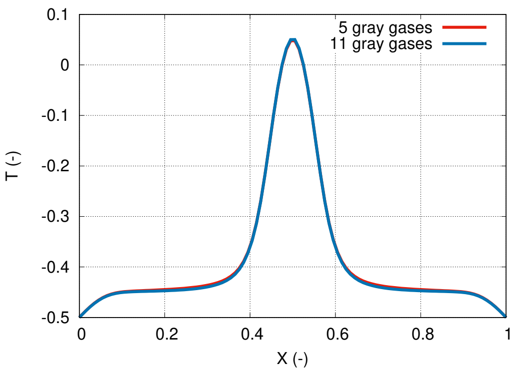

(c) Temperature profile along the line at $Z = 0.5$

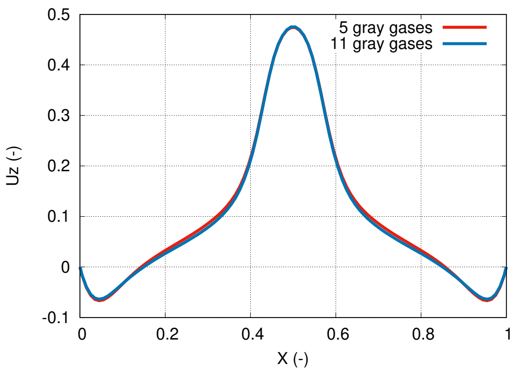

(d) Vertical velocity profile along the line at $Z = 0.5$

Figure 4.5: Profiles of temperature and vertical velocities at different crosslines in the median plane ($Y = 0.5$).

N_g	Convective Nusselt number	Radiative Nusselt number
5	36.59	211.34
11	36.68	211.15
Relative Difference (%)	0.24	0.09

Table 4.5: Mean convective and radiative Nusselt numbers at a lateral wall of the obstacle.

The comparisons show that using only 5 gray gases in the SLW model is enough, in this type of problem, to achieve an acceptable level of accuracy within a very affordable computational cost. Concretely, the simulations are run on one core of *Intel(R) Xeon(R) CPU E5-2620 @ 2GHz*. With 11 gases, it needs 182 hours of CPU time while with 5 gases, it reduces to 103 hours (56 % compared to the 11 gas model) to reach the same physical simulation time.

4.2 Coupling with radiation in the gray gas assumption

In this part, we analyze the effect of radiation on the flow structure and heat transfer in a simple manner, by assuming that the medium filling the cavity is gray and has uniform radiative properties. This assumption allow us to study adimensionally the effect of gas radiation on the flow structure and heat transfer via the non-dimensional optical thickness. This parameter is defined as $\tau = \kappa L$ related to the cavity size, L and the absorption coefficient κ. Different fluid opacities may be considered by changing the optical thickness values.

All calculations were performed at $Ra = 5 \cdot 10^6$ and $Pr = 0.71$ and $\theta_0 = 11.1$. The emissivity of the hot and cold walls is 1 and of the adiabatic surface is 0.

As the adiabatic walls are assumed to be purely reflective, there is no radiative-convective coupling when $\tau = 0$ (transparent medium). This limiting case serves as the reference for determining the radiation effects on the flow field.

4.2.1 Steady flows

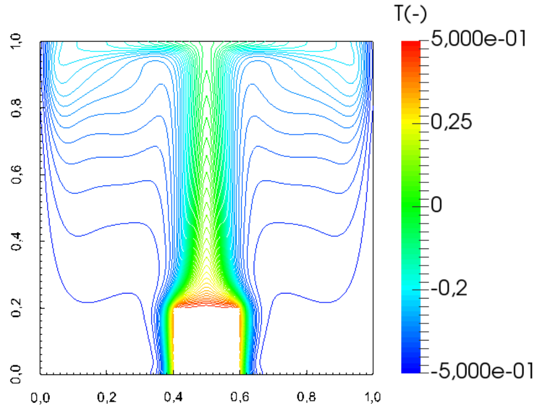

(a) Transparent medium

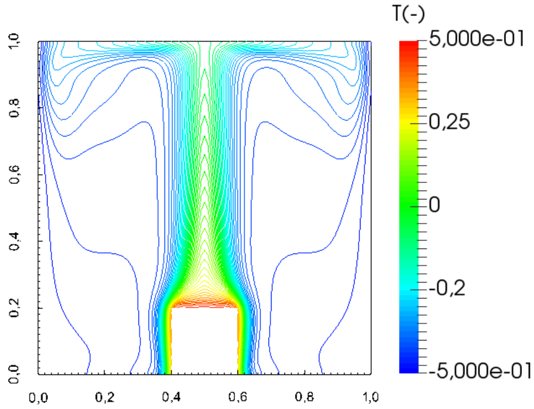

(b) $\tau = 0.1$

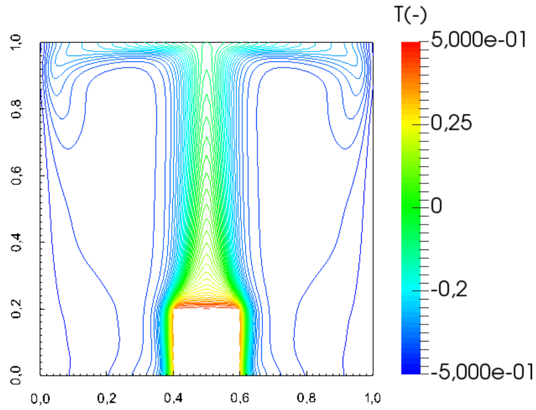

(c) $\tau = 0.2$

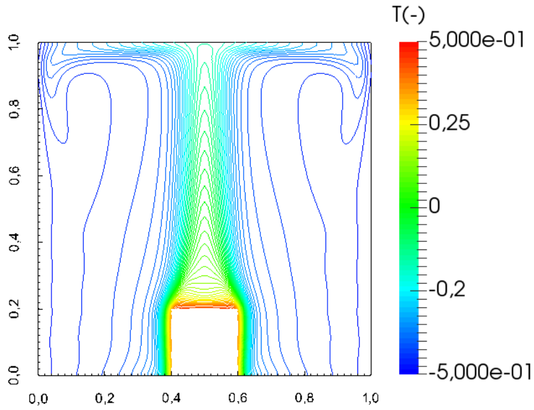

(d) $\tau = 0.5$

Figure 4.6: Temperature $\frac{T-T_{ref}}{T_h-T_c}$ distribution in the median plane ($Y = 0.5$) for different fluid opacities.

Figure 4.6 displays the thermal fields in the median plane ($Y = 0.5$) for different case studies ranging from a transparent medium to an optical thickness of $\tau = 0.5$. All these configurations lead to a steady state solution. Further increasing τ may yield periodic flows, as will be described in the next paragraph (4.2.2).

It is observed in figure 4.6 a nearly vertical stratification in absence of radiation on both sides of the cavity. But this distribution is broken when the radiative effects are introduced. The hot surfaces of the obstacle radiate toward the absorbing fluid between the heater and the cold wall of the enclosure (see figure 4.7 a). At medium and high levels ($Z = 0.5, 0.8$) (see figure 4.7 b,c), radiation cools down the fluid, since the gas in this region emits more than it absorbs. This is demonstrated by the negative values of the radiative source term (see figure 4.9 b,d,f). And the higher optical thickness, the stronger the radiation effects are. Overall, the radiative transport levels the temperature field in the cavity, at least in the range of opacities we have investigated.

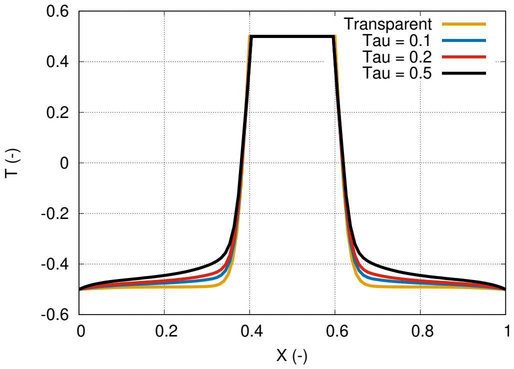

(a) Z=0.1

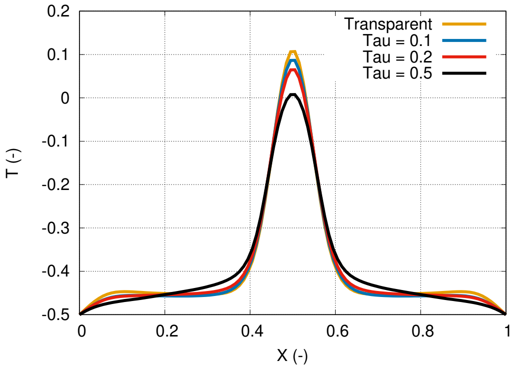

(b) Z=0.5

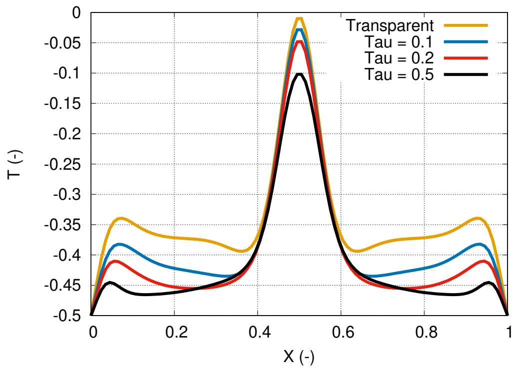

(c) Z=0.8

Figure 4.7: Temperature $\frac{T-T_{ref}}{T_h-T_c}$ profiles at different Z-crosslines in the median plane ($Y = 0.5$).

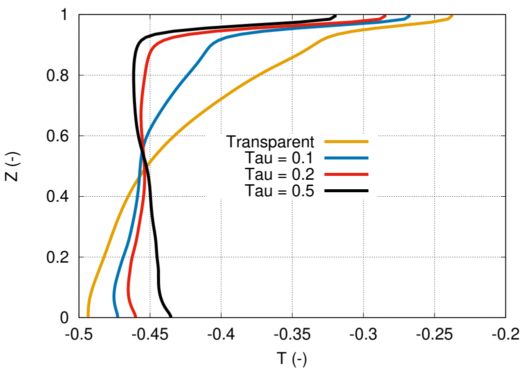

(a) X=0.2 or 0.8

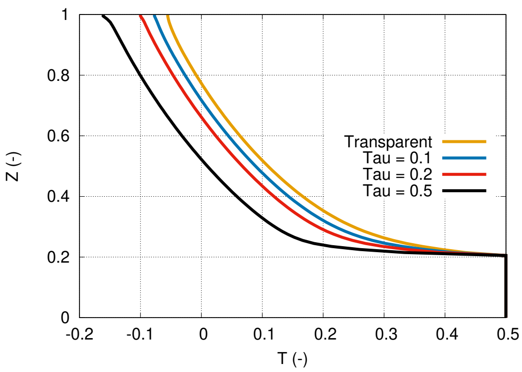

(b) X=0.5

Figure 4.8: Temperature $\frac{T-T_{ref}}{T_h-T_c}$ profiles at different X-crosslines in the median plane ($Y = 0.5$).

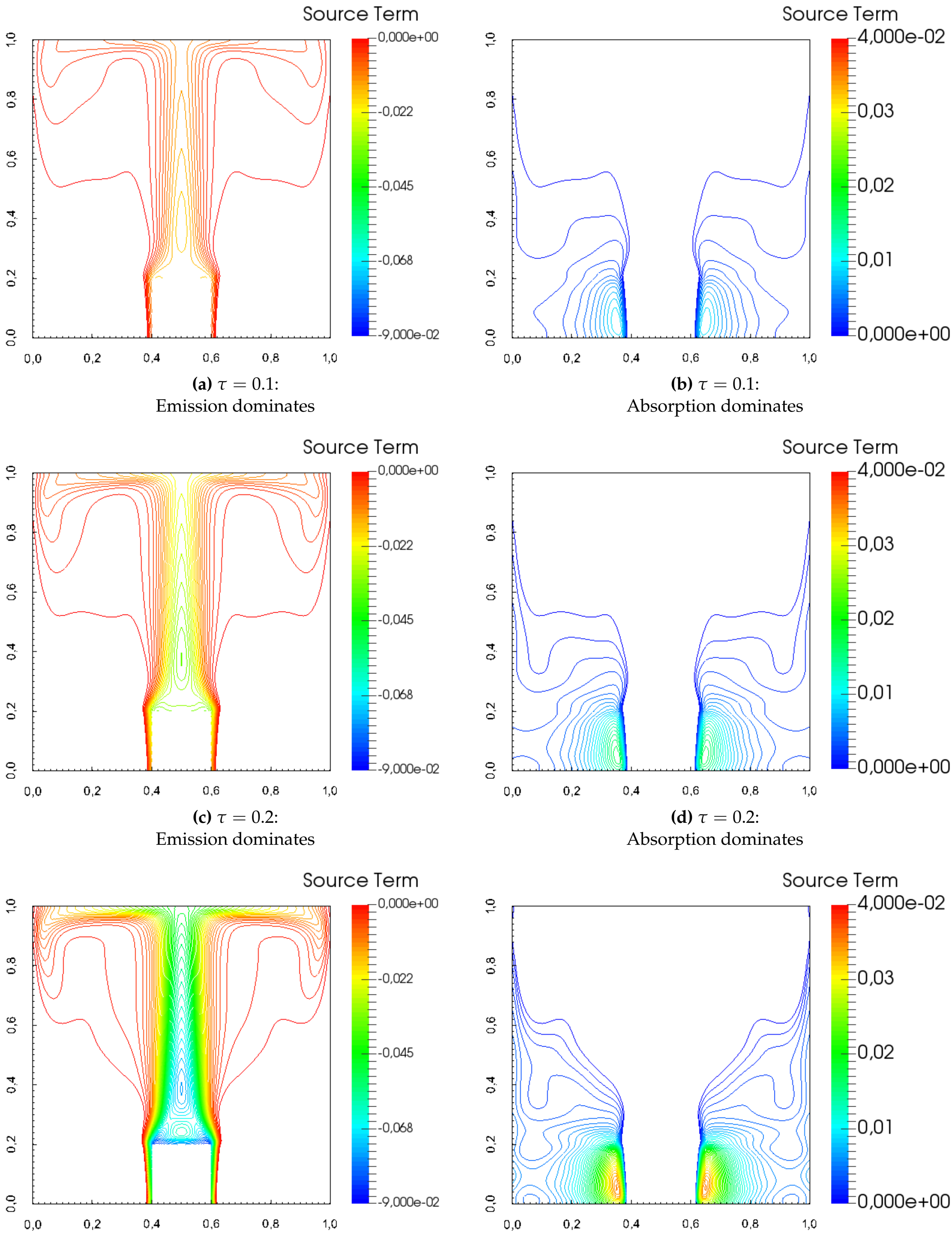

(a) $\tau = 0.1$: Emission dominates

(b) $\tau = 0.1$: Absorption dominates

(c) $\tau = 0.2$: Emission dominates

(d) $\tau = 0.2$: Absorption dominates

(e) $\tau = 0.5$: Emission dominates

(f) $\tau = 0.5$: Absorption dominates

Figure 4.9: Distribution of radiative source term in the median plane ($Y = 0.5$) at different optical thicknesses. Sources are normalized by $4\sigma T_{ref}^4/L$.

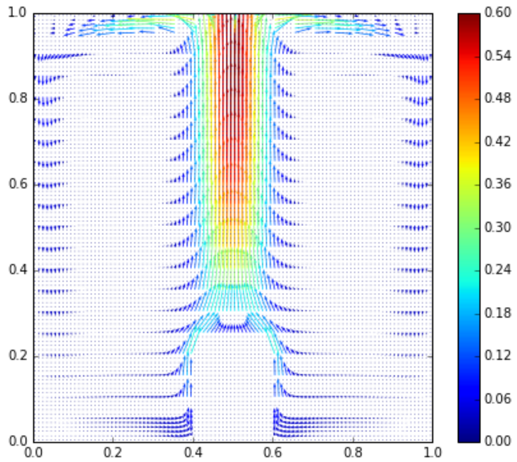

(a) Transparent medium

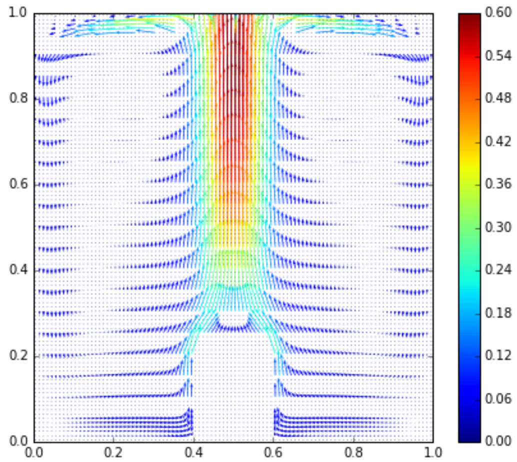

(b) $\tau = 0.1$

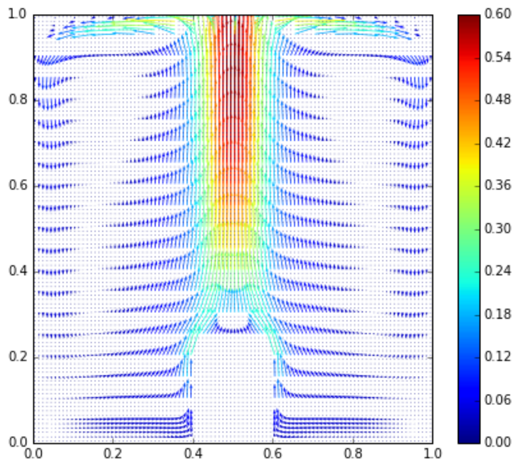

(c) $\tau = 0.2$

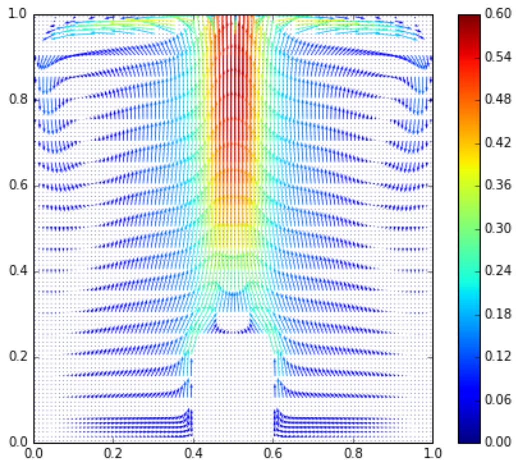

(d) $\tau = 0.5$

Figure 4.10: Velocity field on the median plane ($Y = 0.5$) for different fluid opacities. Velocities are normalized by U_{ref}.

Figure 4.10 represents the velocity vectors in the mid-depth plane ($Y = 0.5$) for different values of the optical thickness. It is shown that, as the opacity increases, the fluid is more accelerated, inside the plume and next to the cavity surfaces. It is also observed the broadening of the plume and of the vertical boundary layers near the cavity walls when the radiation effects is considered (compared to the transparent cases). Besides, we observe that the plume at $\tau = 0.1$ and $\tau = 0.2$ keeps the same cone shape. However, as the $\tau = 0.5$, the structure of the plume changes: it is compressed at medium altitude and takes the form of an hourglass. The reason is that, when the optical thickness increases, the temperature in the lower part of the cavity increases (see figure 4.8 a) due to the absorption effect (see figure 4.9 f). As a result, the fluid in this region is pushed up, and then collides with the downward boundary layers near the cavity vertical wall.

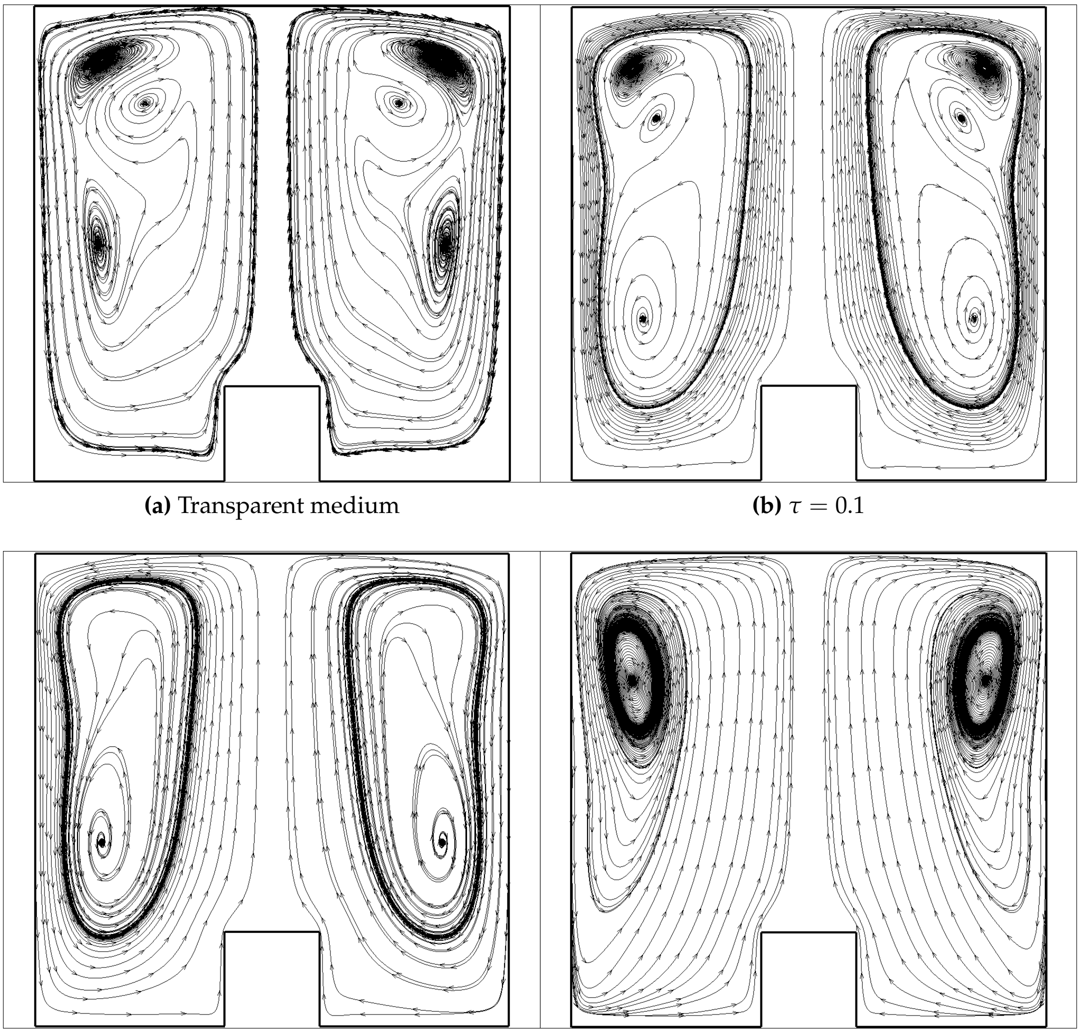

(a) Transparent medium

(b) $\tau = 0.1$

(c) $\tau = 0.2$

(d) $\tau = 0.5$

Figure 4.11: Flow lines[2] on the median plane ($Y = 0.5$) for different fluid opacities.

Regarding the flow structure, there are three spirals, which are associated to low velocities and cannot be found in the vector field above, on each side of the cavity (see figure 4.11 a) when the medium is transparent. However, when the medium participates to radiation, the number of spirals decreases (see figure 4.11 b,c,d). The profiles of vertical velocities at different Z-levels (figure 4.12) reveal that the fluid that was stagnant in the transparent case is now moving. As a consequence, the ascending plume and the descending movement along the cavity walls interfere and create a shear flow. Besides, we also observe the broadening of the obstacle vertical boundary layers (figure 4.12 a). As the optical thickness increases, this effect is accentuated and at $\tau = 0.5$, these boundary layers broaden enough to reach the cavity lateral walls and even block the downward flow (slow down and redirect). In addition, the mass transport driven by the plume is increased, causing an acceleration of the return stream along the ceiling (mainly) and the floor (to a lesser extent) (see figure 4.13 a).

[2]These flow lines represent the trajectory of fluid particles uniformly placed in the plane $Y = 0.5$. Each of them is generated by integration of velocity values.

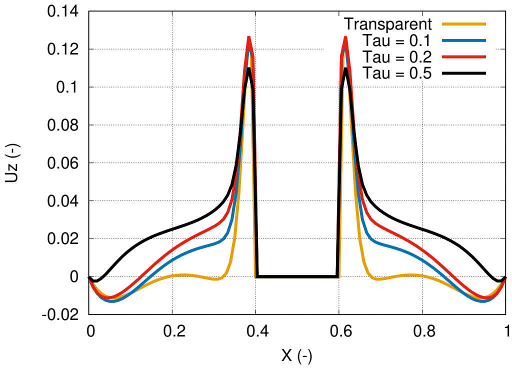

(a) $Z = 0.1$

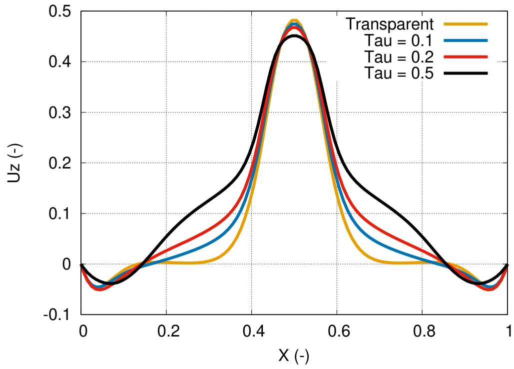

(b) $Z = 0.5$

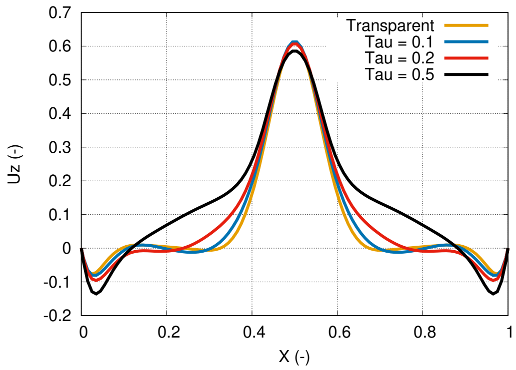

(c) $Z = 0.8$

Figure 4.12: Profiles of vertical velocities $\frac{w}{U_{ref}}$ at different Z-crosslines in the median plane ($Y = 0.5$).

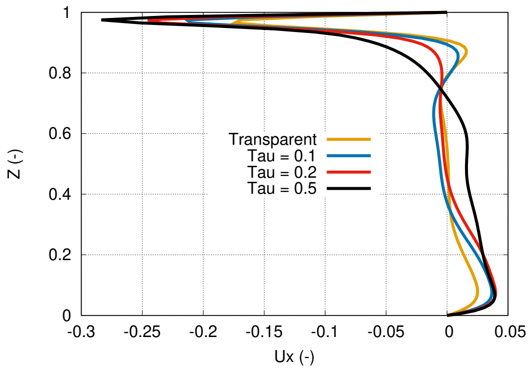

(a) X=0.2 or X=0.8

Figure 4.13: Profiles of horizontal velocities $\frac{u}{U_{ref}}$ at different X-crosslines in the median plane ($Y = 0.5$).

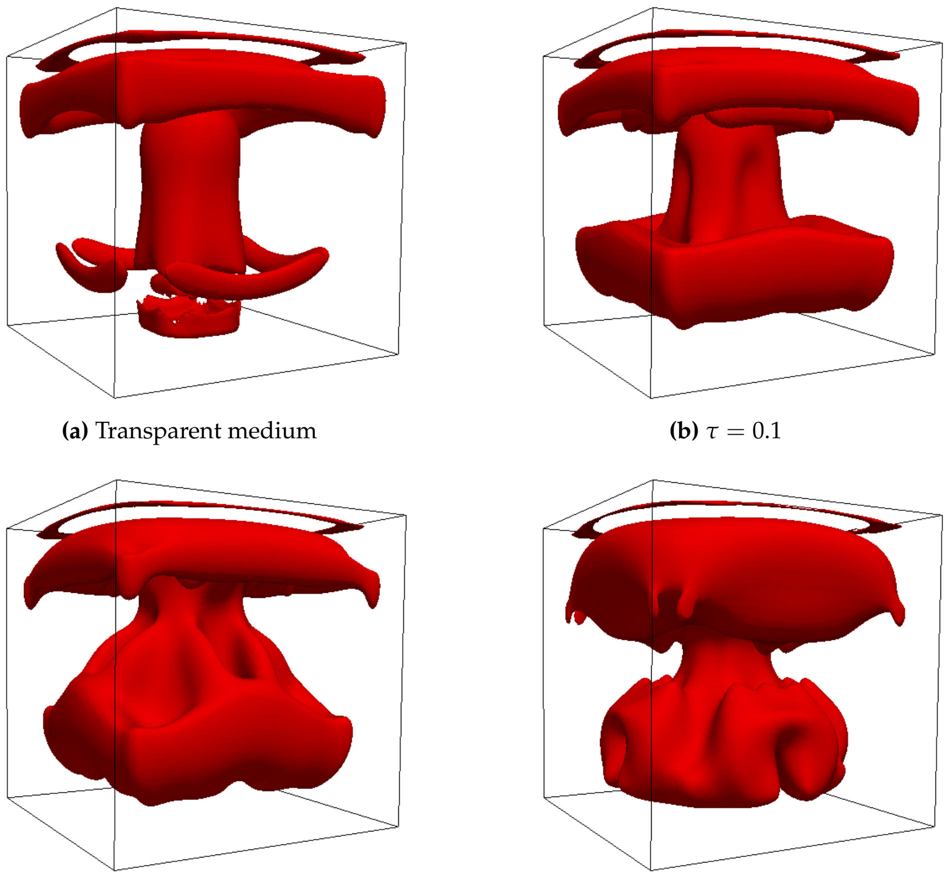

(a) Transparent medium **(b)** $\tau = 0.1$

(c) $\tau = 0.2$ **(d)** $\tau = 0.5$

Figure 4.14: Representation of the Q-criterion at $Q = 0.02$ in the cavity. Values are normalized by U_{ref}^2/L^2.

For further analyzing the flow structure, we investigate the Q-criterion[3], which is used as a method to identify the swirl zones within the fluid (where $Q > 0$). $Q < 0$ stands for the regions where the deformation dominates over the rotation. Concerning the 3-D structures, we observe that the swirl takes place in the area between the plume flow and its re-circulation along the cavity walls. Looking closely at figure 4.14, which represents the iso-surfaces at $Q = 0.02$[4], we denote an expansion of the surfaces as the opacity increases. This means that the trend of auto-rotation dominates over deformation, becoming a global effect rather than a local phenomenon as it can be seen in figure 4.14 a. This explains the disappearance of the spiral flows. We have also considered the distribution of negative values of Q plotted in the median plane ($Y = 0.5$) (see figure 4.15). The differences observed in the patterns of the $Q = -0.02$ iso-value lines for different fluid opacities result from the interference of the upward plume and downward boundary layers where, literally, the deformation dominates over rotation.

[3]See appendix C for the definition of the Q-criterion.
[4]This value was found to produce the best illustration of the modifications in the flow structure.

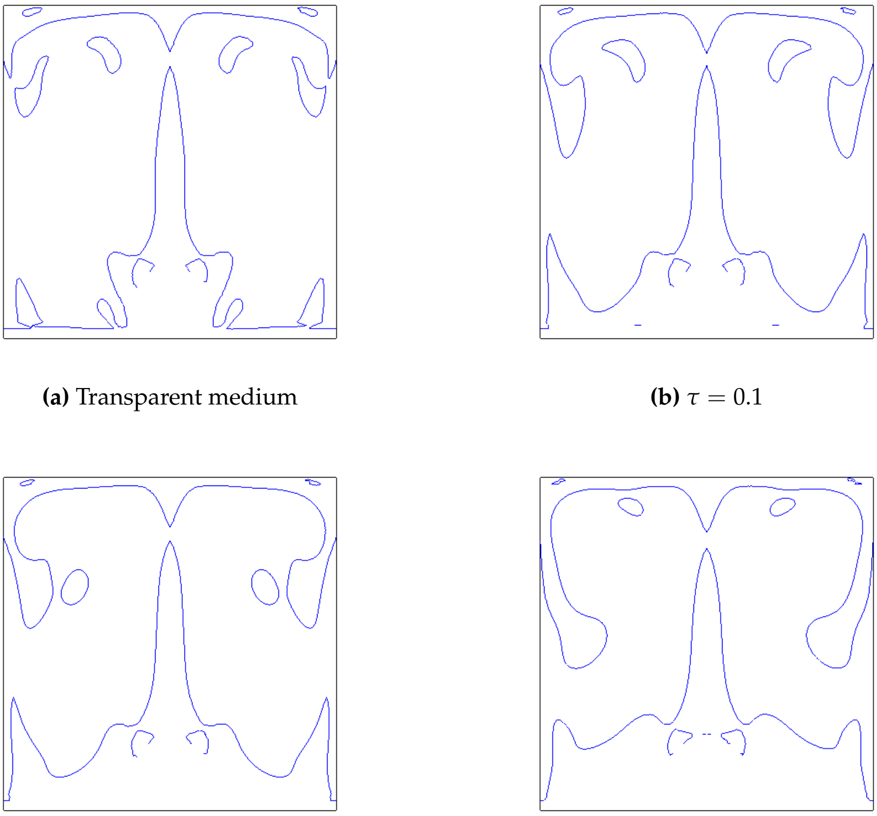

(a) Transparent medium

(b) $\tau = 0.1$

(c) $\tau = 0.2$

(d) $\tau = 0.5$

Figure 4.15: Isovalue lines at $Q = -0.02$ in the median plane ($Y = 0.5$). Values are normalized by U_{ref}^2/L^2.

4.2.2 Unsteady flows

The two cases $\tau = 1$ and $\tau = 2$ are now considered. The case $\tau = 1$ leads to an unsteady laminar flow (see figure 4.17 a), while the other produces turbulent results (see figure 4.17 b). The turbulent behavior can also be demonstrated by the observation of the spectrum analysis where we do not found any dominant frequency (see figure 4.18). We only investigate here the case at $\tau = 1$.

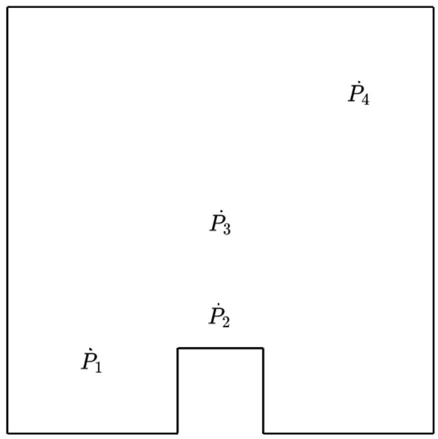

Figure 4.16: Considered points for tracking the time evolution of temperature.

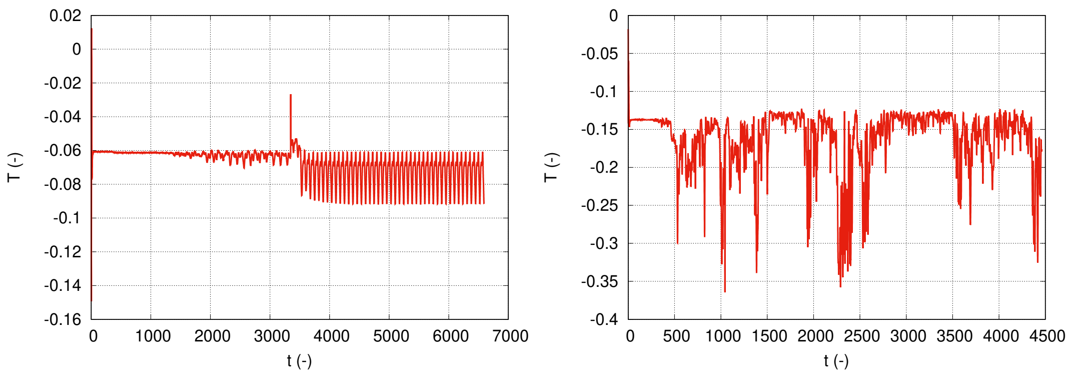

(a) $\tau = 1$ **(b)** $\tau = 2$

Figure 4.17: Time evolution of temperature $\frac{T-T_{ref}}{T_h-T_c}$ at the center point of the cavity P_3: $(X, Y, Z) = (0.5, 0.5, 0.5)$ at different optical thicknesses.

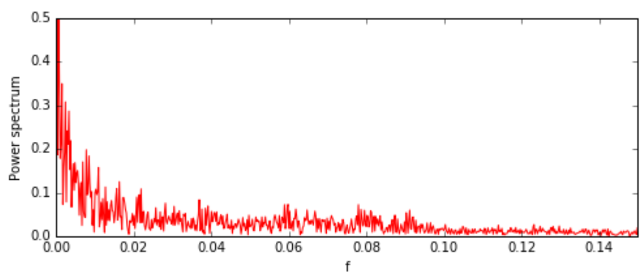

Figure 4.18: Power spectrum of the temperature signal at the point P_3: $(X, Y, Z) = (0.5, 0.5, 0.5)$ at $\tau = 2$

When $\tau = 1$, the periodical fluctuations are evidenced on the time evolution of temperature at different positions in the median plane of the cavity (see figure 4.16). The Fast Fourier Transform has been performed to determine the frequencies of the oscillations and then plotted in the figures below (figures 4.19-4.22).

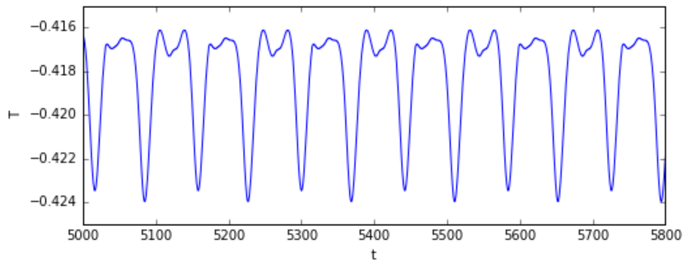

(a) Time evolution of temperature

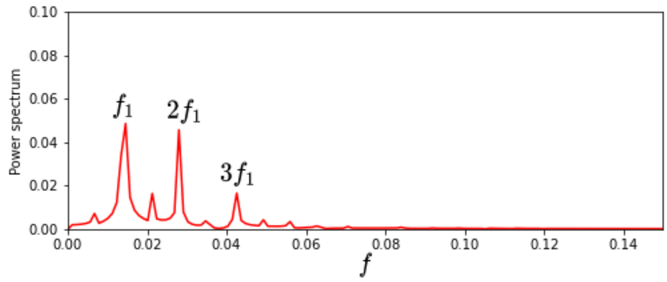

(b) Power spectrum

Figure 4.19: Time evolution and power spectrum of the temperature signal at the point P_1: $(X, Y, Z) = (0.2, 0.5, 0.2)$ in temporal range [5000:5800] at $\tau = 1$.

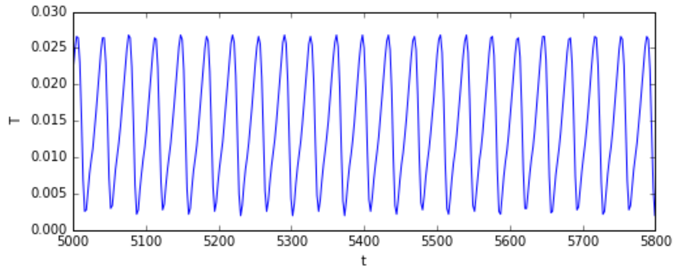

(a) Time evolution of temperature

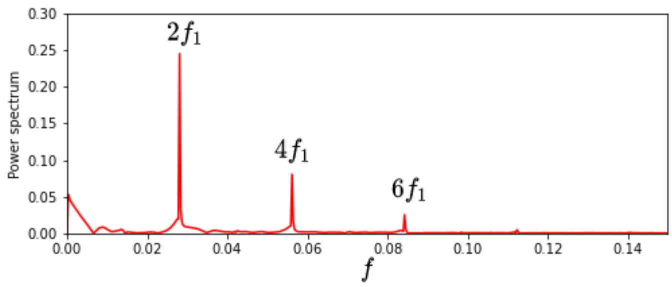

(b) Power spectrum

Figure 4.20: Time evolution and power spectrum of the temperature signal at the point P_2: $(X, Y, Z) = (0.5, 0.5, 0.3)$ in temporal range [5000:5800] at $\tau = 1$.

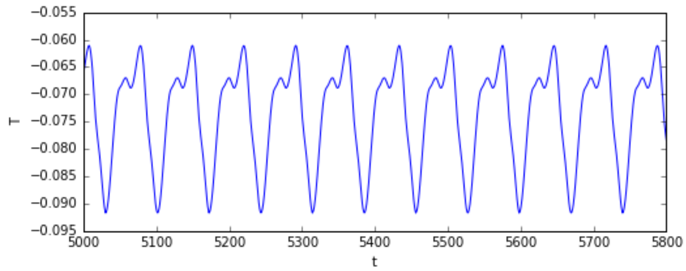

(a) Time evolution of temperature

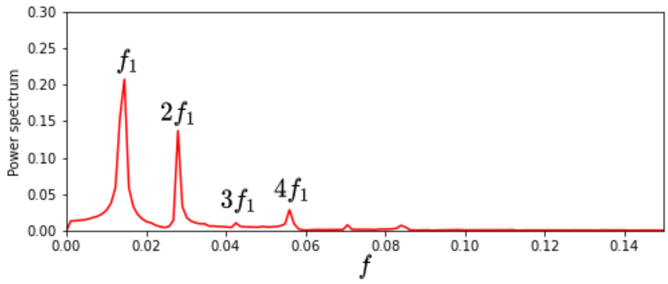

(b) Power spectrum

Figure 4.21: Time evolution and power spectrum of the temperature signal at the point P_3: $(X, Y, Z) = (0.5, 0.5, 0.5)$ in temporal range [5000:5800] at $\tau = 1$.

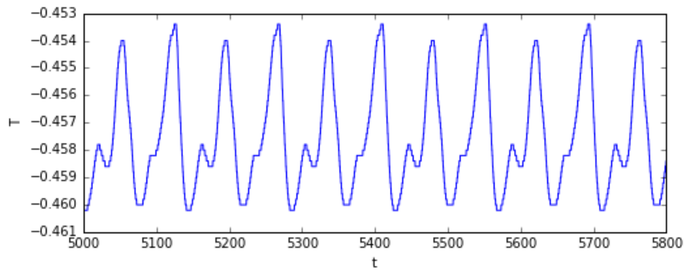

(a) Time evolution of temperature

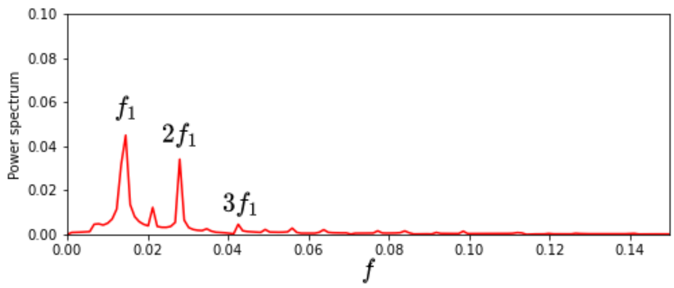

(b) Power spectrum

Figure 4.22: Time evolution and power spectrum of the temperature signal at the point P_4: $(X, Y, Z) = (0.8, 0.5, 0.8)$ in temporal range [5000:5800] at $\tau = 1$.

At point P_2 (see figure 4.20), the Fourier analysis yields a fundamental frequency $f = 0.028$ and its two harmonics $f_2 = 2f$ and $f_3 = 3f$. On the other hand, at point P_1 (see figure 4.19), P_3 (see figure 4.21) and P_4 (see figure 4.22), it reduces to $f_1 = 0.014$.

However, the frequency of 0.028 is present at all the considered positions, even when it is not the fundamental one. It may refer to a global phenomenon while other identified frequencies belong to the local fluctuations.

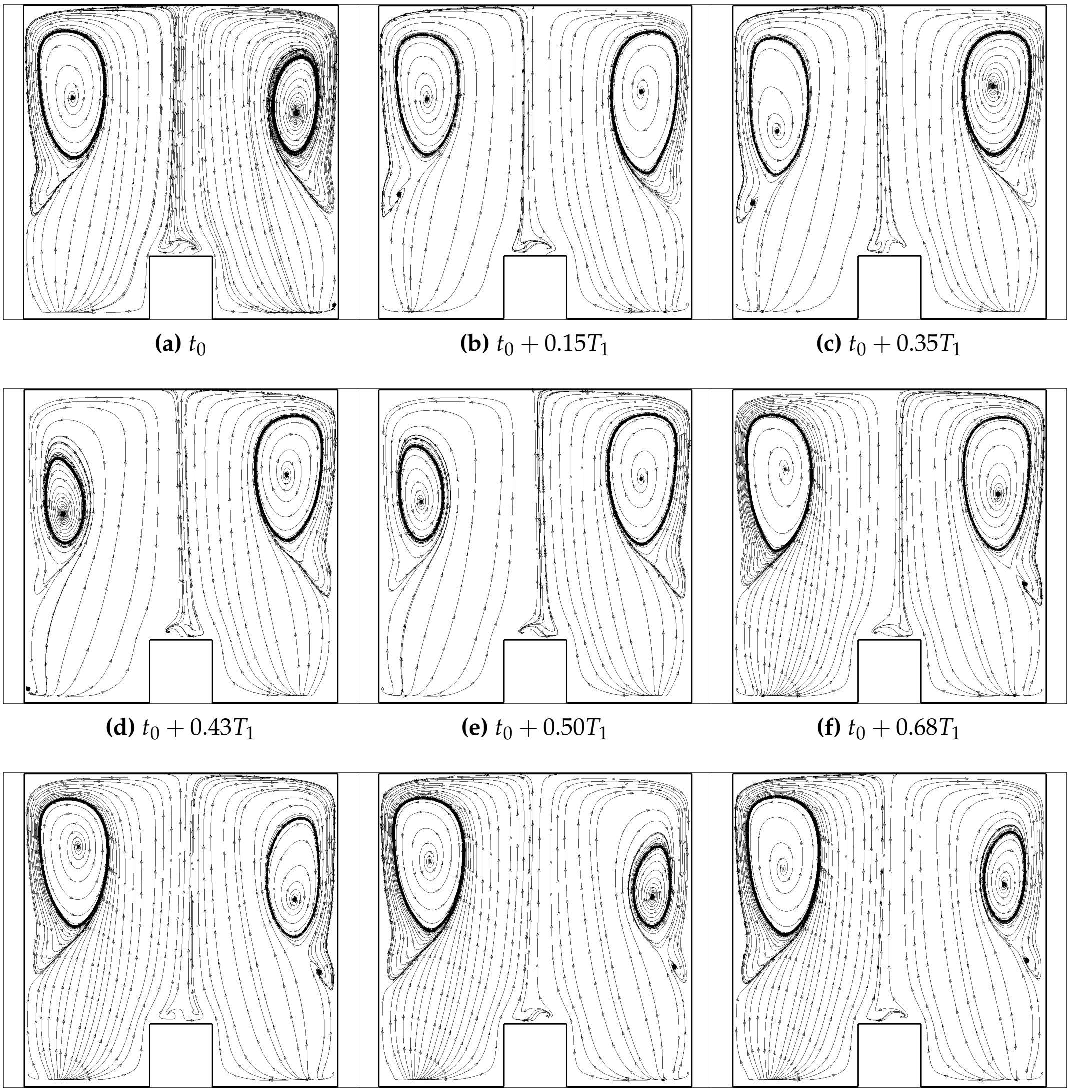

(a) t_0 **(b)** $t_0 + 0.15T_1$ **(c)** $t_0 + 0.35T_1$

(d) $t_0 + 0.43T_1$ **(e)** $t_0 + 0.50T_1$ **(f)** $t_0 + 0.68T_1$

(g) $t_0 + 0.83T_1$ **(h)** $t_0 + 0.93T_1$ **(i)** $t_0 + T_1$

Figure 4.23: Flow lines in the median plane ($Y = 0.5$) at different instants over one period ($T_1 = 72$) at $\tau = 1$.

The figures 4.23 show the flow lines at different instants over one oscillation period recorded at P_3. It is observed the appearance and vanishing of the two small eddies right above the upper surface of the obstacle. This process is periodically repeated with a frequency that is exactly the fundamental one f_1 returned by the FFT. We, therefore, may conclude that this phenomenon drives the fluctuations of temperature considered at P_3. A similar conclusion was reported by Souayeh et al. [15] for the results in a square cavity with a hot obstacle located on its floor. In addition, Bouafia and Daube [19] have pointed out that this type of unsteadiness is due to the shear instabilities, which occur in the zones of high velocity gradient within the primary flow.

However, differing from these two references, in our results, it is also observed the deformation of two large flow cells on both sides of the plume and, in addition, the appearance and vanishing of the small vortices near the vertical walls of the cavity (below the large cells). This alteration may explain the local frequencies found in the signal recorded at P_1, P_3, P_4.

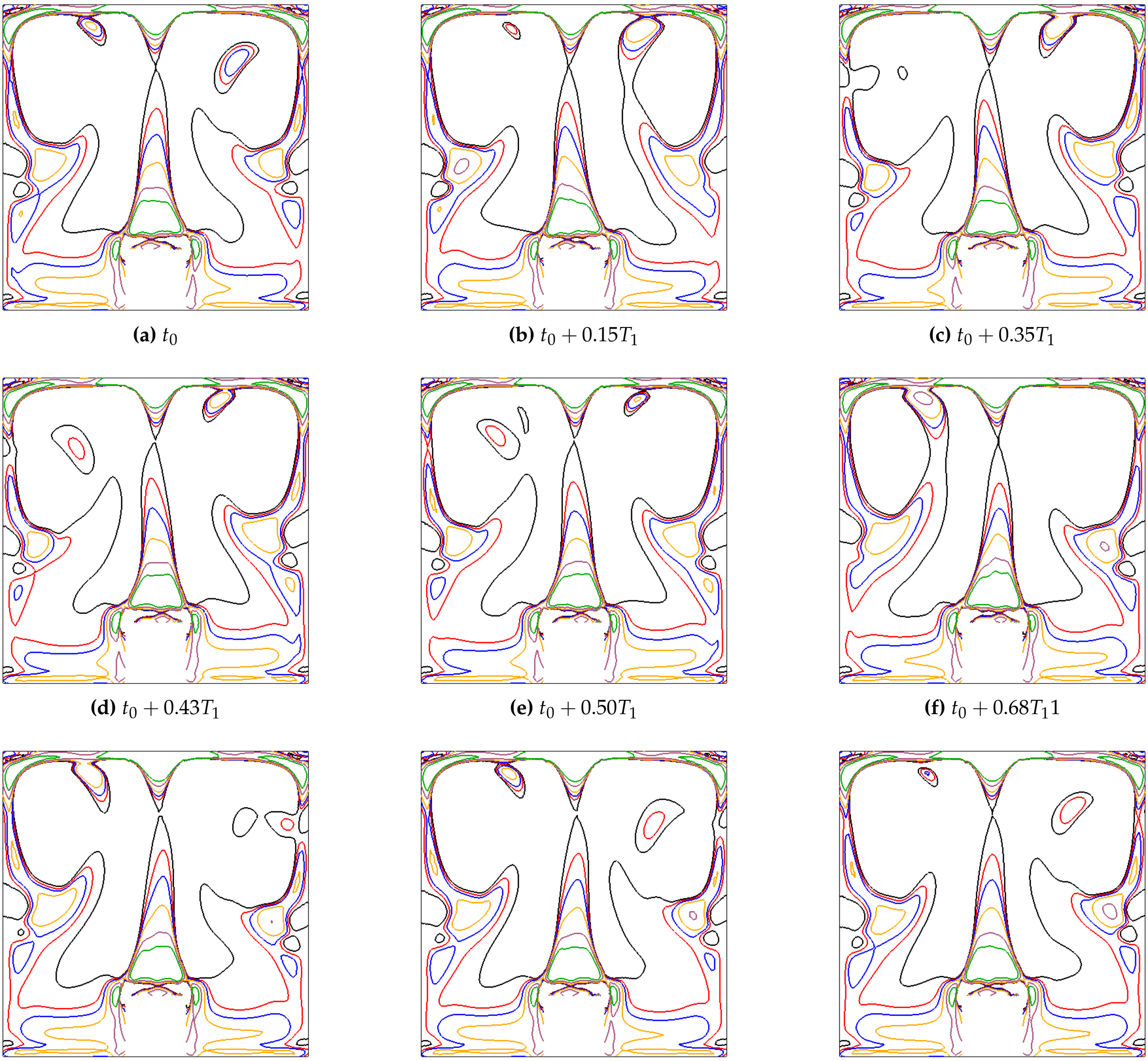

(a) t_0 **(b)** $t_0 + 0.15T_1$ **(c)** $t_0 + 0.35T_1$

(d) $t_0 + 0.43T_1$ **(e)** $t_0 + 0.50T_1$ **(f)** $t_0 + 0.68T_1 1$

(g) $t_0 + 0.83T_1$ **(h)** $t_0 + 0.93T_1$ **(i)** $t_0 + T_1$

Figure 4.24: Negative values of Q-criterion in the median plane ($Y = 0.5$) at different instants over one period ($T_1 = 72$) at $\tau = 1$ (Black: 0; Red: -0.1; Blue: -0.2; Orange: -0.4; Purple: -1; Green: -2). Values are normalized by U_{ref}^2/L^2.

Figure 4.24 displays the Q distribution recorded at P_3 in the mid-depth plane ($Y = 0.5$) with six iso-values at different instants within one period. We here consider the evolution of the rate of shear strain which is represented by the negative values of Q. It is observed the formation and the deformation of the bubble zones where the rate of strain dominates over the vorticity. This demonstrates the shear instability which occurs due to the interference of a continuous fluid at two velocities. In addition, this process repeats periodically with exactly the fundamental frequency that is found from Fourier Transform process.

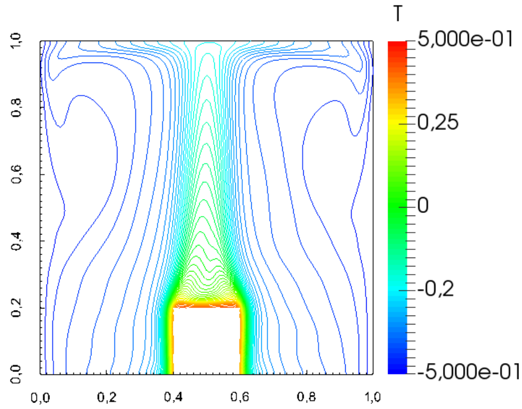

Figure 4.25: Temperature field $\frac{T-T_{ref}}{T_h-T_c}$ at an instant in the median plane ($Y = 0.5$).

For further discussing, we observe that in figure 4.25 there are not any core horizontally stratification of the fluid density (equivalently represented by temperature stratification), which following Le Quéré and Behnia [156] is the structure that can sustain the internal gravity waves (with the fundamental frequency f is smaller than the cut-off Brunt-Väisälä one f_{BV}). We therefore conclude that the fluctuation propagating inside the cavity cannot be related to either the internal gravity waves or the traveling waves (where $f > f_{BV}$).

As a conclusion, the radiation with an opacity at $\tau = 1$ has changed the distribution of the temperature field in the cavity. This alters the dynamic field which experiences shear instabilities in the zones of high velocity gradient. It induces the deformations of fluid circulations in the areas right above the hot obstacle, next to the vertical walls of the enclosure and between the upward plume and downward boundary layers flow, which are repeated periodically. Furthermore, increasing the fluid opacity ($\tau = 2$) leads to a turbulent flow.

4.3 Coupling between Pure Thermal Convection and Radiation in a Real Gas mixture

We now move from a fictitious gas to a real $air - H_2O$ mixture. It involves an absorbing-emitting component (H_2O) diluted at different concentrations into a transparent gas (dry air). The actual absorption spectrum of water vapor must be considered to allow realistic simulations. To that end, and following the discussion presented in Chapter 2, we resort to the SLW model associated to the rank correlated approach. Concerning the boundary conditions, the obstacle surfaces are considered as black ($\epsilon = 1$) and prescribed at $T_h = 580K$ [5], the vertical walls are also black ($\epsilon = 1$) and uniformly maintained at $T_c = 530K$, while the ceiling and the floor are assumed perfectly reflective ($\epsilon = 0$) and adiabatic.
The characteristic parameters of the simulations are presented in the table below

[5]Except the bottom one, which is in contact with the floor of the cavity

(Table 4.6):

x (%)	Ra	Pr	Pl
5	$4.663 \cdot 10^6$	$7.251 \cdot 10^{-1}$	$4.394 \cdot 10^{-3}$
10	$4.693 \cdot 10^6$	$7.351 \cdot 10^{-1}$	$4.392 \cdot 10^{-3}$
20	$4.753 \cdot 10^6$	$7.553 \cdot 10^{-1}$	$4.389 \cdot 10^{-3}$

Table 4.6: Description of the cases of calculation.

In the range of Rayleigh numbers under consideration, the flow remains laminar and it always reaches a steady state. Unlike with the gray gas assumption, the radiative properties now depends on the local temperature inside the cavity. Therefore, the absorption coefficient is not uniform and thus we cannot use a single (gray) non-dimensional number τ to fully characterize each configuration.

In each case, the results are compared to the reference (transparent) values, which are generated using the same gas mixture, but without including any radiation effects in volume.

4.3.1 Velocity and thermal fields

Figures 4.26 display the thermal field in the median plane ($Y = 0.5$) in both cases of transparent and participating media at different concentration of water vapor. The most sensitive effect of radiation (at these concentrations) is a slight broadening of the temperature contours in the lower half of the cavity (Figures 4.26 b,d,f). The radiant flux coming from the hot surfaces of the obstacle heats up the medium between the heater and the vertical walls of the cavity. As a result, the nearly vertical thermal stratification in absence of radiation is broken. The air (outside the thermal plume), therefore, slightly becomes more uniform in temperature.

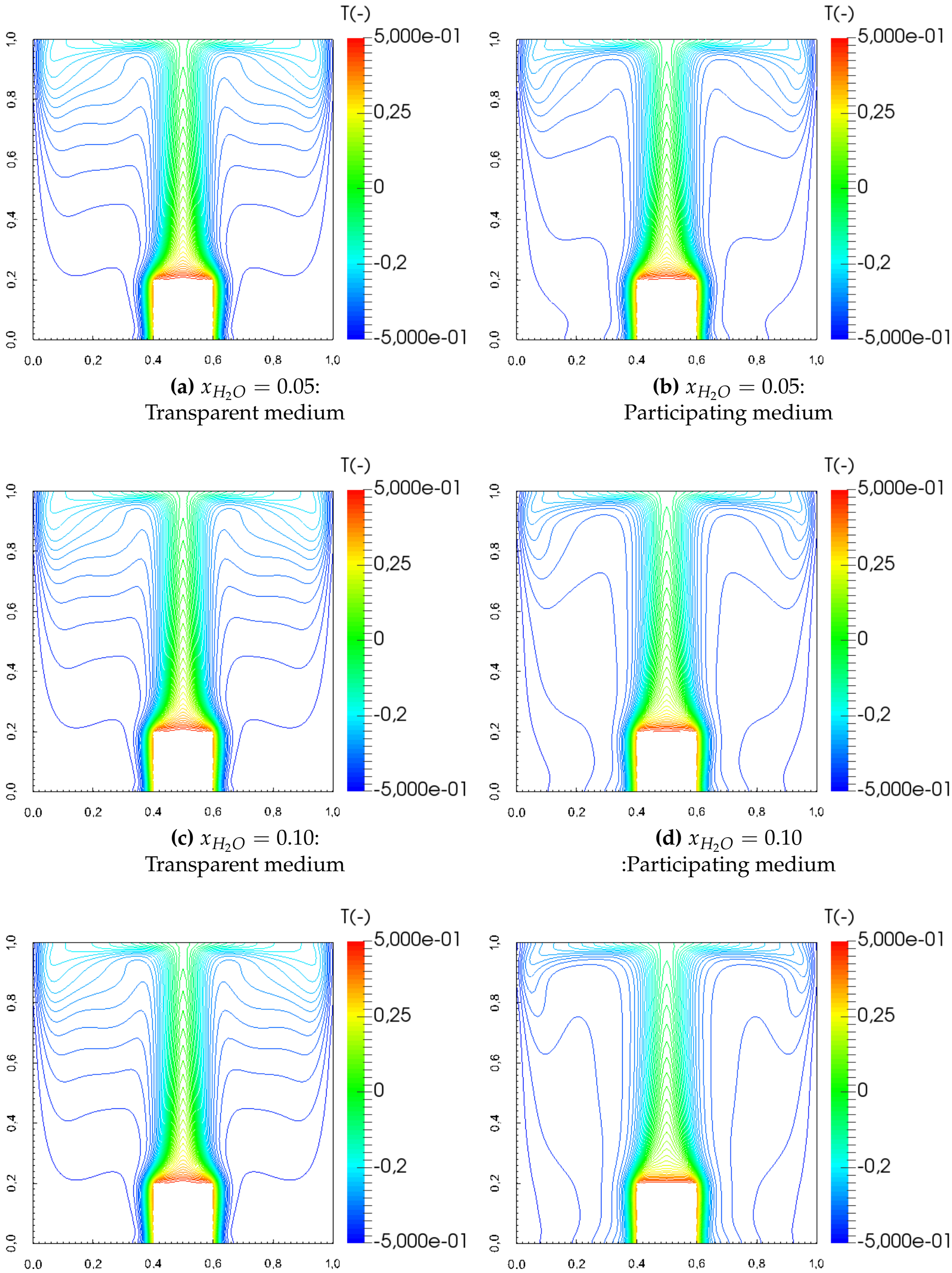

(a) $x_{H_2O} = 0.05$: Transparent medium

(b) $x_{H_2O} = 0.05$: Participating medium

(c) $x_{H_2O} = 0.10$: Transparent medium

(d) $x_{H_2O} = 0.10$:Participating medium

(e) $x_{H_2O} = 0.20$: Transparent medium

(f) $x_{H_2O} = 0.20$:Participating medium

Figure 4.26: 2D-contours of temperature $\frac{T-T_{ref}}{T_h-T_c}$ in the median plane of the cavity ($Y = 0.5$) at different mole fractions of water vapor.

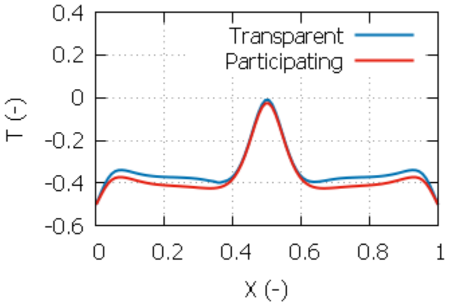

(a) $x_{H_2O} = 0.05 : Z = 0.8$

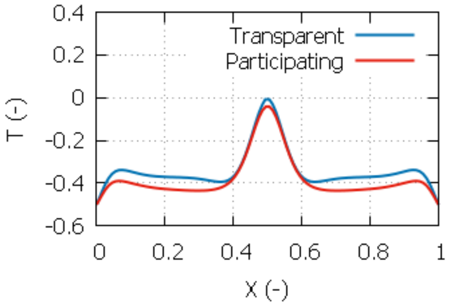

(b) $x_{H_2O} = 0.10 : Z = 0.8$

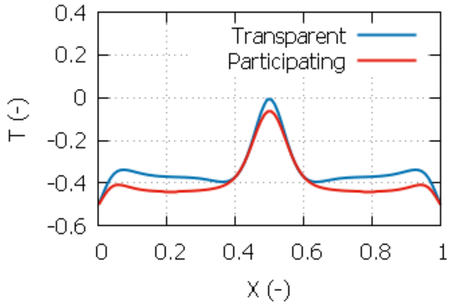

(c) $x_{H_2O} = 0.20 : Z = 0.8$

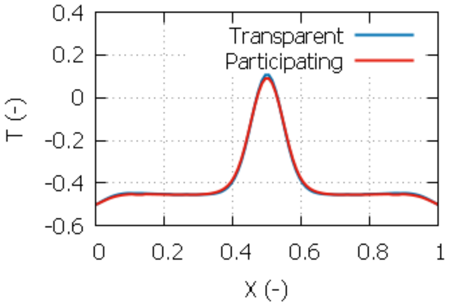

(d) $x_{H_2O} = 0.05 : Z = 0.5$

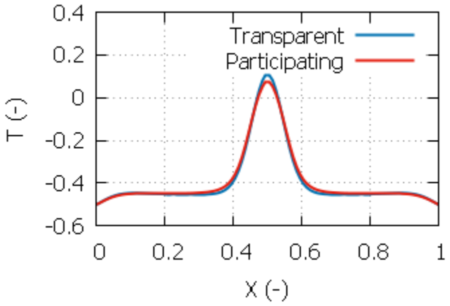

(e) $x_{H_2O} = 0.10 : Z = 0.5$

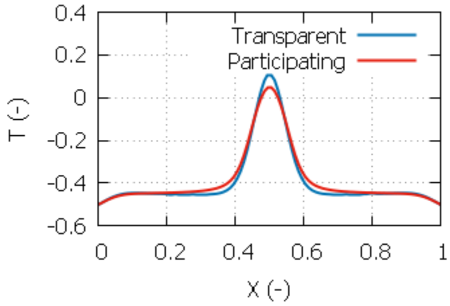

(f) $x_{H_2O} = 0.20 : Z = 0.5$

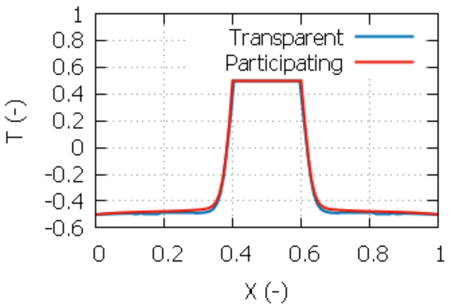

(g) $x_{H_2O} = 0.05 : Z = 0.1$

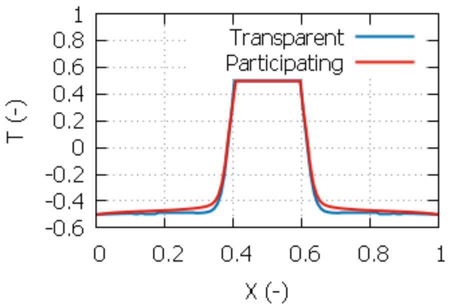

(h) $x_{H_2O} = 0.10 : Z = 0.1$

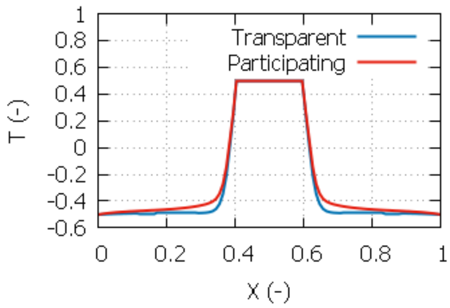

(i) $x_{H_2O} = 0.20 : Z = 0.1$

Figure 4.27: Temperature $\frac{T-T_{ref}}{T_h-T_c}$ profiles along different Z-crosslines in the median plane ($Y = 0.5$) at different concentration of water vapor.

As a whole, radiation does not significantly change the thermal profile along the centerline ($Z = 0.5$) (see figures 4.27 d,e,f) and in the lower half of the cavity ($Z = 0.1$) (see figures 4.27 g,h,i). But at a higher position ($Z = 0.8$) (see figures 4.27 a,b,c), a slight decrease of temperature in the re-circulation zone between the plume and the wall boundary layer can now be observed. In this region of low convective transport, the gas radiates toward the cold surfaces and the colder parts of the fluid (it emits more than it absorbs): this results in a negative radiative source within the fluid (see figures 4.28 a,c,e).

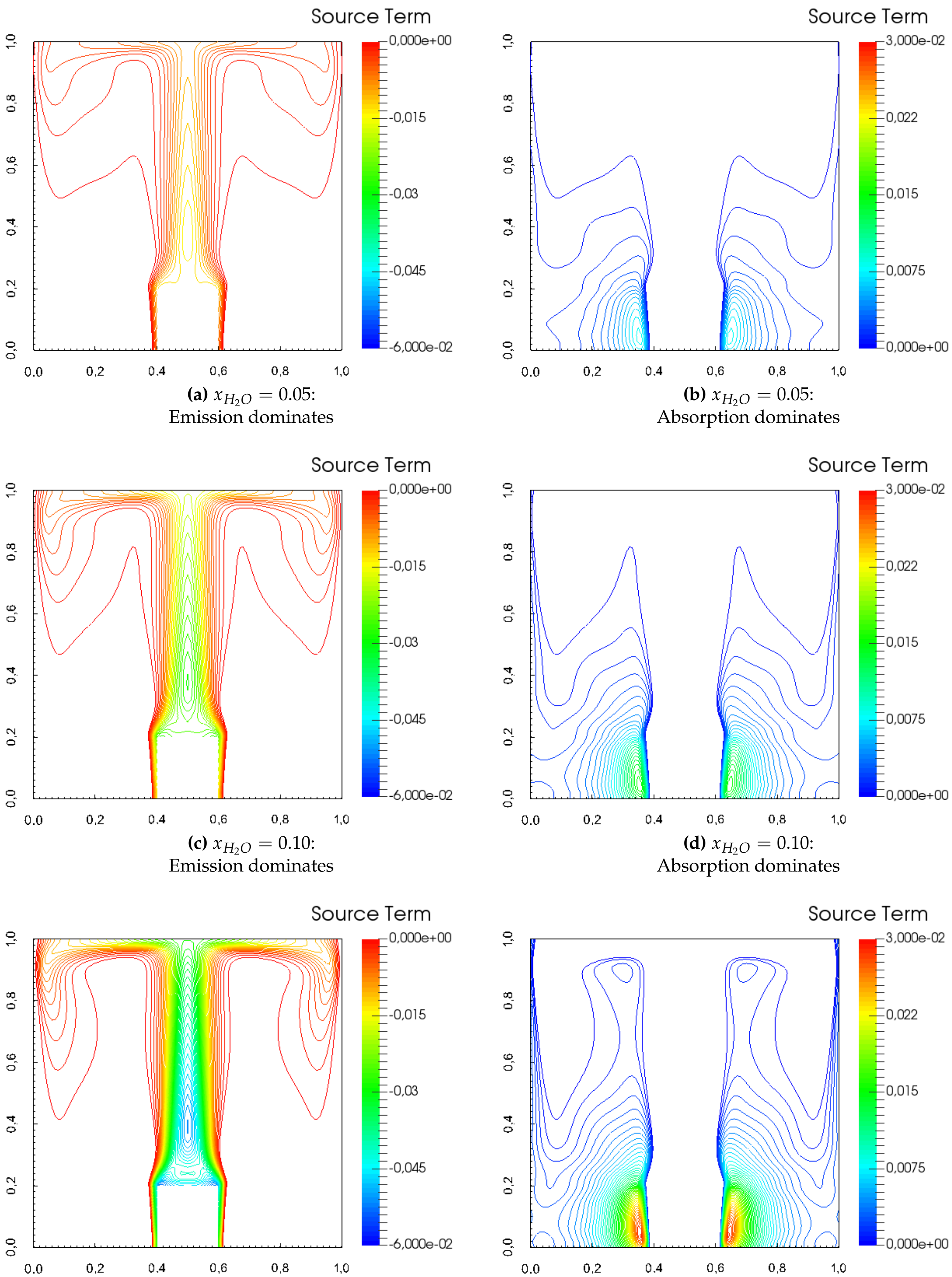

(a) $x_{H_2O} = 0.05$: Emission dominates

(b) $x_{H_2O} = 0.05$: Absorption dominates

(c) $x_{H_2O} = 0.10$: Emission dominates

(d) $x_{H_2O} = 0.10$: Absorption dominates

(e) $x_{H_2O} = 0.20$: Emission dominates

(f) $x_{H_2O} = 0.20$: Absorption dominates

Figure 4.28: Distribution of radiative source term in the median plane ($Y = 0.5$) at different mole fractions of water vapor. Sources are normalized by $4\sigma T_{ref}^4/L$.

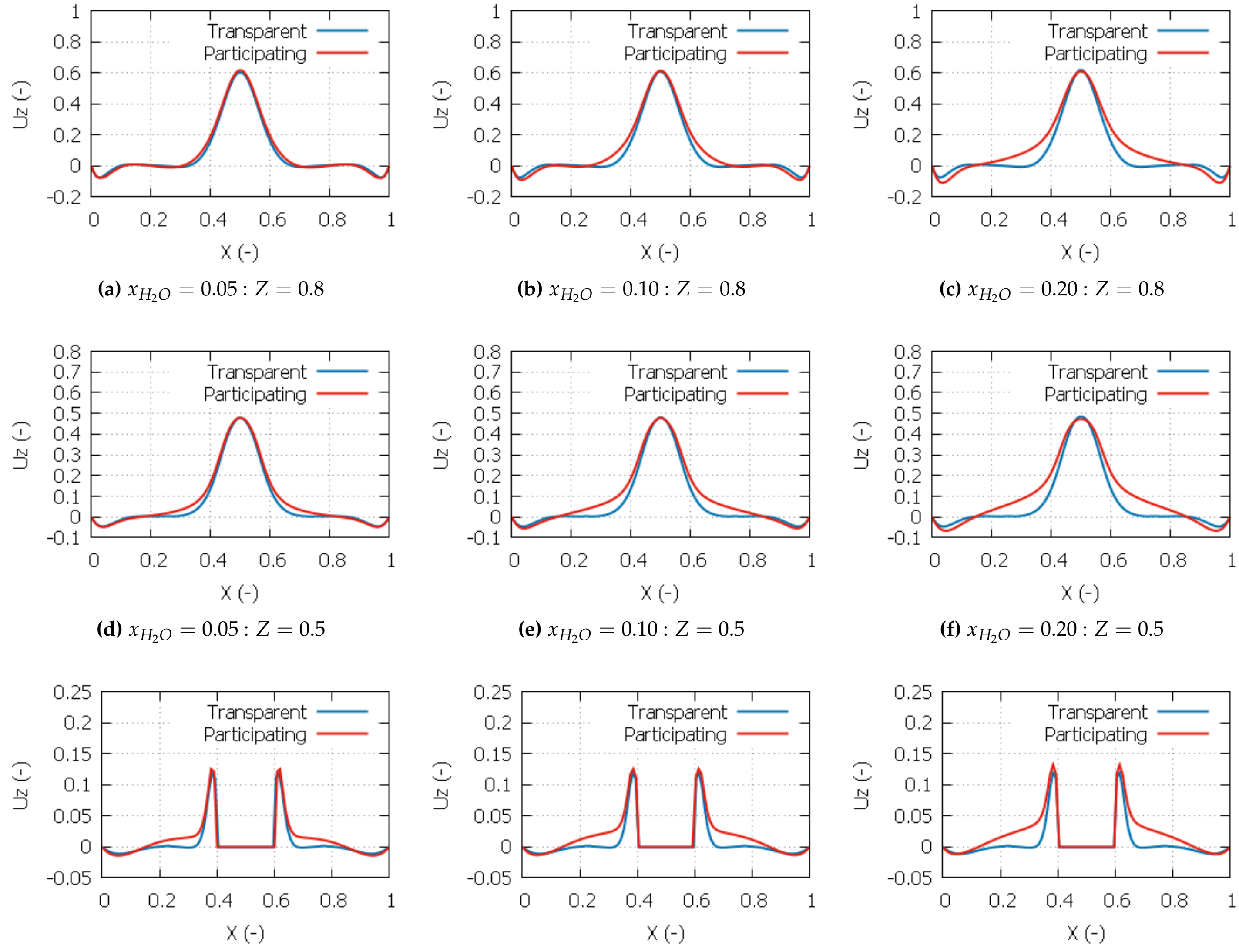

(a) $x_{H_2O} = 0.05 : Z = 0.8$ **(b)** $x_{H_2O} = 0.10 : Z = 0.8$ **(c)** $x_{H_2O} = 0.20 : Z = 0.8$

(d) $x_{H_2O} = 0.05 : Z = 0.5$ **(e)** $x_{H_2O} = 0.10 : Z = 0.5$ **(f)** $x_{H_2O} = 0.20 : Z = 0.5$

(g) $x_{H_2O} = 0.05 : Z = 0.1$ **(h)** $x_{H_2O} = 0.10 : Z = 0.1$ **(i)** $x_{H_2O} = 0.20 : Z = 0.1$

Figure 4.29: Profiles of vertical velocities $\frac{w}{U_{ref}}$ at different Z-crosslines in the median plane ($Y = 0.5$) at different concentration of water vapor.

Moreover, the change in the thermal field alters the buoyancy forces in the cavity. Consequently, the vertical velocities slightly increase near the lateral walls and significantly near the plume flow (see figure 4.29). The two boundary layers (climbing along the obstacle, descending along the wall) now interfere and create a shear flow in this region.

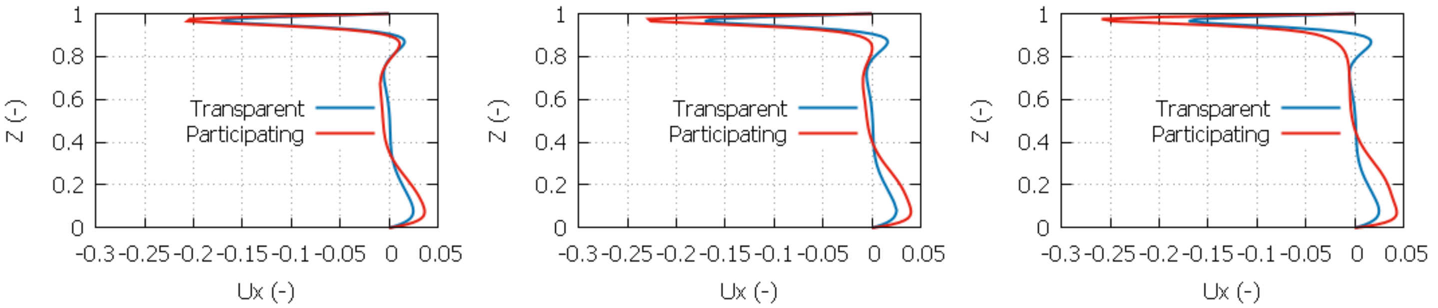

(a) $x_{H_2O} = 0.05$: X=0.2 **(b)** $x_{H_2O} = 0.10$: X=0.2 **(c)** $x_{H_2O} = 0.20$: X=0.2

Figure 4.30: Profiles of horizontal velocities $\frac{u}{U_{ref}}$ at different X-crosslines in the median plane ($Y = 0.5$) at different concentration of water vapor.

Another change in the fluid motion can be found in the profiles of horizontal velocities along the vertical cross-sections, which are displayed in figure 4.30 a. Compared to the transparent case, the fluid near the ceiling and the floor of the enclosure is accelerated. This is due to an increase in the mass flow driven by the plume. These alterations of the velocity field are enhanced when the medium becomes more absorbing: compare figures 4.29 b,e,h and 4.30 b ($x_{H_2O} = 0.10$) versus 4.29 c,f,i and 4.30 c ($x_{H_2O} = 0.20$).

Figure 4.31 represents the velocity vectors in the mid-depth plane ($Y = 0.5$) for three concentrations of the absorbing component. They display the typical patterns explaining the formation of the plume. The fluid is accelerated along the lateral surfaces of the hot body, goes up and then combines above the top surface of the obstacle. Here, the fluid between the plume and its surrounding is pushed upward by the buoyancy force created by the temperature difference. The hot fluid moves along the ceiling of the enclosure and then flows down near the cold walls. Besides, it is clearly observed that the plume broadens and the boundary layers near vertical walls get thicker when the radiation effects are present (compared to the transparent cases).

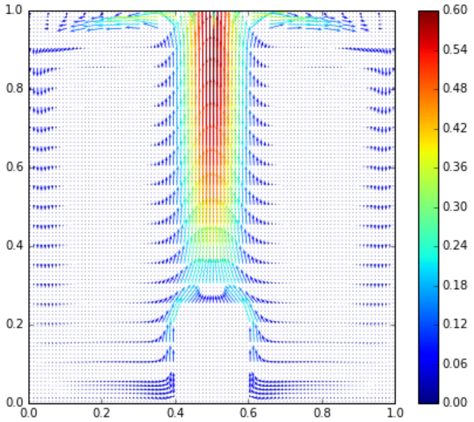

(a) $x_{H_2O} = 0.05$:
Transparent medium

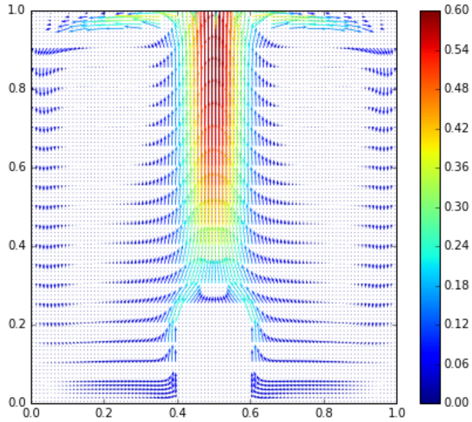

(b) $x_{H_2O} = 0.05$:
Participating medium

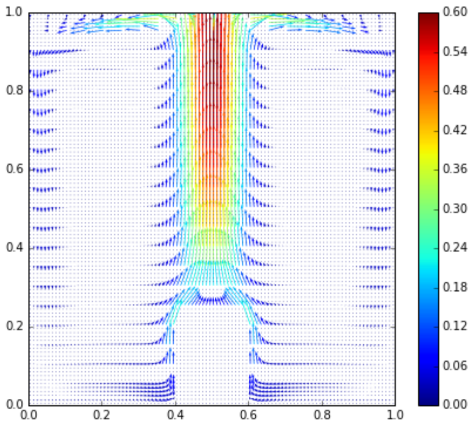

(c) $x_{H_2O} = 0.10$:
Transparent medium

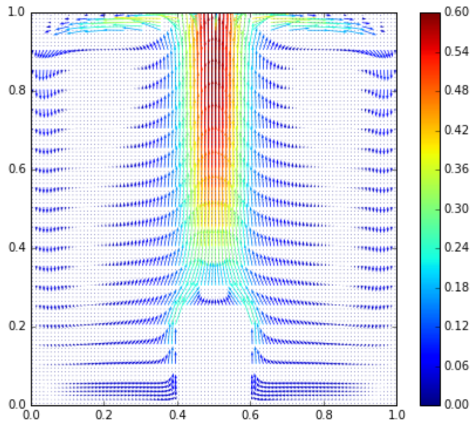

(d) $x_{H_2O} = 0.10$:
Participating medium

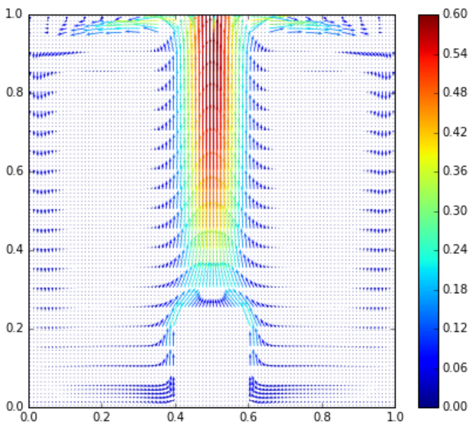

(e) $x_{H_2O} = 0.20$:
Transparent medium

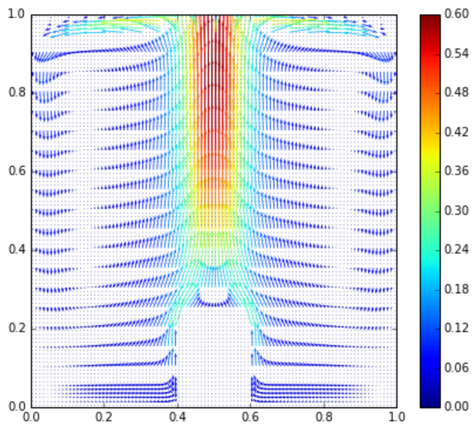

(f) $x_{H_2O} = 0.20$:
Participating medium

Figure 4.31: Velocity field in the median plane ($Y = 0.5$) at different mole fractions of water vapor. Velocities are normalized by U_{ref}.

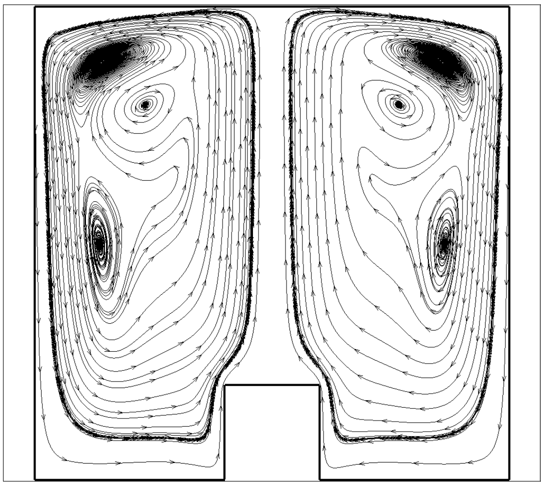

(a) $x_{H_2O} = 0.05$:
Transparent medium

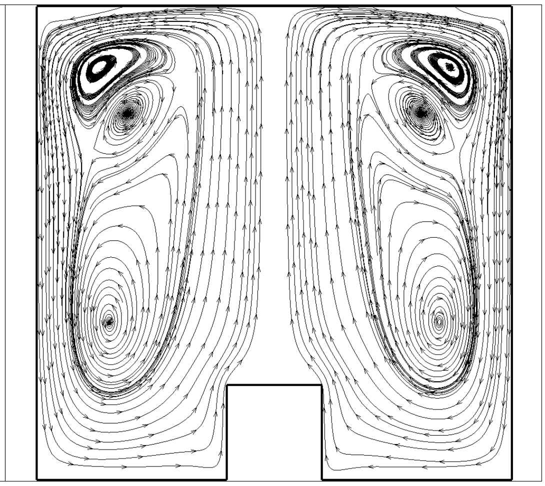

(b) $x_{H_2O} = 0.05$:
Participating medium

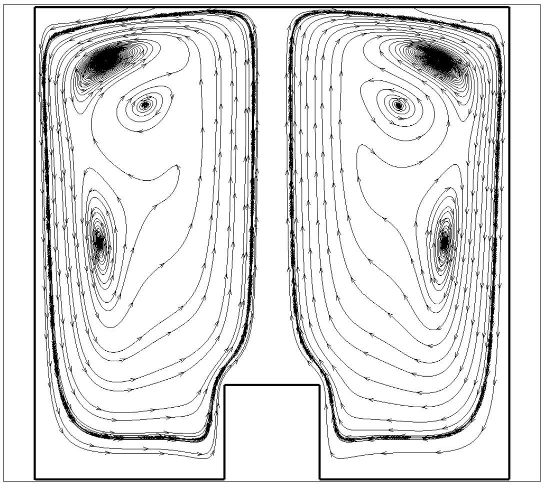

(c) $x_{H_2O} = 0.10$:
Transparent medium

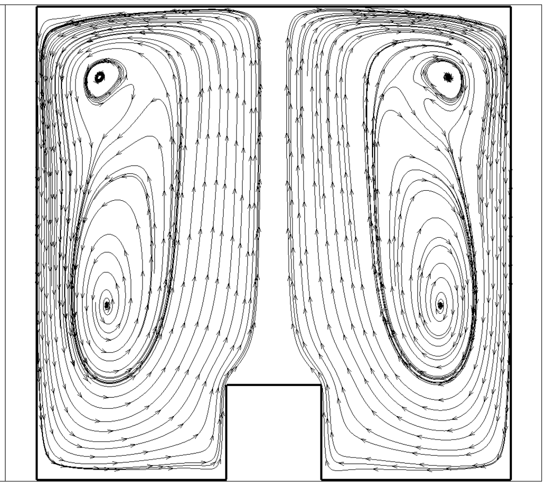

(d) $x_{H_2O} = 0.10$:
Participating medium

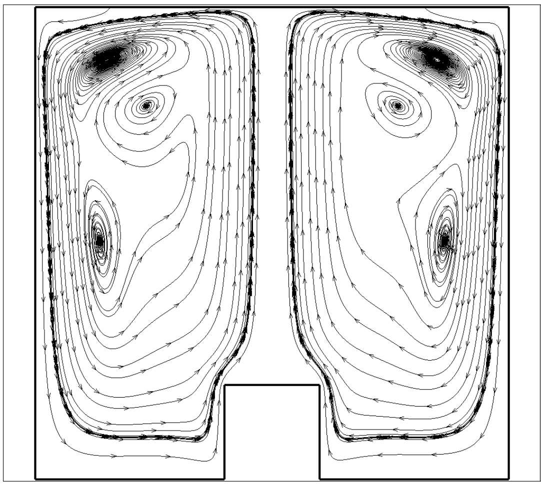

(e) $x_{H_2O} = 0.20$:
Transparent medium

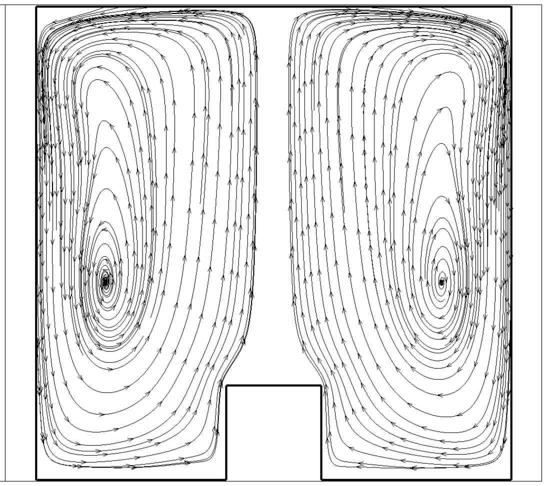

(f) $x_{H_2O} = 0.20$:
Participating medium

Figure 4.32: Flow lines in the median plane ($Y = 0.5$) at different mole fractions of water vapor.

Similar modifications in dynamic and thermal field were reported by Billaud, Saury, and Lemonnier [6] for a differentially heated cavity: gas radiation was found to accelerate the global circulation and to set into motion some parts of the fluid that were stagnant in the transparent case.

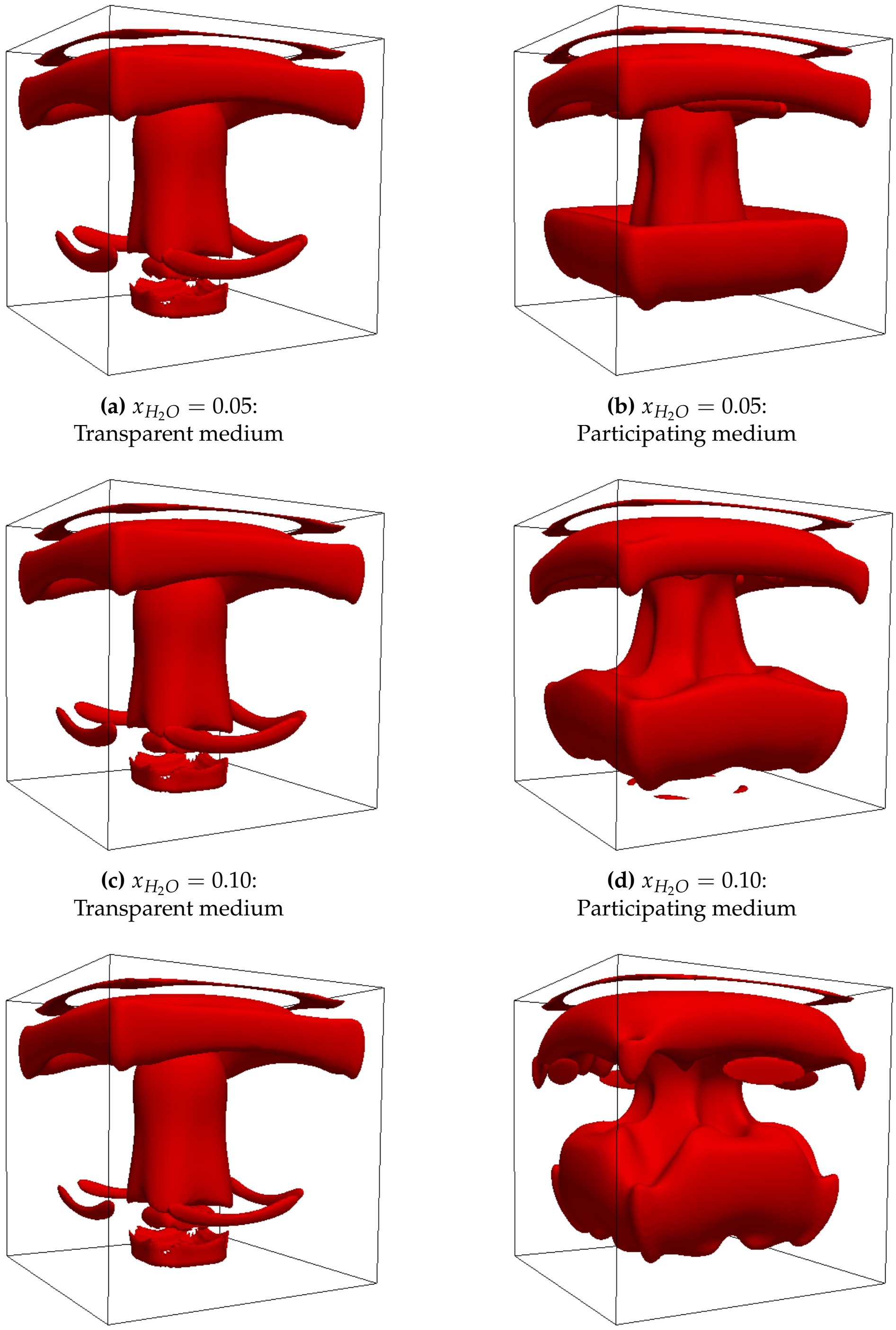

(a) $x_{H_2O} = 0.05$: Transparent medium

(b) $x_{H_2O} = 0.05$: Participating medium

(c) $x_{H_2O} = 0.10$: Transparent medium

(d) $x_{H_2O} = 0.10$: Participating medium

(e) $x_{H_2O} = 0.20$: Transparent medium

(f) $x_{H_2O} = 0.20$: Participating medium

Figure 4.33: Representation of Q-criterion at $Q = 0.02$ in the cavity at different mole fractions of water vapor. Values are normalized by U_{ref}^2/L^2.

Regarding the 3-D structure of the flow, figures 4.33 represent the distributions of the Q inside the cavity. As in the previous section (gray gas), we observe that the iso-surfaces $Q = 0.02$ extends when the fluid opacity - linked to the concentration of water vapor - increases. The spirals observed in the figures 4.32 now disappear gradually as the medium becomes more absorbing.

4.3.2 Heat Transfer

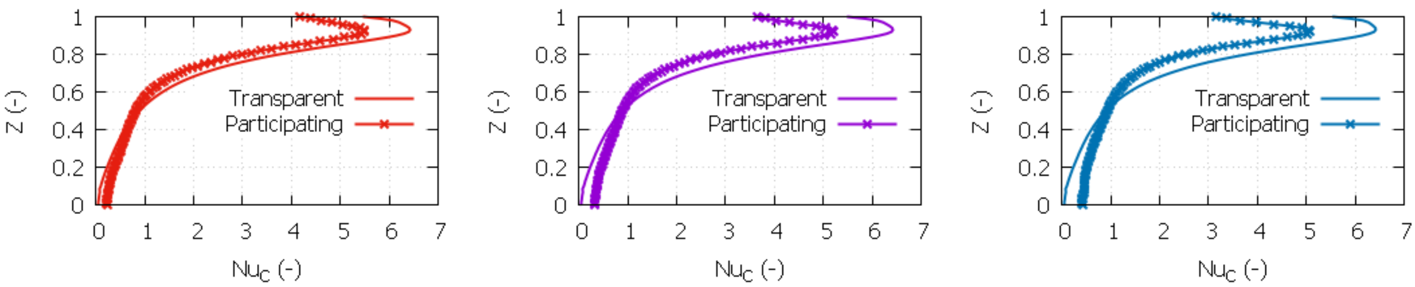

(a) $x_{H_20} = 0.05$ **(b)** $x_{H_20} = 0.10$ **(c)** $x_{H_20} = 0.20$

Figure 4.34: Local convective Nusselt number along the vertical centerline of any lateral wall of the cavity.

The plots in the figure 4.34 clearly show that the convective Nusselt number along the centerline of any vertical wall of the enclosure is decreased close to the roof of the cavity and increased elsewhere. The reason is that, in the upper part, the fluid was cooled down (figures 4.28 a,c,e) before reaching the lateral walls. On the other hand, in the lower part, absorption dominates over the emission (figures 4.28 b,d,f), thus, the medium is heated up and the thermal gradient is increased. However, the increased part does not compensate the decreased one. Therefore, overall, the average convective Nusselt number over the vertical wall of the enclosure is reduced (see table 4.7).

This decreasing trend in the local convective Nusselt number is also found when considering the vertical hot surfaces of the obstacle. This is illustrated in figure 4.35. The reason is that the thermal gradient is reduced when radiation is considered. Indeed, the fluid is warmed up (by absorption) along the floor of the enclosure before arriving at the vertical hot surfaces of the obstacle. Consequently, the average values of Nu_C displayed in table 4.9 are decreased when the radiation is taken into account.

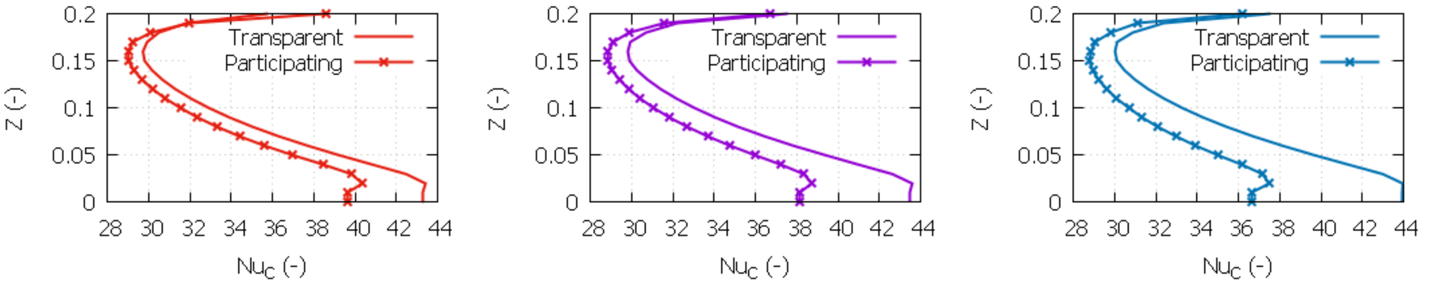

(a) $x_{H_20} = 0.05$ **(b)** $x_{H_20} = 0.10$ **(c)** $x_{H_20} = 0.20$

Figure 4.35: Local convective Nusselt number along vertical center line of each lateral surfaces of the obstacle.

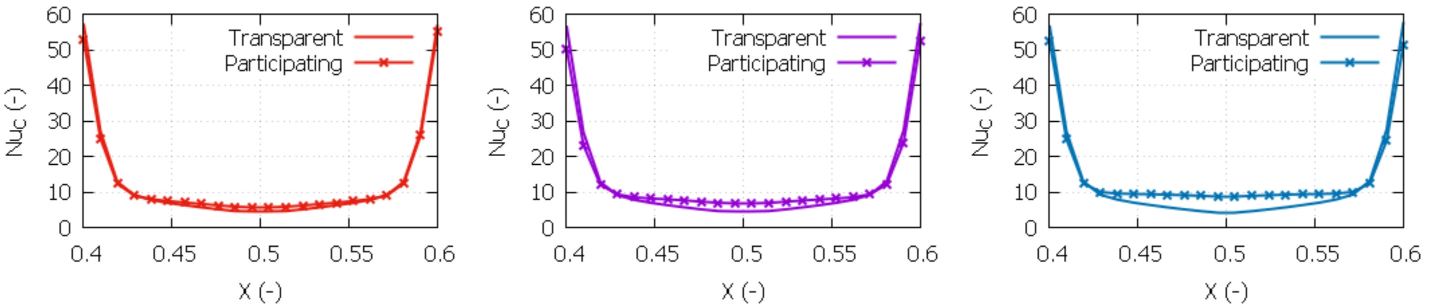

(a) $x_{H_20} = 0.05$ **(b)** $x_{H_20} = 0.10$ **(c)** $x_{H_20} = 0.20$

Figure 4.36: Local convective Nusselt number along horizontal centerline of the obstacle top surface.

However, it is observed that the convective transfer along the horizontal upper surface of the obstacle increases. When radiation is present, the fluid layer near the hot surfaces becomes cooler due to emission (it is evidenced by the negative values of the radiative source in the figures 4.28. Consequently, the thermal gradient in this region is enhanced, which induces the increase in local values of Nusselt number with the appearance of the radiation (figure 4.36). This explains the higher average convective Nusselt number obtained in table 4.9.
The values of average convective Nusselt number and average total Nusselt number, which are defined as $\overline{Nu} = \frac{1}{A}\int_A Nu(\mathbf{s})dA$, are presented in the tables below:

$x_{H_2O}(\%)$	Convective Nusselt number		Total Nusselt number	
	Transparent	Participating	Transparent	Participating
5	1.67	1.34	12.47	12.38
10	1.67	1.27	12.48	12.33
20	1.68	1.24	12.50	12.26

Table 4.7: Average convective and total Nusselt number along any vertical wall of the cavity.

Regarding the total heat transfer, tables 4.7, 4.8 and 4.9 reveal that, compared to the transparent cases, the average total Nusselt number along any black surfaces is

x_{H_2O}(%)	Convective Nusselt number		Total Nusselt number	
	Transparent	Participating	Transparent	Participating
5	38.28	37.09	252.07	250.25
10	38.34	36.75	252.19	249.31
20	38.57	36.59	252.59	247.93

Table 4.8: Average convective and total Nusselt number along any vertical wall of the obstacle.

x_{H_2O}(%)	Convective Nusselt number		Total Nusselt number	
	Transparent	Participating	Transparent	Participating
5	14.12	14.50	239.91	238.26
10	14.17	14.90	240.03	236.92
20	14.30	15.85	240.34	234.74

Table 4.9: Average convective and total Nusselt number along horizontal upper wall of the obstacle.

decreased. This, along the vertical walls, is due to the drop off in the convective Nusselt number. In addition, the attenuation of radiative transfer by the absorbing medium also contributes to the reduction of total thermal transport, especially, when considering this quantity along the upper surfaces of the obstacle, where the convective transfer is accelerated.

4.4 Conclusions

In this chapter, we have presented our calculation of pure thermal convection coupled to gas radiation in a cavity (size $L = 0.25m$) containing a hot source (size $l = 0.05m$). Firstly, the sensitivities of the results with respect to spatial discretization, angular discretization and spectral divisions have been studied in order to select the most suitable computation settings for subsequent calculations. In more details, the simulations have been performed using a 100^3 uniform grid, the S_8 quadrature for the discrete direction set and the SLW model (associated with RC approach) with 5 gray gases.

Next, the computations on the thermal convection in the enclosure filled by gray gas (at different opacities) or real gas (SLW model) (at different molar fraction of water vapor) mixtures have been investigated. The comparisons between obtained results and the reference pointed out the influences of radiation effects:

- Radiation tends to non-uniformly accelerate the boundary layers along the cavity wall and the hot inner obstacle. It also makes moving some parts of the fluid that were stagnant in the transparent cases. The plume flow and its recirculation interfere and create shear flow patterns.

- Radiation partly modifies the thermal gradient near the bounding surfaces of the cavity: the convective Nusselt values are increased in the upper half and decreased in the lower half. However, at the horizontal surface of the obstacle, this thermal gradient is strengthened.

- Radiation modifies the nearly vertical thermal stratification outside the plume and slightly uniformizes the medium temperature.

- In real gases, radiation reduces the total thermal transfer, especially the convective part on the vertical walls and the radiative exchange between the upper surface of the obstacle and the ones of the cavity.

- All these effects increase when the medium becomes more absorbing (in the considered range of optical thicknesses and molar fraction).

- Besides, in the case of a gray gas, when the optical thickness of the medium is unity, radiation makes the flow depart from the steadiness and reach a unsteady regime. This mechanism is due to the shear instability created by the interference of ascending plume and the boundary layers flowing downward. It is worth mentioning that, at $\tau = 2$, the flow becomes totally turbulent at $Ra = 5 \cdot 10^6$.

Chapter 5

Double Diffusive Convection Coupled to Gas Radiation

In double diffusive convection, there are two gradients that govern the flow: the thermal and the concentration ones. The relative magnitude of the induced driving forces is defined by the mass-to-thermal buoyancy ratio N:

$$N = \frac{\beta_C \Delta C}{\beta_T \Delta T} \tag{5.1}$$

where $\Delta C = C_h - C_l$, $\Delta T = T_h - T_c$. Its sign characterizes the cooperating (> 0) or opposing (< 0) effects of these two gradients.

In the frame of this work, we have performed some calculations in double diffusive convection including cases where gas radiation is accounted for. Predictions without radiation (transparent fluid) are also provided at different mass-to-thermal buoyancy ratios and serve as reference for highlighting the influence of radiant transport on the flow characteristics.

5.1 Gray gas model

All the calculations are performed at $Ra = 5.10^6$, $Le = 1$ (allowing a perfect overlap of the thermal and concentration boundary layers), $Pl = 4.43 \cdot 10^{-3}$ and $\theta_0 = 11.1$.
A high concentration of the absorbing species is prescribed on all the surfaces of the obstacle (C_h), and a null concentration ($C_l = 0$) along the vertical walls of the cavity. The emissivity of the bounding surfaces (including the obstacle) are set to unity except the ceiling and the floor, which are considered as perfectly reflecting.
In all subsequent computations, the absorption coefficient is made proportional to the local concentration. We will therefore consider that :

$$\kappa(C^*) = \kappa_0 \frac{C^*}{C_{ref}} \tag{5.2}$$

where C^* is a dimensional value and κ_0 and $C_{ref} = \frac{C_h + C_l}{2}$ are the reference absorption coefficient and reference concentration, respectively. Using the dimensionless quantity $C = (C^* - C_{ref})/(C_h - C_l)$ in (5.2) yields:

$$\kappa(C) = \kappa_0 \cdot (2C + 1) \tag{5.3}$$

All the results presented hereafter are normalized using the reference temperature $T_{ref} = \frac{T_h+T_c}{2}$, the reference concentration $C_{ref} = \frac{C_h+C_l}{2}$ the reference length L, the reference velocity $U_{ref} = \alpha\frac{\sqrt{Ra}}{L}$ and the reference time $\frac{L^2}{\alpha\sqrt{Ra}}$.

5.1.1 Mass-to-Thermal Buoyancy ratio $N = 1$

We assume that the fluid supplied by the (hot) obstacle and removed by the (cold) cavity walls is lighter than the main component of the mixture. Differences in concentration then create a convective motion in the same direction as those induced by the thermal gradient (cooperative action) and the magnitude of these two effects (mass and thermal) are similar ($N = 1$ and $Le = 1$).

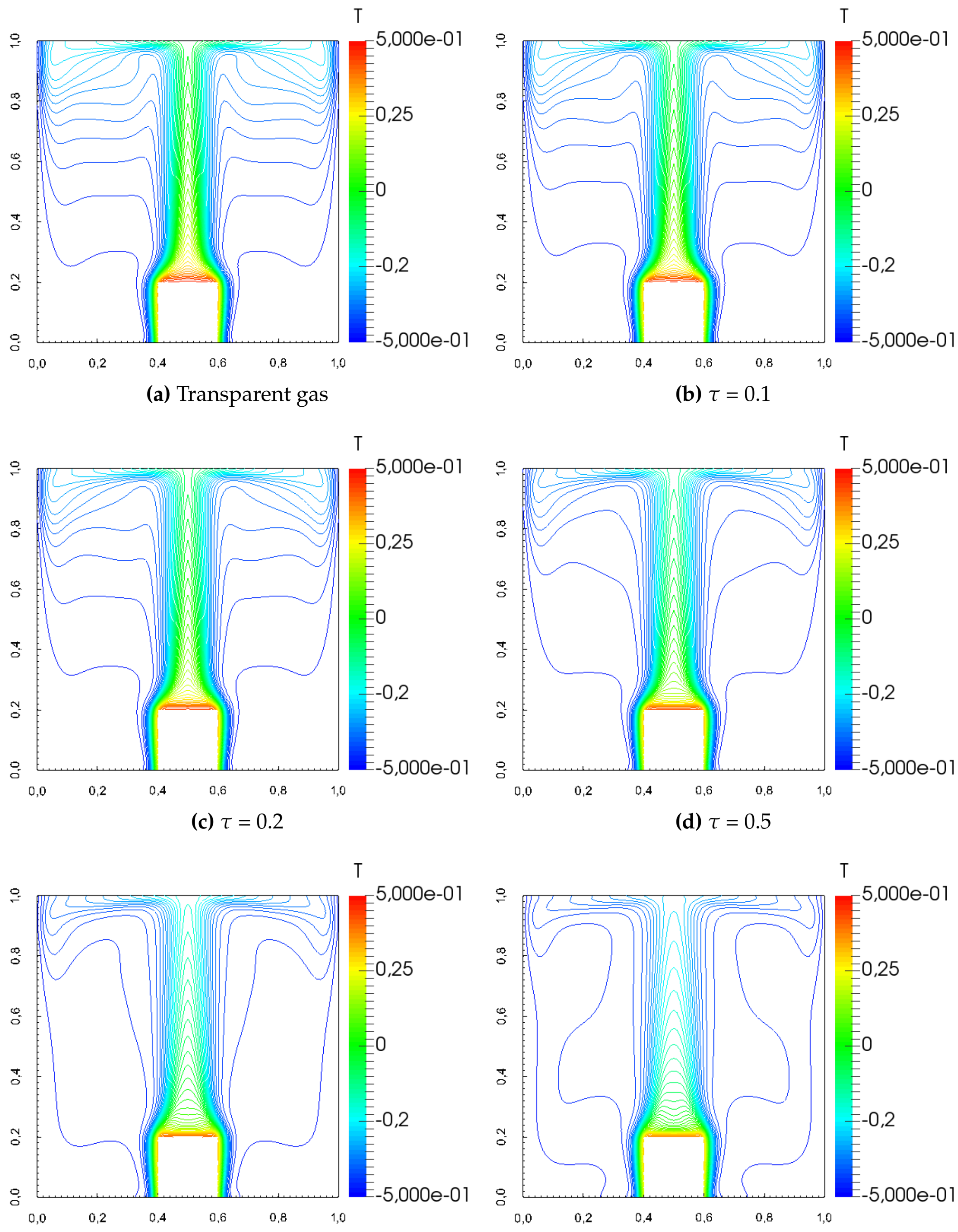

(a) Transparent gas **(b)** $\tau = 0.1$ **(c)** $\tau = 0.2$ **(d)** $\tau = 0.5$ **(e)** $\tau = 1$ **(f)** $\tau = 2$

Figure 5.1: Thermal field $\frac{T-T_{ref}}{T_h-T_c}$ in the median plane of the cavity ($Y = 0.5$) for different fluid opacities: cooperating cases, $N = 1$.

Figures 5.1 a-f describe the thermal field in the median plane of the cavity ($Y = 0.5$) for different fluid opacities ranging from a transparent medium ($\tau = 0$) to $\tau = 2$. At low value of τ (optically thin limit), a nearly vertical stratification is established between the plume and the boundary layers along the cavity walls. No obvious change in this pattern occurs below $\tau = 0.2$ or even $\tau = 0.5$. That was already observed in the case of combined radiation and pure thermal convection (homogeneous mixture). As the optical thickness goes beyond unity, we clearly recognize the transformation of the thermal field. Moreover, the temperature profiles along different horizontal crosslines (see figure 5.2) prove that the temperature at medium ($Z = 0.5$) and high levels ($Z = 0.8$) decreases significantly when radiation is taken into account. The vertical temperature distributions plotted in figure 5.3 confirm this trend. The hot fluid carried by the plume emits towards the cold walls and, therefore, its temperature decreases with respect to the transparent case. The amplitude of this phenomenon, which is also illustrated by figures 5.4-5.8, increases with the optical thickness, at least in the range of values we have investigated[1]. On the other hand, the lower part of the cavity ($Z = 0.1$) is mainly driven by the two differentially heated surfaces (the obstacle and the cold walls): it is less sensitive to gas radiation.

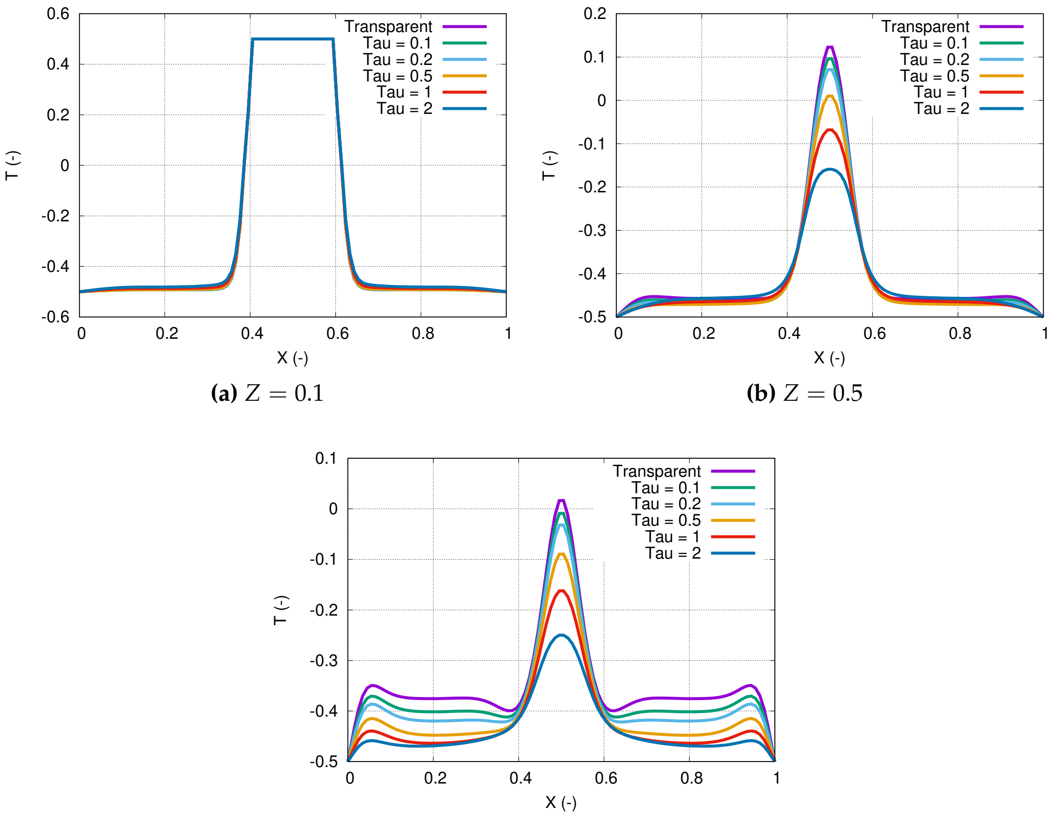

(a) $Z = 0.1$ **(b)** $Z = 0.5$

(c) $Z = 0.8$

Figure 5.2: Temperature $\frac{T-T_{ref}}{T_h-T_c}$ profiles along Z-crosslines in the median plane ($Y = 0.5$): cooperating flow, $N = 1$

[1]If we increase the fluid opacity, we will ultimately find an opaque situation, where there are no more radiative effects.

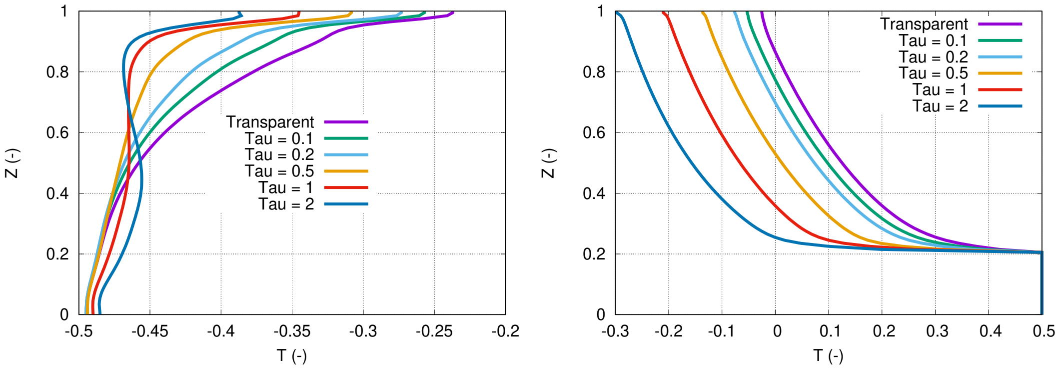

(a) $X = 0.2$ **(b)** $X = 0.5$

Figure 5.3: Temperature $\frac{T-T_{ref}}{T_h-T_c}$ profiles along different X-crosslines in the median plane ($Y = 0.5$): cooperating flow, $N = 1$

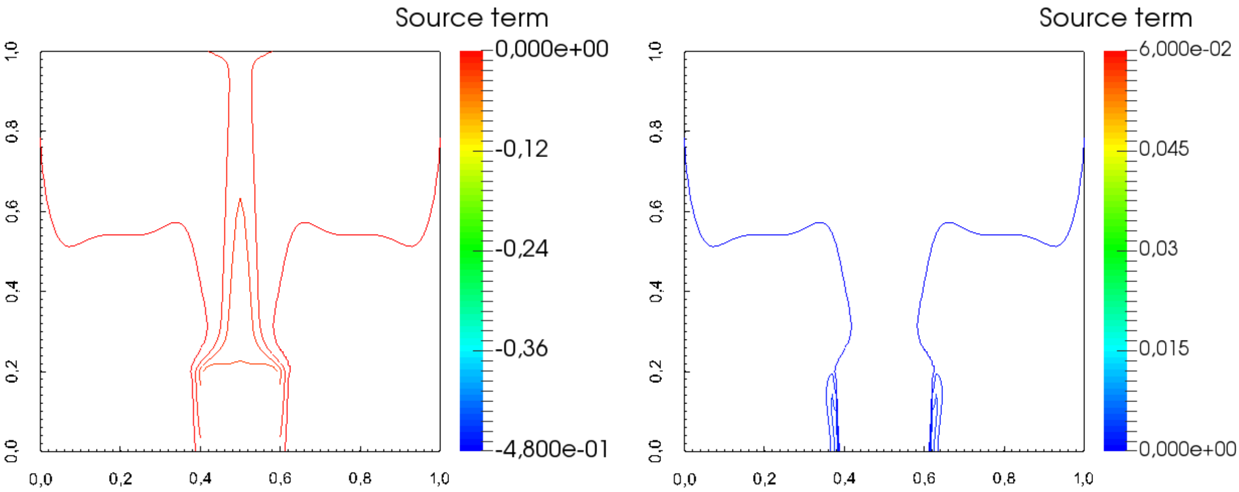

(a) Emission dominates **(b)** Absorption dominates

Figure 5.4: Distribution of radiative source term in the median plane ($Y = 0.5$): cooperating case, $N = 1$, $\tau = 0.1$. Sources are normalized by $4\sigma T_{ref}^4/L$.

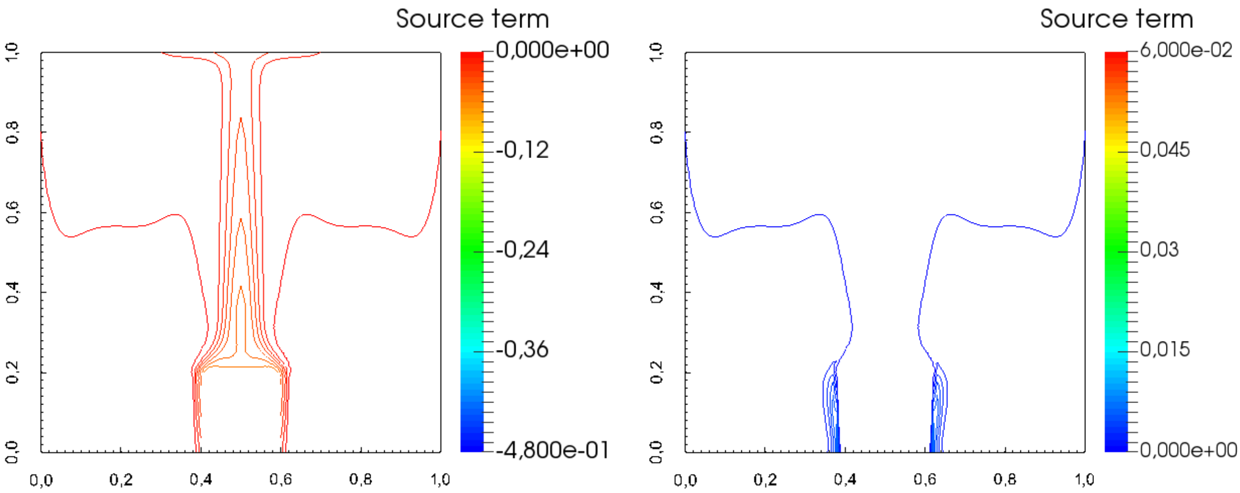

(a) Emission dominates **(b)** Absorption dominates

Figure 5.5: Distribution of radiative source term in the median plane ($Y = 0.5$): cooperating case, $N = 1$, $\tau = 0.2$. Sources are normalized by $4\sigma T_{ref}^4/L$.

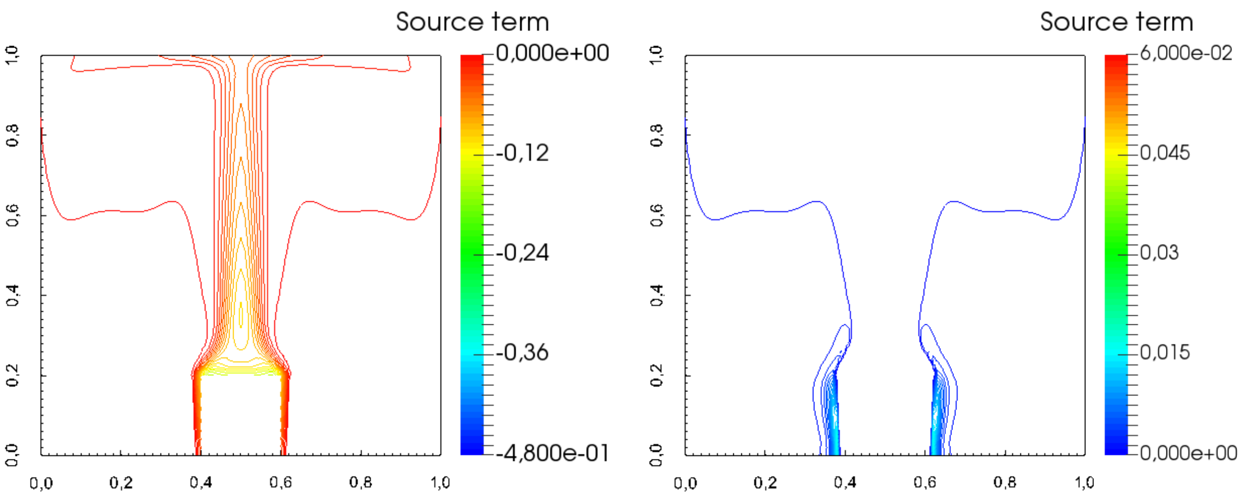

(a) Emission dominates **(b)** Absorption dominates

Figure 5.6: Distribution of radiative source term in the median plane ($Y = 0.5$): cooperating case, $N = 1$, $\tau = 0.5$. Sources are normalized by $4\sigma T_{ref}^4/L$.

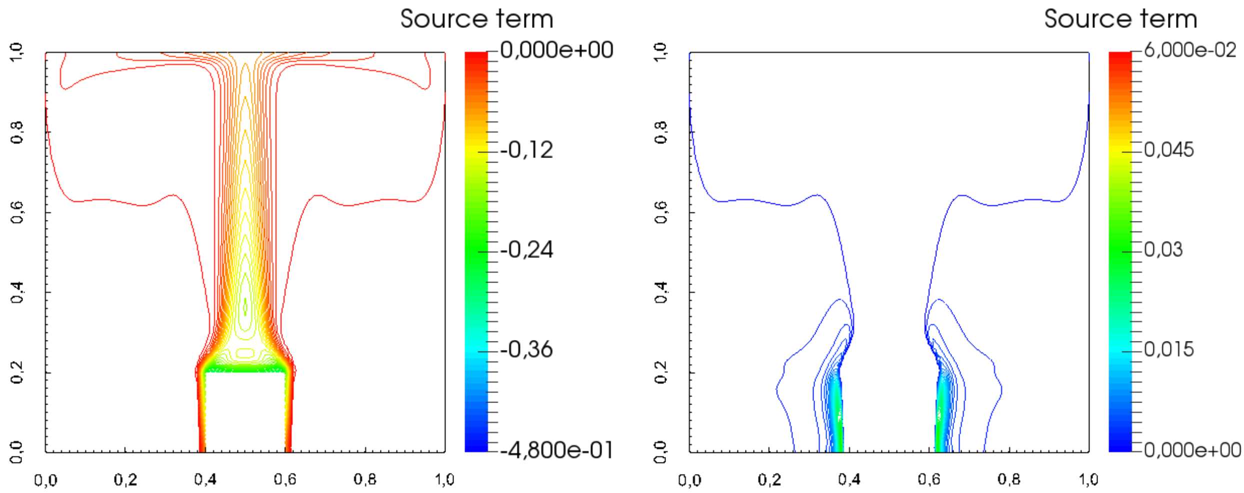

(a) Emission dominates **(b)** Absorption dominates

Figure 5.7: Distribution of radiative source term in the median plane ($Y = 0.5$): cooperating case, $N = 1$, $\tau = 1$. Sources are normalized by $4\sigma T_{ref}^4/L$.

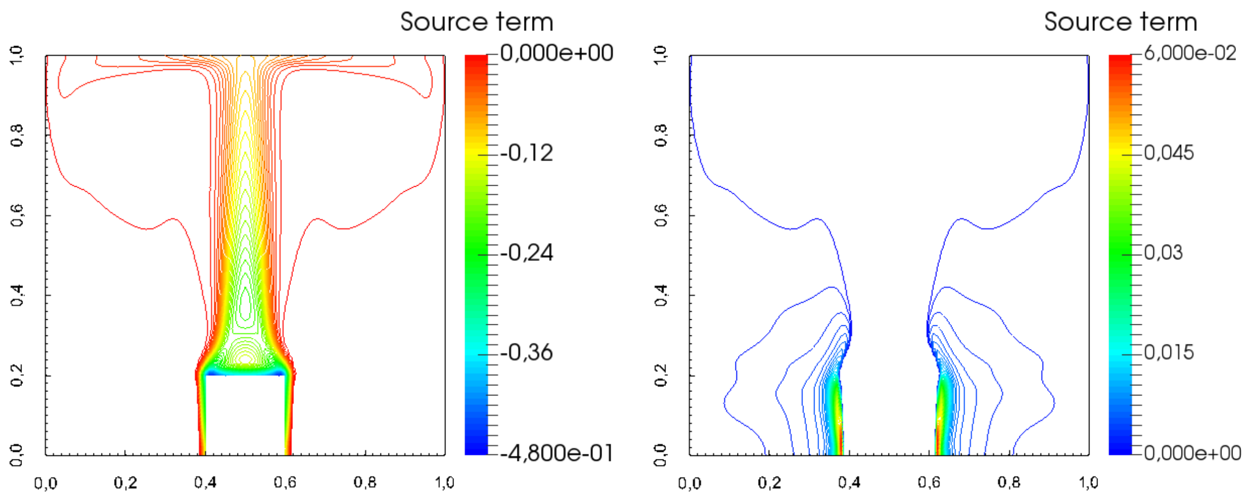

(a) Emission dominates **(b)** Absorption dominates

Figure 5.8: Distribution of radiative source term in the median plane ($Y = 0.5$): cooperating case, $N = 1$, $\tau = 2$. Sources are normalized by $4\sigma T_{ref}^4/L$.

Figure 5.4, 5.5, 5.6, 5.7, 5.8 display the values of the radiative source term in the median plane ($Y = 0.5$) of the cavity. We recall that negative values correspond to the regions where the fluid emits more than it absorbs and conversely for positive values. The observed distributions are representative of double diffusive convection because of the concentration-dependent absorption coefficient. There are regions where κ is very low (even 0), and where radiation, consequently, has little effects on the fluid. This phenomenon distinguishes the combined radiation - double diffusive convection from radiation and pure thermal convection.

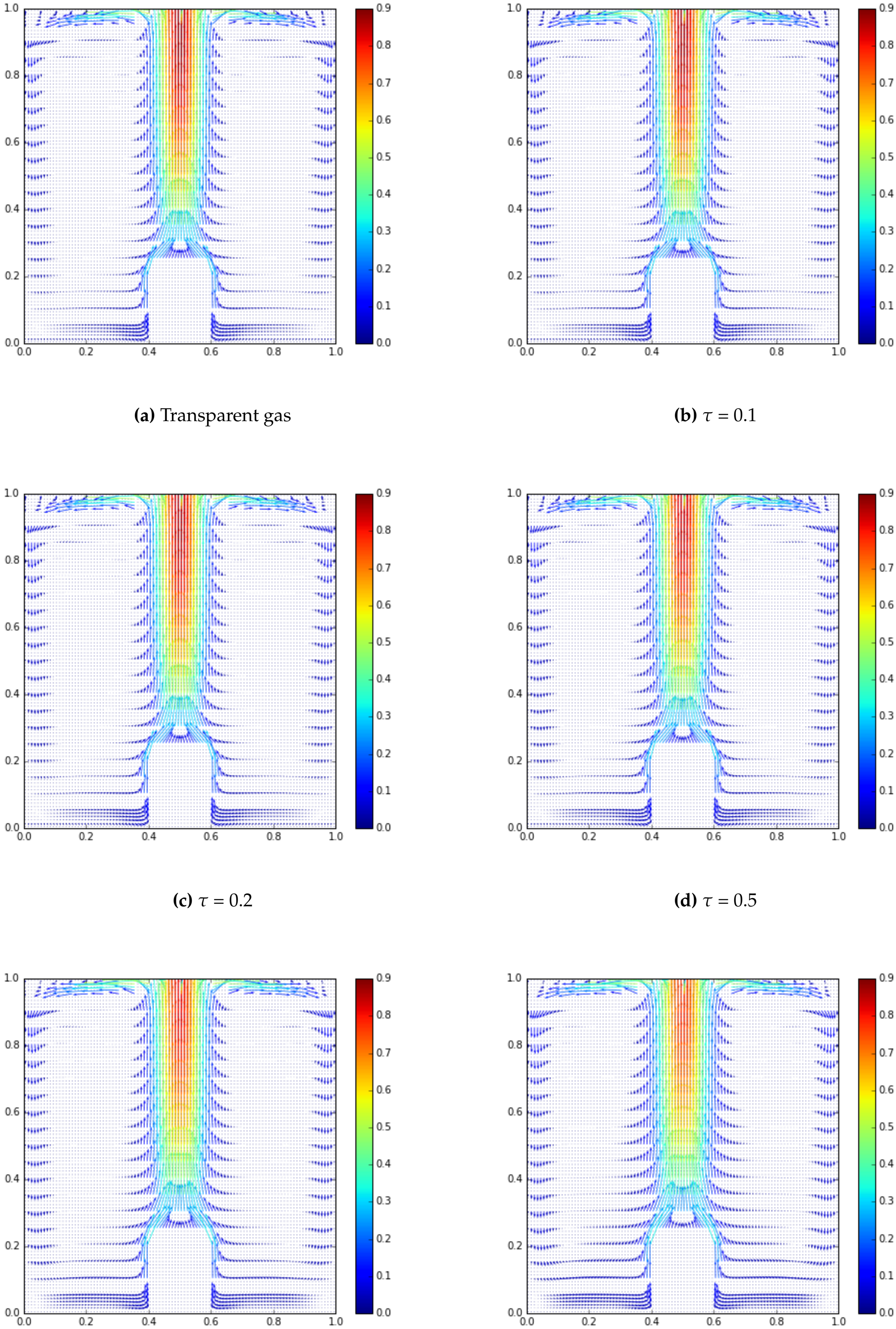

(a) Transparent gas

(b) $\tau = 0.1$

(c) $\tau = 0.2$

(d) $\tau = 0.5$

(e) $\tau = 1$

(f) $\tau = 2$

Figure 5.9: Vector field in the median plane of the cavity ($Y = 0.5$) for different fluid opacities: cooperating case, $N = 1$. Velocities are normalized by U_{ref}.

The velocity vectors in figure 5.9 illustrate the impacts of radiation on the fluid motion. There are no significant changes in the flow structure, but a slight broadening of the plume is observed at $\tau = 2$. The horizontal profiles of vertical velocity in the median plane display more clearly the difference. At low altitude ($Z = 0.1$) (see figure 5.10 a), the fluid near the obstacle and the vertical walls of the cavity is accelerated while, at intermediate and high altitudes ($Z = 0.5$; 0.8) (see figures 5.10 b,c), the only evident change is the drop of the maximum velocity (the peak of the profiles). This is due to the decrease of temperature in the plume, which alters the buoyancy source. Besides, the profile of horizontal velocity along the vertical crossline ($X = 0.2$) (see figure 5.11 a) proves that the boundary layers near the floor and the ceiling of the enclosure are also accelerated. The circulation near the bottom brings cooled fluid from the cavity wall to the region between the obstacle and the enclosure (near the floor). The fluid is further heated up by the radiation coming from the hot cube. At a higher opacity, the radiative effects dominate over the convective transfer and the fluid, in this region, becomes warmer (but not as much as in the thermal convection case). Simultaneously, the medium close to the ceiling emits more than it absorbs, and, thus, becomes cooler. These two tendencies explain the typical distribution of the thermal field mentioned above.

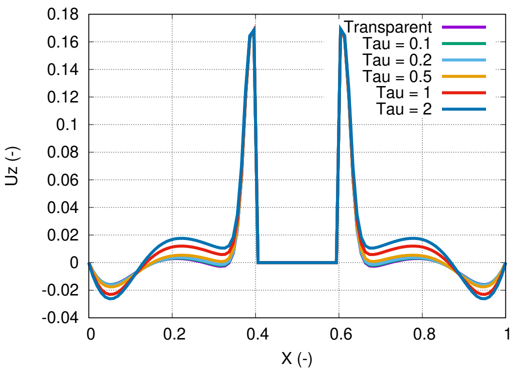

(a) $Z = 0.1$

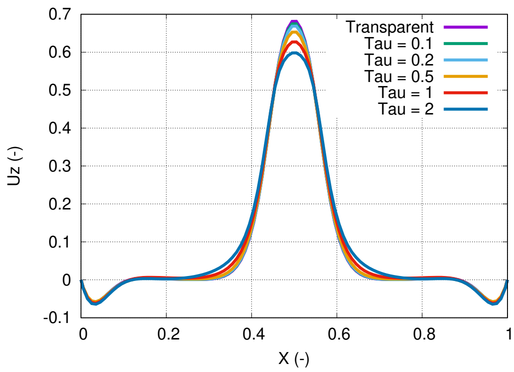

(b) $Z = 0.5$

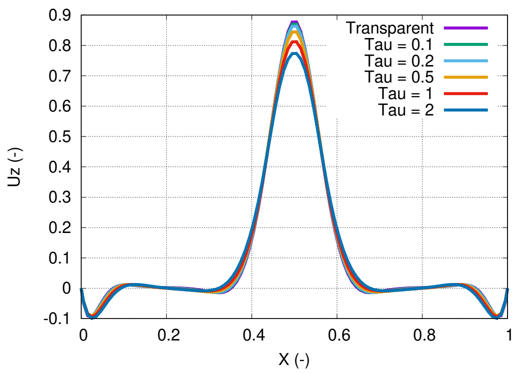

(c) $Z = 0.8$

Figure 5.10: Vertical velocity $\frac{w}{U_{ref}}$ profiles along different Z-crosslines in the median plane ($Y = 0.5$): cooperating case, $N = 1$.

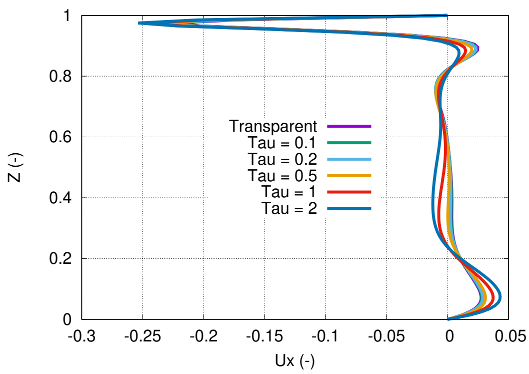

(a) $X = 0.2$

Figure 5.11: Horizontal velocity $\frac{u}{U_{ref}}$ profiles along different X-crosslines in the median plane ($Y = 0.5$): cooperating case, $N = 1$.

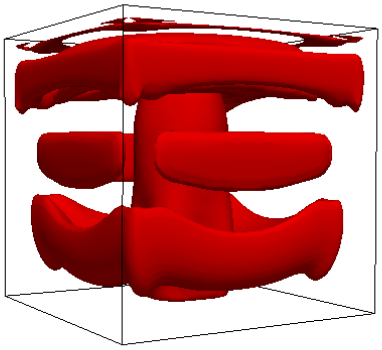

(a) Transparent gas

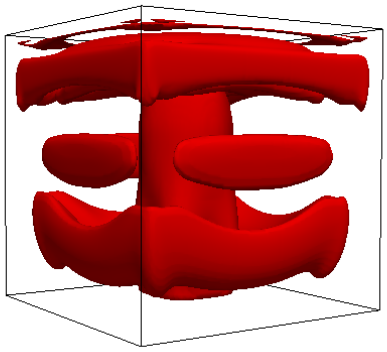

(b) $\tau = 0.1$

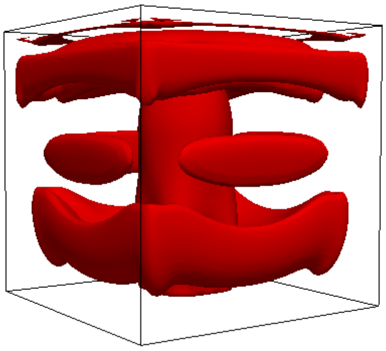

(c) $\tau = 0.2$

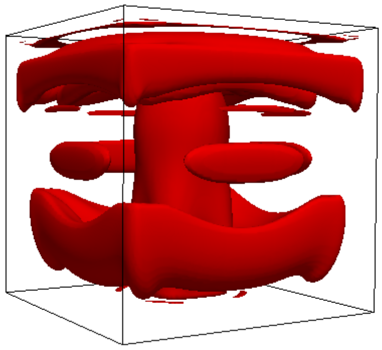

(d) $\tau = 0.5$

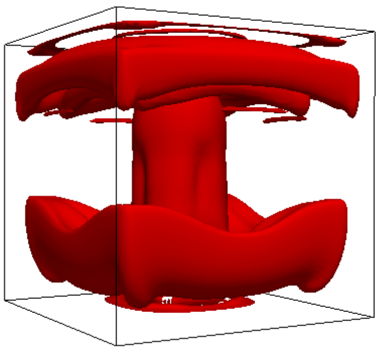

(e) $\tau = 1$

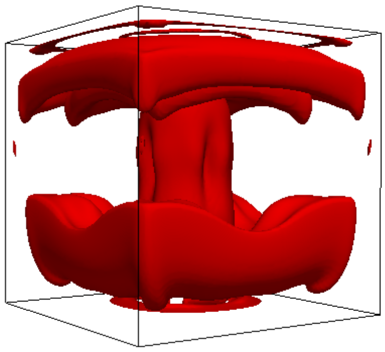

(f) $\tau = 2$

Figure 5.12: Iso-surface of the Q-criterion at the value 0.01 in the cavity. Values are normalized by U_{ref}^2/L^2.

Figure 5.12 represents the iso-surfaces of value 0.01 of the Q inside the cavity. It can be observed that, when the optical thickness is one or more, several of these iso-surfaces disappear. This illustration gives a better view of the changes experienced by the flow structure depending on the fluid opacity.

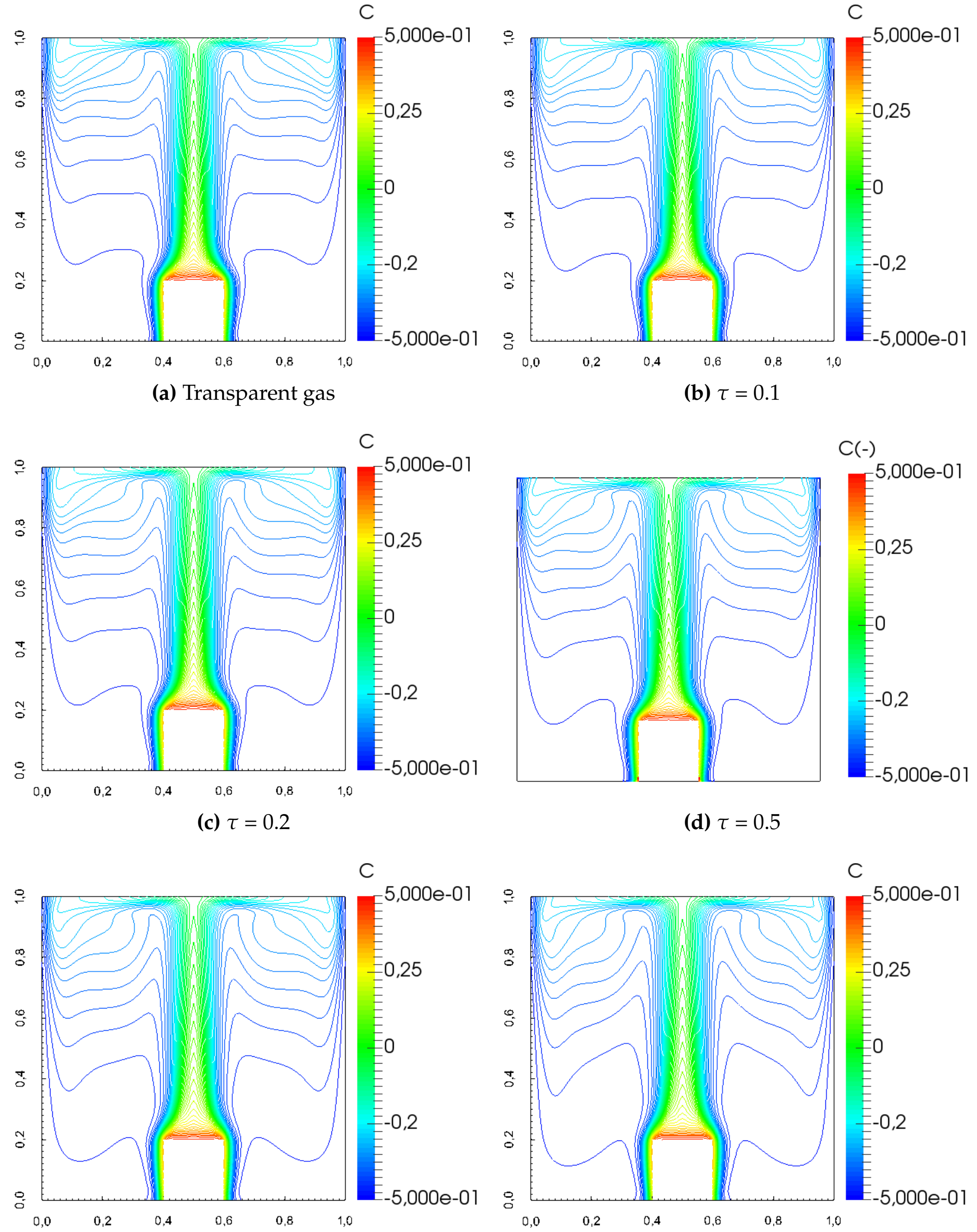

(a) Transparent gas
(b) $\tau = 0.1$
(c) $\tau = 0.2$
(d) $\tau = 0.5$
(e) $\tau = 1$
(f) $\tau = 2$

Figure 5.13: Concentration field $\frac{C - Cref}{C_h - C_l}$ in the median plane of the cavity ($Y = 0.5$) for different fluid opacities: cooperating case, $N = 1$.

Concerning the concentration field, no significant differences are found in the calculations with and without the radiative effects (see figure 5.13). This observation still holds when considering the concentration profiles along different cross lines (see figures 5.14 and 5.15). The reason is that gas radiation does not directly influence the concentration field, but only through the dynamic field and, as presented above, radiation does not significantly alter the flow structure.

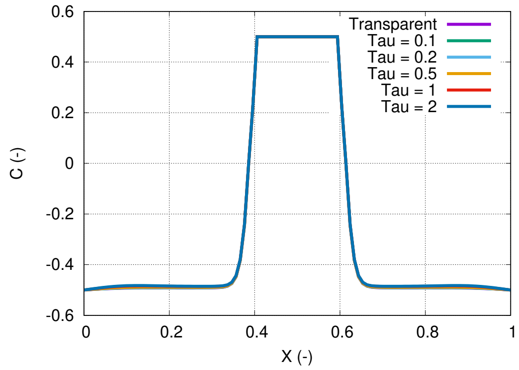

(a) $Z = 0.1$

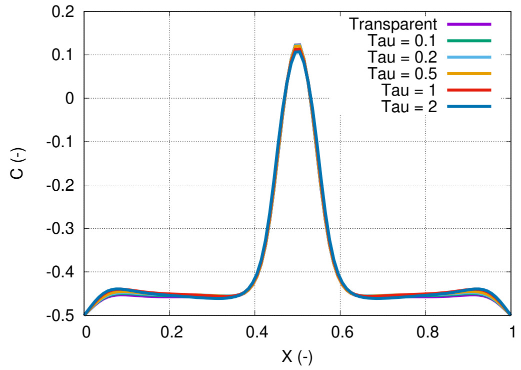

(b) $Z = 0.5$

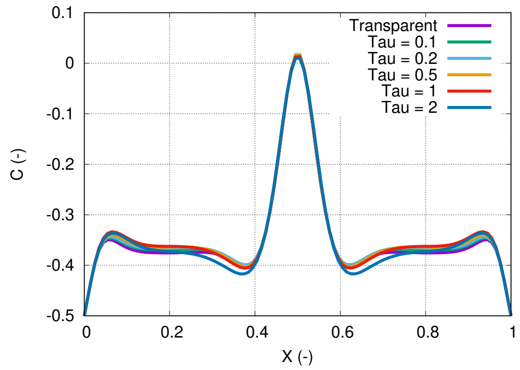

(c) $Z = 0.8$

Figure 5.14: Concentration $\frac{C-Cref}{C_h-C_l}$ profiles along different Z-crosslines in the median plane ($Y = 0.5$): cooperating case, $N = 1$.

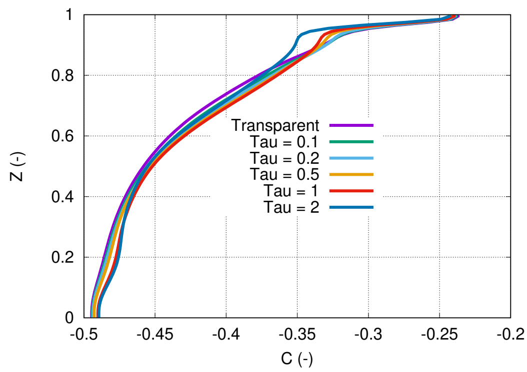

(a) $X = 0.2$

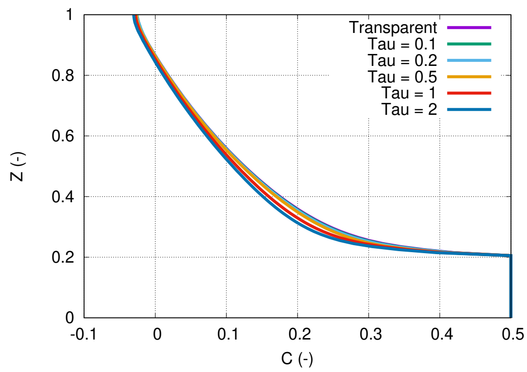

(b) $X = 0.5$

Figure 5.15: Concentration $\frac{C-C_{ref}}{C_h-C_l}$ profiles along different X-crosslines in the median plane ($Y = 0.5$): cooperating case, $N = 1$.

5.1.2 Mass-to-Thermal Buoyancy ratio $N = 2$

In this case, the temperature and concentration gradients still cooperate ($N > 0$) but the mass driving force dominates over the thermal one ($N > 1$).

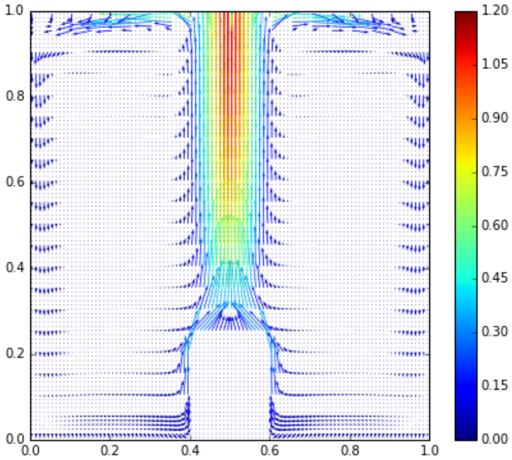

(a) Transparent gas

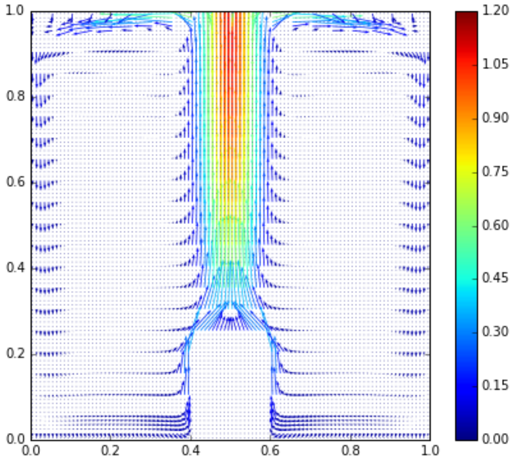

(b) $\tau = 0.1$

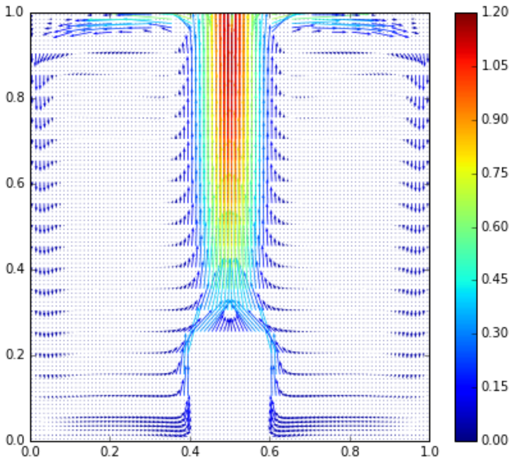

(c) $\tau = 0.2$

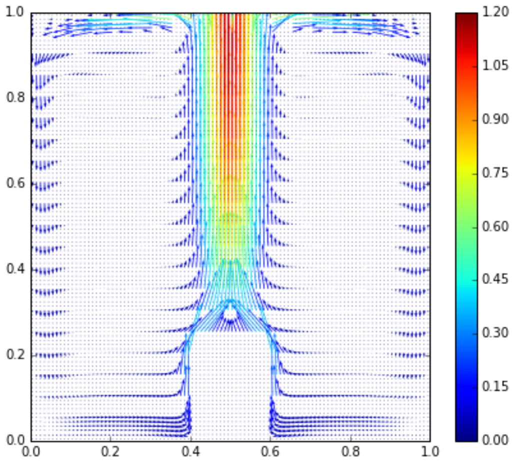

(d) $\tau = 0.5$

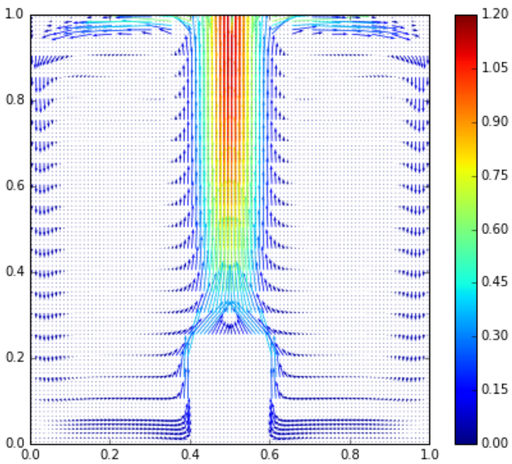

(e) $\tau = 1$

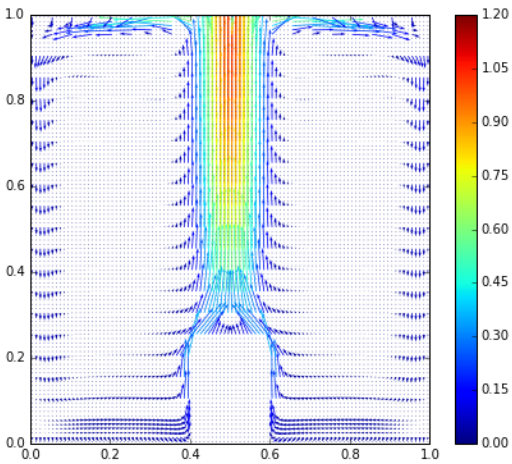

(f) $\tau = 2$

Figure 5.16: Velocity vectors in the median plane of the cavity ($Y = 0.5$) for different fluid opacities: cooperating case, $N = 2$. Velocities are normalized by U_{ref}.

Compared to the reference results (transparent case), the flow field in participating medium at different opacities has no evident change when we consider the velocity vectors (see figure 5.16). It is observed in all the plots a motionless volume of fluid between the ascending plume and the descending boundary layers along the cavity walls.

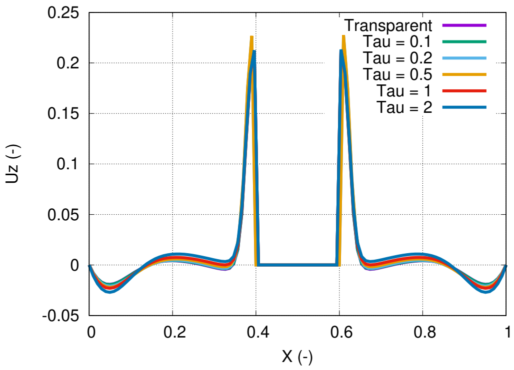

(a) $Z = 0.1$

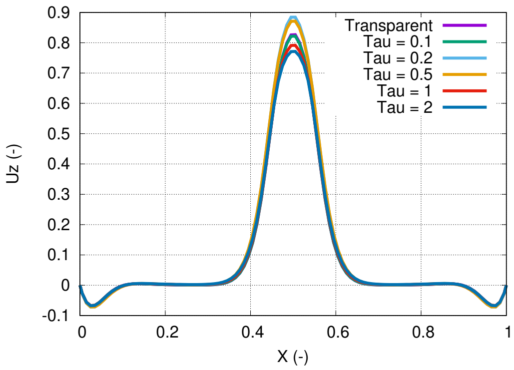

(b) $Z = 0.5$

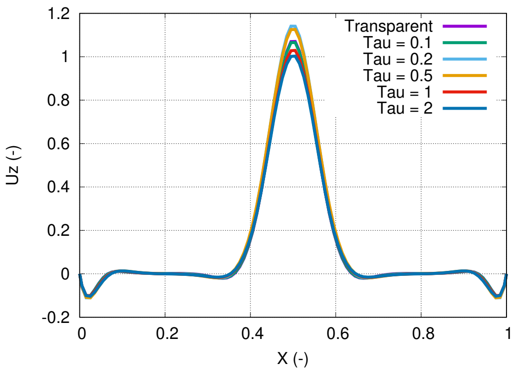

(c) $Z = 0.8$

Figure 5.17: Vertical velocity $\frac{w}{U_{ref}}$ profiles along different Z-crosslines in the median plane ($Y = 0.5$): cooperating case, $N = 2$.

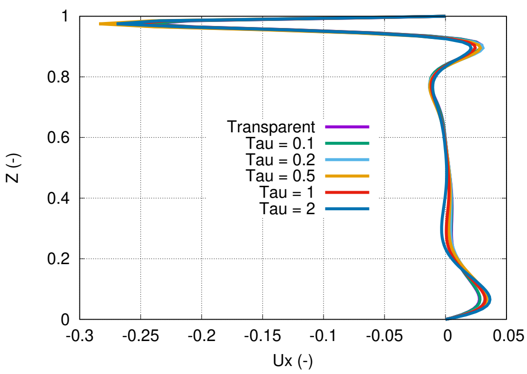

(a) $X = 0.2$

Figure 5.18: Horizontal velocity $\frac{u}{U_{ref}}$ profiles along different X-crosslines in the median plane ($Y = 0.5$): cooperating case, $N = 2$.

However, some differences are found when considering the dynamic profiles along the horizontal cross lines: a slight decrease of the maximum velocity at medium and high levels ($Z = 0.5$ and $Z = 0.8$) and a weak acceleration of the fluid near the cavity walls and the hot body surfaces ($Z = 0.1$). It can also be seen in the representation of the Q-criterion (see figure 5.19) that the flow structure is preserved at all the optical thicknesses, except a stretching of the iso-surface at mid-height of the enclosure (see figure 5.19). The reasons for this unchanged flow structure is that the mass gradient governs the fluid motion. Therefore, radiation, which primarily acts on the temperature field, has a weak impact on the dynamic field.

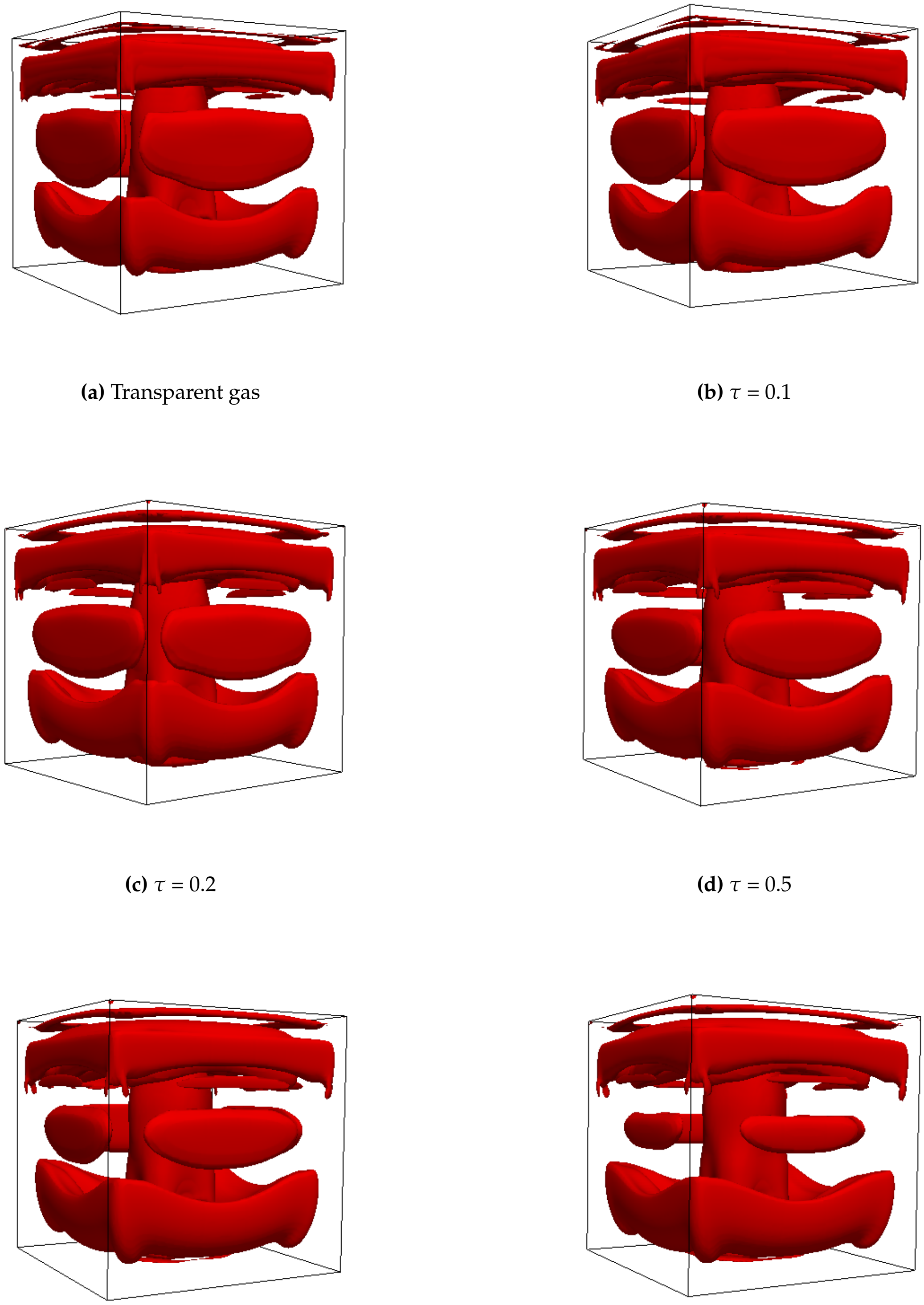

(a) Transparent gas

(b) $\tau = 0.1$

(c) $\tau = 0.2$

(d) $\tau = 0.5$

(e) $\tau = 1$

(f) $\tau = 2$

Figure 5.19: Iso-surface of the Q-criterion at the value 0.01 in the cavity. Values are normalized by U_{ref}^2/L^2.

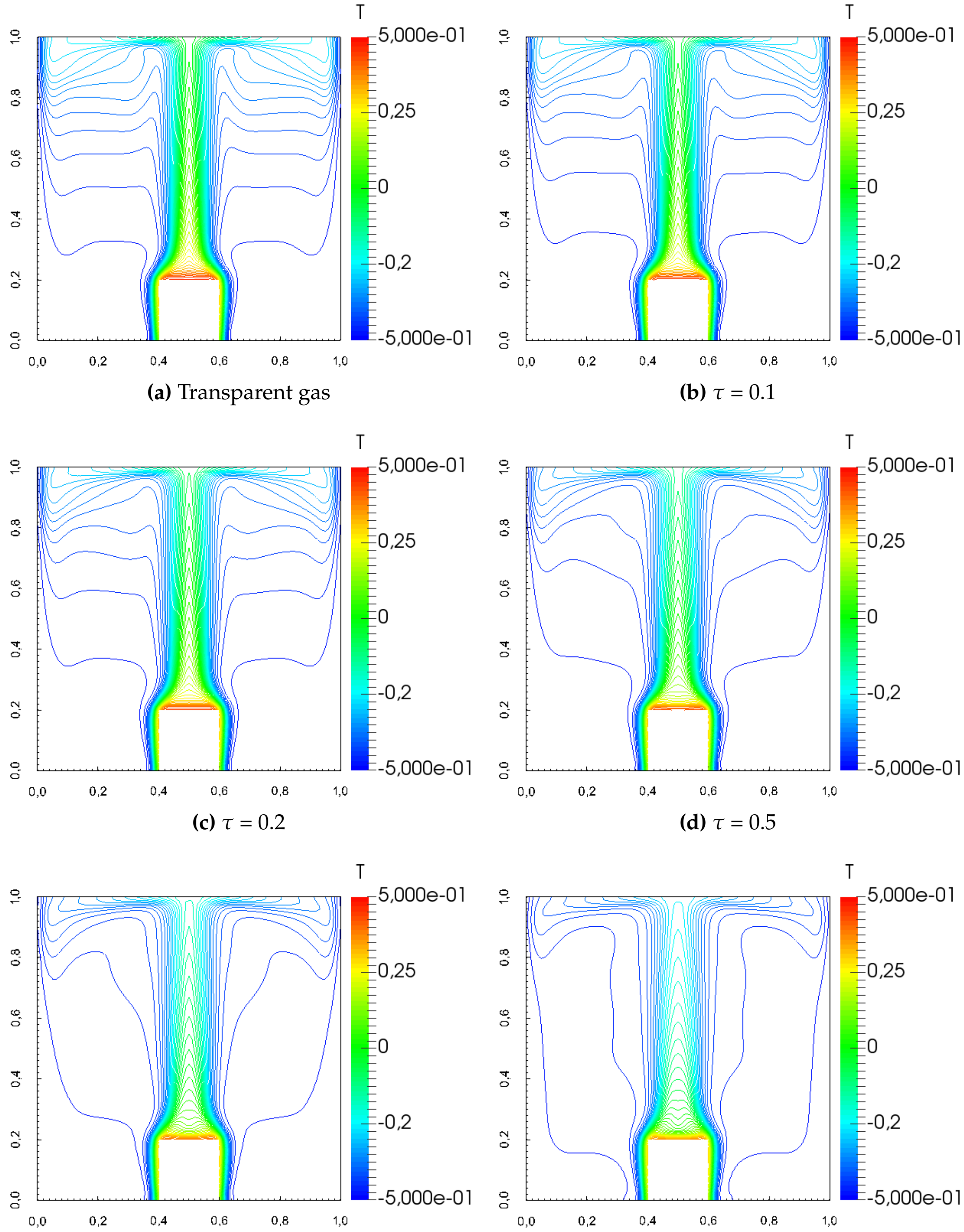

(a) Transparent gas **(b)** $\tau = 0.1$

(c) $\tau = 0.2$ **(d)** $\tau = 0.5$

(e) $\tau = 1$ **(f)** $\tau = 2$

Figure 5.20: Thermal field in the median plane of the cavity ($Y = 0.5$) for different fluid opacities: cooperating case, $N = 2$.

Although the dynamic is not significantly altered, radiation, as usual, plays an important role in redistributing the thermal energy. Due to emission, the fluid at medium ($Z = 0.5$) and high ($Z = 0.8$) positions (see figures 5.21 a, 5.22 a, 5.23 a, 5.24 a and 5.25 a) reduces its temperature level (see figure 5.26 b,c) while the boundary layers around the obstacle at low altitude ($Z = 0.1$) are warmed up (see figure 5.26 a) by absorption (see figures 5.21 b, 5.22 b, 5.23 b, 5.24 b and 5.25 b). These two effects create the typical structure of the thermal field (see figure 5.20) already found when $N = 1$.

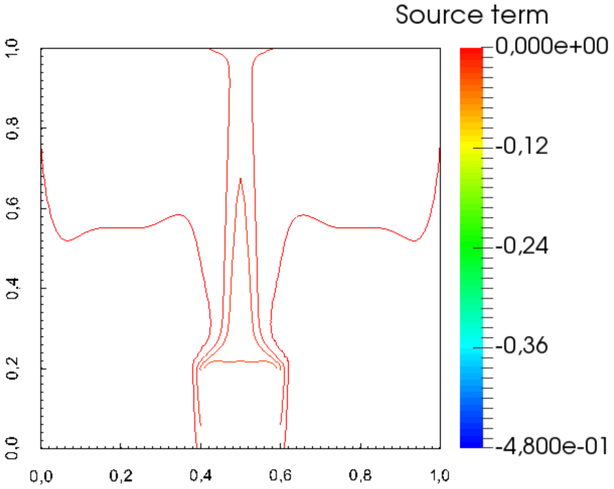

(a) Emission dominates

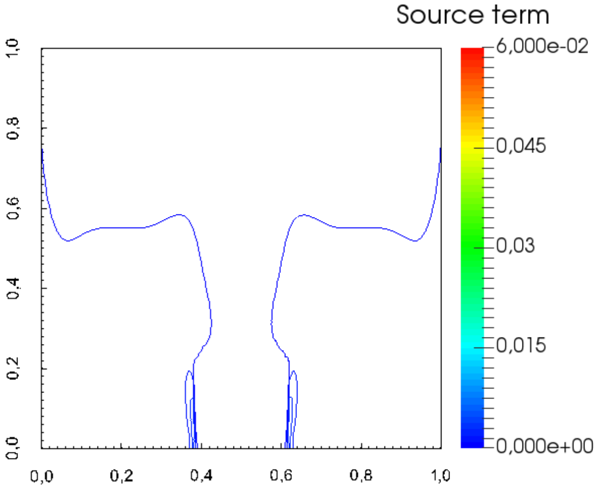

(b) Absorption dominates

Figure 5.21: Distribution of radiative source term in the median plane ($Y = 0.5$): cooperating case, $N = 2$, $\tau = 0.1$. Sources are normalized by $4\sigma T_{ref}^4/L$.

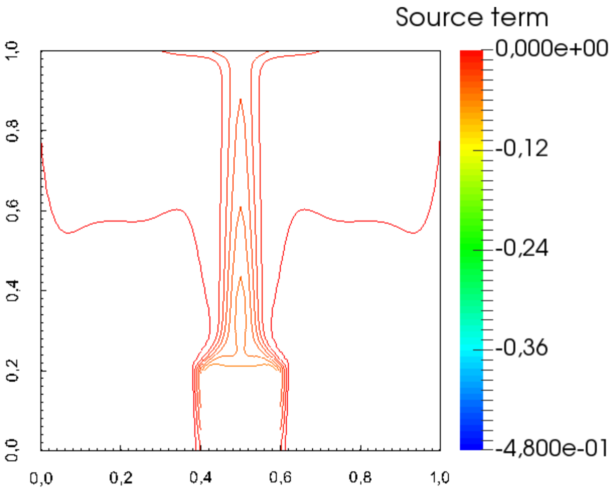

(a) Emission dominates

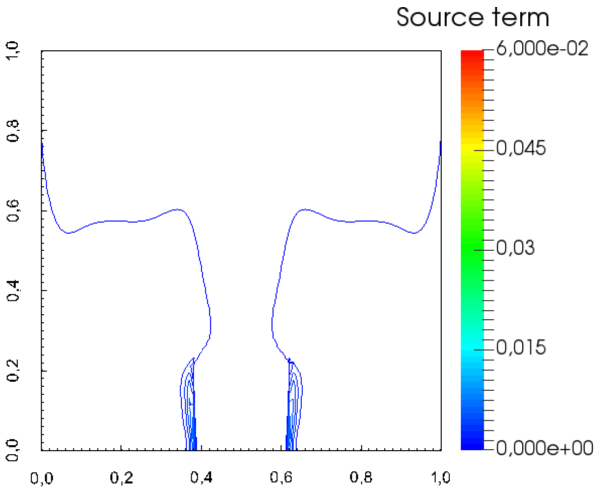

(b) Absorption dominates

Figure 5.22: Distribution of radiative source term in the median plane ($Y = 0.5$): cooperating case, $N = 2$, $\tau = 0.2$. Sources are normalized by $4\sigma T_{ref}^4/L$.

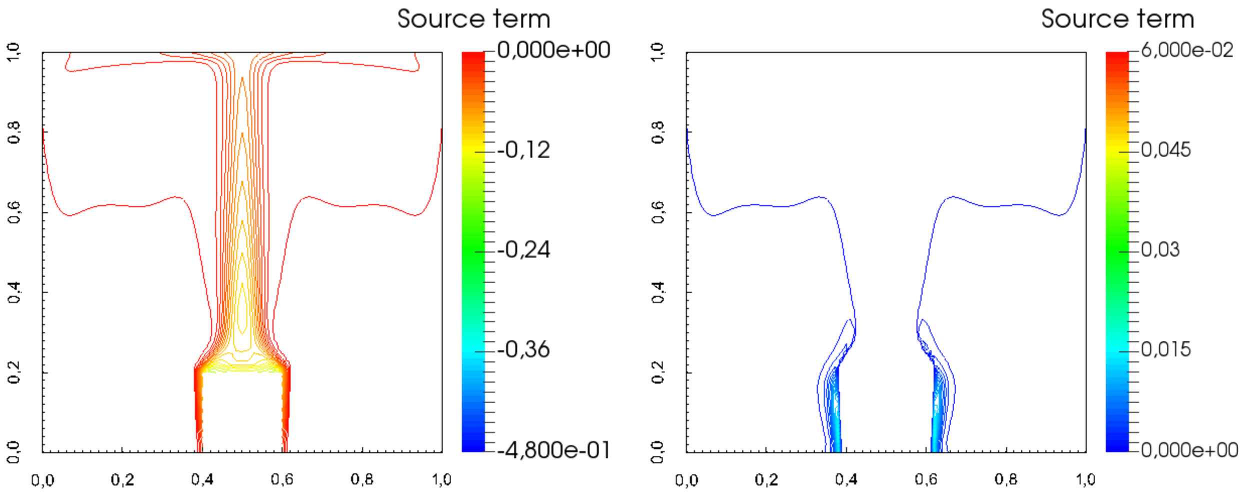

(a) Emission dominates **(b)** Absorption dominates

Figure 5.23: Distribution of radiative source term in the median plane ($Y = 0.5$): cooperating case, $N = 2$, $\tau = 0.5$. Sources are normalized by $4\sigma T_{ref}^4/L$.

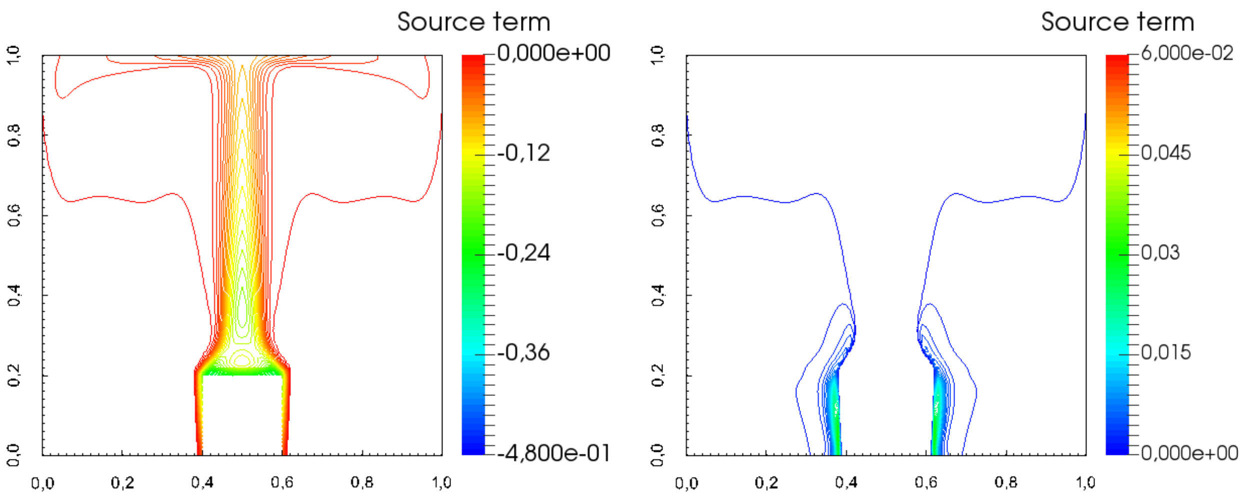

(a) Emission dominates **(b)** Absorption dominates

Figure 5.24: Distribution of radiative source term in the median plane ($Y = 0.5$): cooperating case, $N = 2$, $\tau = 1$. Sources are normalized by $4\sigma T_{ref}^4/L$.

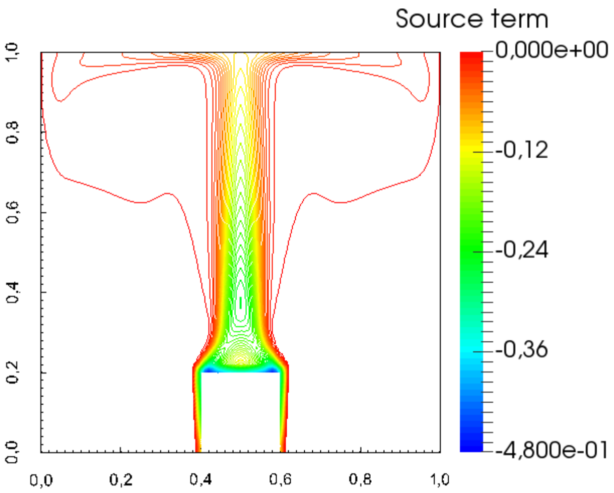

(a) Emission dominates

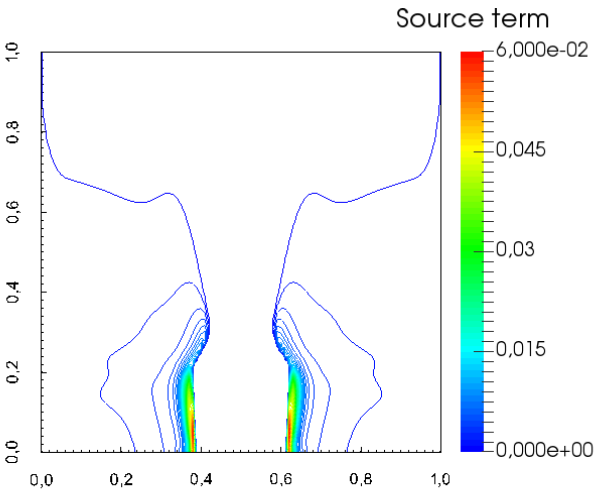

(b) Absorption dominates

Figure 5.25: Distribution of radiative source term in the median plane ($Y = 0.5$): cooperating case, $N = 2$, $\tau = 2$. Sources are normalized by $4\sigma T_{ref}^4/L$.

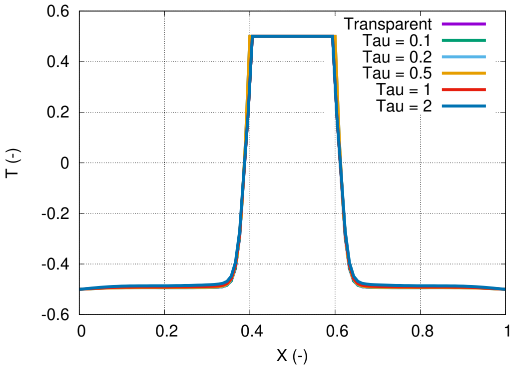

(a) $Z = 0.1$

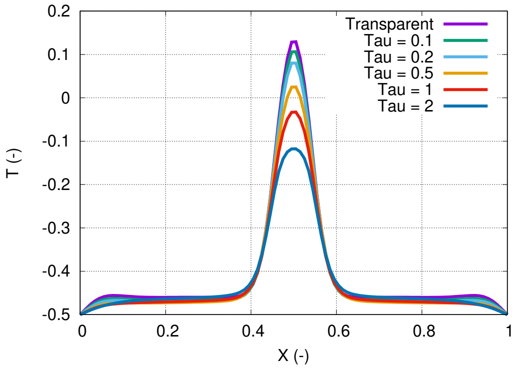

(b) $Z = 0.5$

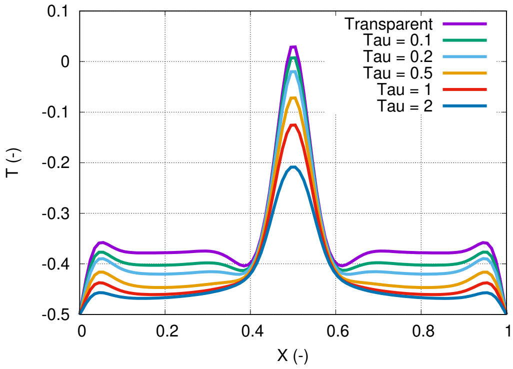

(c) $Z = 0.8$

Figure 5.26: Temperature $\frac{T-Tref}{T_h-T_c}$ profiles along different Z-crosslines in the median plane ($Y = 0.5$): cooperating case, $N = 2$.

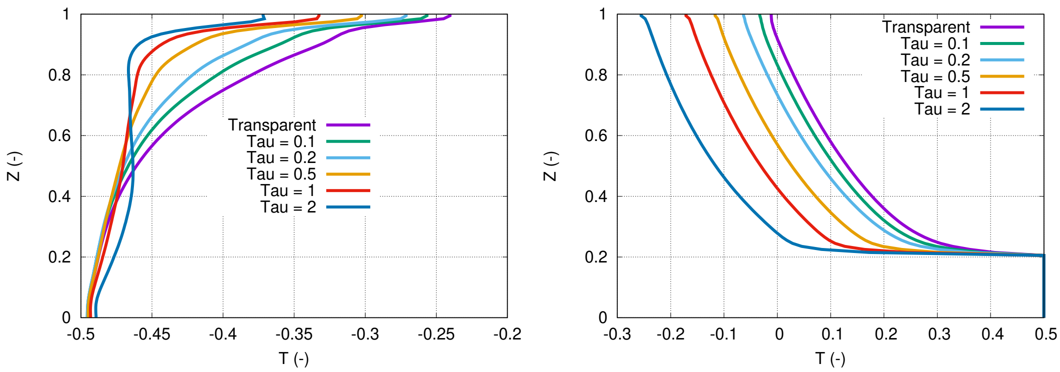

(a) $X = 0.2$

(b) $X = 0.5$

Figure 5.27: Temperature $\frac{T-Tref}{T_h-T_c}$ profiles along different X-crosslines in the median plane ($Y = 0.5$): cooperating case, $N = 2$.

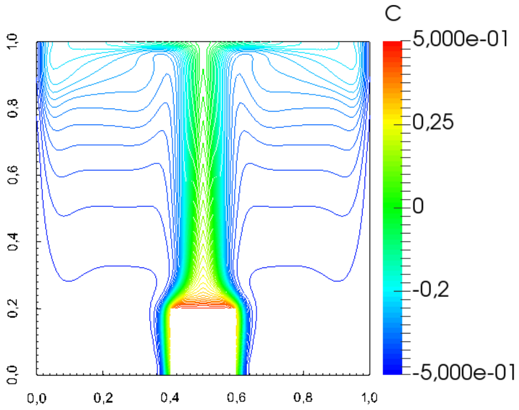

(a) Transparent gas

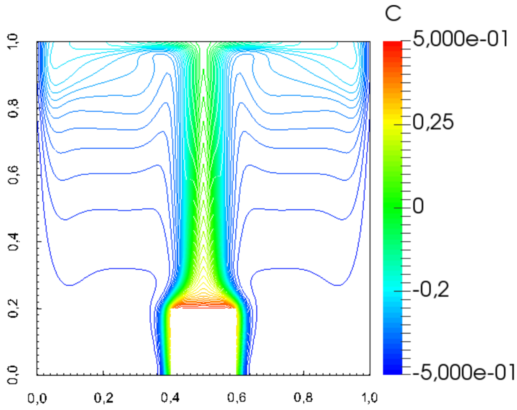

(b) $\tau = 0.1$

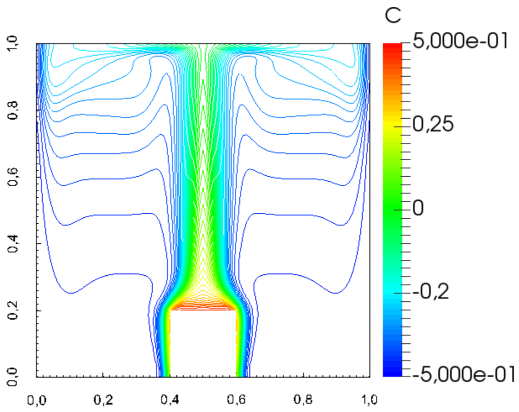

(c) $\tau = 0.2$

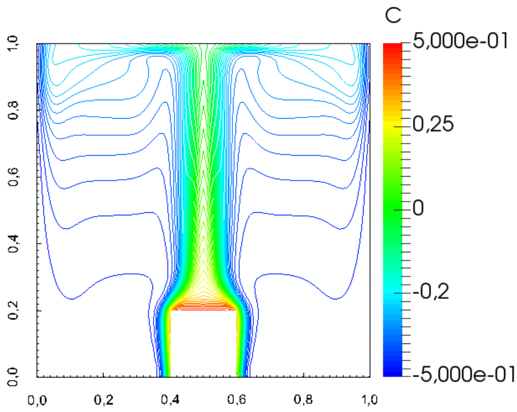

(d) $\tau = 0.5$

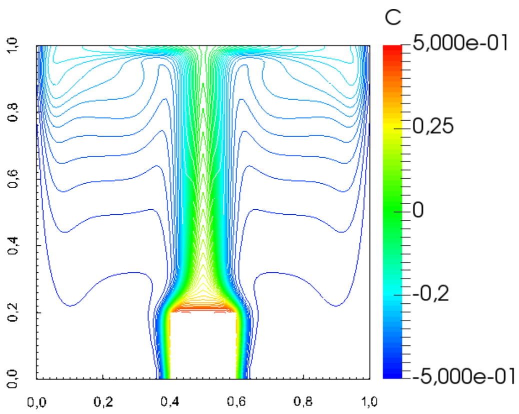

(e) $\tau = 1$

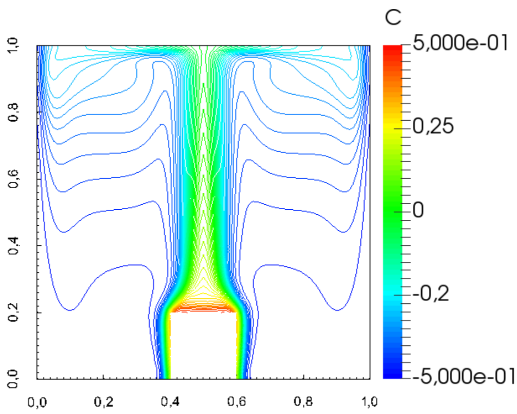

(f) $\tau = 2$

Figure 5.28: Concentration field in the median plane of the cavity ($Y = 0.5$) for different fluid opacities: cooperating case, $N = 2$.

There is no obvious change in the concentration field when the radiation effects are taken into account. C is stratified nearly vertically along the plume boundaries (see figure 5.28). The almost unchanged structure of its distribution is confirmed when plotting different profiles along the horizontal and vertical crosslines at various positions in the cavity (see figures 5.29 and 5.30).

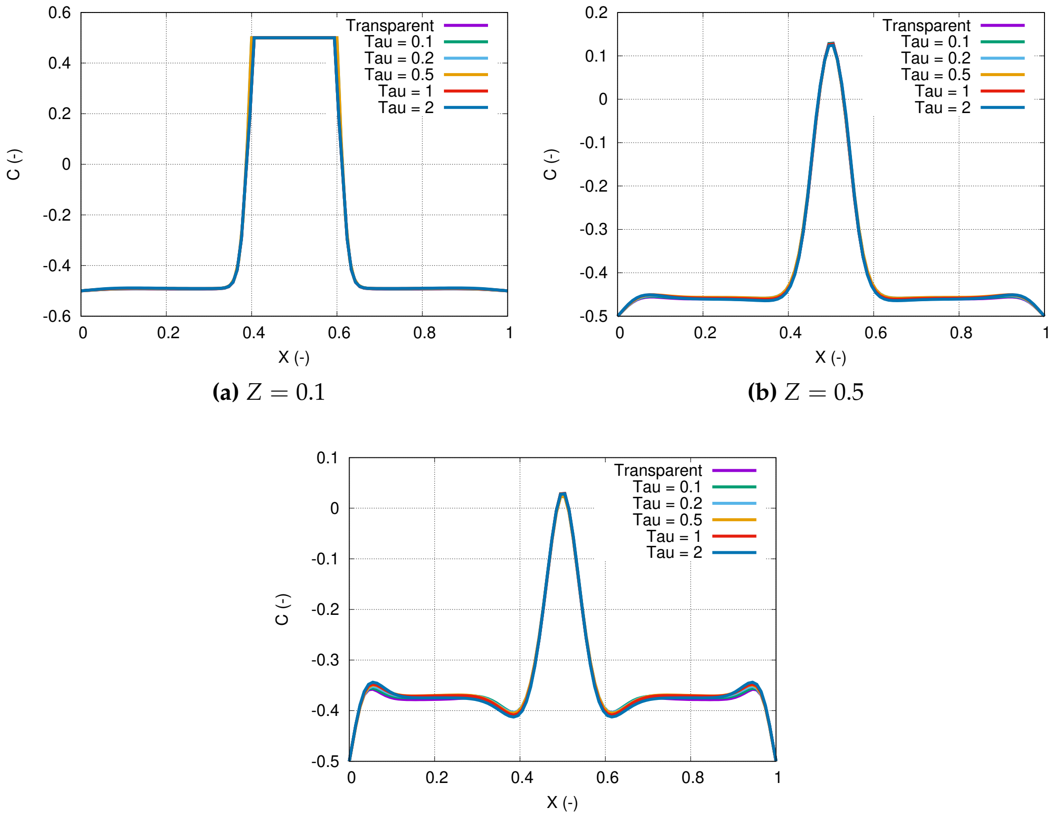

(a) $Z = 0.1$ **(b)** $Z = 0.5$ **(c)** $Z = 0.8$

Figure 5.29: Concentration $\frac{C-C_{ref}}{C_h-C_l}$ profiles along different Z-crosslines in the median plane ($Y = 0.5$): cooperating case, $N = 2$.

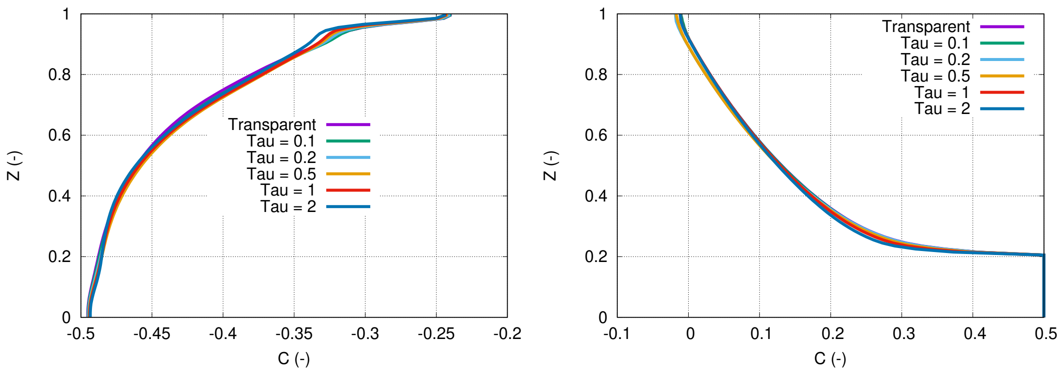

(a) $X = 0.2$ **(b)** $X = 0.5$

Figure 5.30: Concentration $\frac{C-C_{ref}}{C_h-C_l}$ profiles along different X-crosslines in the median plane ($Y = 0.5$): cooperating case, $N = 2$.

5.1.3 Mass-to-Thermal Buoyancy ratio $N = -1$

We now assume that the fluid supplied by the (hot) obstacle and removed by the (cold) cavity walls is heavier than the main component of the mixture. In the specific case where $N = -1$, the thermal and mass buoyancy forces have exactly the same magnitude ($|N| = 1$), but act in opposite directions ($N < 0$). Literally, the momentum source created by the temperature and concentration gradients cancel each other[2] (since $Le = 1$). As a result, the fluid remains motionless. However, this holds for a transparent medium only. When volume radiation is taken into account, the similarity of temperature and concentration distributions is broken. A flow structure is then established.

[2]The nondimensional buoyancy source term in the momentum equation is $\rho_0 g \beta_T \Delta T(NC + T)$. When $Le = 1$, the conservation of species and the energy equation are identical and share the same boundary conditions. Therefore, the nondimensional T and C-fields are identical and, when $N = -1$, the buoyancy force goes to zero.

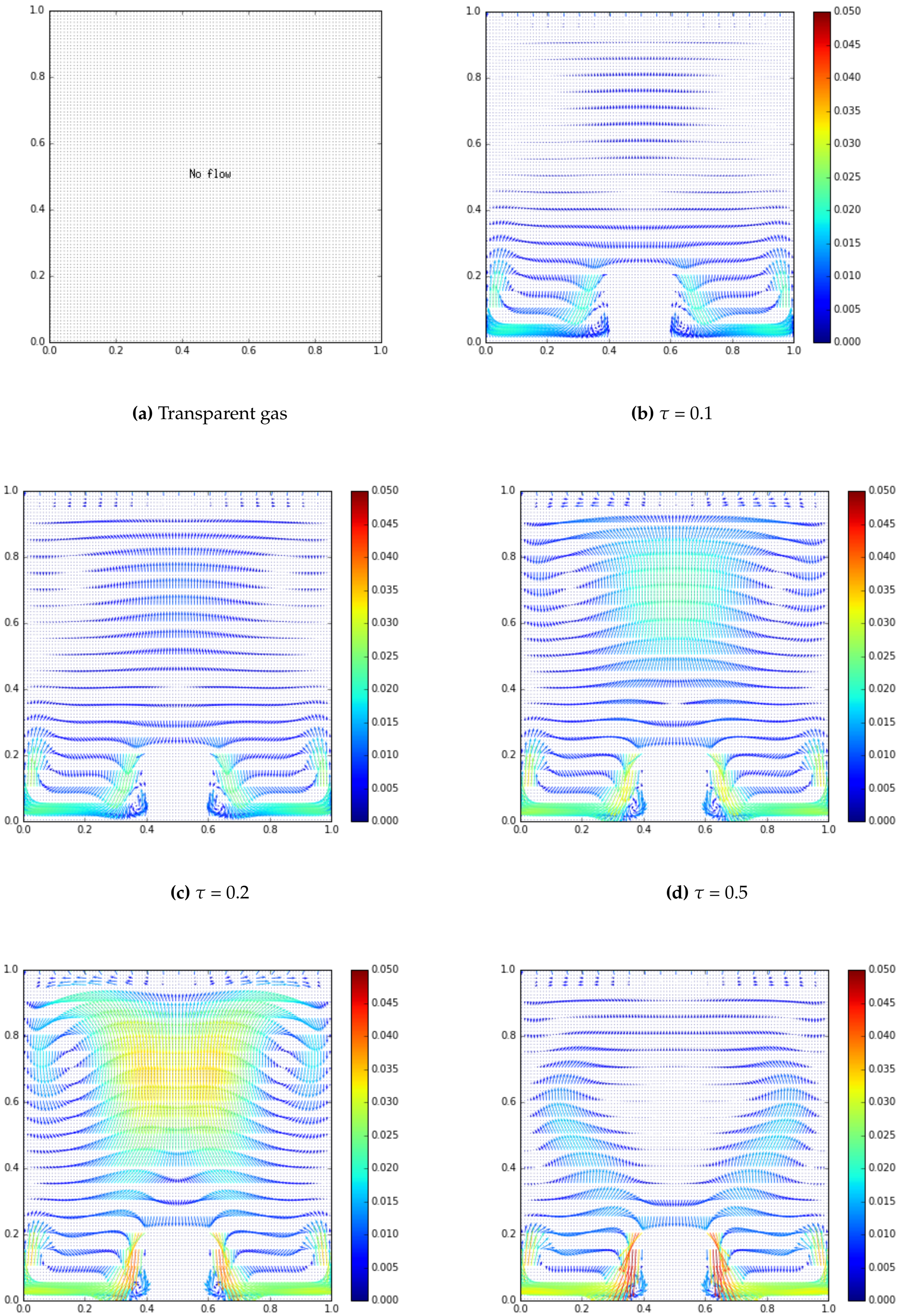

(a) Transparent gas

(b) $\tau = 0.1$

(c) $\tau = 0.2$

(d) $\tau = 0.5$

(e) $\tau = 1$

(f) $\tau = 2$

Figure 5.31: Velocity vectors in the median plane ($Y = 0.5$) of the cavity for different fluid opacities: opposing case, $N = -1$. Velocities are normalized by U_{ref}.

Figure 5.31 represents the velocity field in the mid-depth plane ($Y = 0.5$) of the cavity. Because radiation has broken the symmetry between the thermal and concentration fields, the fluid is now set into motion. Investigation of the velocity profiles (see figures 5.32 a,b,c and 5.33 a) reveals that, in the lower part of the cavity ($Z = 0.1$), the flow is dominated by the mass gradient. It descends along the obstacle (at high concentration) and climbs along the cavity walls (at low concentration). These two motions are well separated. In addition, there exists at all opacities a thermal boundary sublayer along the hot source vertical walls. On the other hand, a thermally driven motion prevails in the upper part of the cavity ($Z = 0.8$). We recognize an ascending plume in the center and descending boundary layers along the lateral cold walls. However, at $\tau = 1$, an increase in concentration on the plume axis tends to limit the vertical movement and causes the plume to spread. From $\tau = 2$, the flow dynamic is very attenuated (at the limit, if the opacity were infinite, one would retrieve the motionless solution of the transparent case). At intermediate levels ($Z = 0.5$), the situation is more complex. At low opacities ($\tau = 0.1, 0.2$), there simultaneously exists a thermally driven flow (above the hot obstacle) and a mass governed one (ascending boundary layers along the cavity walls). At $\tau = 0.5$ and 1, the flow is totally driven by the thermal gradient (ascending plume and descending boundary layers along the cold walls). Moreover, the thermal plume expands as the opacity increases from 0.1 to 1 (see figures 5.31 b-e). At $\tau = 1$, the intensification of the mass force slows down the plume and tends to separate it into two parts (see figures 5.31 e and 5.32 b). At $\tau = 2$, this separation is complete and the hot fluid is pushed toward the side walls. Near these surfaces, the fluid temperature is increased but it drops at the center of the cavity. This alters the thermal buoyancy force and thus, can explain the typical pattern of the velocity field. However, temperature and concentration act together on the flow. We therefore consider the dimensionless buoyancy source term[3] plotted at different levels (figures 5.32 j,k,l). At $Z = 0.5$ we observe that, for $\tau = 2$, this quantity raises up near the vertical walls and then drops in the center, which more clearly demonstrates the formation of the fluid movements. The increase of the Boussinesq source can be explained by a locally dominant thermal effect induced by radiative absorption (see figure 5.38 b for positive radiative source term).

[3]This quantity is defined as $\beta_T(T_h - T_c)(NC + T)$.

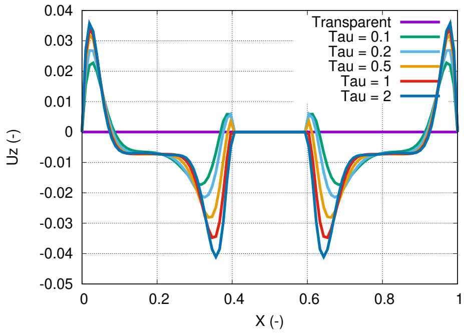

(a) $Z = 0.1$: U_z

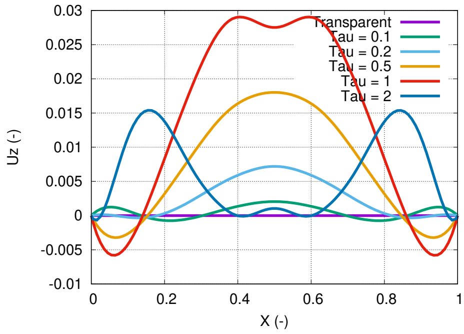

(b) $Z = 0.5$: U_z

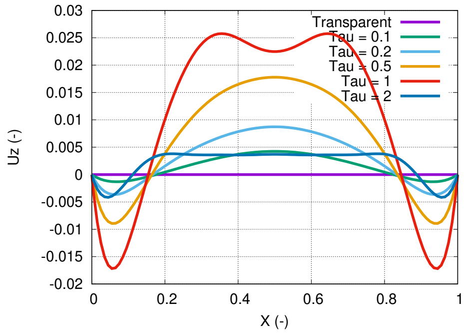

(c) $Z = 0.8$: U_z

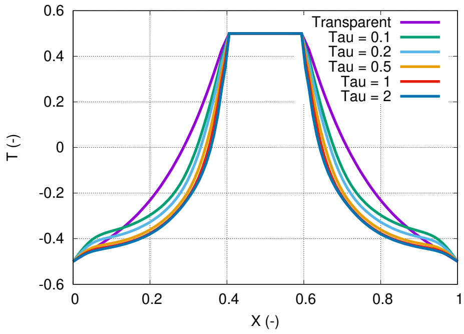

(d) $Z = 0.1$: T

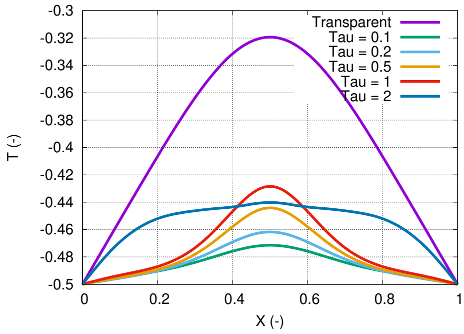

(e) $Z = 0.5$: T

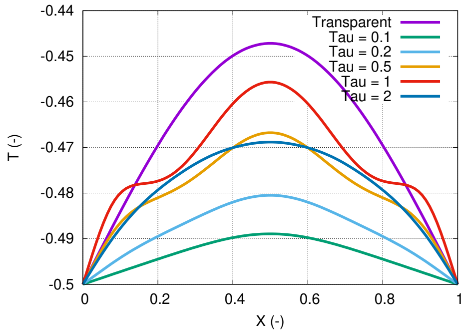

(f) $Z = 0.8$: T

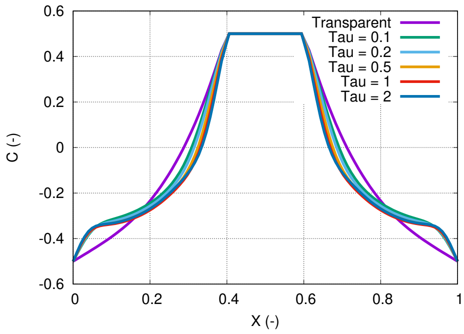

(g) $Z = 0.1$: C

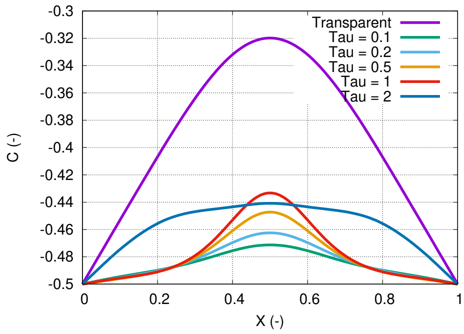

(h) $Z = 0.5$: C

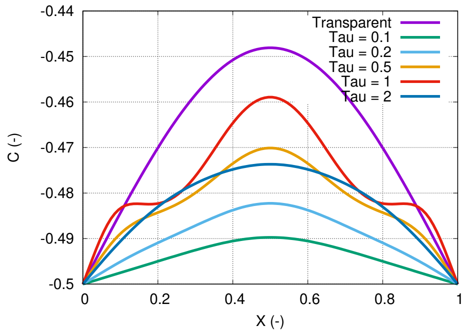

(i) $Z = 0.8$: C

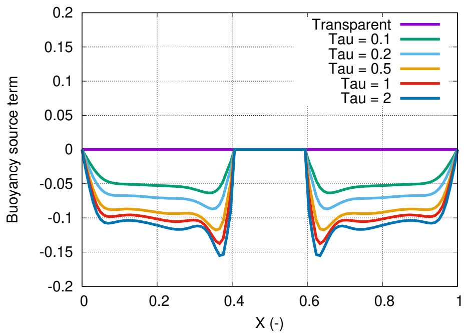

(j) $Z = 0.1$: Buoyancy source term

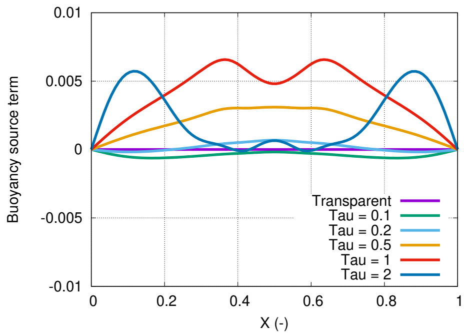

(k) $Z = 0.5$: Buoyancy source term

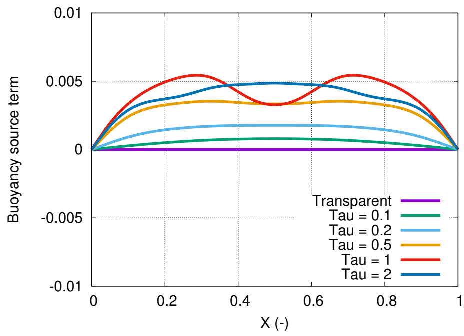

(l) $Z = 0.8$: Buoyancy source term

Figure 5.32: Vertical velocity $\frac{w}{U_{ref}}$, temperature $\frac{T-T_{ref}}{T_h-T_c}$, concentration $\frac{C-C_{ref}}{C_h-C_l}$ and dimensionless buoyancy source term profiles along different Z-crosslines in the median plane ($Y = 0.5$): opposing case, $N = -1$.

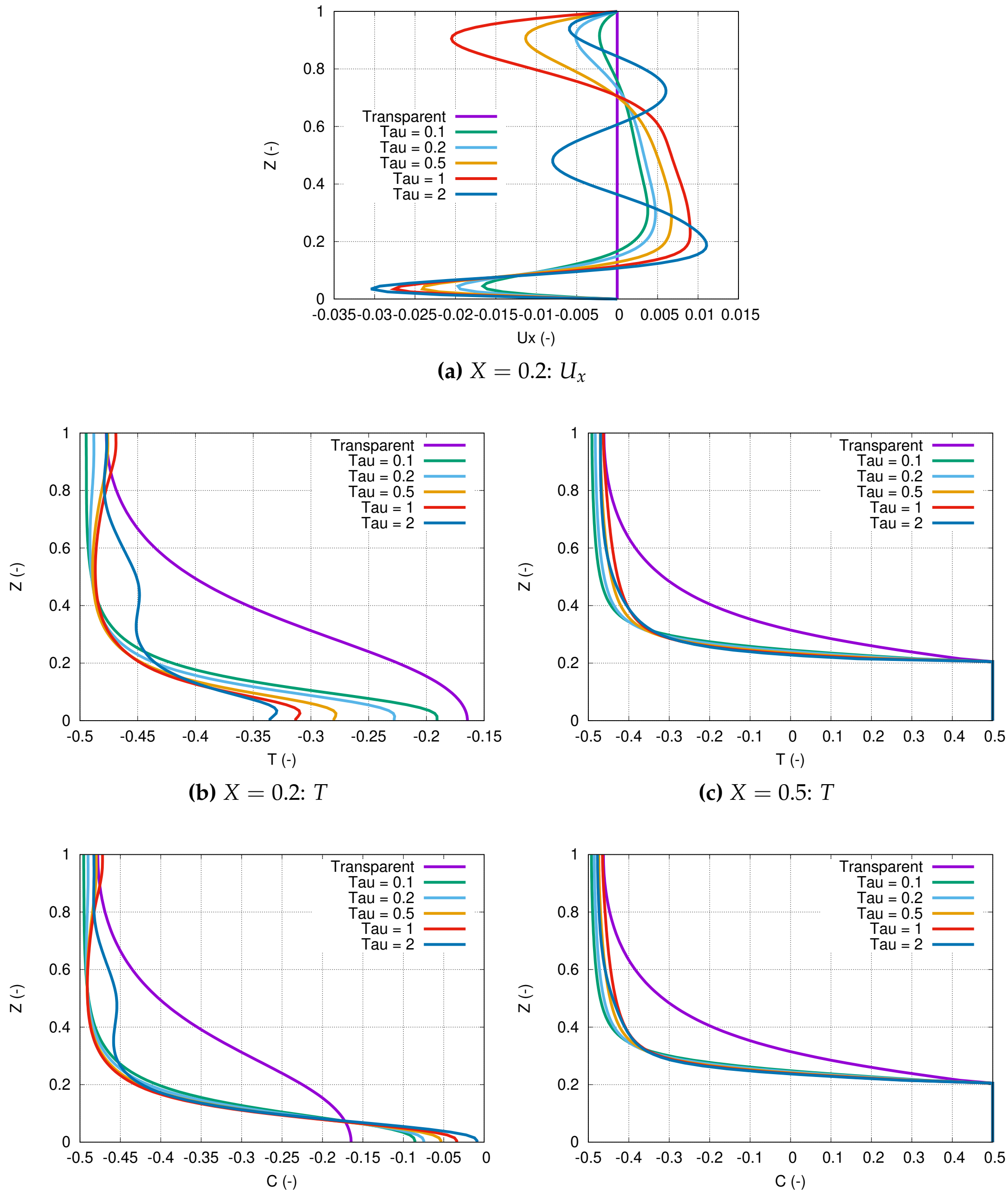

(a) $X = 0.2$: U_x

(b) $X = 0.2$: T

(c) $X = 0.5$: T

(d) $X = 0.2$: C

(e) $X = 0.5$: C

Figure 5.33: Horizontal velocity $\frac{u}{U_{ref}}$, temperature $\frac{T-T_{ref}}{T_h-T_c}$ and concentration $\frac{C-C_{ref}}{C_h-C_l}$ profiles along different X-crosslines in the median plane ($Y = 0.5$): opposing case, $N = -1$.

Introducing gas radiation dramatically changes the thermal field, due to the appearance of convective motions. In the lower part of the cavity ($Z = 0.1$), near the obstacle (figure 5.32 d), the temperature is reduced as the opacity increases (5.33 b). Indeed, although the mass driven flow is slightly accelerated (which can brings more fluid at high temperature from the obstacle to the cavity walls), the radiative emission always dominates over absorption. This effect becomes stronger with the optical thickness (see figures 5.34 a, 5.35 a, 5.36 a, 5.37 a and 5.38 a for negative values of radiative source term). It explains the cooling down of the medium. However, at intermediate and high levels (figure 5.32 e,f), an opposite trend is observed. The temperature augments as the fluid opacities varies from 0.1 to 1 (even though when compared to the transparent case, it is still decreased for all considered τ). This change is more obvious inside the plume. There, the fluid absorbs more than it emits (see figures 5.34 b, 5.35 b, 5.36 b and 5.37 b), in addition, the plume is spread up. These two processes warm up the medium. However, at $\tau = 2$, this tendency is reversed. At $Z = 0.8$, temperature is decreased compared to the solution at $\tau = 1$ (see figure 5.32 f). This is due to the damping of the plume motion. At $Z = 0.5$, thermal level is almost risen up except a drop off in the center. Here, the typical upward circulation brings more hot fluid toward side walls but the amount sent to the center of the enclosure is cut down(see figures 5.31 f and 5.32 b).

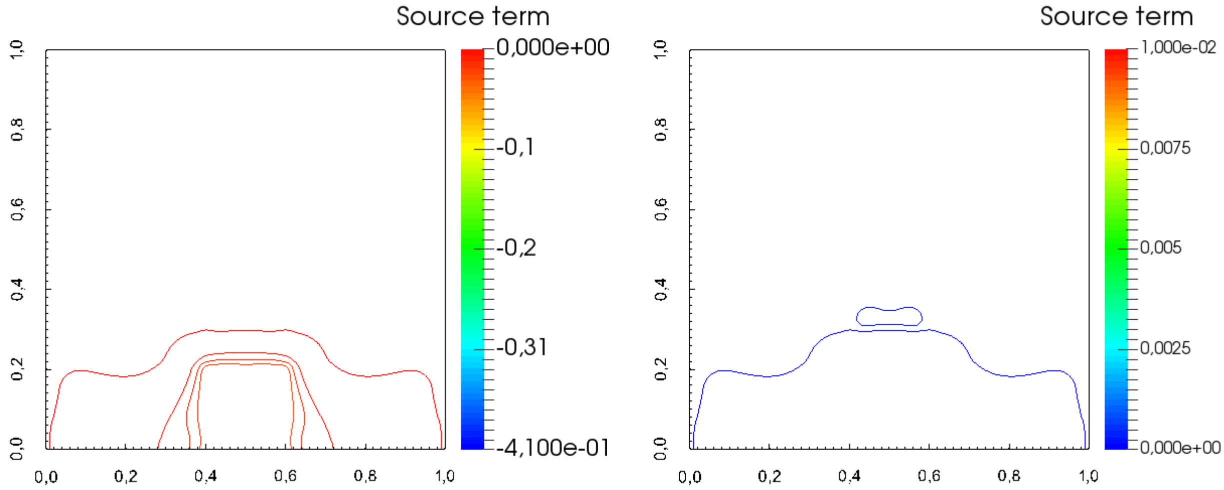

(a) Emission dominates **(b)** Absorption dominates

Figure 5.34: Distribution of radiative source term in the median plane ($Y = 0.5$): opposing case, $N = -1$, $\tau = 0.1$. Sources are normalized by $4\sigma T_{ref}^4/L$.

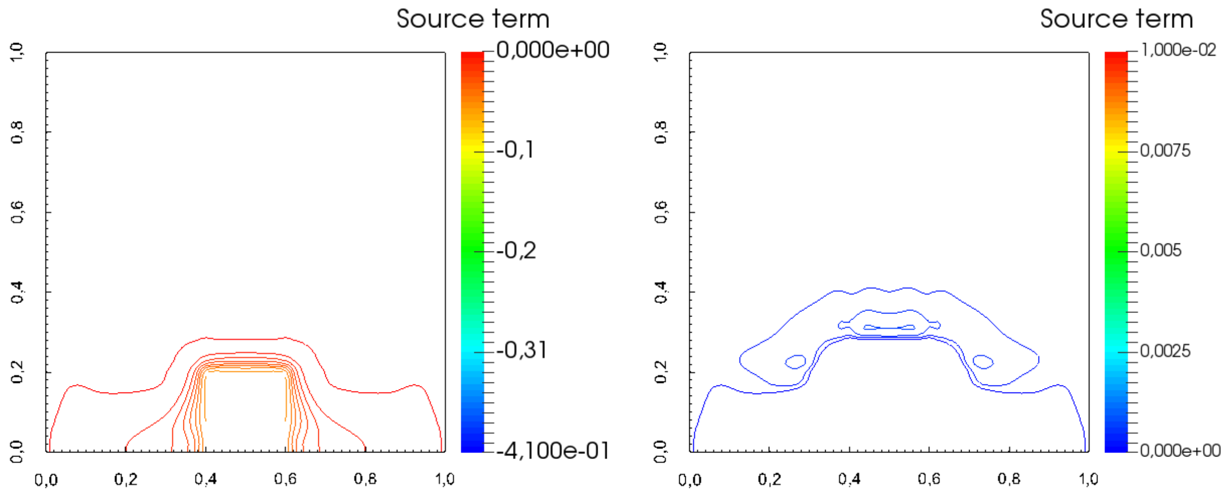

(a) Emission dominates **(b)** Absorption dominates

Figure 5.35: Distribution of radiative source term in the median plane ($Y = 0.5$): opposing case, $N = -1$, $\tau = 0.2$. Sources are normalized by $4\sigma T_{ref}^4/L$.

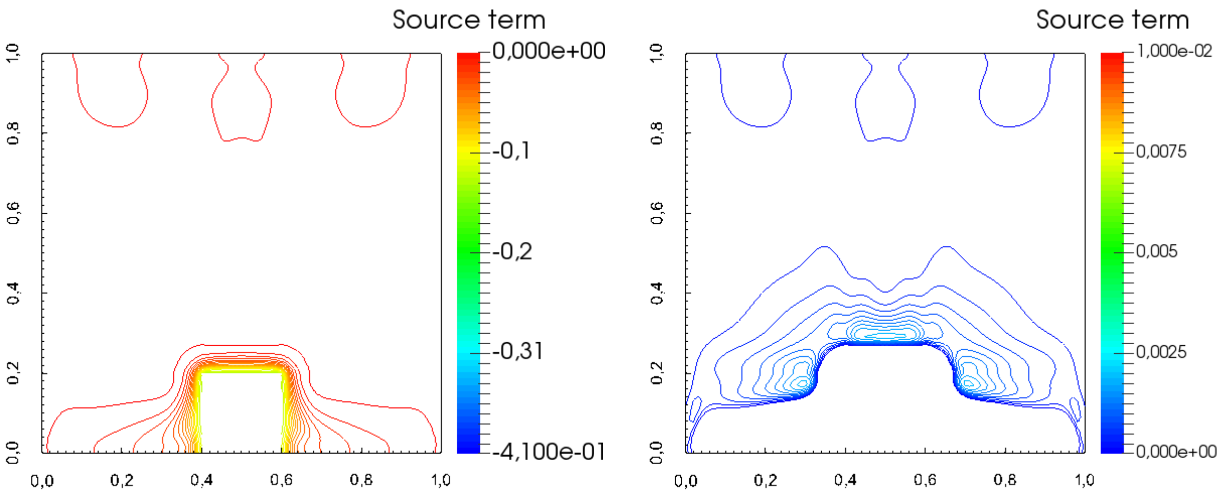

(a) Emission dominates **(b)** Absorption dominates

Figure 5.36: Distribution of radiative source term in the median plane ($Y = 0.5$): opposing case, $N = -1$, $\tau = 0.5$. Sources are normalized by $4\sigma T_{ref}^4/L$.

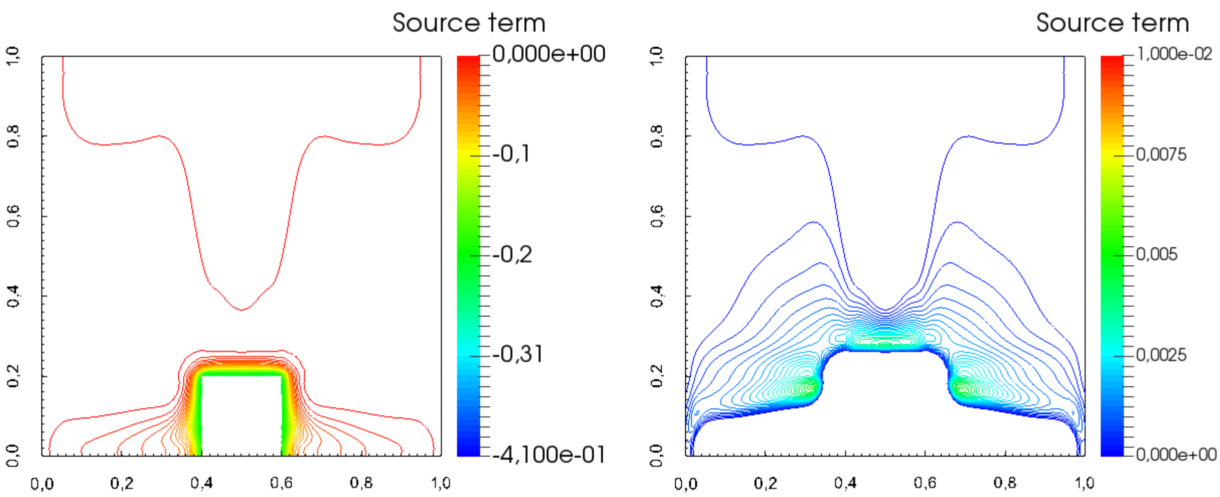

(a) Emission dominates **(b)** Absorption dominates

Figure 5.37: Distribution of radiative source term in the median plane ($Y = 0.5$): opposing case, $N = -1$, $\tau = 1$. Sources are normalized by $4\sigma T_{ref}^4/L$.

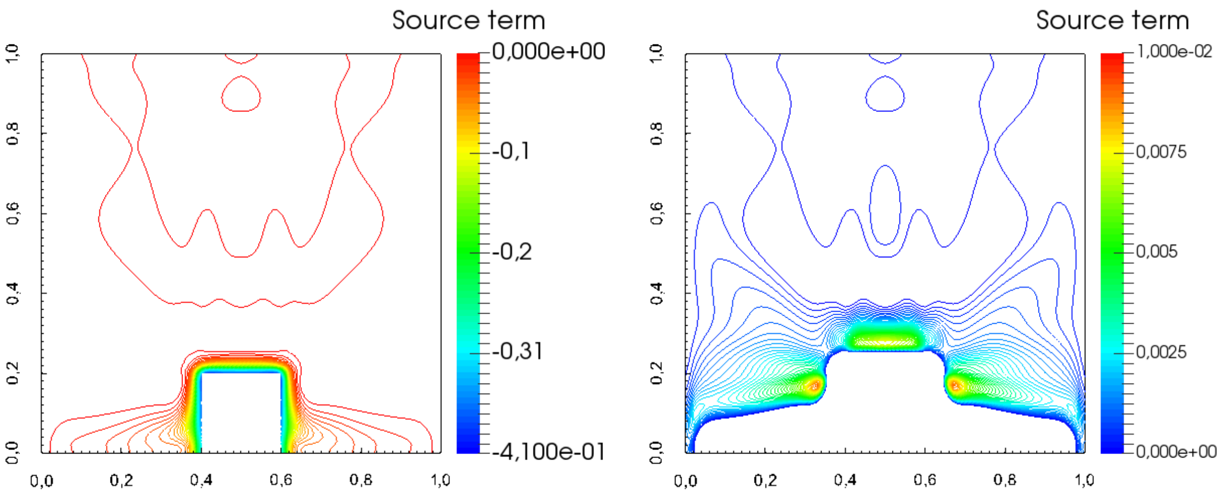

(a) Emission dominates

(b) Absorption dominates

Figure 5.38: Distribution of radiative source term in the median plane ($Y = 0.5$): opposing case, $N = -1$, $\tau = 2$. Sources are normalized by $4\sigma T_{ref}^4/L$.

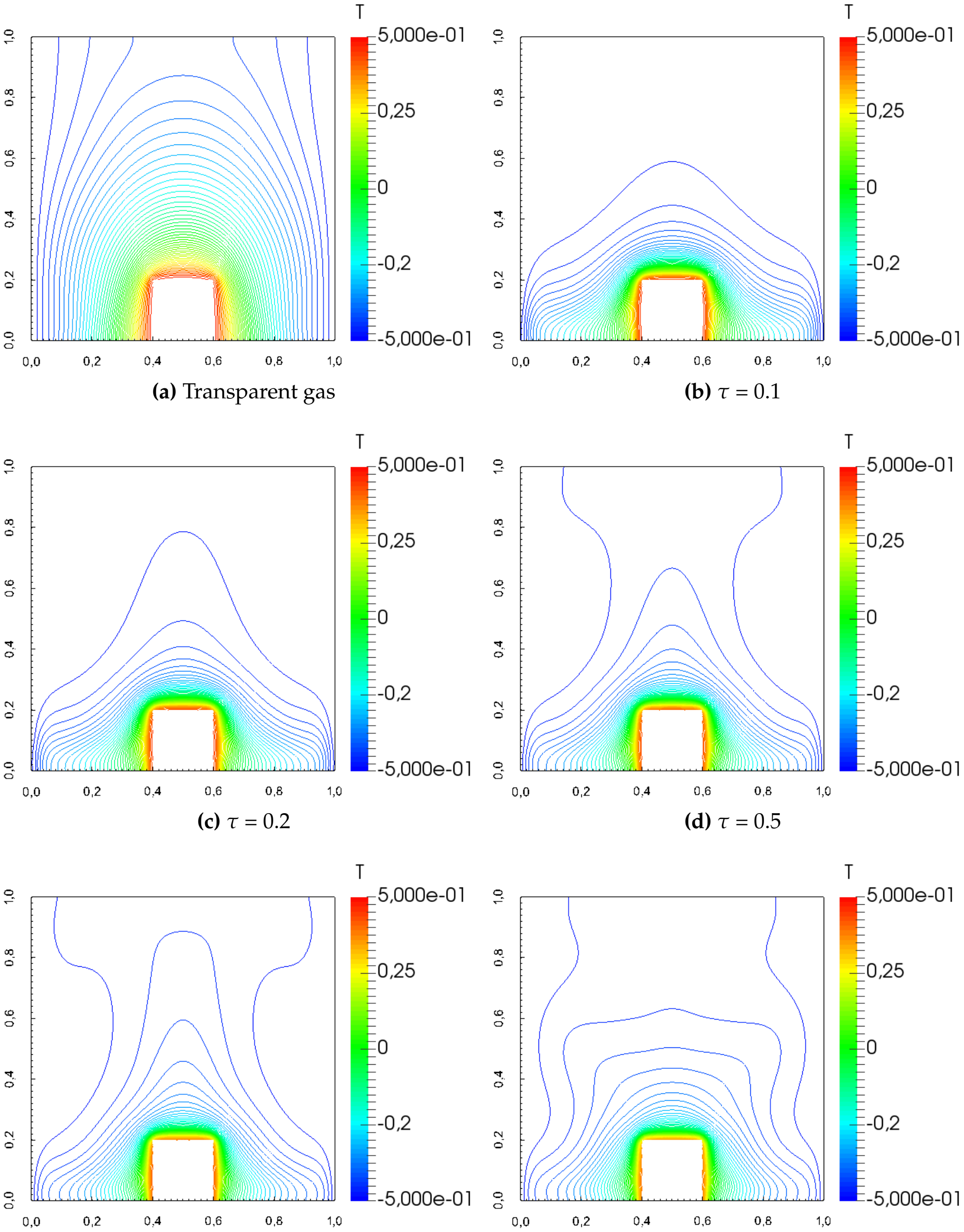

(a) Transparent gas

(b) $\tau = 0.1$

(c) $\tau = 0.2$

(d) $\tau = 0.5$

(e) $\tau = 1$

(f) $\tau = 2$

Figure 5.39: Thermal field $\frac{T-T_{ref}}{T_h-T_c}$ in the median plane ($Y = 0.5$) for different fluid opacities: opposing case, $N = -1$.

The evolution of concentration field displays the same trends as for temperature except at the bottom of the cavity near the vertical cold walls. Here the values of C increase compared to the transparent case (see figures 5.32 g and 5.33 d). This is due to the acceleration of the mass driven flow, which inputs more highly concentrated fluid from the obstacle surfaces (see figure 5.33 a).

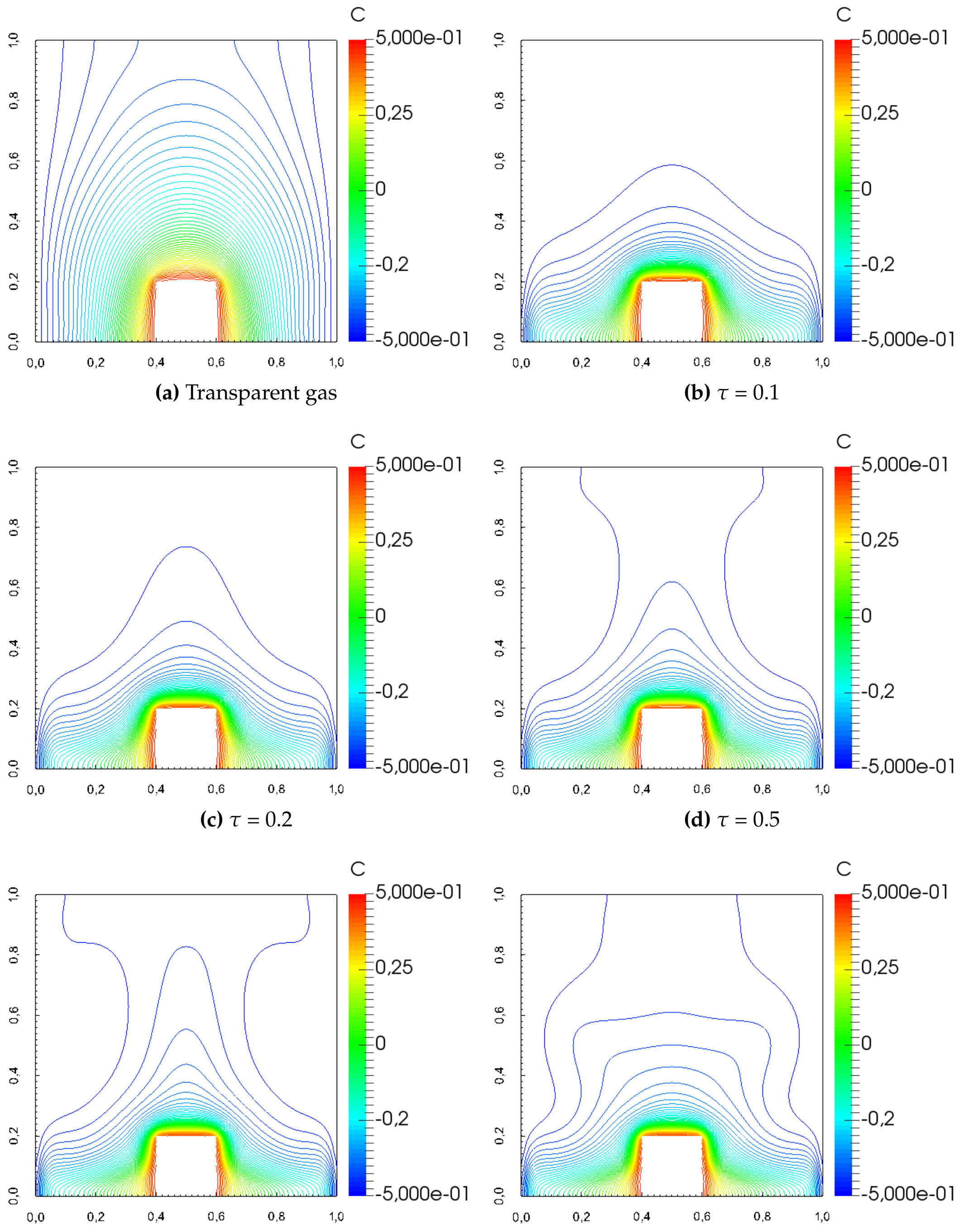

(a) Transparent gas **(b)** $\tau = 0.1$ **(c)** $\tau = 0.2$ **(d)** $\tau = 0.5$ **(e)** $\tau = 1$ **(f)** $\tau = 2$

Figure 5.40: Distribution of concentration $\frac{C-C_{ref}}{C_h-C_l}$ in the median plane ($Y = 0.5$) for different fluid opacities: opposing case, $N = -1$.

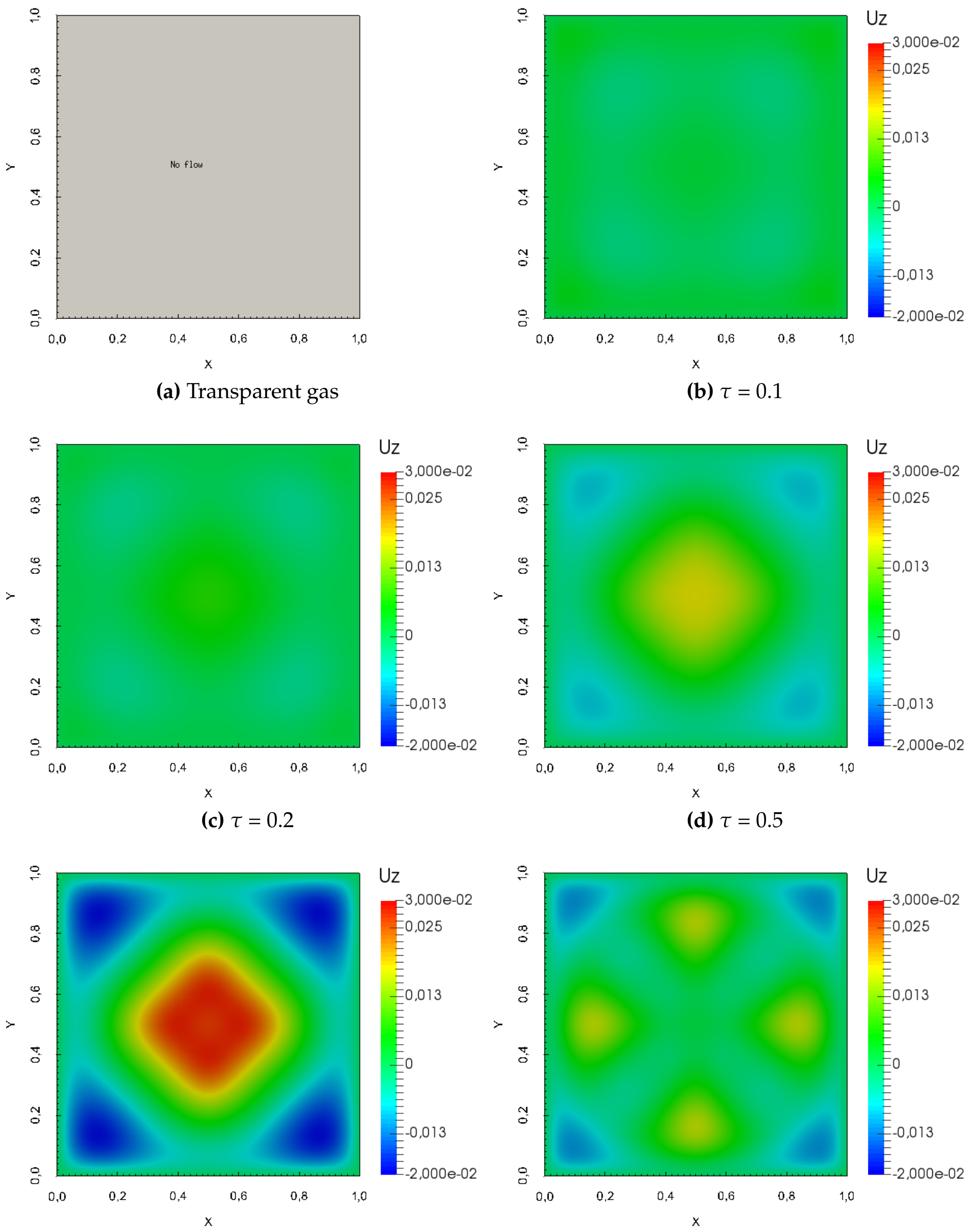

(a) Transparent gas **(b)** $\tau = 0.1$

(c) $\tau = 0.2$ **(d)** $\tau = 0.5$

(e) $\tau = 1$ **(f)** $\tau = 2$

Figure 5.41: Vertical velocities $\frac{w}{U_{ref}}$ across the mid-height plane ($Z = 0.5$) for different fluid opacities: opposing case, $N = -1$.

Figure 5.41 displays the vertical velocity distribution across the mid-height horizontal plane ($Z = 0.5$). It more clearly illustrate the flow structure, and especially the redistribution of the vertical movements that ensures the mass conservation. Close to its origin, the plume displays a quasi square cross section but turned by 45° with respect to the obstacle geometry. This pattern is generated by the fluid input due to the ascending boundary layers along the obstacle verticle surfaces and by the interactions with recirculation flows in the corners of the cavtiy.

The flow structure is also illustrated when considering the Q-criterion (see figure 5.42). New iso-surfaces of $Q = 0.002$ (for instance) appear and are transformed as the medium becomes more absorbing.

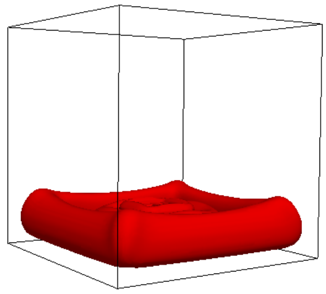

(a) $\tau = 0.1$

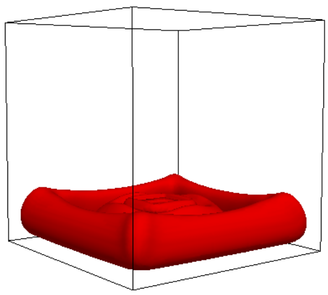

(b) $\tau = 0.2$

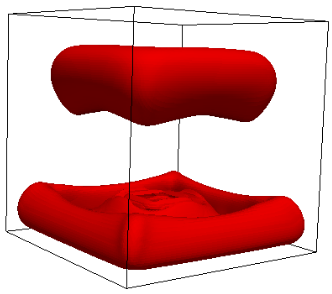

(c) $\tau = 0.5$

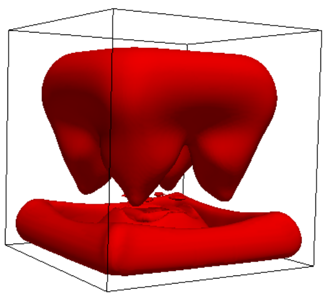

(d) $\tau = 1$

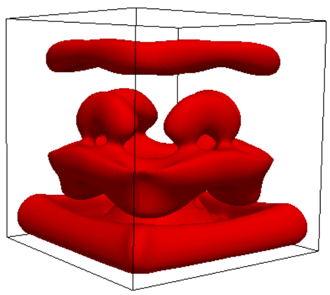

(e) $\tau = 2$

Figure 5.42: Iso-surface of the Q-criterion at the value 0.002 in the cavity for different fluid opacities: opposing case, $N = -1$. Values are normalized by U_{ref}^2/L^2.

5.1.4 Mass-to-Thermal Buoyancy ratio $N = -2$

In this section, we assume that $N = -2$. We therefore consider the case where the mass driven force dominates over the thermal one ($|N| > 1$). These two forces still act in opposite directions ($N < 0$).

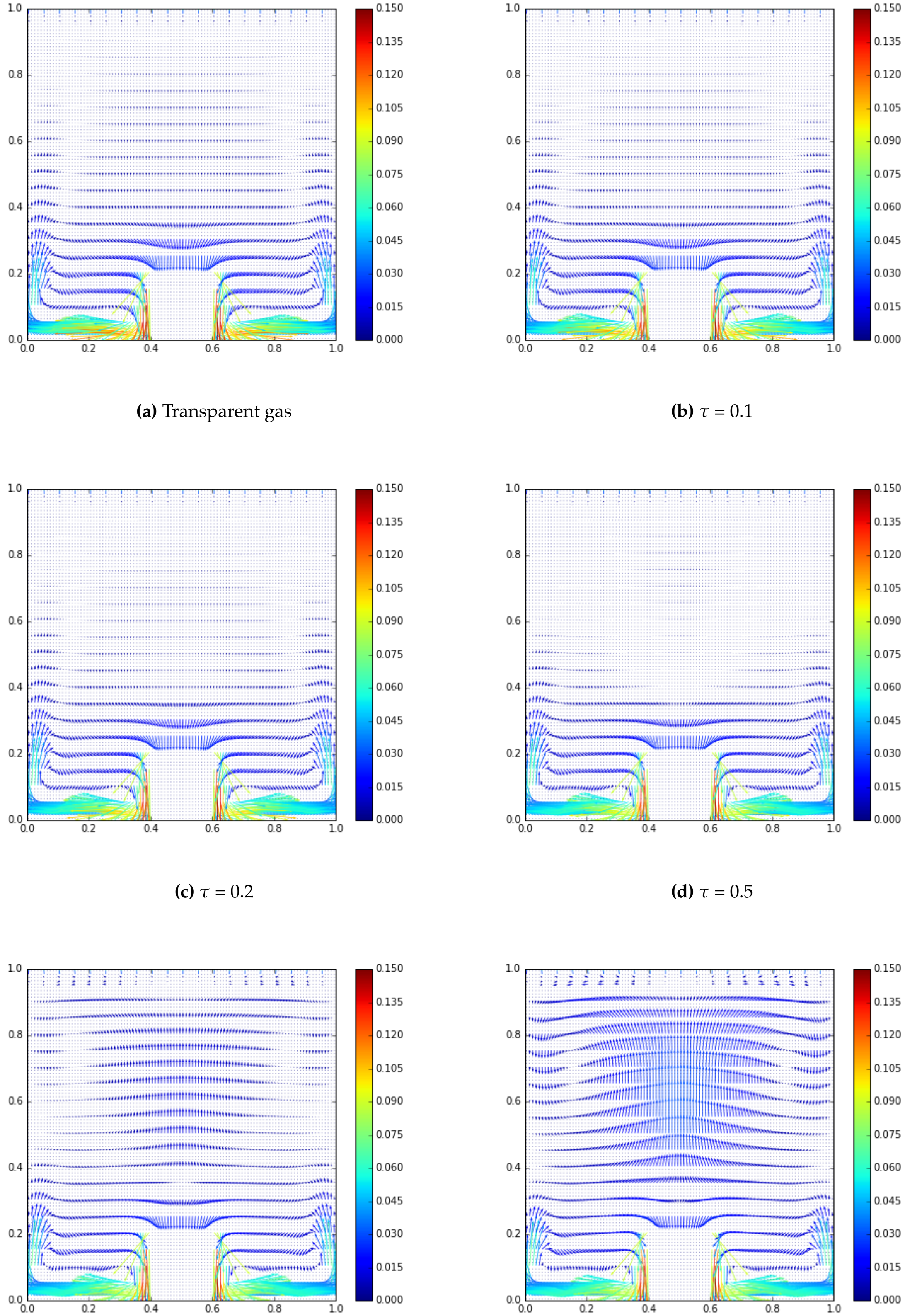

(a) Transparent gas

(b) $\tau = 0.1$

(c) $\tau = 0.2$

(d) $\tau = 0.5$

(e) $\tau = 1$

(f) $\tau = 2$

Figure 5.43: Velocity vectors in the median plane ($Y = 0.5$) for different fluid opacities: opposing case, $N = -2$. Velocities are normalized by U_{ref}.

When the medium is transparent (see figure 5.43 a), the convective motion is fully driven by the concentration gradient. Near the hot obstacle, the fluid at high concentration is heavier and, therefore, flows downward. Close to the cavity vertical walls, the cold fluid at low concentration is pushed upward because the opposite trend induced by temperature is too weak. These two motions create a global clockwise circulation in the left part of the enclosure (and counterclockwise in the right). As the opacity increases up to $\tau = 0.5$, the flow structure changes. In higher parts of the cavity ($Z = 0.8$), for τ between 0.1 and 0.2, the dynamic structure is preserved (ascending boundary layers near the vertical walls and descending flow in the center) except a slight slow down (see figure 5.44 c). From $\tau = 0.5$, the fluid motion is increasingly dominated by the thermal gradient. And at $\tau = 1; 2$, we clearly observe an ascending plume in the center and the descending movements near the cavity lateral walls. These two motions interfere and create a shear flow pattern. It can also be noted an acceleration of the fluid circulation near the ceiling (see figure 5.45 a). At $Z = 0.5$, the tendency is the same as at $Z = 0.8$ except that, at $\tau = 1$, in the region close to the cold walls, there are upward motions instead of downward flows (see figure 5.44 b). This can be explained by the formation of new thermally driven flows above the obstacle. However, in the lower part of the cavity, there is no significant change except a slight slow down of the fluid near the bottom of the enclosure (see figure 5.45 a). The flow, in this region, is governed by the mass gradient for all the considered optical thicknesses.

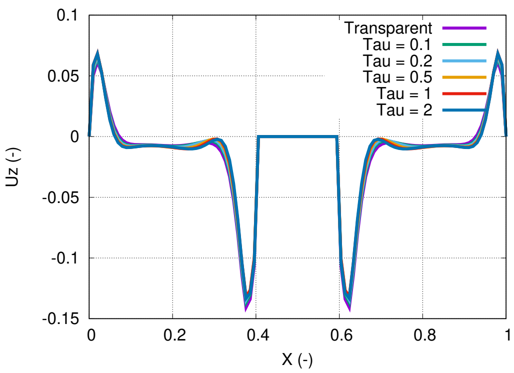

(a) $Z = 0.1$

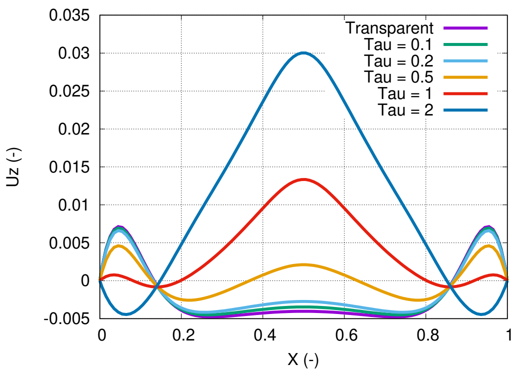

(b) $Z = 0.5$

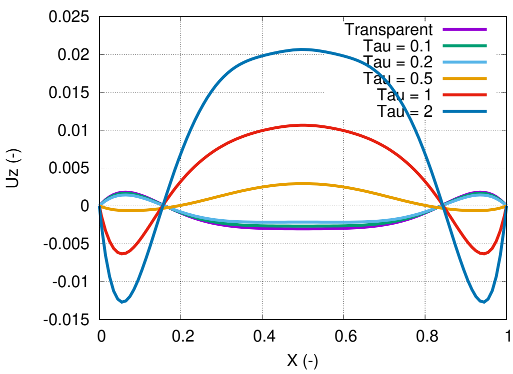

(c) $Z = 0.8$

Figure 5.44: Vertical velocity $\frac{w}{U_{ref}}$ profiles along different Z-crosslines in the median plane ($Y = 0.5$): opposing case, $N = -2$.

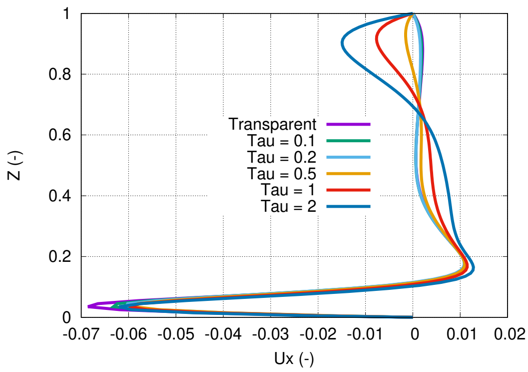

(a) $X = 0.2$

Figure 5.45: Horizontal velocity $\frac{u}{U_{ref}}$ profiles along different X-crosslines in the median plane ($Y = 0.5$): opposing case, $N = -2$.

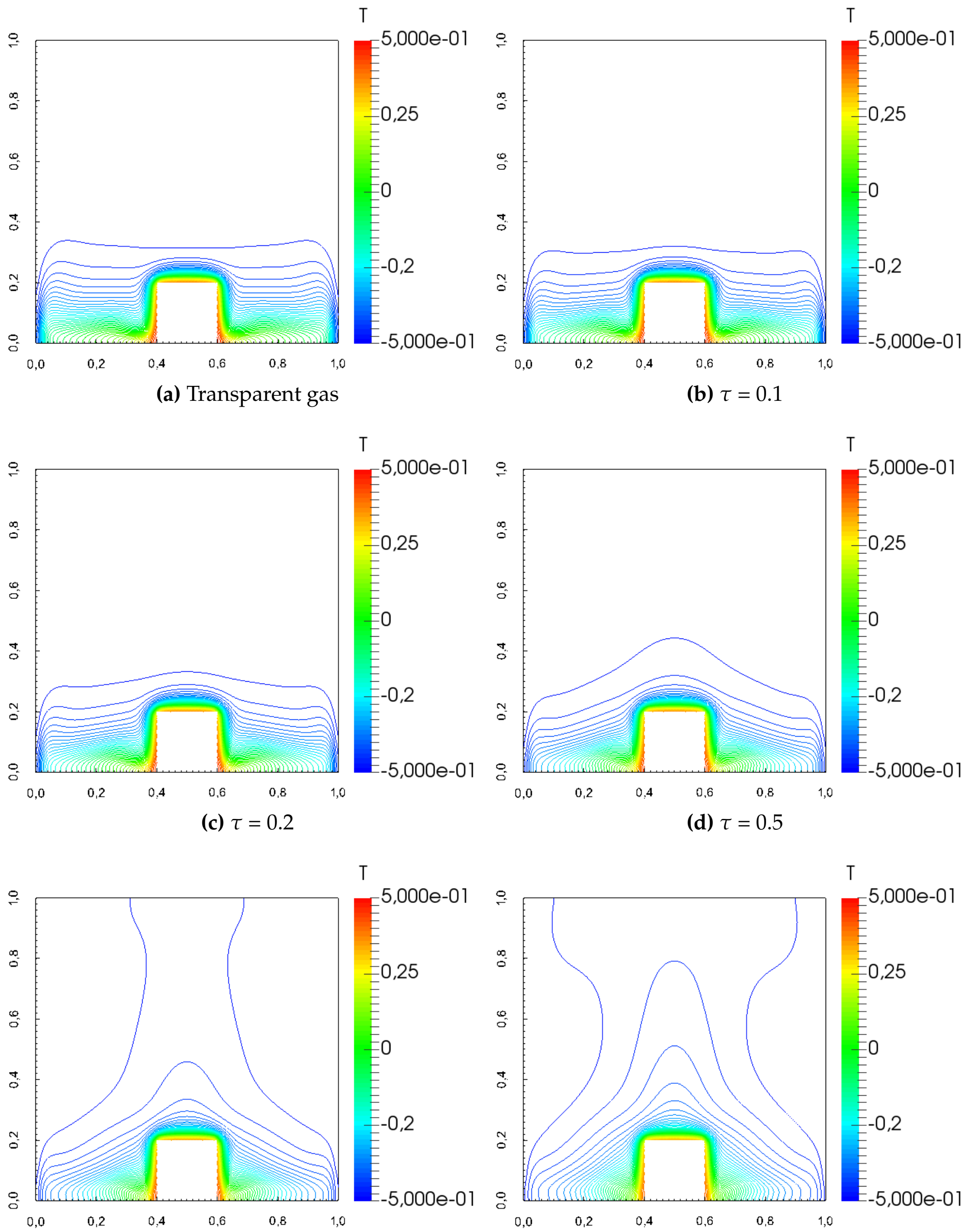

(a) Transparent gas

(b) $\tau = 0.1$

(c) $\tau = 0.2$

(d) $\tau = 0.5$

(e) $\tau = 1$

(f) $\tau = 2$

Figure 5.46: Thermal field $\frac{T-T_{ref}}{T_h-T_c}$ in the median plane ($Y = 0.5$) for different fluid opacities: opposing case, $N = -2$.

As the medium opacity increases, the transformations of the thermal patterns from nearly horizontal lines to inclined and vertical ones are clearly displayed and still denote the development of a thermal plume inside the cavity (see figure 5.46). In addition, the temperature profiles at different positions show that, at low level ($Z = 0.1$), the medium is less homogeneous in temperature: the fluid is more cooled down near the cavity walls and more warmed up around the obstacle (see figure 5.47 a). The fluid at intermediate and high altitude ($Z = 0.5; 0.8$) also gets warmer with the increase of the opacity (see figures 5.47 b,c). On the other hand, radiation has little effect in the upper part of the cavity (see figures 5.49-5.53). However, at intermediate altitude, the radiative absorption dominates over the emission with the increase of the optical thickness (see figures 5.49 b-5.53 b): here, the fluid is warmed up (see figure 5.48 b for positive radiative source term). This increases the thermal gradient, which counters, then dominates over the concentration gradient and, finally, generates the thermal plume. This flow brings the fluid at high temperature to the layers near the ceiling and the vertical walls of the enclosure, which explain the increase of thermal level in these regions.

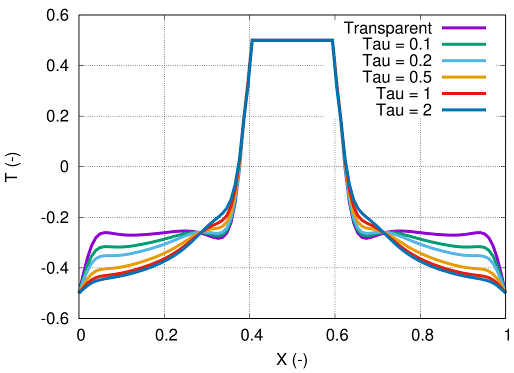

(a) $Z = 0.1$

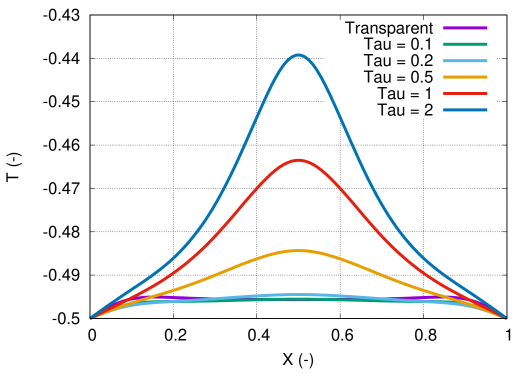

(b) $Z = 0.5$

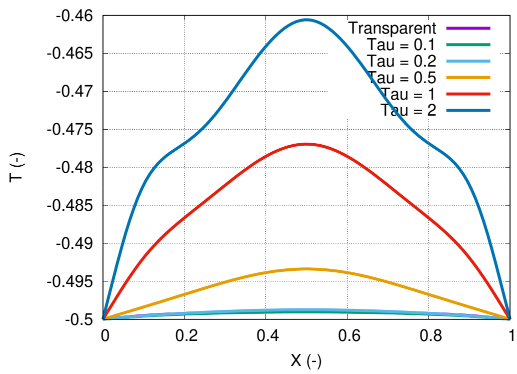

(c) $Z = 0.8$

Figure 5.47: Temperature $\frac{T-T_{ref}}{T_h-T_c}$ profiles along different Z-crosslines in the median plane ($Y = 0.5$): opposing case, $N = -2$.

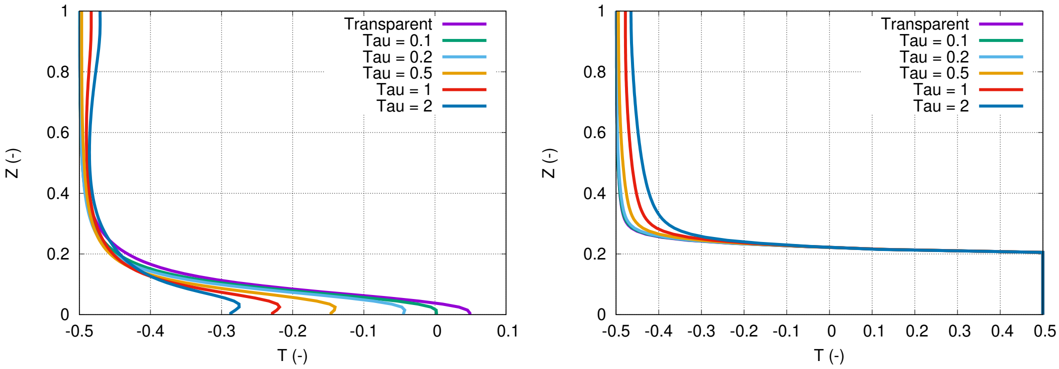

(a) $X = 0.2$ **(b)** $X = 0.5$

Figure 5.48: Temperature $\frac{T-T_{ref}}{T_h-T_c}$ profiles along different X-crosslines in the median plane ($Y = 0.5$): opposing flow, $N = -2$.

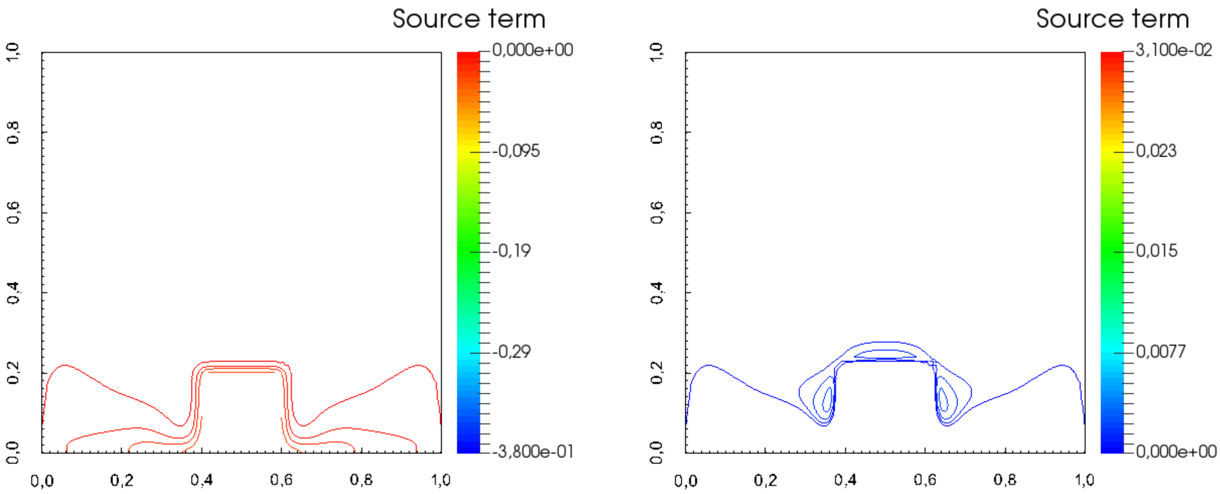

(a) Emission dominates **(b)** Absorption dominates

Figure 5.49: Distribution of radiative source term in the median plane ($Y = 0.5$): opposing case, $N = -2$, $\tau = 0.1$. Sources are normalized by $4\sigma T_{ref}^4/L$.

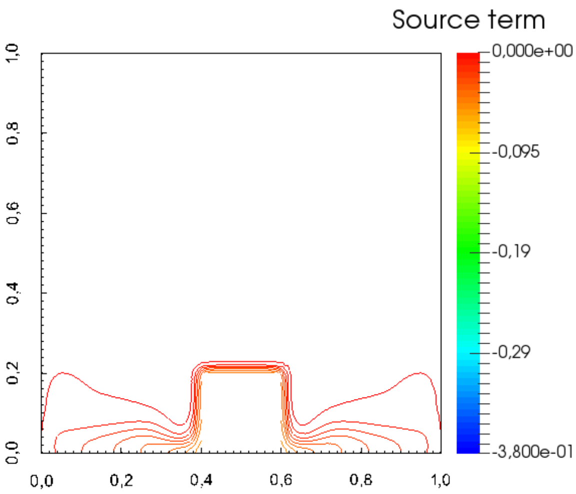

(a) Emission dominates

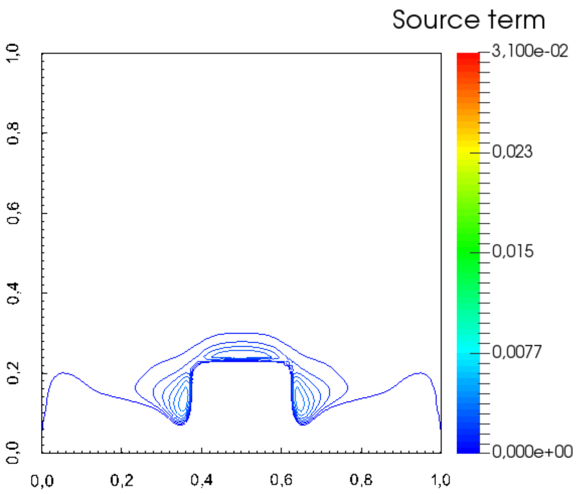

(b) Absorption dominates

Figure 5.50: Distribution of radiative source term in the median plane ($Y = 0.5$): opposing case, $N = -2$, $\tau = 0.2$. Sources are normalized by $4\sigma T_{ref}^4/L$.

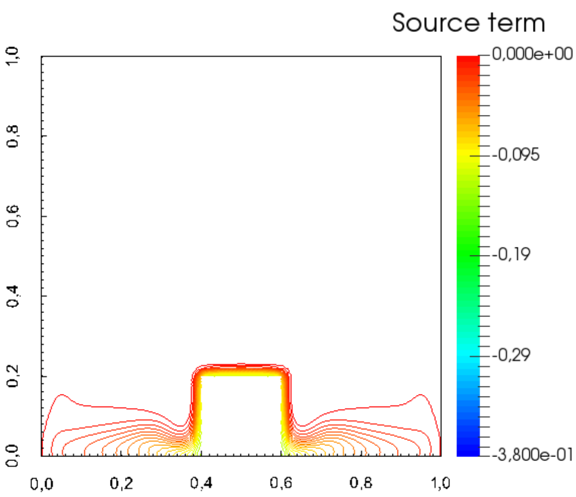

(a) Emission dominates

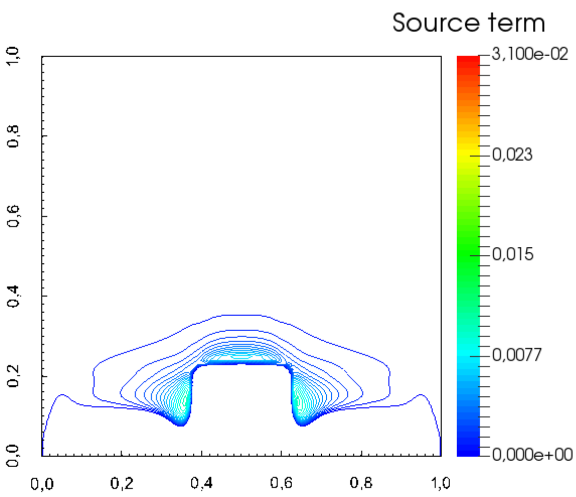

(b) Absorption dominates

Figure 5.51: Distribution of radiative source in the median plane ($Y = 0.5$): opposing case, $N = -2$, $\tau = 0.5$. Sources are normalized by $4\sigma T_{ref}^4/L$.

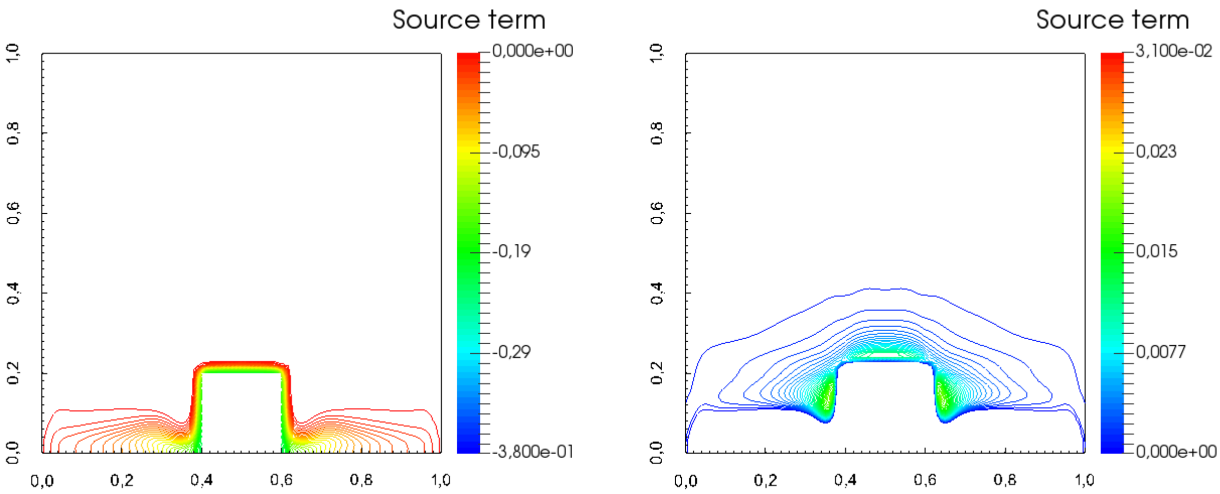

(a) Emission dominates **(b)** Absorption dominates

Figure 5.52: Distribution of radiative source term in the median plane ($Y = 0.5$): opposing case, $N = -2$, $\tau = 1$. Sources are normalized by $4\sigma T_{ref}^4/L$.

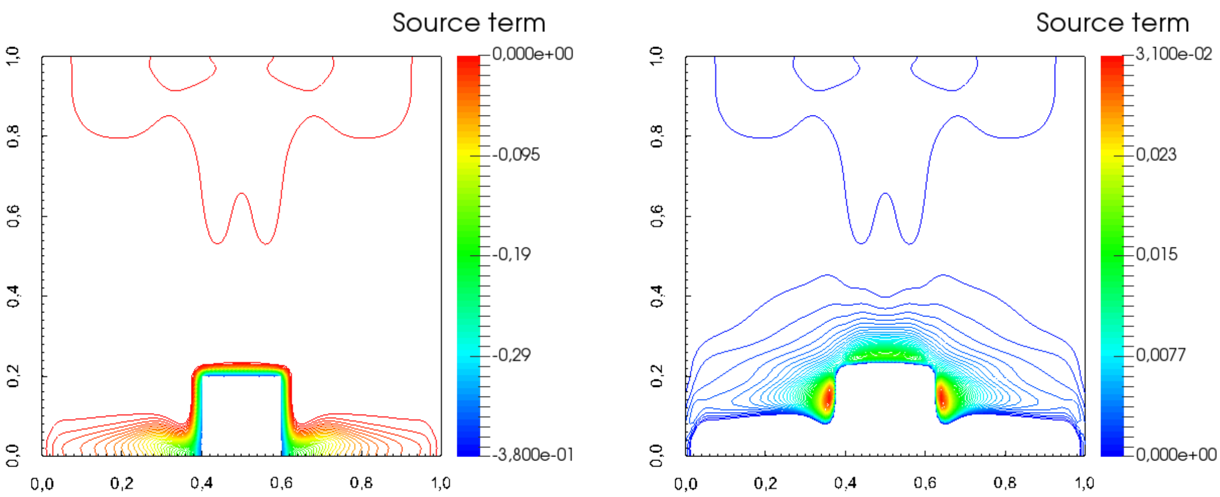

(a) Emission dominates **(b)** Absorption dominates

Figure 5.53: Distribution of radiative source term in the median plane ($Y = 0.5$): opposing case, $N = -2$, $\tau = 2$. Sources are normalized by $4\sigma T_{ref}^4/L$.

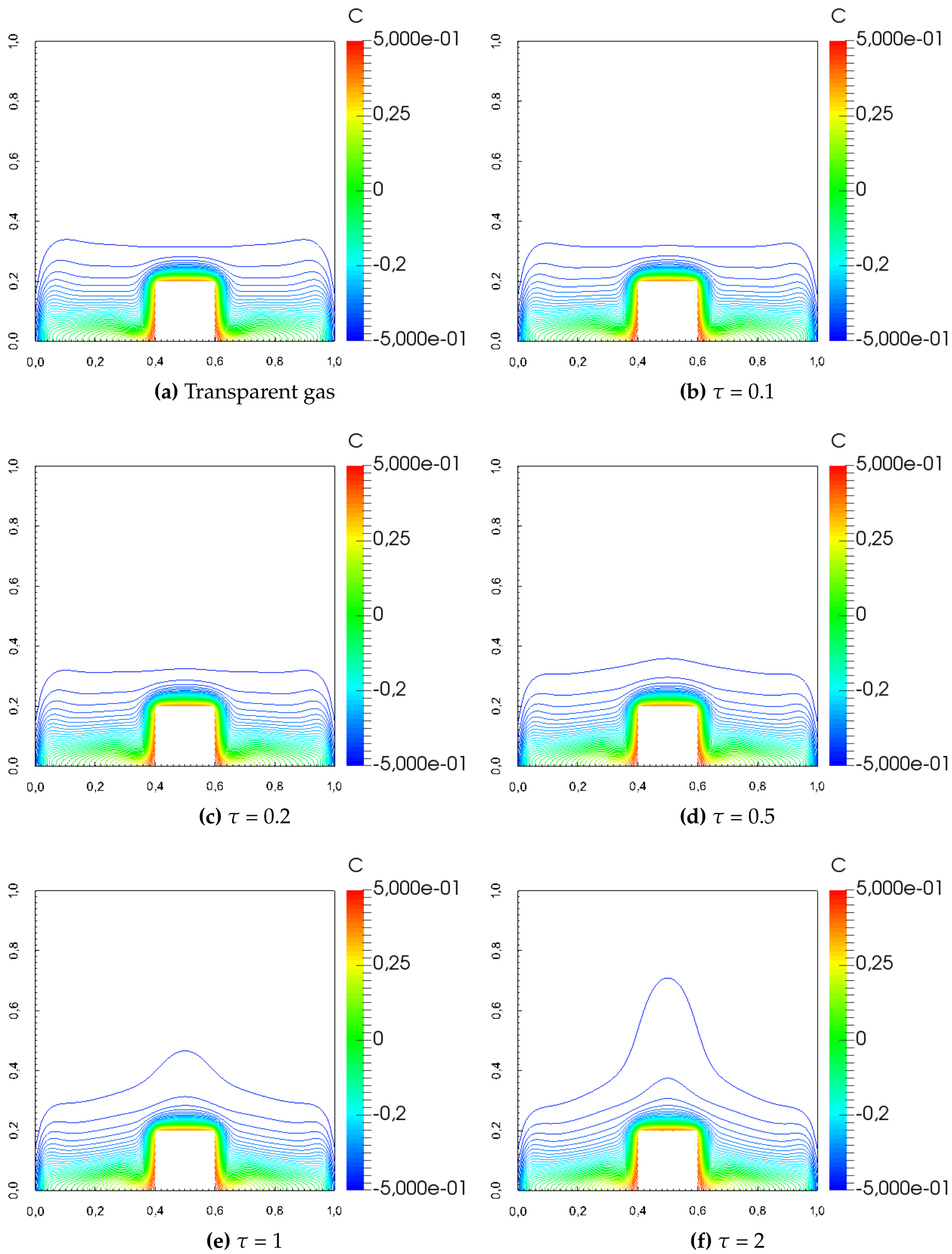

(a) Transparent gas **(b)** $\tau = 0.1$

(c) $\tau = 0.2$ **(d)** $\tau = 0.5$

(e) $\tau = 1$ **(f)** $\tau = 2$

Figure 5.54: Concentration $\frac{C - C_{ref}}{C_h - C_l}$ field in the median plane ($Y = 0.5$) for different fluid opacities, $N = -2$.

There are no significant changes in the concentration field as the optical thickness remains below $\tau = 0.5$ (see figures 5.54 and 5.55). At low level ($Z = 0.1$) the concentration increases near the obstacle surfaces and decreases near the vertical walls (see figure 5.55 a). This alteration is strengthened with the increases in opacity. However, an opposite trend is observed in the upper half of the cavity: the concentration is augmented near the cold surfaces as the medium becomes more absorbing (see figure 5.55 b,c). These changes come from the transformation in the flow structure.

Indeed, the thermally driven flow brings more fluid at high concentration from the region above the obstacle upward. Besides, the slow down of the fluid motion along the bottom results in a drop of concentration near the vertical walls in the lower half of the enclosure.

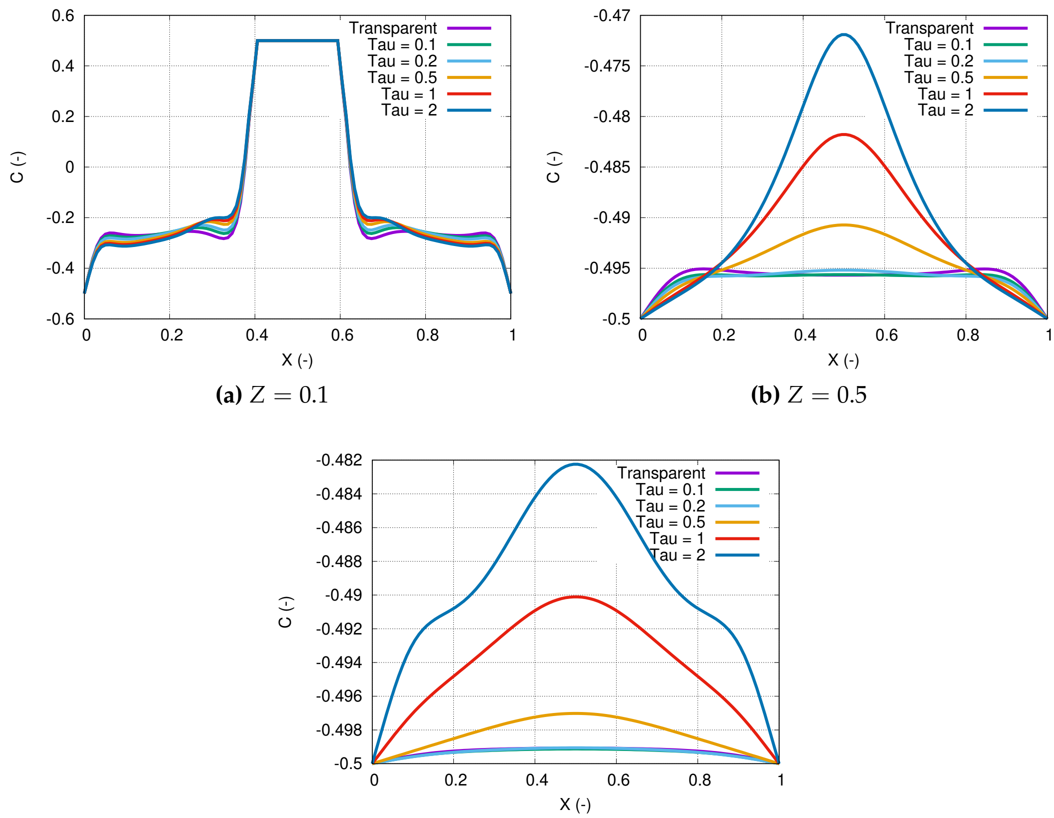

(a) $Z = 0.1$ **(b)** $Z = 0.5$ **(c)** $Z = 0.8$

Figure 5.55: Concentration $\frac{C-C_{ref}}{C_h-C_l}$ profiles along different Z-crosslines in the median plane ($Y = 0.5$): opposing case, $N = -2$.

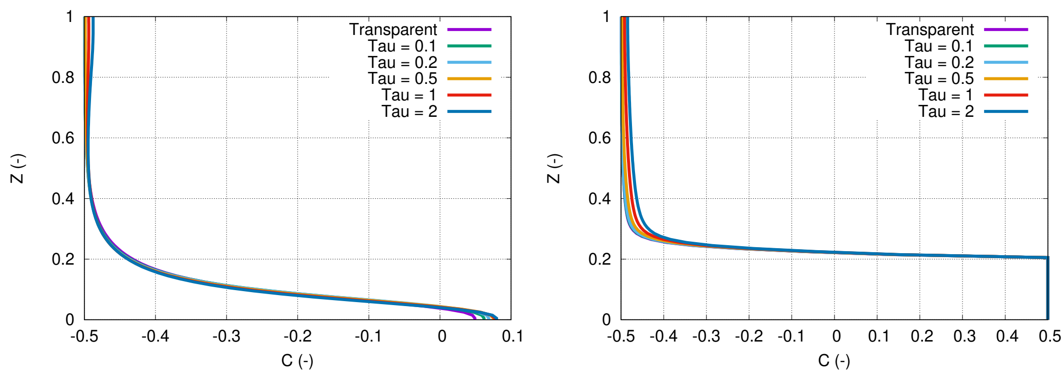

(a) $X = 0.2$ **(b)** $X = 0.5$

Figure 5.56: Concentration $\frac{C-C_{ref}}{C_h-C_l}$ profiles along different X-crosslines in the median plane ($Y = 0.5$): opposing case, $N = -2$.

The alterations in flow structures are also illustrated in figure 5.57, which displays the iso-surfaces of the Q-criterion. The formation and expansion of the new iso-surfaces are easily observed, showing the stronger impact of the radiative effects with the increase of opacity.

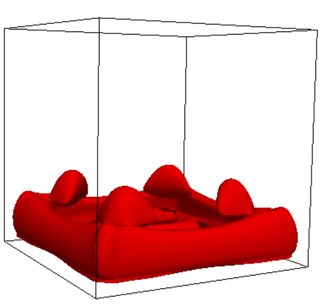

(a) Transparent gas

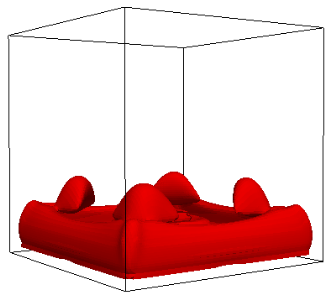

(b) $\tau = 0.1$

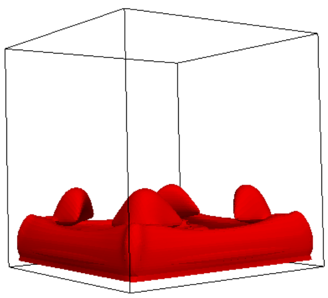

(c) $\tau = 0.2$

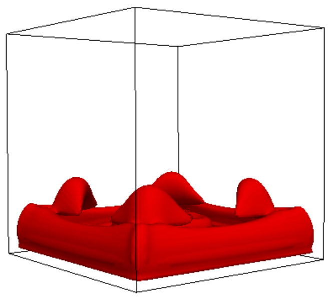

(d) $\tau = 0.5$

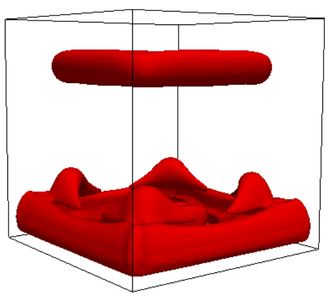

(e) $\tau = 1$

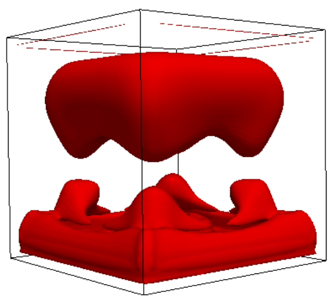

(f) $\tau = 2$

Figure 5.57: Iso-surface of the Q-criterion at the value 0.002 in the cavity for different fluid opacities: opposing case, $N = -2$. VValues are normalized by U_{ref}^2 / L^2.

5.1.5 Synthesis

In this chapter, we analyze the influences of the radiation of a gas mixture on the double diffusive convection, using the gray gas assumption. The calculations were performed at different mass-to-thermal buoyancy ratios ($N = -2; -1; 1; 2$) (which describes the flow characteristics: cooperating or opposing and mass driven or thermally governed) and different values of the optical thickness defined as $\tau = \kappa_0 \times L$ ($\tau = 0.1; 0.2; 0.5; 1; 2$). The comparisons between the obtained results and the reference solutions (transparent case) reveal the transformations inside the enclosure which are summarized as:

- Cooperating flow

  At $N = 1$, introducing gas radiation does not significantly affect the concentration field. It slightly accelerates the boundary layers but reduces the maximum velocity inside the plume. Volume radiation tends to thermally homogenize the medium. It decreases the temperature in the upper half of the cavity and redistributes the iso thermal patterns (from nearly vertical stratification into horizontal one). Increasing the opacity of the medium strengthens these effects.
  At $N = 2$, the same modifications take place but with weaker magnitudes.

- Opposing flow

  At $N = -1$, for a transparent medium, no flow occurs in the cavity due to the perfect symmetry of the thermal and concentration gradients. But with radiation, this balance is broken and new fluid motions are established. The movement in the lower part of the cavity is dominated by the mass gradient for all the considered optical thicknesses but, at medium and high levels, the thermal gradient governs the flow. For τ between 0 and 1, radiation intensifies the thermal plume. However at $\tau = 1$, the increase of concentration in the axis of the plume limits the vertical motion and causes it to spread. At $\tau = 2$, these changes are strengthened, resulting in the plume separation with a zone of nearly motionless fluid in the center of the cavity. In addition, gas radiation reduces the temperature in the regions near the obstacle vertical surfaces. Above the source, temperature is generally reduced compared to transparent case, it increases with the opacity except in the center of the enclosure at $\tau = 2$. The alteration of the concentration field are the same as for the thermal one except a slight increase of this quantity near the vertical cold walls in the lower part of the cavity.

  At $N = -2$, gas radiation affects the dynamic, the thermal and the concentration field in the same manner as for $N = -1$ with the changes in optical thicknesses (in the participating mediums). However, the temperature and concentration fields are reduces at the intermediate and high levels when comparing to the transparent case.

5.2 Real gas mixtures

This section deals with the coupling of double diffusive convection and radiation in real gas mixtures (dry air and an absorbing-emitting component, which can be viewed as a pollutant). The physical properties of the fluid depend on its compositions and are calculated using the expressions detailed in appendix A. In this study, we consider either $air - H_2O$ or $air - CO_2$ mixtures. Depending on the added component, this leads to two types of flow: opposing or cooperating. Water vapor, which is lighter than air, creates a mass driven force acting in the same direction as the thermal one (cooperating case). On the other hand, the $air - CO_2$ mixture yields opposing flows caused by two counter-direction forces as the molar mass of CO_2 is larger than that of dry air. Regarding the boundary conditions, we recall that the cavity vertical walls are maintained at $T_c = 530K$ and $C_l = 0$ while the obstacle surfaces are set to $T_h = 580K$ and a given concentration of pollutant C_h. All the active walls are black and the adiabatic ones are purely reflective.

5.2.1 $Air - H_2O$ mixture

As presented above, this mixture generates a cooperating flow in the cavity. The characteristic non-dimensional numbers related to this configuration are listed in table 5.1. All the values are comparable to those of the gray case (§5.1). However, the Lewis number is now about 0.8 and the mass boundary layers are then expected to be slightly thicker than the thermal ones. The average mole fraction of pollutant (here H_2O) is defined as:

$$x = \frac{C_{ref} * R * T_{ref}}{P} \tag{5.4}$$

where R is universal gas constant and P is the pressure (here 1 atm). We recall that $C_{ref} = \frac{C_h + C_l}{2}$, or, when $C_l = 0$ (as it is assumed here), $C_h/2$.
The x-parameter is given three different values 5%, 10% and 20%. It leads to three different types of flow: temperature driven ($N < 1$), balanced thermal and mass effects ($N \approx 1$) and mass driven ($N > 1$).

x (%)	N	Ra_T	Pr	Le	Pl
5	0.426	$4.663 \cdot 10^6$	0.725	0.833	$4.394 \cdot 10^{-3}$
10	0.87	$4.693 \cdot 10^6$	0.735	0.824	$4.392 \cdot 10^{-3}$
20	1.81	$4.753 \cdot 10^6$	0.755	0.808	$4.389 \cdot 10^{-3}$

Table 5.1: Configuration parameters: $air - H_2O$ mixture.

5.2.1.1 Velocity, thermal and concentration fields

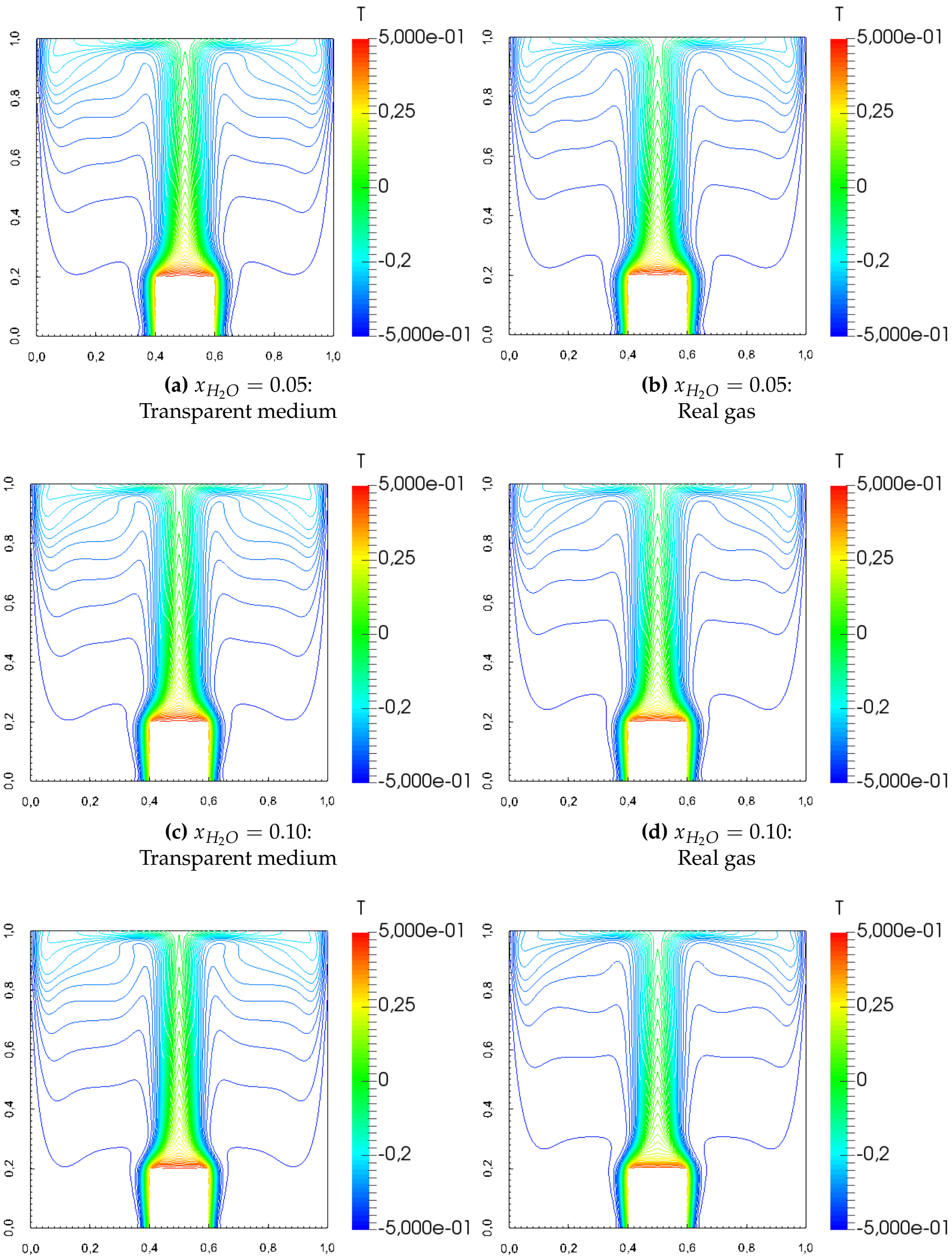

(a) $x_{H_2O} = 0.05$: Transparent medium

(b) $x_{H_2O} = 0.05$: Real gas

(c) $x_{H_2O} = 0.10$: Transparent medium

(d) $x_{H_2O} = 0.10$: Real gas

(e) $x_{H_2O} = 0.20$: Transparent medium

(f) $x_{H_2O} = 0.20$: Real gas

Figure 5.58: Thermal field $\frac{T-T_{ref}}{T_h-T_c}$ in the median plane of the cavity ($Y = 0.5$) at different mole fractions of water vapor.

Figure 5.58 represents the thermal field in the median plane ($Y = 0.5$) in both cases of transparent and participating media at different average mole fractions of water vapor. Gas radiation does not induce any significant change, except a slight expansion between the iso lines (in the region between the plume and the cold walls) at $x_{H_2O} = 0.20$ (see 5.58 f). This illustrate a slight thermal homogenization of the fluid.

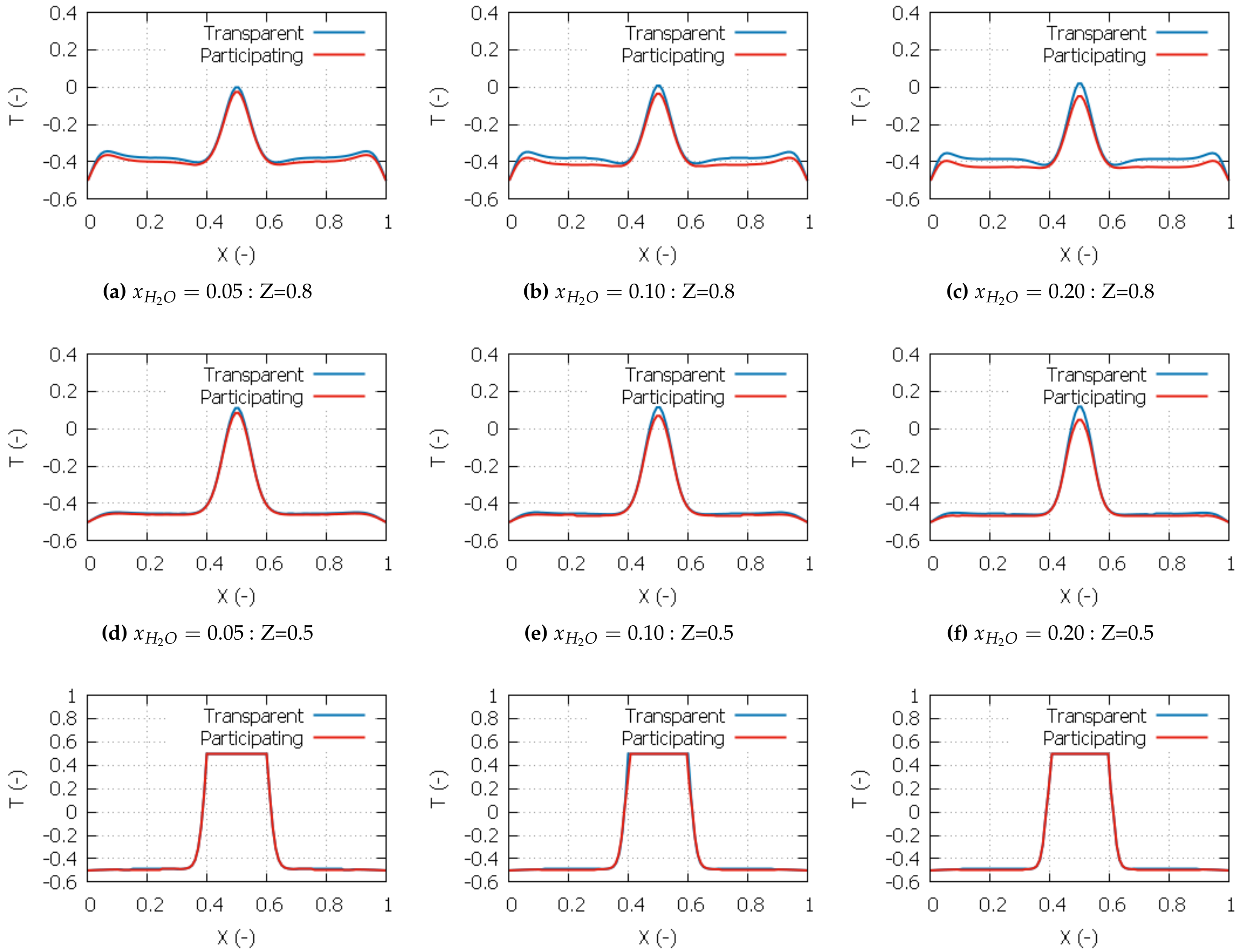

(a) $x_{H_2O} = 0.05$: Z=0.8 **(b)** $x_{H_2O} = 0.10$: Z=0.8 **(c)** $x_{H_2O} = 0.20$: Z=0.8

(d) $x_{H_2O} = 0.05$: Z=0.5 **(e)** $x_{H_2O} = 0.10$: Z=0.5 **(f)** $x_{H_2O} = 0.20$: Z=0.5

(g) $x_{H_2O} = 0.05$: Z=0.1 **(h)** $x_{H_2O} = 0.10$: Z=0.1 **(i)** $x_{H_2O} = 0.20$: Z=0.1

Figure 5.59: Temperature $\frac{T-T_{ref}}{T_h-T_c}$ profiles along different Z-crosslines in the median plane ($Y = 0.5$) at different average mole fractions of water vapor.

The temperature profiles along horizontal and vertical crosslines (see figures 5.59 and 5.60) confirms the above observation. Indeed, at $Z = 0.8$ (figures 5.59 a,b,c), the presence of the radiation decreases the temperature for all the average mole fractions (it explains the thermal homogenization inside the cavity). This evidences the domination of radiative emission in these regions (see figures 5.61 a, 5.61 c and 5.61 e). The plots along vertical lines (see figure 5.60) carries the same information. In the lower half of the enclosure, the thermal structure does not experience any remarkable alterations.

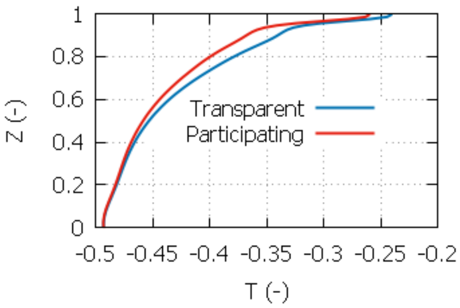

(a) $x_{H_2O} = 0.05$: X=0.2 or 0.8

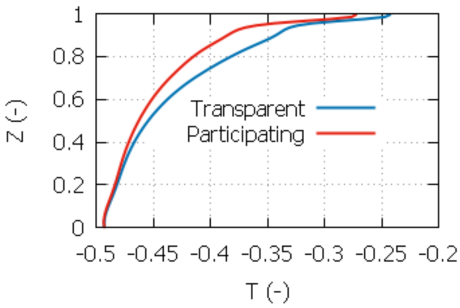

(b) $x_{H_2O} = 0.10$: X=0.2 or 0.8

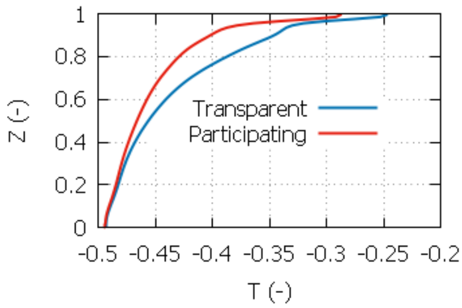

(c) $x_{H_2O} = 0.20$: X=0.2 or 0.8

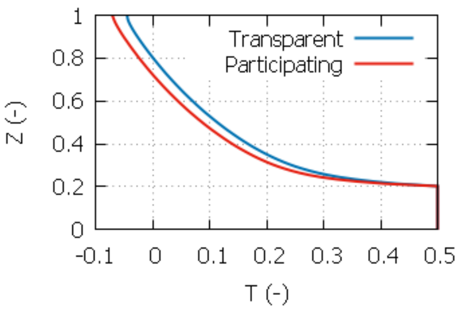

(d) $x_{H_2O} = 0.05$: X=0.5

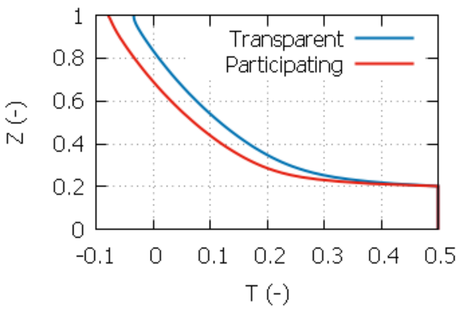

(e) $x_{H_2O} = 0.10$: X=0.5

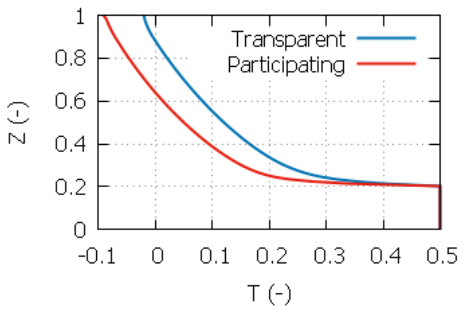

(f) $x_{H_2O} = 0.20$: X=0.5

Figure 5.60: Temperature $\frac{T-T_{ref}}{T_h-T_c}$ profiles along different X-crosslines in the median plane ($Y = 0.5$) at different average mole fractions of water vapor.

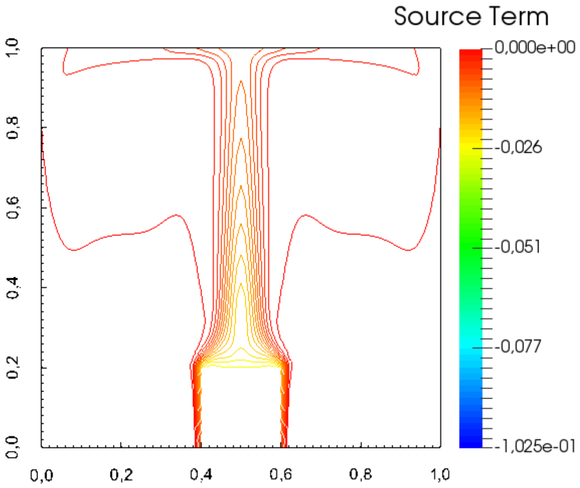

(a) $x_{H_2O} = 0.05$:
Emission dominates

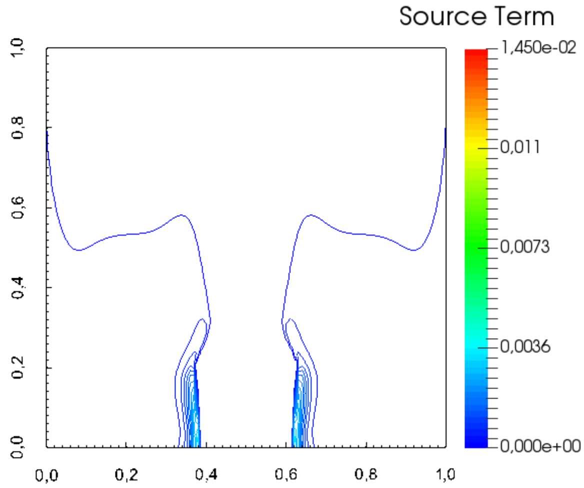

(b) $x_{H_2O} = 0.05$:
Absorption dominates

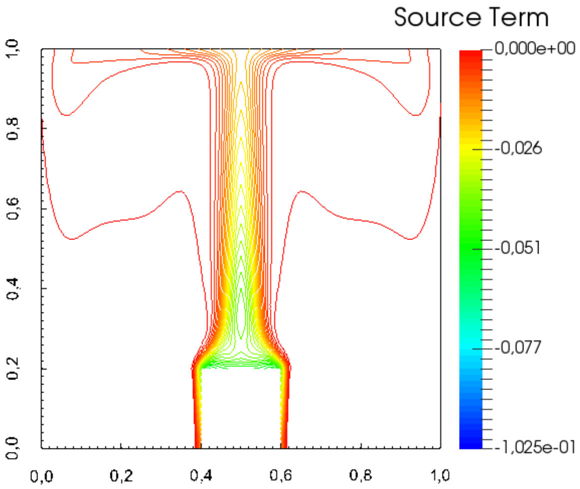

(c) $x_{H_2O} = 0.10$:
Emission dominates

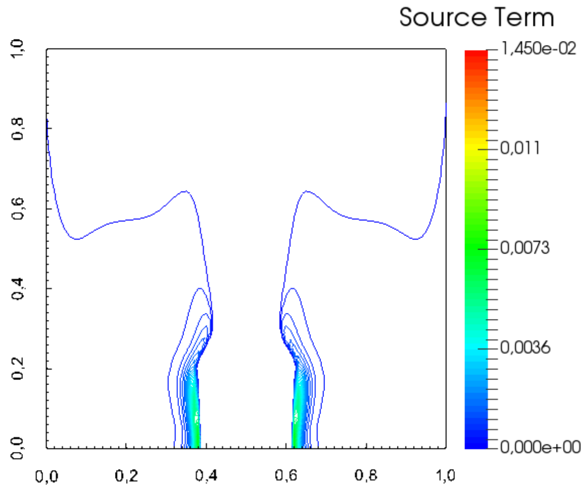

(d) $x_{H_2O} = 0.10$:
Absorption dominates

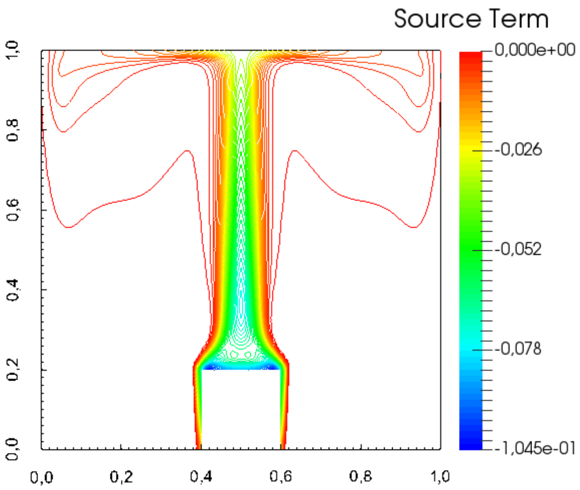

(e) $x_{H_2O} = 0.20$:
Emission dominates

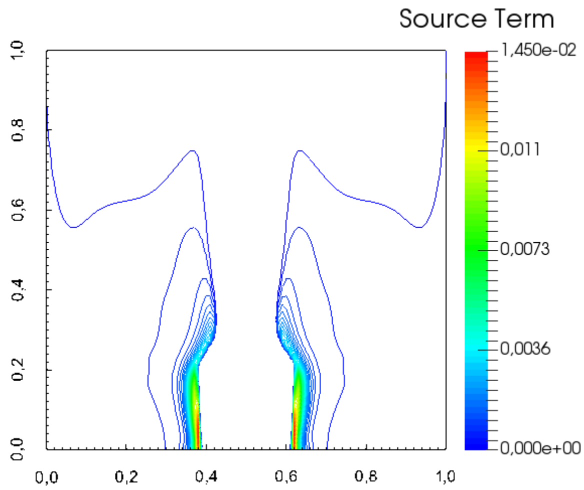

(f) $x_{H_2O} = 0.20$:
Absorption dominates

Figure 5.61: Distribution of radiative source term in the median plane ($Y = 0.5$) at different mole fractions of water vapor. Sources are normalized by $4\sigma T_{ref}^4/L$.

The distribution of the radiative source term (see figure 5.61) shows that radiation affects the fluid in the upper half of the cavity, inside the plume and in a limited region around the hot vertical surfaces. In particular, there is no significant radiative effect near the vertical bounding walls in the lower half of the cavity (which differs from the homogeneous cases). This explains the unchanged thermal distribution in this region.

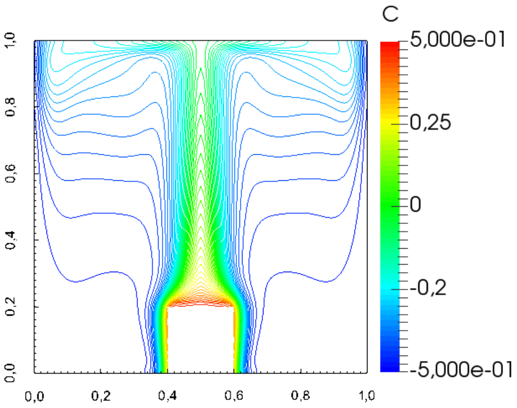

(a) $x_{H_2O} = 0.05$: Transparent medium

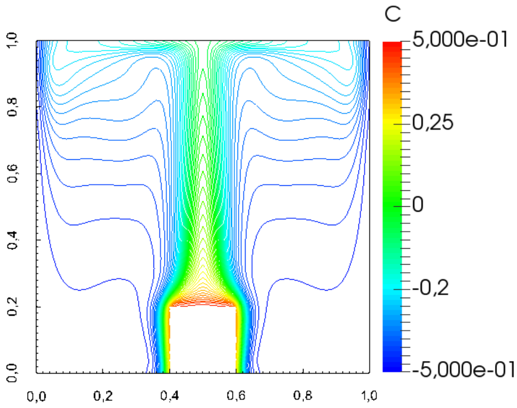

(b) $x_{H_2O} = 0.05$: Real gas

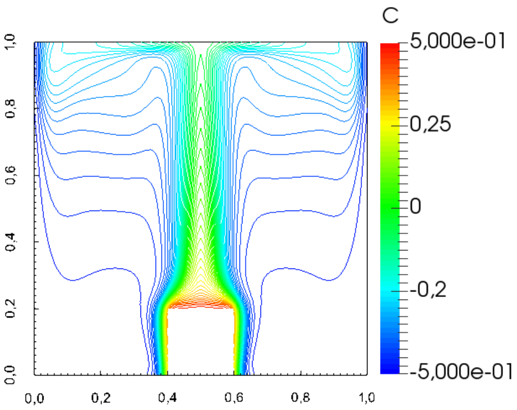

(c) $x_{H_2O} = 0.10$: Transparent medium

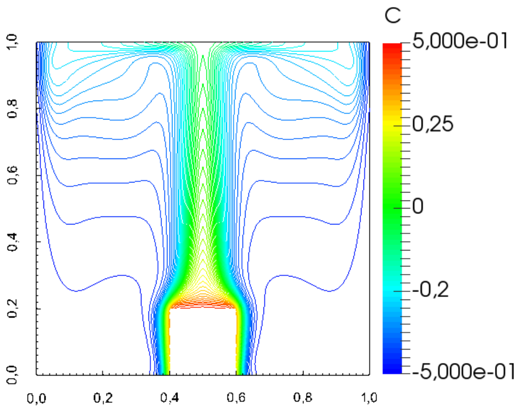

(d) $x_{H_2O} = 0.10$: Real gas

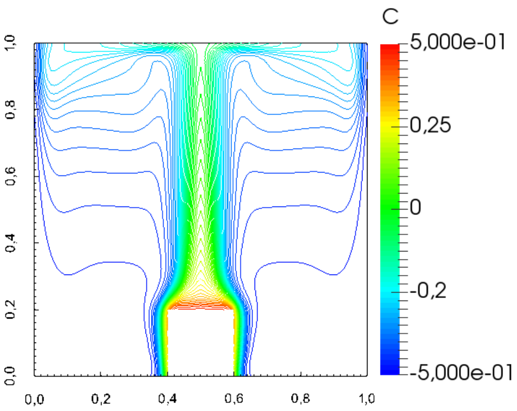

(e) $x_{H_2O} = 0.20$: Transparent medium

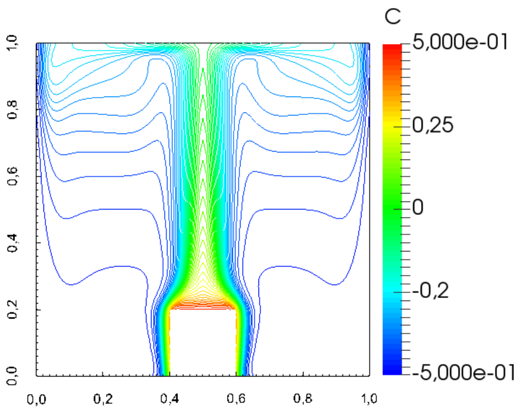

(f) $x_{H_2O} = 0.20$: Real gas

Figure 5.62: Concentration $\frac{C-C_{ref}}{C_h-C_l}$ field in the median plane of the cavity ($Y = 0.5$) at different mole fractions of water vapor.

Figures 5.62 displays the concentration distribution in the median plane ($Y = 0.5$) of the cavity. This field essentially remains insensitive to gas radiation.

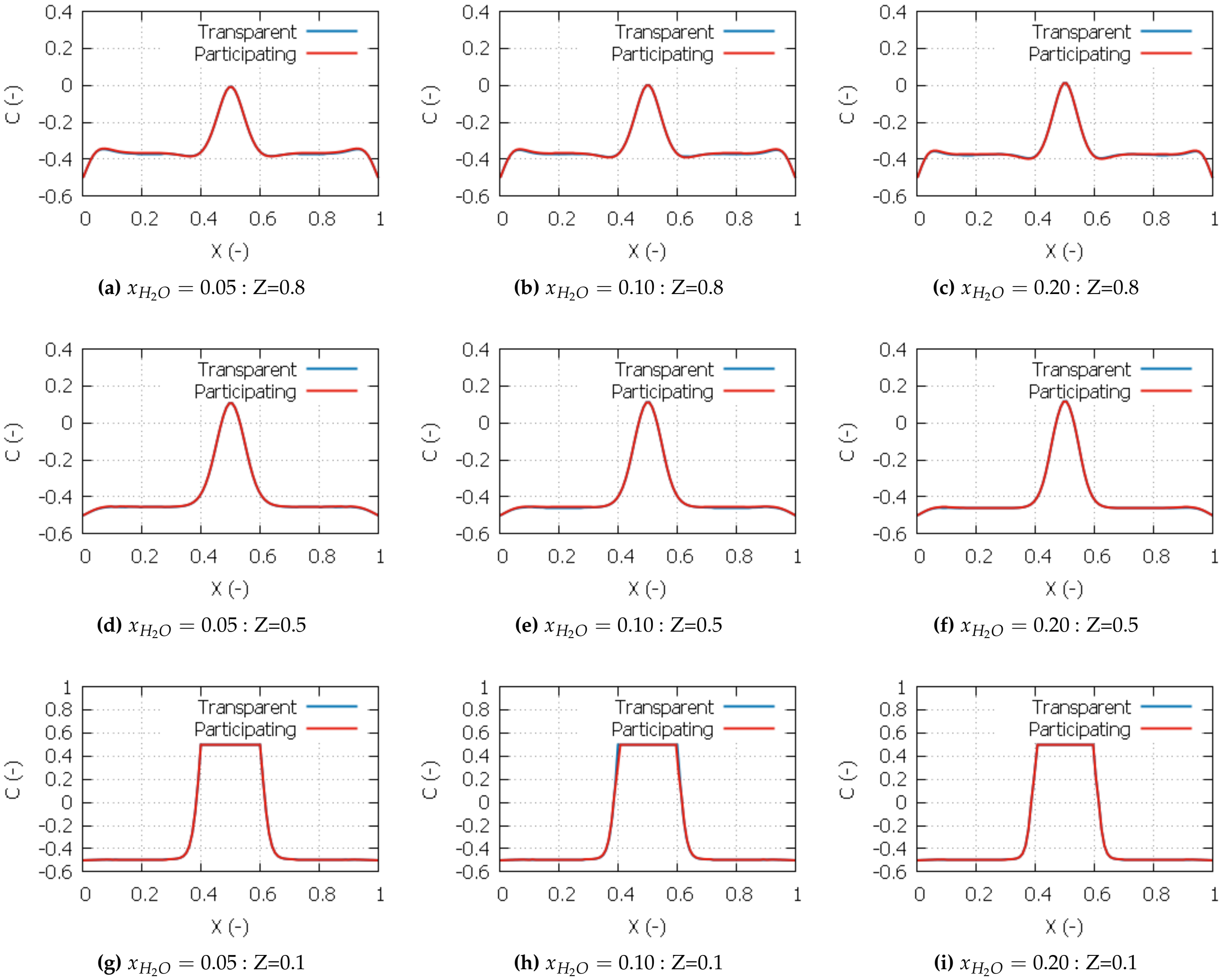

(a) $x_{H_2O} = 0.05$: Z=0.8
(b) $x_{H_2O} = 0.10$: Z=0.8
(c) $x_{H_2O} = 0.20$: Z=0.8
(d) $x_{H_2O} = 0.05$: Z=0.5
(e) $x_{H_2O} = 0.10$: Z=0.5
(f) $x_{H_2O} = 0.20$: Z=0.5
(g) $x_{H_2O} = 0.05$: Z=0.1
(h) $x_{H_2O} = 0.10$: Z=0.1
(i) $x_{H_2O} = 0.20$: Z=0.1

Figure 5.63: Concentration $\frac{C-C_{ref}}{C_h-C_l}$ profiles along different Z-crosslines in the median plane ($Y = 0.5$) at different average mole fractions of water vapor.

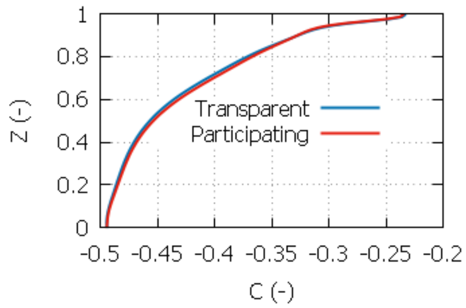

(a) $x_{H_2O} = 0.05$: X=0.2 or 0.8

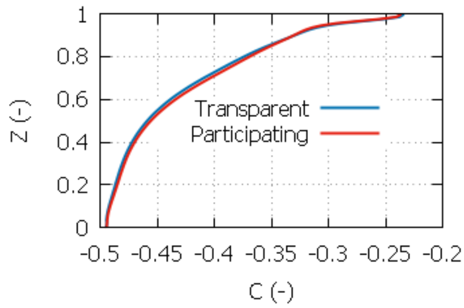

(b) $x_{H_2O} = 0.10$: X=0.2 or 0.8

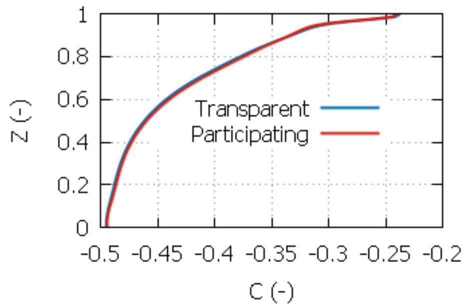

(c) $x_{H_2O} = 0.20$: X=0.2 or 0.8

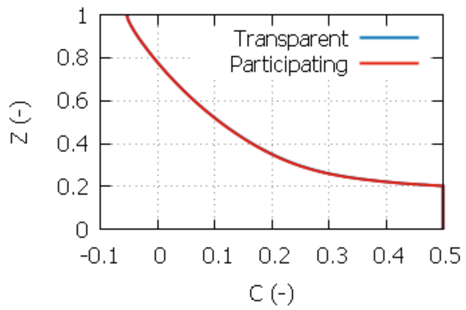

(d) $x_{H_2O} = 0.05$: X=0.5

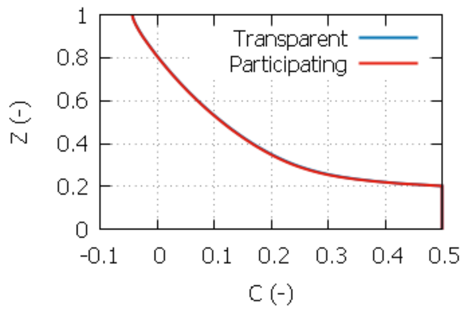

(e) $x_{H_2O} = 0.10$: X=0.5

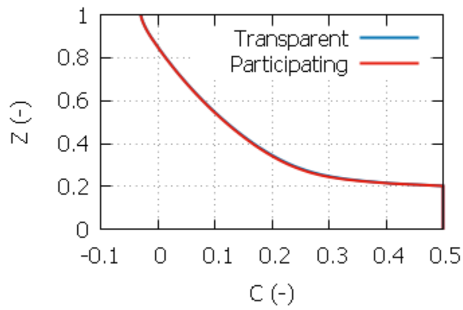

(f) $x_{H_2O} = 0.20$: X=0.5

Figure 5.64: Concentration $\frac{C-C_{ref}}{C_h-C_l}$ profiles along different X-crosslines in the median plane ($Y = 0.5$) at different average mole fractions of water vapor.

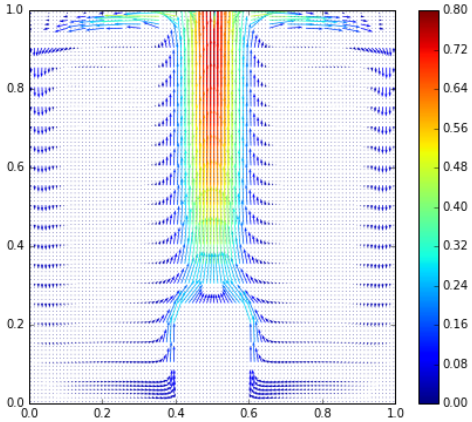

(a) $x_{H_2O} = 0.05$:
Transparent medium

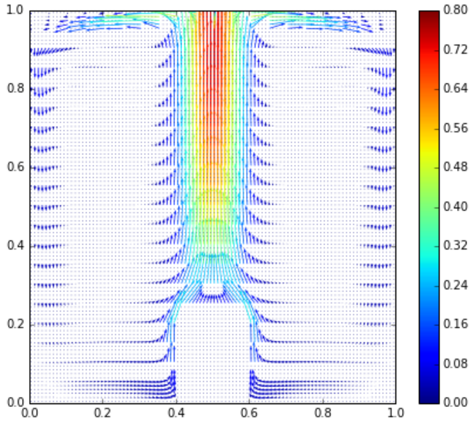

(b) $x_{H_2O} = 0.05$: Real gas

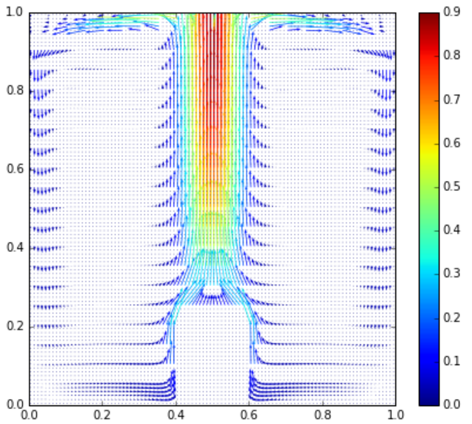

(c) $x_{H_2O} = 0.10$:
Transparent medium

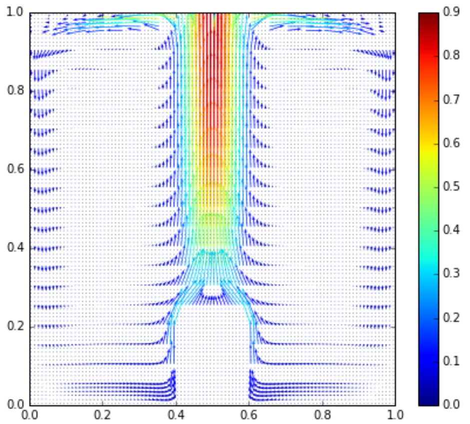

(d) $x_{H_2O} = 0.10$: Real gas

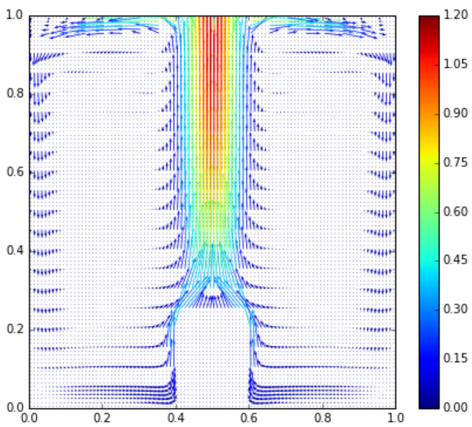

(e) $x_{H_2O} = 0.20$:
Transparent medium

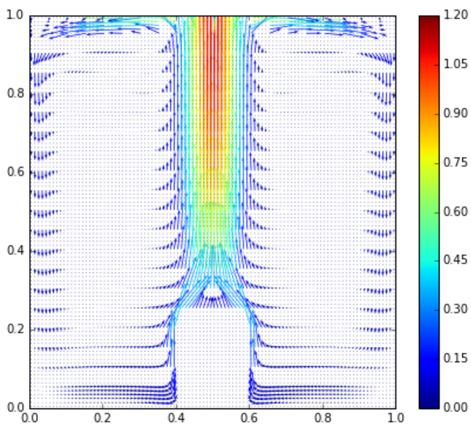

(f) $x_{H_2O} = 0.20$: Real gas

Figure 5.65: Velocity vector in the median plane of the cavity ($Y = 0.5$) at different mole fraction of water vapor. Velocities are normalized by U_{ref}.

Figure 5.65 represents the velocity field in the median plane ($Y = 0.5$) of the cavity. A global circulation is established within the enclosure, combining a climbing plume above the hot obstacle and descending boundary layers along the vertical walls. Including gas radiation does not significantly change these distributions (compared to the transparent cases).

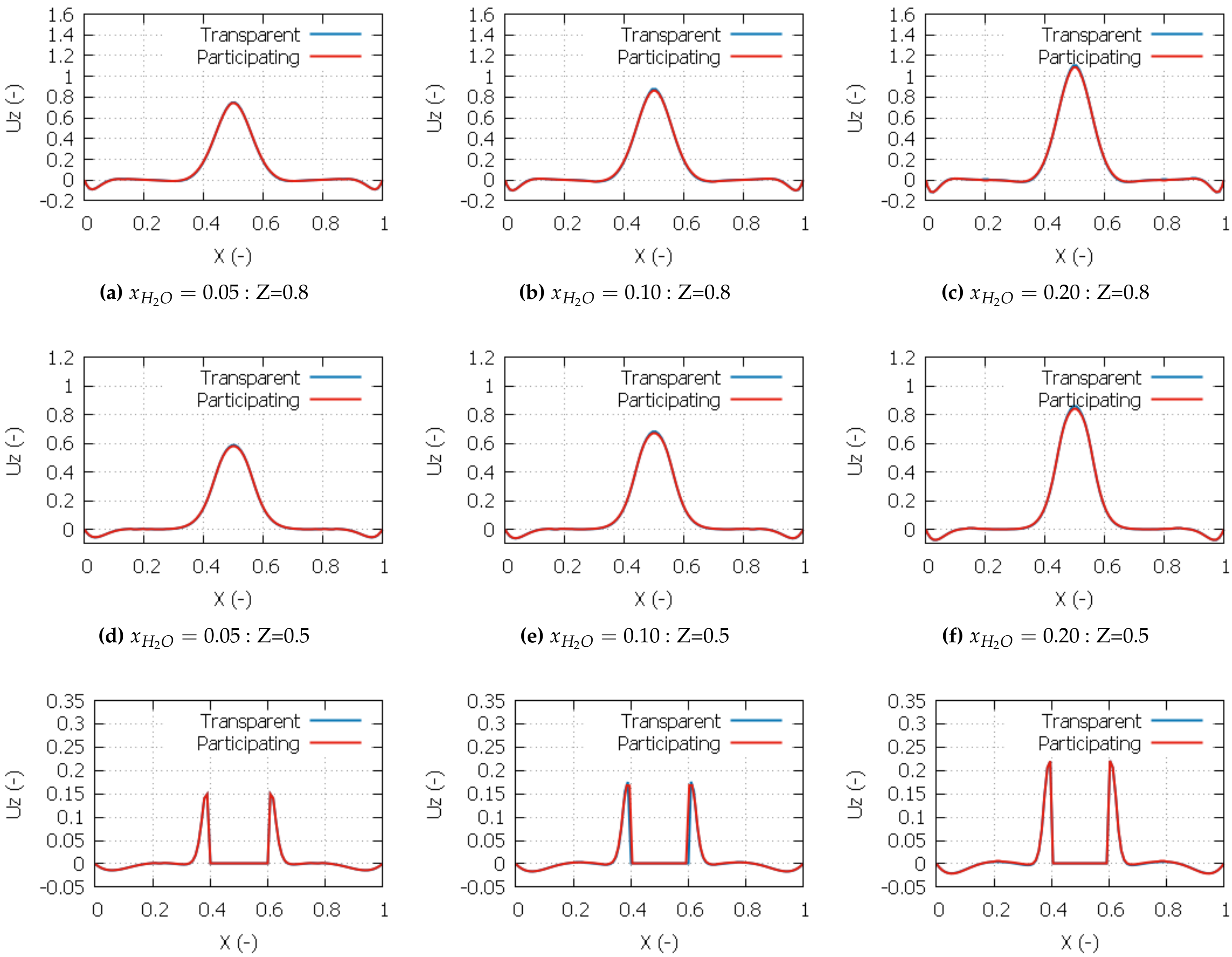

(a) $x_{H_2O} = 0.05$: Z=0.8 **(b)** $x_{H_2O} = 0.10$: Z=0.8 **(c)** $x_{H_2O} = 0.20$: Z=0.8

(d) $x_{H_2O} = 0.05$: Z=0.5 **(e)** $x_{H_2O} = 0.10$: Z=0.5 **(f)** $x_{H_2O} = 0.20$: Z=0.5

(g) $x_{H_2O} = 0.05$: Z=0.1 **(h)** $x_{H_2O} = 0.10$: Z=0.1 **(i)** $x_{H_2O} = 0.20$: Z=0.1

Figure 5.66: Vertical velocities $\frac{w}{U_{ref}}$ profiles at different Z-crosslines in the median plane ($Y = 0.5$) at different average mole fractions of water vapor.

Cinematic profiles along horizontal and vertical crosslines (see figure 5.66 and 5.67) show that, in the transparent cases, as the proportion of water vapor increases, the magnitude of the velocity also augments. However, introducing gas radiation does not impact the flow characteristics. At low molar fraction of water vapor, although the thermally driven force dominates over the mass one, the change in the temperature is too weak to bring any significant alteration to the momentum source and, in turn, to the dynamical structure. As x_{H_2O} rises up to 0.10 and then 0.20, the domination of the thermally induced force decreases and that of mass origin now prevails. Consequently, gas radiation has weaker and weaker impact on the dynamic structure in the enclosure.

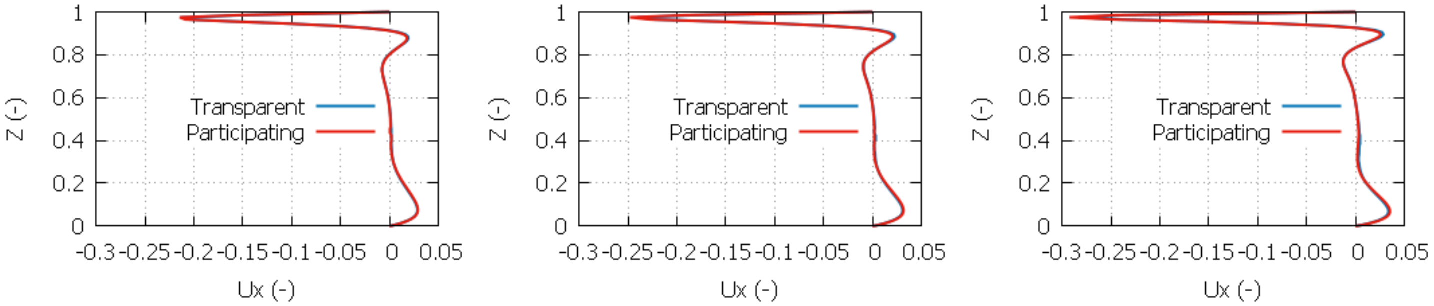

(a) $x_{H_2O} = 0.05$: X=0.2 (b) $x_{H_2O} = 0.10$: X=0.2 (c) $x_{H_2O} = 0.20$: X=0.2

Figure 5.67: Horizontal velocities $\frac{u}{U_{ref}}$ profiles at different X-crosslines in the median plane (Y=0.5) at different average mole fractions of water vapor.

5.2.1.2 Heat and Mass Transfer

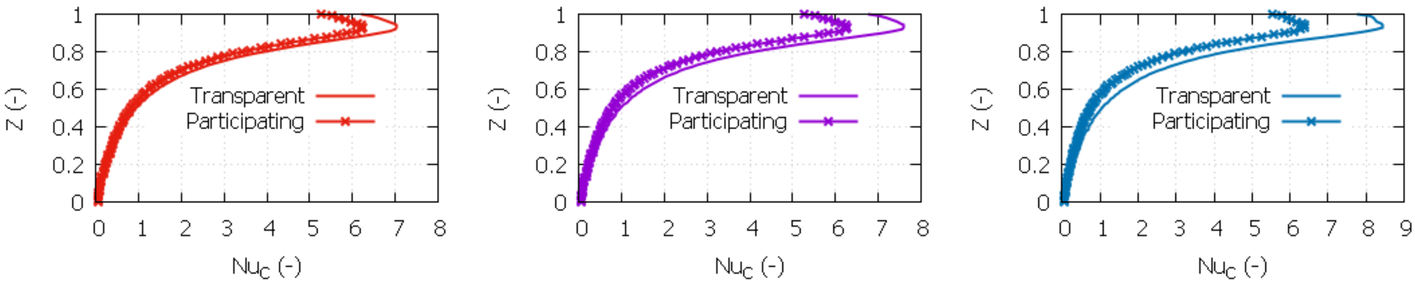

(a) $x_{H_20} = 0.05$ (b) $x_{H_20} = 0.10$ (c) $x_{H_20} = 0.20$

Figure 5.68: Local convective Nusselt number along a vertical centerline of any lateral wall of the cavity.

Figure 5.68 displays the distribution of the convective Nusselt number along the center line of any vertical wall of the cavity. It is observed that gas radiation reduces this parameter. Indeed, although the dynamic structure remains unchanged at all the considered mole fractions, the temperature of the fluid close to the vertical boundaries is reduced by emission. It decreases the thermal gradient and this effect gets stronger as the quantity of water vapor increases.

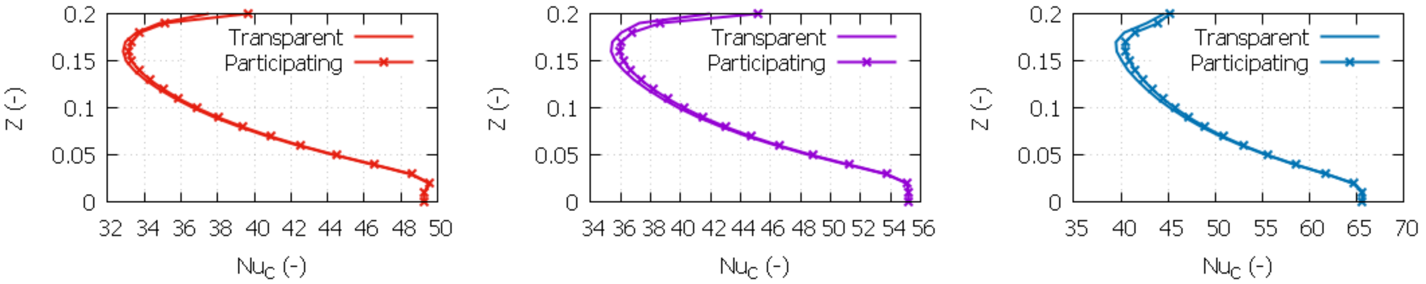

(a) $x_{H_20} = 0.05$ **(b)** $x_{H_20} = 0.10$ **(c)** $x_{H_20} = 0.20$

Figure 5.69: Local convective Nusselt number along a vertical center line of each lateral surfaces of the obstacle.

In contrast to the homogeneous case, the convective Nusselt number slightly increases along the vertical hot surfaces when radiation is taken into account (see figure 5.69). In this region, the thermal gradient augments due to emission of the gas layers close to the hot surfaces (which reduces the fluid temperature).

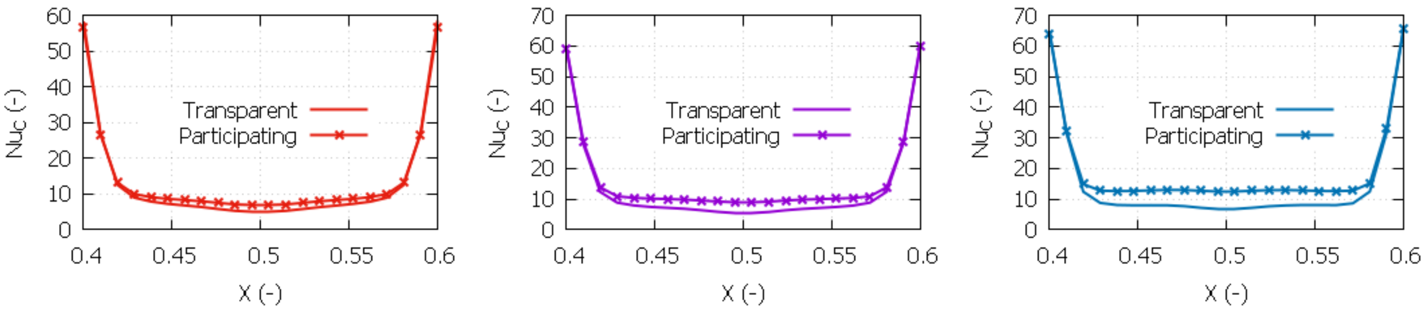

(a) $x_{H_20} = 0.05$ **(b)** $x_{H_20} = 0.10$ **(c)** $x_{H_20} = 0.20$

Figure 5.70: Local convective Nusselt number along an horizontal centerline of the obstacle top surface.

On the horizontal hot surface, the convective Nusselt number augments when gas radiation is considered (see figure 5.70) since the nearby fluid is cooled down by emission (as evidenced by negative values of radiative source in figures 5.61 a,c,e). As a result, the thermal gradient is enhanced, inducing a higher value of the convective Nusselt number.

The values of averaged convective Nusselt numbers and average total Nusselt numbers[4], which are defined as $\overline{Nu} = \frac{1}{A}\int_A Nu(\mathbf{s})dA$, are listed in the tables below:

[4]These parameters are defined in chapter 2

x(%)	Convective Nusselt number		Total Nusselt number	
	Transparent	Participating	Transparent	Participating
5	1.82	1.56	12.62	12.59
10	1.96	1.53	12.77	12.71
20	2.20	1.55	13.02	12.92

Table 5.2: Average convective and total Nusselt numbers on any vertical cavity wall: double diffusive convection and radiation in an $air - H_2O$ mixture.

x(%)	Convective Nusselt number		Total Nusselt number	
	Transparent	Participating	Transparent	Participating
5	41.77	42.07	255.56	255.29
10	45.27	45.67	259.12	258.45
20	50.93	51.55	264.95	263.64

Table 5.3: Average convective and total Nusselt numbers on any obstacle vertical surface: double diffusive convection and radiation in an $air - H_2O$ mixture.

x(%)	Convective Nusselt number		Total Nusselt number	
	Transparent	Participating	Transparent	Participating
5	14.72	15.65	240.51	239.27
10	15.32	17.19	241.18	238.88
20	16.63	19.82	242.67	238.33

Table 5.4: Average convective and total Nusselt numbers on the obstacle horizontal surface: double diffusive convection and radiation in an $air - H_2O$ mixture.

Regarding the transparent cases, tables 5.2, 5.3 and 5.4 show that, as the proportion of water vapor increases, the mean convective Nusselt number is risen up along all active surfaces. This comes from the speed up of the fluid motion as mentioned above. When gas radiation takes place, although the dynamic structure remains unchanged, the convective thermal transport is now altered. At the vertical cold walls, this quantity is dramatically reduced (see figure 5.68) and keeps almost the same value for all the considered molar fractions (the reason is the stronger and stronger radiative emission in the upper part of the cavity as the quantity of water vapor increases, which lessens the thermal gradient). At the hot surfaces, the convective transport is pulled up (by an increase of the thermal gradient due to emission). Besides, radiative transfer is attenuated by the absorption of the medium. These effects induce the drop of the average total Nusselt numbers.

Regarding mass transfer, the average Sherwood number, which is defined as $\overline{Sh} = \frac{1}{A} \int_A Sh(\mathbf{s}) dA$ is insensitive to radiation (see tables 5.5, 5.6 and 5.7), since radiative transport has no significant impact on the flow structure (see figures 5.66 and 5.67).

x(%)	Sherwood number	
	Transparent	Real gas mixture
5	1.785	1.783
10	1.906	1.905
20	2.106	2.104

Table 5.5: Averaged Sherwood number on any cavity lateral wall: double diffusive convection and radiation in an $air - H_2O$ mixture.

x(%)	Sherwood number	
	Transparent	Real gas mixture
5	41.144	41.204
10	44.081	44.081
20	48.850	48.812

Table 5.6: Averaged Sherwood number on any obstacle vertical wall: double diffusive convection and radiation in an $air - H_2O$ mixture.

x(%)	Sherwood number	
	Transparent	Real gas mixture
5	13.769	13.731
10	14.283	14.246
20	15.239	15.198

Table 5.7: Averaged Sherwood number on the obstacle horizontal wall: double diffusive convection and radiation in an $air - H_2O$ mixture.

5.2.2 $Air - CO_2$ mixture

We now turn to a case of the double diffusive convection coupled to gas radiation in an $air - CO_2$ mixture. As introduced in the beginning of the chapter, this combination generates opposite flows inside the cavity. The characteristic dimensionless numbers related to this configuration are listed in the table 5.8. The average mole fractions of the CO_2 are still defined as $x = \frac{C_{ref} * R * T_{ref}}{P}$ and are given two different values: 10% and 20% . It leads to two types of fluid motion: balanced thermal and mass effects ($|N| \approx 1$) and mass governed ($|N| > 1$).

x (%)	N	Ra	Pr	Le	Pl
10	-1.102	$5.269 \cdot 10^6$	0.716	1.282	$4.338 \cdot 10^{-3}$
20	-2.100	$5.958 \cdot 10^6$	0.717	1.204	$4.284 \cdot 10^{-3}$

Table 5.8: Configuration parameters: $air - CO_2$ mixture

The case with 5% concentration of CO_2 is not studied here. It was found to generate a non-symmetric flow (in presence of radiation) in a symmetric configuration. Its characteristics deserve a more focused study.

5.2.2.1 Mixture at $x_{CO_2} = 0.10$

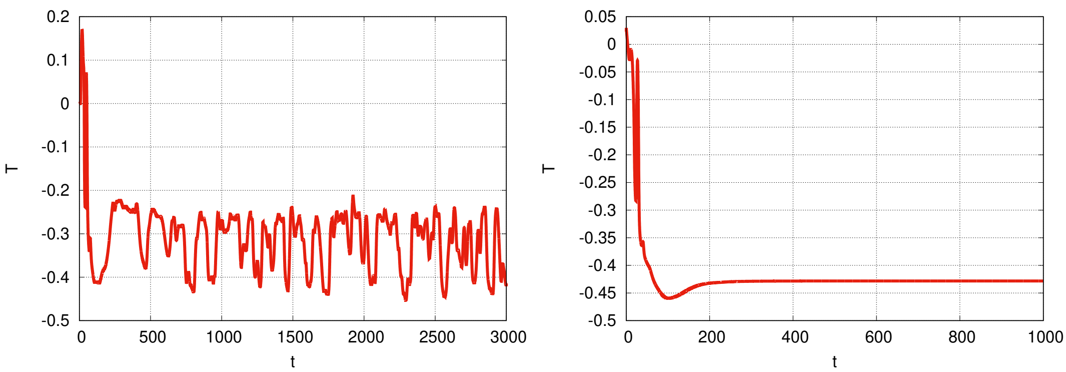

(a) Transparent medium

(b) $Air - CO_2$ mixture at $x_{H_2O} = 0.10$

Figure 5.71: Time evolution of temperature at the center point of the cavity $(X, Y, Z) = (0.5, 0.5, 0.5)$ at x_{CO_2}=0.10

In the transparent case, we receive an unsteady signal in the cavity, which is illustrated by the time evolution of the temperature at the center point ($(X, Y, Z) = (0.5, 0.5, 0.5)$) (see figure 5.71a). However when radiation is introduced, the flow converges again towards a steady state.

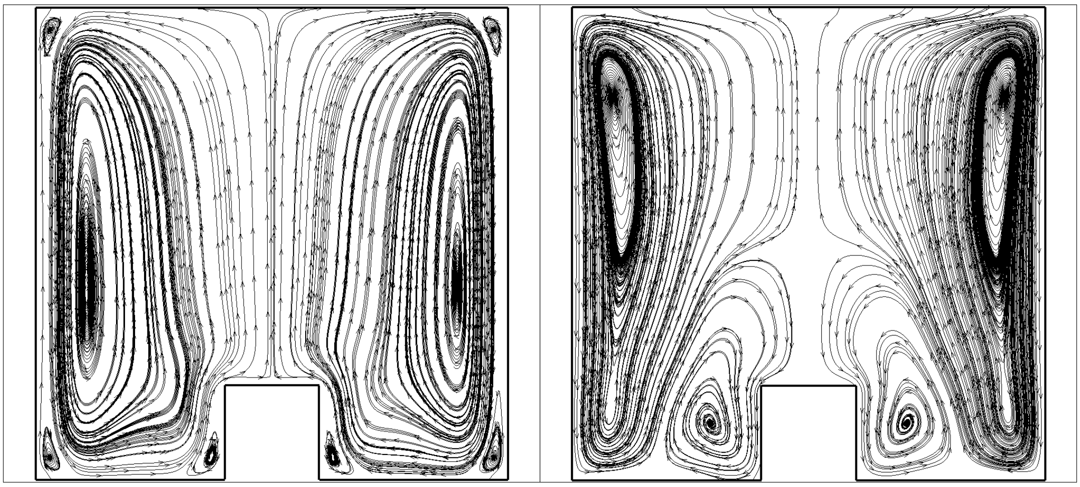

(a) Tranparent medium: $t = 1$

(b) Participating medium: $t = 1$

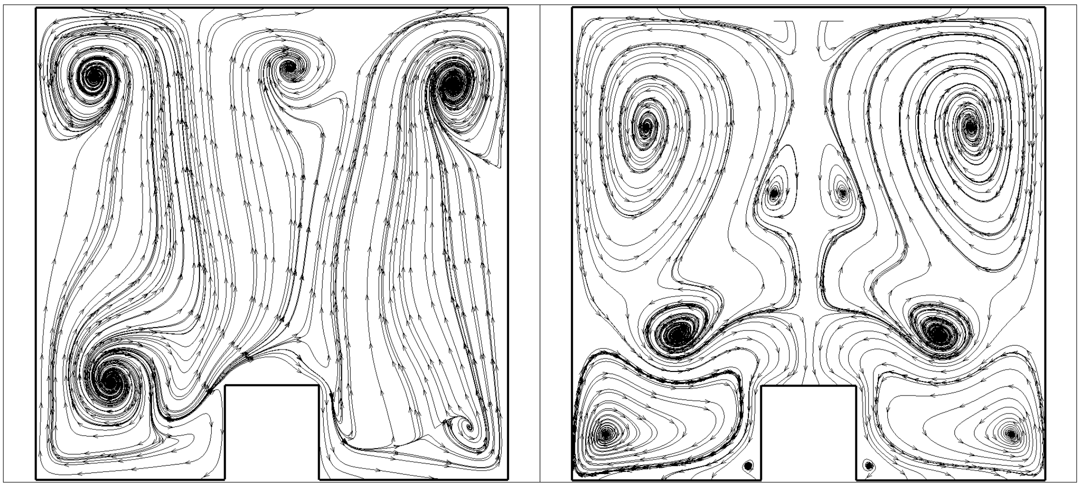

(c) Tranparent medium: $t = 666$

(d) Participating medium: $t = 666$

Figure 5.72: Flow lines on the median plane of the cavity ($Y = 0.5$) at different instants.

In this configuration, the temperature diffuses faster than the pollutant ($Le > 1$). Therefore, close to the vertical surfaces of the obstacle, the fluid is initially heated more quickly than loaded in CO_2. As a result, in the transparent case at $t = 1$, the buoyancy force of mass origin is less dominant than the thermal one in these regions (the large thermally driven flow cells with the small mass governed ones in the corners are presented in the figure 5.72 a). As time elapses, the mass driven motion dominates but only weakly ($|N| = 1.102$) (for instance, see figure 5.72 c at $t = 666$). The fluid circulations driven by these two effects unpredictably interact and create the fluctuations inside the cavity. Simultaneously, in the upper part of the enclosure, the increase of concentration in the plume axis also restraints the vertical motion and this contributes to the observed oscillation.

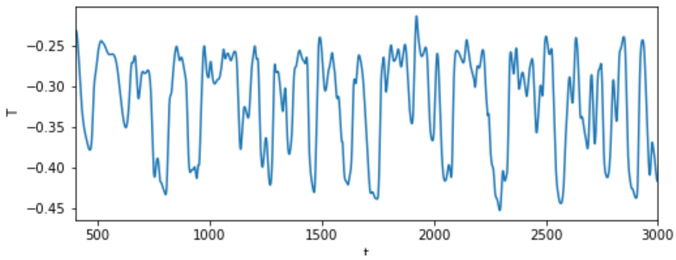

(a) Time evolution of temperature

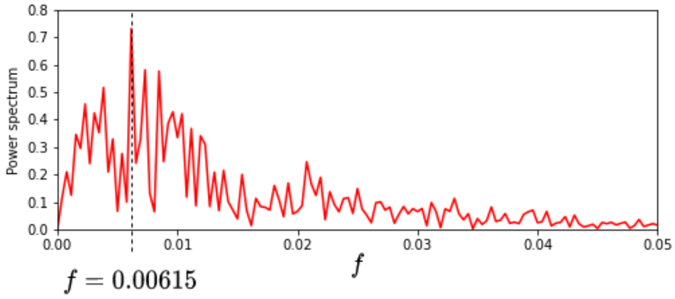

(b) Power spectrum

Figure 5.73: Time evolution and power spectrum of the temperature signal at the point $(X, Y, Z) = (0.5, 0.5, 0.5)$ in temporal range $[400 : 3000]$ at $x_{CO_2} = 0.10$: transparent medium.

Several authors have found a similar flow pattern in differentially heated cavities ($N = -1.102$ and $Le = 1.282$), namely a large thermal recirculation in the center, and mass driven cells in the corners ([157], [158], [159]). Such configurations are likely to yield oscillatory solutions attributed to the thermosolutal instability. This phenomenon is induced by a local and abrupt variation in fluid density caused by a uniform "bubble" bursting in temperature or concentration (see figure 5.74). Compared to their works, we observe the similar patterns in our configuration: large thermally induced flow cells above the obstacle and the mass driven ones in the lower part of the cavity. On the other hand, the spectrum analysis of the temperature signal in temporal range $[400 : 3000]$ shows that there are many frequencies which govern the fluctuations in the cavity (see figure 5.73). They come from the periods which are comparable to the time scale of thermal diffusion through the temperature boundary layer thickness (δ_t), $\frac{\delta_t}{\alpha}$. This parameter corresponds to the dense zone of the temperature contours ([158]) (see figure 5.74). For instance, the thermal boundary layer thickness determined at $t = 775$ is $\delta_t = 0.066(m)$ (mean value of boundary layer thicknesses determined from two cavity vertical walls which are represented in the figure 5.75). The frequency calculated from this value is comparable to the most significant one observed in the figure 5.73 b: $f = 0.00615$. However, the plot of the thermal field at different instants in figure 5.74 do not show any periodic behavior. We, therefore, conclude that the flow inside the cavity is turbulent with a dominant frequency, which could be related to the thermosolutal instability rather than other mechanisms.

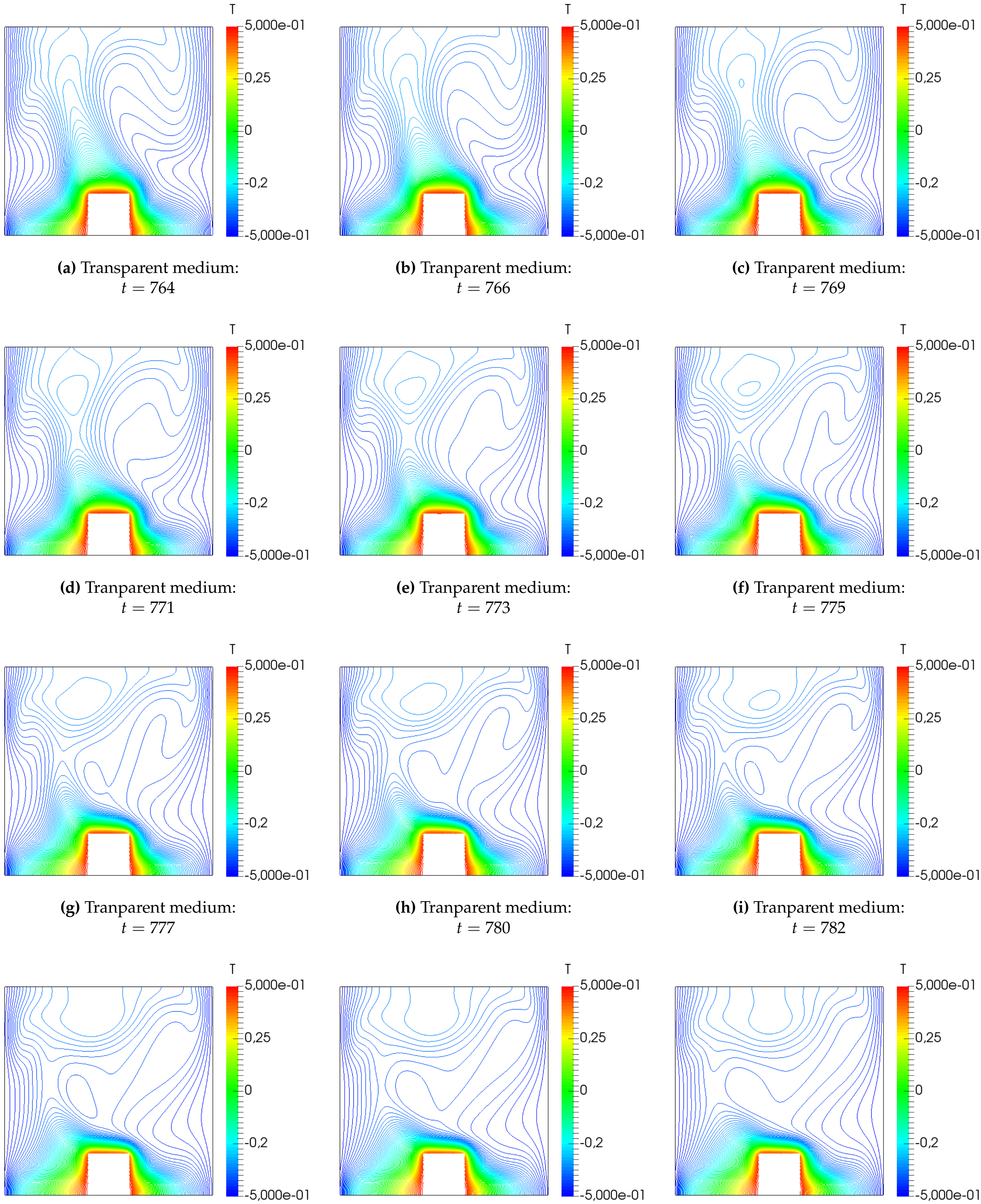

(a) Transparent medium: $t = 764$

(b) Tranparent medium: $t = 766$

(c) Tranparent medium: $t = 769$

(d) Tranparent medium: $t = 771$

(e) Tranparent medium: $t = 773$

(f) Tranparent medium: $t = 775$

(g) Tranparent medium: $t = 777$

(h) Tranparent medium: $t = 780$

(i) Tranparent medium: $t = 782$

(j) Tranparent medium: $t = 784$

(k) Tranparent medium: $t = 786$

(l) Tranparent medium: $t = 789$

Figure 5.74: Thermal field $\frac{T-T_{ref}}{T_h-T_c}$ of the cavity ($Y = 0.5$) at different instants.

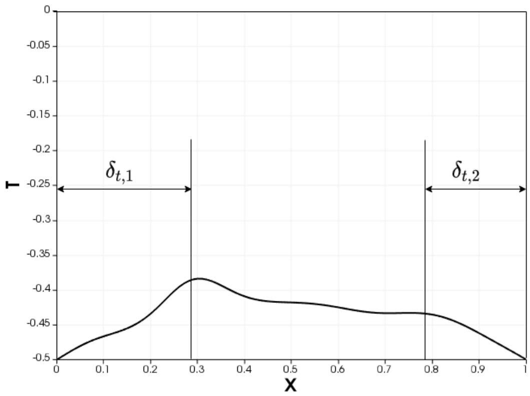

Figure 5.75: Temperature $\frac{T-T_{ref}}{T_h-T_c}$ profile at $Z = 0.5$ in the median plane at $t = 775$

When gas radiation is introduced, initially at $t = 1$, we do not find the same structure as in the transparent case (see figure 5.72 b). Radiation, in this situation, decreases the temperature of the fluid layers along the vertical surfaces of the obstacle (see figure 5.76) due to the domination of emission, see figure 5.77 a for negative values of radiative source. Consequently, it reduces the thermal force near these walls and indirectly, intensifies the concentration one. As a result, we clearly observe the domination of the mass driven flow around the obstacle, while the thermally induced circulation occurs in the rest of the enclosure (see figure 5.72 b). As time elapses, the mass origin effect completely dominates in the lower part of the cavity (for instance, see figure 5.72 d for flow lines at $t = 666$). But in the upper part, the mass force (due to the increase of the concentration in the plume axis) is now balanced by the thermal one. The reason is the enhancement of the temperature by absorption (see figure 5.77 b for positive values of radiative source) which increases the thermal gradient. We, therefore, conclude that, radiation stabilizes the flow.

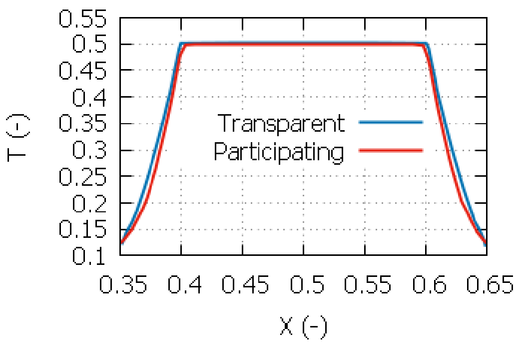

Figure 5.76: Temperature $\frac{T-T_{ref}}{T_h-T_c}$ profile at $Z = 0.1$ in the range $X = [0.35 : 0.65]$ at $t = 1$

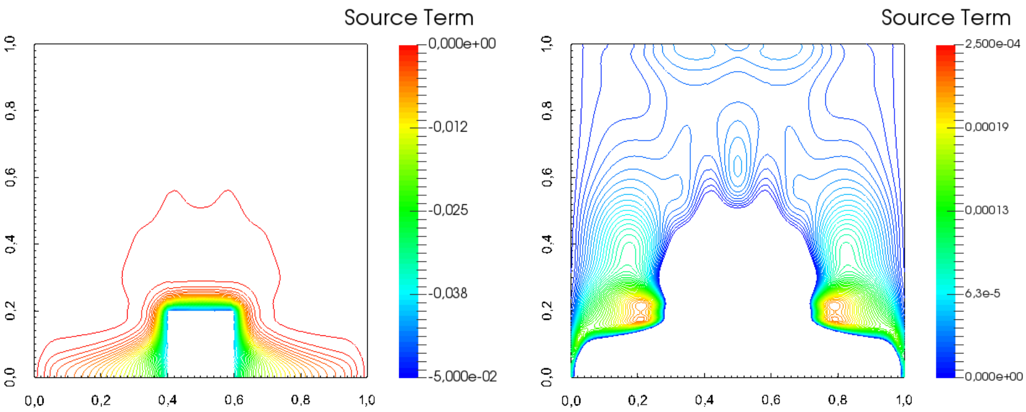

(a) Emission dominates

(b) Absorption dominates

Figure 5.77: Distribution of radiative source term in the median plane ($Y = 0.5$) at $x_{CO_2} = 0.10$. Sources are normalized by $4\sigma T_{ref}^4/L$

5.2.2.2 Mixture at $x_{CO_2} = 0.20$

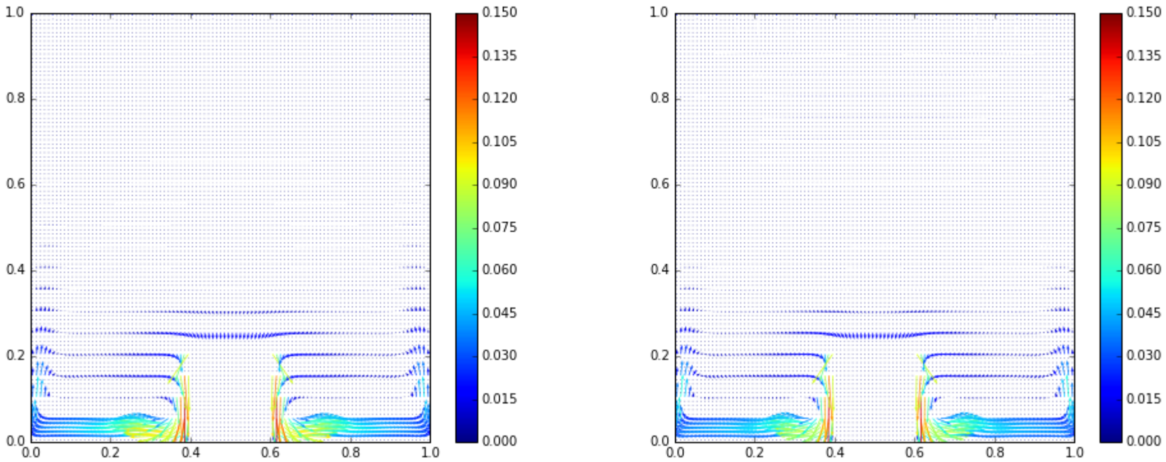

(a) Transparent medium

(b) Real gas

Figure 5.78: Velocity vector in the median plane of the cavity ($Y = 0.5$) at $x_{CO_2} = 0.20$. Velocities are normalized by U_{ref}

Figure 5.78 displays the velocity field in the median plane of the enclosure ($Y = 0.5$). In both cases, the flow is driven by the mass gradient (fluid circulations in the lower half of the cavity). For better analyzing the change in the dynamic structure, we investigate the velocities profiles along the different crosslines (see figures 5.79 a,b,c and 5.80 a). At low level ($Z = 0.1$), there exists a nearly motionless zone, which separates the descending boundary layers along the obstacle and those ascending along the cavity walls. As radiation is considered, the same situation is found except a slight decrease of vertical velocity in the region close to the obstacle (see figure see figures 5.79 a). Indeed, the presence of radiation increases temperature (by absorption). Therefore, the thermal gradient is strengthened and weakens the domination of mass effect, resulting in the slow down of the fluid circulation near the bottom (see figure 5.80 a). At intermediate altitude ($Z = 0.5$), in the transparent medium, although we can see a complex flow with a weak thermal plume in the center and upward boundary layers near the cold walls, mass gradient still governs the fluid motions. As radiation is taken into account, the impact of thermal gradient increases and exceeds the mass one (due to radiative absorption). The changes are obvious (compared to the velocity magnitude in this region): the significant deceleration of the fluid layers next to the cold walls and a stronger thermal plume (see 5.79 b). At high level ($Z = 0.8$), this tendency is more pronounced (see 5.79 c). We also observe the acceleration of the boundary layer at the ceiling, while it was nearly an unmoving region in the transparent medium (see figure 5.80 a). When radiation is considered, the mass driven flow is totally replaced by the thermal one (upward plume and downward bounding layers). However, these changes are not significant when comparing to the velocity magnitude in the lower part of the enclosure.

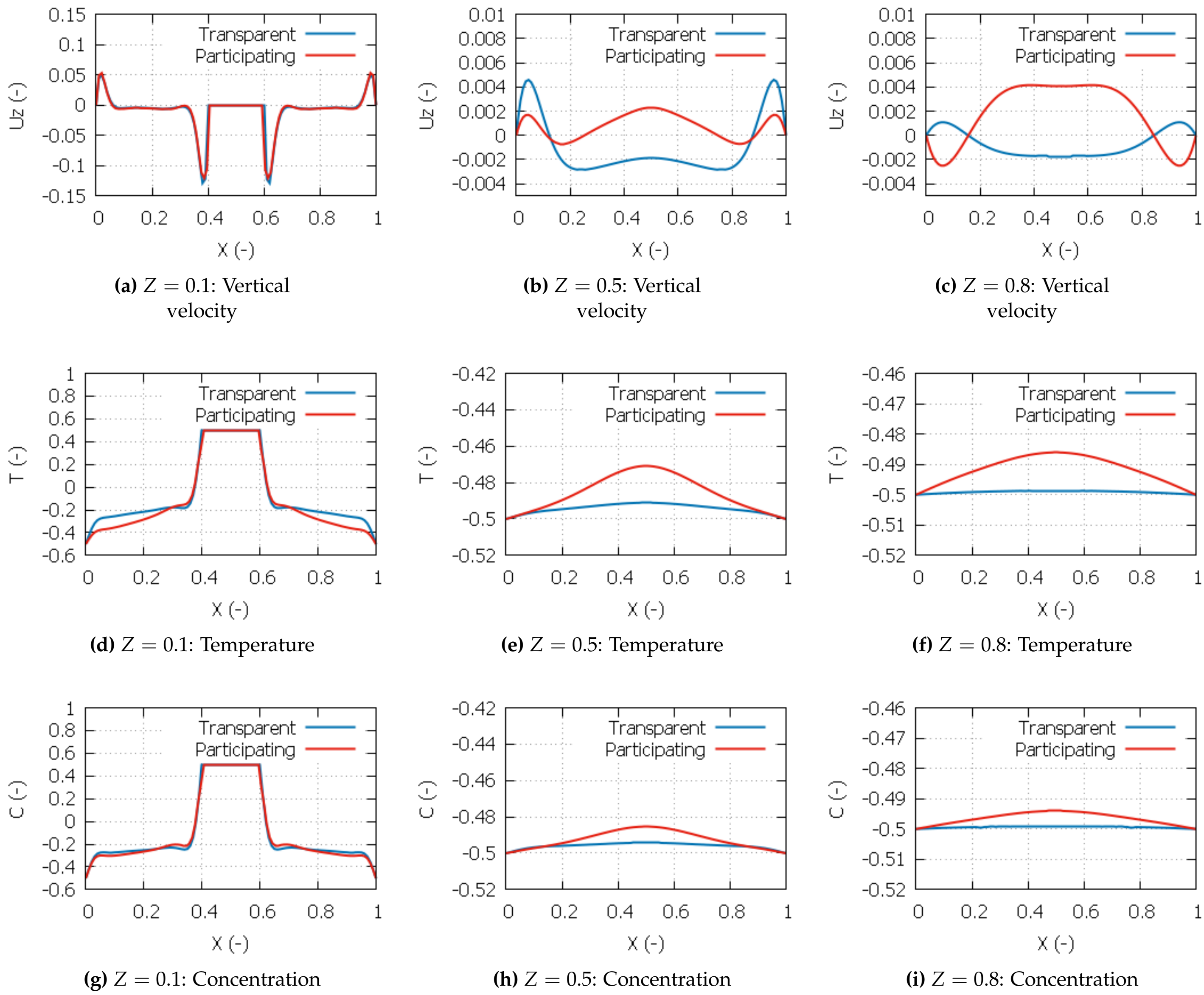

(a) $Z = 0.1$: Vertical velocity

(b) $Z = 0.5$: Vertical velocity

(c) $Z = 0.8$: Vertical velocity

(d) $Z = 0.1$: Temperature

(e) $Z = 0.5$: Temperature

(f) $Z = 0.8$: Temperature

(g) $Z = 0.1$: Concentration

(h) $Z = 0.5$: Concentration

(i) $Z = 0.8$: Concentration

Figure 5.79: Vertical velocity $\frac{w}{U_{ref}}$, temperature $\frac{T-T_{ref}}{T_h-T_c}$ and concentration $\frac{C-C_{ref}}{C_h-C_l}$ profiles along different Z-crosslines in the median plane ($Y = 0.5$) at $x_{CO_2} = 0.20$

Here ($Z = 0.1$), radiation makes the temperature decrease near the bounding vertical and bottom walls but slightly increase near the obstacle lateral surfaces (see figures 5.79 d, 5.80 b). In details, the fluid close to the cold walls emits more than it absorbs (see figure 5.82 a for negative values of radiative source term), therefore, reduces its thermal levels. At intermediate and high level ($Z = 0.5; 0.8$), compared to the transparent case, the temperature is marginally leveled up (see figures 5.79 e,f and 5.80 c). The reason is that the domination of radiative absorption over emission in the region above the obstacle (see figure 5.82 b for positive values of radiative source term) strengthens the thermal plume which brings more fluid at high temperature toward the ceiling of the cavity.

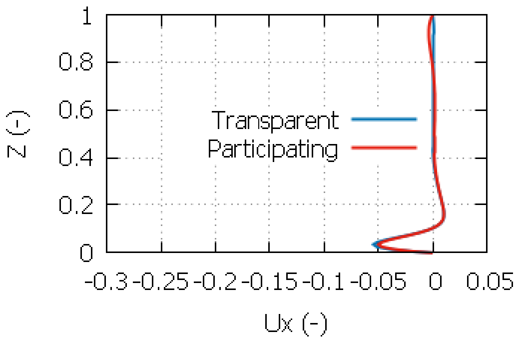

(a) $X = 0.2$

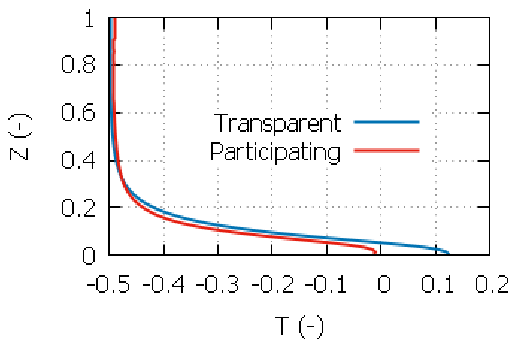

(b) $X = 0.2$

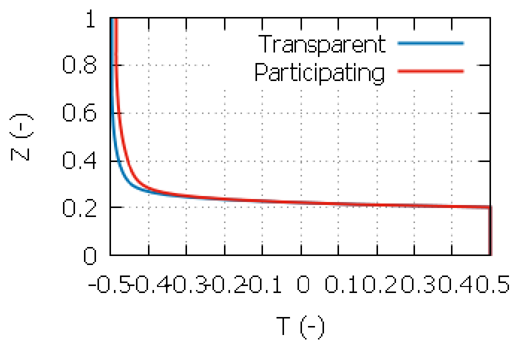

(c) $X = 0.5$

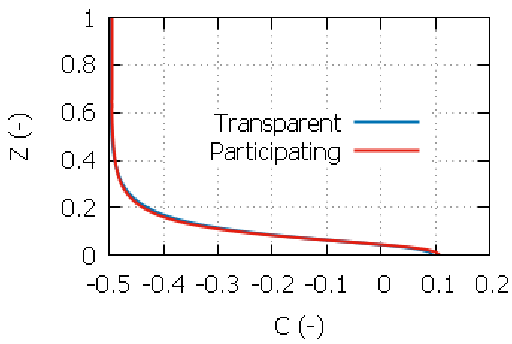

(d) $X = 0.2$

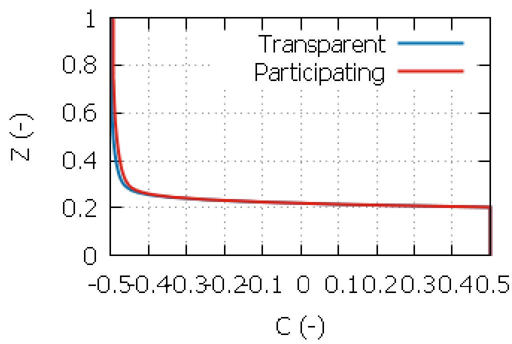

(e) $X = 0.5$

Figure 5.80: Horizontal velocity $\frac{u}{U_{ref}}$, temperature $\frac{T-T_{ref}}{T_h-T_c}$ and concentration $\frac{C-C_{ref}}{C_h-C_l}$ profiles along different X-crosslines in the median plane ($Y = 0.5$) at $x_{CO_2} = 0.20$

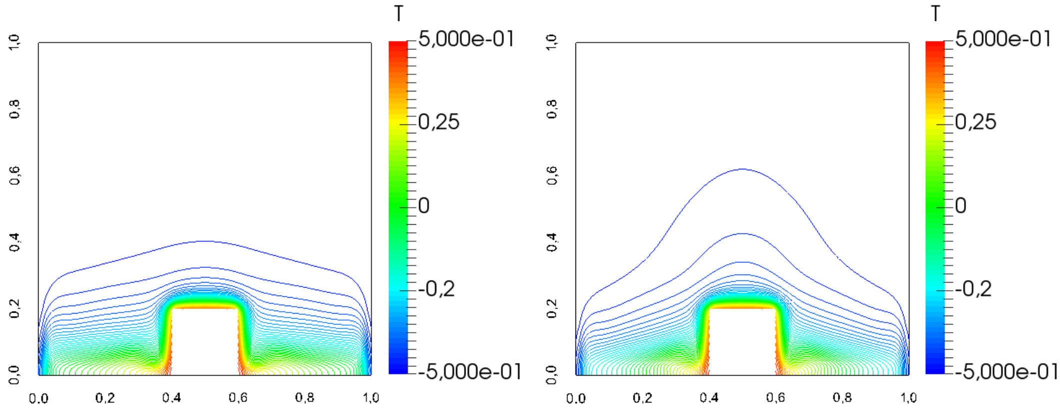

(a) Transparent medium **(b)** Real gas

Figure 5.81: Thermal field $\frac{T-T_{ref}}{T_h-T_c}$ in the median plane of the cavity ($Y = 0.5$) at $x_{CO_2} = 0.20$

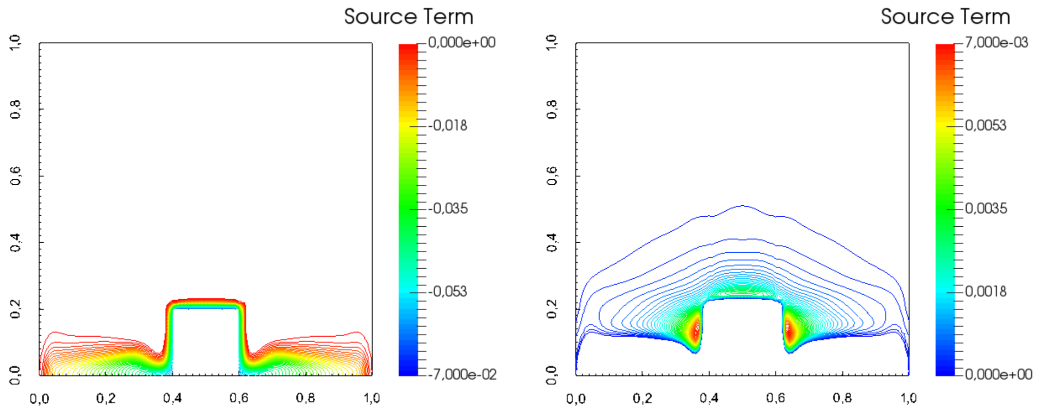

(a) Emission dominates **(b)** Absorption dominates

Figure 5.82: Distribution of radiative source term in the median plane ($Y = 0.5$) at $x_{CO_2} = 0.20$. Sources are normalized by $4\sigma T_{ref}^4/L$

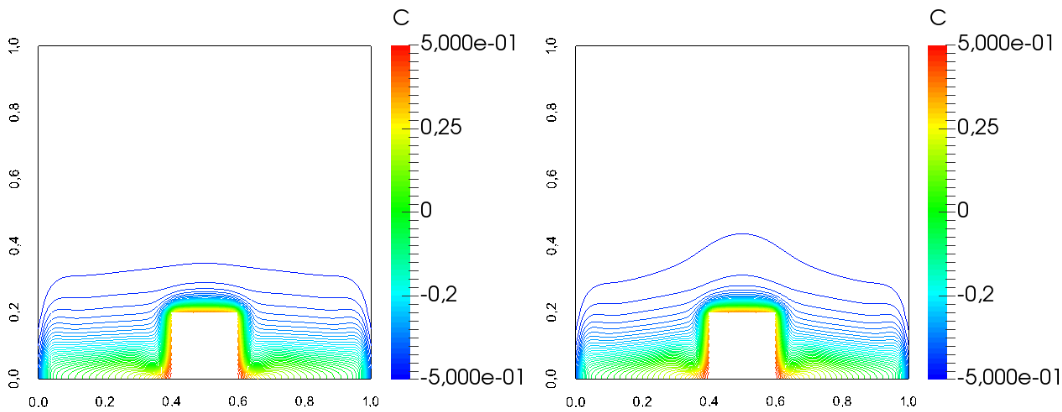

(a) Transparent medium **(b)** Real gas

Figure 5.83: Concentration field $\frac{C-C_{ref}}{C_h-C_l}$ in the median plane of the cavity ($Y = 0.5$) at $x_{CO_2} = 0.20$

Regarding the concentration distribution, the slow down of the mass driven flow in the lower part of the cavity ($Z = 0.1$) induces a slight decrease of this quantity near the cavity vertical walls (see figure 5.79 g). However, in the upper part, the enhancement of the thermal plume carries more high loaded fluid upward, resulting in the increase of the concentration in these regions (see 5.79 h,i). The redistribution of this field is also illustrated in figure 5.83.

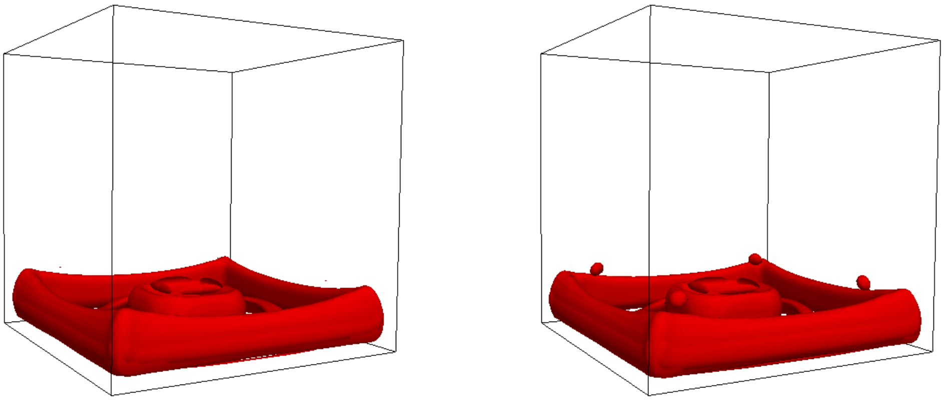

(a) Transparent gas **(b)** Real gas

Figure 5.84: Iso-surface of the Q-criterion at the value 0.01 in the cavity at $x_{CO2} = 0.20$. Values are normalized by U_{ref}^2/L^2

The Q-criterion illustrated in figure 5.84 shows that the presence of radiation does not significantly modify the dynamic structure in the cavity.

5.2.2.3 Heat and Mass Transfer

Position	Convective Nusselt number		Total Nusselt number	
	Transparent	Participating	Transparent	Participating
Cavity lateral wall	1.41	0.77	12.49	12.28
Obstacle vertical wall	27.22	27.84	246.46	241.66
Obstacle horizontal wall	32.46	33.50	264.01	262.33

Table 5.9: Average convective and total Nusselt number on active walls of the cavity and of the obstacle for double diffusive convection and radiation in the $air - CO_2$ mixture at $x_{CO_2} = 0.20$

Table 5.9 represents the mean convective and total Nusselt numbers on the active walls of the cavity and of the obstacle. When radiation is accounted for, the mean convective Nusselt number decreases at the cavity walls. Conversely, it slightly increases on the hot source surfaces. We recall that the fluid near the cold walls is cooled down by emission, resulting in a decrease of the thermal gradient. On the hot source horizontal surface, the average convective quantity is slightly augmented (radiative emission lowers the temperature of the nearby fluid). Besides, the radiative transfer is attenuated by absorption of the medium. Concerning the average total Nusselt number, this quantity is lessened on all the active surfaces.

Position	Sherwood number	
	Transparent	Real gas mixture
Cavity lateral wall	1.75	1.70
Obstacle vertical wall	34.68	33.53
Obstacle horizontal wall	36.40	35.84

Table 5.10: Averaged Sherwood number on active walls of the cavity and of the obstalce for double diffusive convection in the $air - CO_2$ mixture at $x_{CO_2} = 0.20$

Introducing gas radiation slightly decreases the mass transfer inside the cavity (see table 5.10). Indeed, although the thermal plume is reinforced in the upper part of the cavity, which can raise up the concentration transport, it does not compensate for the reduction in this quantity due to the slow down of the mass driven flow in the lower part of the enclosure.

5.2.3 Synthesis

This section presents the study of the double diffusive convection coupled to the radiation of a real gas mixture in a cavity hosting a hot obstacle. The composition involves either H_2O or CO_2 which respectively induces cooperating or opposing flows in the enclosure. The computations are carried out at different average mole fractions of the absorbing species. The comparisons between the obtained results and the reference solutions (transparent case) reveal the impacts of gas radiation of the flow structure and heat and mass transfer, which are summarized as below:

- $Air - H_2O$ mixture
  The presence of radiation does not influence the dynamic structure inside the cavity at all the considered average mole fractions. Consequently, the concentration field is found unchanged compared to the transparent case. However, gas absorption lessens the thermal level at the intermediate and high level of the enclosure.

  Regarding the transport processes, radiation slightly reduces the convective transfer on the bounding walls of the cavity. But it marginally increases this quantitiy on the vertical surfaces of the obstacle and more significantly on the hot upper face. Besides, radiative transfer is attenuated by absorption through the medium, especially between the upper surface of the obstacle and the cavity walls. In turn, the total heat transfer is lessened. Because the dynamic behavior is not much altered when radiation is accounted for, the mass transfer in the enclosure remains nearly unchanged.

- $Air - CO_2$ mixture
  In this configuration, at $x_{CO_2} = 0.10$, in transparent medium, the turbulent flow occurs with a domninant frequency which maybe due to the thermosolutal instability in a transparent medium. However, when the gas radiation, the fluid motion is stabilized. Radiation increases the thermal gradient which balance the effect of the concentration one in the plume region.

At $x_{CO_2} = 0.20$, gas radiation tends to slow down the mass driven flow in the lower part of the cavity but intensifies the thermal plume in the upper part. In addition, it also alters the thermal field: a slight increase of temperature is observed at intermediate and high levels and around the obstacle but a drop is found near the region close to the lower part of the vertical walls. The modification tendency in the concentration field is found similar for the thermal field except a slight augmentation of this quantity near the floor. Besides, introducing radiation reduces the total thermal transfer: the convective part near the vertical walls and the radiative transport along the obstacle upper surface. It also slightly decreases the mass transfer.

5.3 Conclusion

In this chapter, we analyze the influences of radiation of a gas mixture on the double diffusive convection, using the gray gas assumption and real gas model. The comparisons between the obtained results and the reference solutions (transparent case) reveal the transformations inside the enclosure which are summarized as:

- Cooperating flow

  Introducing gas radiation does not significantly affect the concentration field. It slightly accelerates the boundary layers but reduces the maximum velocity inside the plume. Volume radiation tends to thermally homogenize the medium. It decreases the temperature in the upper half of the cavity.

  Radiation slightly reduces the convective Nusselt number on the bounding walls of the cavity. But it marginally increases these quantities on the vertical surfaces of the obstacle and significantly augments those on the hot upper face. Besides, radiative transfer is attenuated by absorption of the medium, especially between the upper surface of the obstacle and ones of the cavity. In turn, the total heat transfer is lessened. Because the dynamic behavior is not much altered when radiation is accounted for, the mass transfer in the enclosure remains nearly unchanged.

  All these effects are strengthened when the medium becomes more absorbing (in the considered range of optical thicknesses and molar fraction).

- Opposing flow

  Generally, the movement in the lower part of the cavity is dominated by the mass gradient but at medium and high levels, the thermal one governs the flow. Radiation also intensifies the thermal plume. However, the increase of concentration in the axis of the plume limits the vertical motion and causes it to spread. In addition, gas radiation reduces the temperature in the regions near the obstacle vertical surfaces. Above the source, temperature is generally reduced compared to transparent case. The alteration of the concentration field are the same as for the thermal one except a slight increase of this quantity near the vertical cold walls in the lower part of the cavity. These effects are reinforced with the optical thickness.

  Particularly, in the $air - CO_2$ mixture, at $x_{CO_2} = 0.10$, radiation plays the role of stabilization of the unsteadiness found in the cavity when medium is considered transparent (due to the thermosolutal instability rather than other mechanisms).

  Introducing radiation reduces the total thermal transfer: the part by convective process near the vertical walls and the radiative transport along the obstacle upper surface. In addition, it slightly decreases the mass transfer.

Chapter 6

General Conclusion

In this thesis, we have numerically studied the influence of the radiation of gray gas and real gas mixture on the pure thermal as well as double diffusive natural convection. The considered configuration is a 3D cavity containing a small cubical obstacle located on its floor. This object is prescribed at a high temperature and high concentration in species while the vertical walls of the enclosure are set at low temperature and low concentration. The other horizontal surfaces of the cavity and the floor of the obstacle are assumed adiabatic and impermeable. In addition, the active walls are considered black while the rest are perfectly reflective. The enclosure is filled with either a gray gas or a binary real gas mixture ($air - H_2O$ or $air - CO_2$).

Due to the moderate variation in temperature and concentration, the convective fluid motion inside the cavity is simulated using the Boussinesq approximation. The fluid motion as well as the mass and thermal transport are simultated by Code Saturne v5.0.4. In addition, the radiative transfer equation is solved using the built-in Discrete Ordinates module of this code. However, some improvements in the generation of direction sets and a new SLW model for real gas mixtures have been added. The compatibility and ability of the Code Saturne and our own model have been validated with the previous results given in the references.

Different calculations on the coupled of thermal or double diffusive convection with radiation of gray gas medium or real gas mixtures have been performed. Concerning the thermal convention cases, different gray gases at various opacities and an $air - H_20$ mixture at three different molar fractions (5%, 10% and 20%) of the water vapor have been accounted for. While for double diffusive situations, depending on the mass to thermal buoyancy ratio (N), the fluid motions inside the cavity can be classed into opposing or cooperating flows. Like in the thermal convection, the calculation on the gray gas at several optical thicknesses and on real gas mixtures ($air - H_2O$ and $air - CO_2$) at different average mole fractions have been studied. The main influences of gas radiation on natural convection are summarized as:

Coupling thermal convection and radiation

Generally, in the steady results using either gray gas assumption or real gas model, introducing radiation non-uniformly accelerates the boundary layers of the enclosure and of the hot obstacle. It also makes moving some parts of the motionless fluid observed in the transparent cases. The thermal plume and its recirculation interfere and create shear flow patterns. In addition, radiation reduces the temperature in the upper half of the cavity, while, in the lower part, it lessens this quantity inside the plume but slightly increases around. The heat transfer is also impacted by radiation.

At the cold walls, the convective Nusselt numbers are risen up in the upper part but dropped off in the lower half. At the obstacle horizontal surface, this quantity is significantly increased. In turn, the total thermal transfer is reduced, especially the part by convective process on the vertical walls and by the radiative attenuation due to absorption along the obstacle upper surface. These impacts are enhanced with the optical thickness. Particularly, in gray gas simulations, when the optical thickness of the medium is unity, radiation yeilds a periodic flow. Its mechanism is due to the formation and vanishing of small vortices right above the hot upper surface of the obstacle and of the fluid flow cells in the regions next to the vertical walls of the enclosure. Then, at $\tau = 2$, the circulation becomes turbulent at $Ra = 5 \cdot 10^6$.

Coupling double diffusive convection and radiation

Concerning the cooperating flows, in a gray gas mixture, the presence of volume radiation slightly accelerates the boundary layers but reduces the maximum velocity inside the plume. It tends to lower the temperature in the upper part of the cavity, and thus, homogenizes the thermal field but a higher mass-to-thermal buoyancy ratio has an opposite effect. In all considered cases, the concentration field remains insensitive to radiation. In a real gas mixture ($air - H_2O$), the alteration of the thermal distribution is similar as for gray gas. However, these changes do not bring any notable modifications to the dynamic and the concentration fields. Consequently, the total heat exchange is reduced, while the mass transfer remains unchanged, compared to the transparent medium.

Regarding the cooperating flows in gray gas mixtures, firstly, at $N = -1$, radiation breaks the perfect symmetry between the thermal and the concentration fields. It sets the stagnant fluid (in transparent case) into motion with a mass driven movement in the lower part and a thermal one in the upper part of the cavity. With the increase of the optical thickness, radiation intensifies the thermal plume. However, the increase of concentration in the axis of the plume limits the vertical motion and causes it to spread. In addition, gas radiation reduces the temperature in the regions near the obstacle lateral surfaces. Above the source, the temperature is generally reduced compared to the transparent case. The concentration field is modified in the same manner as the thermal one, except a slight increase of this quantity near the vertical cold walls in the lower part of the cavity. At $N = -2$, gas radiation still affects the dynamic, the thermal and the concentration field, but with a weaker amplitude because of the domination of the mass gradient. In the $air - CO_2$ mixture, at $x_{CO_2} = 0.10$, accounting for radiation stabilizes the flow, which, in the transparent case, was turbulent (with a dominant frequency which maybe due to the thermosolutal instability). At $x_{CO_2} = 0.20$, the modifications tendencies are similar as in a gray gas mixture when mass forces dominate: a slight reinforcement of thermal plume but a slow down of mass driven motion. Concerning the heat and mass transfer, considering gas radiation slightly lessens these quantities.

Perspective

The performed studies reveal the effects of a gas radiation on flow structures and on heat and mass transfer. In perspective, the following points maybe considered:

- Gas mixture with more than two components: In real context of a combustion, the diffusing gas mixture contains many components that can absorb and emit radiation. Therefore, it is necessary to study simultaneously the effects of a multi-component gas mixture to the flow structure and heat transfer. This would involve a modification of the gas radiation model to include more than one absorbing species, through the multiplication method, for instance Solovjov and Webb [160].

- Turbulence regime. With larger temperature gradients or in larger enclosures, the Rayleigh number increases, turning the flow to transition or fully turbulent behaviors. The influences of gas radiation may switch on the flow characteristics (threshold values of Ra, for instance) and the turbulent quantities (intensities, frequencies, correlations) are remarkable problems. The question of a proper modeling of the turbulent-radiation interation may also arise.

- Ambient environment. These computations can be applied for the configuration containing a lower value of the reference temperature, of the temperature difference and of the average mole fraction of pollutant, which simulates the realistic conditions in the building environment. At room temperature, the concentration of radiant species are low (H_2O, especially) but may have a significant role over large distances (several meters).

- Non-Boussinesq simulations. For highly anisothermal and heterogeneous gas mixtures, the thermo-physical properties may significantly vary from one point to another. A non-Boussinesq model is then necessary to correctly simulate the flow behavior. A low Mach model could be implemented.

- Varying the cavity parameters. Cavity size, ratio between the enclosure and the obstacle are key parameters, as well as the surface emissivities.

- Experimental approach. For evaluating the results of the numerical researches, the realistic way is the comparison with experiments. The results from the experiments can help validating the numerical studies. It however remains a challenge to build a device where gas concentration may be prescibed at the boundaries.

- Parallel calculation. The radiative transfer equation can be independently solved for each gray gas and each discrete direction and then, the values of radiative source term (at each cell) and of the incident flux (at each boundary control surface) are summed up. Therefore, these calculations can be simultaneously carried out with the help of parallel computing libraries (OpenMP, Cuda,...). A pioneering work in that field was performed by Cadet [161].

Appendix A

Calculation of the physical properties of a binary mixture

This appendix is using material originating from S.Laouar-Meftah's PhD thesis [32]. The thermal physical properties of the $air - CO_2$ or $air - H_2O$ mixtures are calculated at T_{ref} and C_{ref} (the total pressure P is constant and equals the atmosphere pressure) by using the perfect gas law which are described below. In which, the index i designates a pure absorbing component of the mixture (CO_2 or H_2O) whose thermal physical properties at reference state (T_{ref}, C_{ref}) are given as below:

- Molar density of mixture

$$M = (1 - x_i)M_{air} + x_i M_i \tag{A.1}$$

  x_i and M_i stand for respectively the molar fraction and molar density of absorbing component i of the mixture.

- Mass fraction of the absorbing component i of the mixture

$$y_i = x_i \frac{M_i}{M} \tag{A.2}$$

- Density of the mixture

$$\rho_0 = \frac{PM}{RT_{ref}} \tag{A.3}$$

- Specific heat of the mixture

$$C_p = (1 - y_i)C_{p,air} + y_i C_{p,i} \tag{A.4}$$

- Coefficients of thermal and mass expansion
  Thermal expansion coefficient:

$$\beta_T = -\frac{1}{\rho_0}\left(\frac{\partial \rho}{\partial T}\right)_{P,C} \approx \frac{1}{T_{ref}} \tag{A.5}$$

  Mass expansion coefficient:

$$\beta_C = -\frac{1}{\rho_0}\left(\frac{\partial \rho}{\partial C}\right)_{P,T} \approx \frac{M_{air} - M_i}{\rho_0} \tag{A.6}$$

- Thermal conductivity and dynamic viscosity of the mixture
  The thermal conductivity (λ) and dynamic viscosity (μ) of the mixture are estimated by the formula of Wilke-Wassiljewa ([162]):

$$f = \frac{(1-x_i) f_{air}}{(1-x_i)\phi_{air,air} + x_i \phi_{air,i}} + \frac{x_i f_i}{(1-x_i)\phi_{i,air} + x_i \phi_{i,i}} \tag{A.7}$$

where

$$\phi_{air,air} = \phi_{i,i} = 1 \tag{A.8}$$

$$\phi_{air,i} = \frac{\left[1 + \left(\frac{f_{air}}{f_i}\right)^{0.5} \left(\frac{M_{air}}{M_i}\right)^{0.25}\right]^2}{\left[8\left(1 + \frac{M_{air}}{M_i}\right)\right]^{0.5}} \tag{A.9}$$

$$\phi_{i,air} = \frac{\left[1 + \left(\frac{f_i}{f_{air}}\right)^{0.5} \left(\frac{M_i}{M_{air}}\right)^{0.25}\right]^2}{\left[8\left(1 + \frac{M_i}{M_{air}}\right)\right]^{0.5}} \tag{A.10}$$

and with f is λ or μ
In addition, the thermal diffusivity (α) and kinematic viscosity (ν) are obtained from the expressions:

$$\alpha = \frac{\lambda}{\rho_0 C_p} \tag{A.11}$$

$$\nu = \frac{\mu}{\rho_0} \tag{A.12}$$

- Mass diffusivity of a species into the environment (in this case CO_2/H_2O into air) is calculated by the expression of Fuller and al ([162]):

$$\frac{D_i(T,P)}{D_i(T_1,P_1)} = \frac{P}{P_1}\left(\frac{T}{T_1}\right)^{1.75} \tag{A.13}$$

where i is either CO_2 or H_2O and, $T_1 = 317K$, $P_1 = 1\ atm$, $D_{CO_2} = 1.77 \times 10^{-5}$ m^2/s and $D_{H_2O} = 2.88 \times 10^{-5}\ m^2/s$

Appendix B

Implantation of our model in Code Saturne

We here refer to Code Saturne version 5.0.4.

B.1 Change in the directions set

Subroutine: **cs_rad_transfer_dir(void)** in file **cs_rad_transfer_dir.c**

In this file, we have changed the values associated to discrete directions and their weights for the S_8 quadrature by the ones provided in Balsara [27]. They are presented below:

Parameter	Old value	New value
vec[0]	0.1422555	0.1691276797
vec[1]	0.5773503	0.5773502692
vec[2]	0.8040087	0.7987881413
vec[3]	0.9795543	0.9709745908
weight[0]	0.0992284	0.1598388991
weight[1]	0.1712359	0.146138939
weight[2]	0.4617179	0.173346115

Table B.1: Changes in the S_8 quadrature

B.2 Insertion of our code into the radiative module of Code Saturne

First, we list here our own developed codes. They are motivated by the works of V P Solojov and D Lemonnier.

file: user.h: new library to declare new variables and functions.

```
#ifndef __USER__
#define __USER__

#include "cs_defs.h"
#include "stdio.h"
BEGIN_C_DECLS

 int speca; // 1: H20 2:C02
 int Nggmax; // Number of gray gas
```

```
int P1;
cs_real_t Ru ; //universal gas constant
cs_real_t xaref ; // reference molar fraction
cs_real_t Tref ; // reference temperature
cs_real_t P ; // Normalized pressure
cs_real_t *ka; // reference absorption coeffiecient
cs_real_t *xa; // cell center molar fraction for first absorbant
    ↪ component
cs_real_t *xa1;
cs_real_t kmin; // min absorption cross section
cs_real_t kmax; // max absorption cross section
cs_real_t *xabd; // boundary molar fraction for first absorbant
    ↪ component
cs_real_t *xabd1;
cs_real_t *tempbd; // boundary temperature
cs_real_t Nref; // reference molar density
cs_real_t C[71]; // discrete absorption cross section for tabulated
    ↪ data
cs_real_t PP[10]; // discrete pressure for tabulated data
cs_real_t T[28]; // discrete temperature for tabulated data
cs_real_t YY[9]; // discrete molar fraction for tabulated data
cs_real_t Fdata1[500976]; // Storage of ALBDF
cs_real_t Fdata2[500976];
cs_real_t Fdata3[55664];
cs_real_t Fdata4[55664];

cs_real_t xgs[100]; // parameter of gaussian quadrature
cs_real_t wgs[100];

// initialize required data for SLW model
void setup_uservalue(void);



// locate index of a value of an array
int locate(cs_real_t xx[],
           int n,
           cs_real_t x);

// Generate parameter of gaussian quadrature
void gauss(int Ngmax,
           cs_real_t x[],
           cs_real_t w[]);

// Import necessary spectral data
void data_read(cs_real_t Fdata1[],
               cs_real_t Fdata2[],
               int molecule,
               int P1);
```

```
// Initialize discrete values of concentration, pressure, temperature
    ↪ and molar fraction
 void data_set(void);

// Calculate ALBDF at a thermodynamic state of a binary air-absorbnant
    ↪ component mixture
 cs_real_t FCC(cs_real_t Cabs,
                         cs_real_t Tg,
                         cs_real_t Tb,
                         cs_real_t Y,
                         cs_real_t P,
                         int P1,
                         int molecule,
                         cs_real_t C[],
                         cs_real_t Fdata1[],
                         cs_real_t Fdata2[]);

// Calculate ALBDF for general case.
 cs_real_t FMIX(cs_real_t Cabs,
                             cs_real_t Tg,
                             cs_real_t Tb,
                             cs_real_t Y1,
                             cs_real_t Y2,
                             cs_real_t P,
                             int P1,
                             cs_real_t C[]);

// Determine the absorption cross section equivalent to a ALBDF value
    ↪ at a thermaldynamic state
 cs_real_t CFMIX(cs_real_t F,
                              cs_real_t Tg,
                              cs_real_t Tb,
                              cs_real_t Y1,
                              cs_real_t Y2,
                              cs_real_t P,
                              int P1,
                              cs_real_t C[]);

// SLW model based on Rank-Correlated associated to the lookup table
    ↪ method
 void SLW_RC_LBL(cs_real_t tempk[],
                              cs_real_t tempbd[],
                              int Ngmax,
                              cs_real_t Tref,
                              cs_real_t Y1REF,
                              cs_real_t Y2REF,
                              cs_real_t Y1LOC[],
                              cs_real_t Y2LOC[],
                              cs_real_t Y1FLOC[],
                              cs_real_t Y2FLOC[],
                              unsigned long n_cells,
```

```
                                 unsigned long n_faces,
                                 cs_real_t kgi[],
                                 cs_real_t agi[],
                                 cs_real_t agbi[]);


END_C_DECLS
#endif
```

****

file: user.c: an user file to store user defined functions.

```
#include "cs_defs.h"
#include "stdio.h"
#include "math.h"
#include "user.h"
#include "bft_error.h"
#include "bft_mem.h"
#include "bft_printf.h"

// This function defines the necessary parameters for SLW model
void setup_uservalue(void){
       speca = 2; // 1: H2O 2: CO2
    Nggmax = 5;// Number of gray gas
    P = 1; // Normalized pressure
    Ru = 8.31451; // Universal gas constant
    Tref = 555.0; // Reference temperature
    xaref = 0.10; // Initial mole fraction
 }

// LOOK-UP TABLE METHOD

// determine the location of a value in a sorted list
int locate(cs_real_t xx[],
          int n,
          cs_real_t x){
  unsigned long ju,jm,jl;
  int ascnd;
  int j;

  jl = 0;
  ju = n+1;
  ascnd = (xx[n] >= xx[1]);
  while (ju-jl > 1){
    jm = (ju+jl)/2;
    if (x >= xx[jm] == ascnd)
      jl = jm;
    else
      ju = jm;
  }
  if (x == xx[0]) j = 0;
```

```
  else if (x == xx[n]) j = n-1;
  else j = jl;
  return j;
}
// Gaussian quadratures with order of Ngmax
void gauss(int Ngmax,
          cs_real_t x[],
          cs_real_t w[]){
  int m,i,j,n;
  double z1,z,zm,pp,p2,p3,p1,x2,x1,xm,xl;
  double eps = 3e-14;
  double pi = 2.0*asin(1.0);


  x1 = -1.0;
  x2 = 1.0;
  n = 2*Ngmax;

  m = (n+1)/2;
  xm = 0.5*(x2+x1);
  xl = 0.5*(x2-x1);

  for (i = 1; i <= m; i++)
  {
    z=cos(pi*(i-0.25)/(n+0.5));
    do{
      p1=1.0;
      p2=0.0;
      for ( j = 1; j <= n; j++)
      {
        p3=p2;
        p2=p1;
        p1=((2.0*j-1.0)*z*p2-(j-1.0)*p3)/j;
      }
      pp=n*(z*p1-p2)/(z*z-1.0);
      z1=z;
      z=z1-p1/pp;
    }while(fabs(z-z1)>eps);

    x[i]=xm-xl*z;
    x[n+1-i]=xm+xl*z;
    w[i]=2.0*xl/((1.0-z*z)*pp*pp);
    w[n+1-i]=w[i];
  }

  for ( i = 1; i <= n; i++)
  {
    x[i]=x[n/2+i];
    w[i]=w[n/2+i];
  }
```

```
}
// import data to temporary arrays
void data_read(cs_real_t Fdata1[],
               cs_real_t Fdata2[],
               int molecule,
               int P1){
  FILE *f1;
  FILE *f2;
  unsigned long n,i;
  if (molecule == 1){
    if (P1 == 0){
      f1 = fopen("/ALBDF_DATA/h2o_p0_1.txt","r");
      f2 = fopen("/ALBDF_DATA/h2o_p0_25.txt","r");
    }
    if (P1 == 1){
      f1 = fopen("/ALBDF_DATA/h2o_p0_25.txt","r");
      f2 = fopen("/ALBDF_DATA/h2o_p0_5.txt","r");
    }
    if (P1 == 2){
      f1 = fopen("/ALBDF_DATA/h2o_p0_5.txt","r");
      f2 = fopen("/ALBDF_DATA/h2o_p1.txt","r");
    }
    if (P1 == 3){
      f1 = fopen("/ALBDF_DATA/h2o_p1.txt","r");
      f2 = fopen("/ALBDF_DATA/h2o_p2.txt","r");
    }
    if (P1 == 4){
      f1 = fopen("/ALBDF_DATA/h2o_p2.txt","r");
      f2 = fopen("/ALBDF_DATA/h2o_p4.txt","r");
    }
    if (P1 == 5){
      f1 = fopen("/ALBDF_DATA/h2o_p4.txt","r");
      f2 = fopen("/ALBDF_DATA/h2o_p8.txt","r");
    }
    if (P1 == 6){
      f1 = fopen("/ALBDF_DATA/h2o_p8.txt","r");
      f2 = fopen("/ALBDF_DATA/h2o_p15.txt","r");
    }
    if (P1 == 7){
      f1 = fopen("/ALBDF_DATA/h2o_p15.txt","r");
      f2 = fopen("L/ALBDF_DATA/h2o_p30.txt","r");
    }
    if (P1 > 7){
      f1 = fopen("/ALBDF_DATA/h2o_p30.txt","r");
      f2 = fopen("/ALBDF_DATA/h2o_p50.txt","r");
    }
    for (i = 0; i < 500976; i++){
      fscanf(f1,"%lf",Fdata1+i);
      fscanf(f2,"%lf",Fdata2+i);
    }
    fclose(f1);
```

```
    fclose(f2);
  }

  if (molecule == 2){
    if (P1 == 0){
      f1 = fopen("/ALBDF_DATA/co2_p0_1.txt","r");
      f2 = fopen("/ALBDF_DATA/co2_p0_25.txt","r");
    }
    if (P1 == 1){
      f1 = fopen("/ALBDF_DATA/co2_p0_25.txt","r");
      f2 = fopen("/ALBDF_DATA/co2_p0_5.txt","r");
    }
    if (P1 == 2){
      f1 = fopen("/ALBDF_DATA/co2_p0_5.txt","r");
      f2 = fopen("/ALBDF_DATA/co2_p1.txt","r");
    }
    if (P1 == 3){
      f1 = fopen("/ALBDF_DATA/co2_p1.txt","r");
      f2 = fopen("/ALBDF_DATA/co2_p2.txt","r");
    }
    if (P1 == 4){
      f1 = fopen("/ALBDF_DATA/co2_p2.txt","r");
      f2 = fopen("/ALBDF_DATA/co2_p4.txt","r");
    }
    if (P1 == 5){
      f1 = fopen("/ALBDF_DATA/co2_p4.txt","r");
      f2 = fopen("/ALBDF_DATA/co2_p8.txt","r");
    }
    if (P1 == 6){
      f1 = fopen("/ALBDF_DATA/co2_p8.txt","r");
      f2 = fopen("/ALBDF_DATA/co2_p15.txt","r");
    }
    if (P1 == 7){
      f1 = fopen("/ALBDF_DATA/co2_p15.txt","r");
      f2 = fopen("/ALBDF_DATA/co2_p30.txt","r");
    }
    if (P1 > 7){
      f1 = fopen("/ALBDF_DATA/co2_p30.txt","r");
      f2 = fopen("/ALBDF_DATA/co2_p50.txt","r");
    }
    for (i = 0; i < 55664; i++){
      fscanf(f1,"%lf",Fdata1+i);
      fscanf(f2,"%lf",Fdata2+i);
    }
    fclose(f1);
    fclose(f2);
  }
}

// import data
void data_set(void){
```

```
  for (int i = 0; i < 71; i++)
    {
      double ii = i;
      C[i] = 1e-4*pow((1000/1e-4),(ii/(70)));
    }
/
    T[0] = 300.0;
    for (int i = 1; i < 28; i++)
    {
      T[i] = T[i-1] + 100;
    }

    YY[0] = 0; YY[1] = 0.05; YY[2] = 0.1; YY[3] = 0.2; YY[4] = 0.3;
    YY[5] = 0.4; YY[6] = 0.6; YY[7] = 0.8; YY[8] = 1.0;

    PP[0] = 0.1; PP[1] = 0.25; PP[2] = 0.5; PP[3] = 1; PP[4] = 2;
    PP[5] = 4; PP[6] = 8; PP[7] = 15; PP[8] = 30; PP[9] = 50;

  P1 = locate(PP,9,P);

  data_read(Fdata1,Fdata2,1,P1);
  data_read(Fdata3,Fdata4,2,P1);

  gauss(Nggmax-1,xgs,wgs);
}

// Multi interpolation for calculation of ALBDF
cs_real_t FCC(cs_real_t Cabs,
        cs_real_t Tg,
        cs_real_t Tb,
        cs_real_t Y,
        cs_real_t P,
        int P1,
        int molecule,
        cs_real_t C[],
        cs_real_t Fdata1[],
        cs_real_t Fdata2[]){
  int i,j,k,l,m;
  cs_real_t F;
  cs_real_t Fint[16];
  if (Cabs < C[0]) Cabs = C[0];
  if (Cabs > C[70]) Cabs = C[70];
  if (Tg < 300) Tg = 300;
  if (Tg > 3000) Tg = 3000;
  if (Tb < 300) Tb = 300;
  if (Tb > 3000) Tb = 3000;


  m = locate(T,27,Tg);
  l = locate(T,27,Tb);
  k = locate(C,70,Cabs);
```

```
if (molecule == 1){
  YY[0] = 0; YY[1] = 0.05; YY[2] = 0.1; YY[3] = 0.2; YY[4] = 0.3;
  YY[5] = 0.4; YY[6] = 0.6; YY[7] = 0.8; YY[8] = 1.0;

  j = locate(YY,8,Y);

  i = j*55664+m*1988+l*71+k;

Fint[0]=Fdata1[i]+(Fdata2[i]-Fdata1[i])*(P-PP[P1])/(PP[P1+1]-PP[P1]);
Fint[1]=Fdata1[i+55664]+(Fdata2[i+55664]-Fdata1[i+55664])*(P-PP[P1])
    ↪ /(PP[P1+1]-PP[P1]);
Fint[2]=Fdata1[i+1]+(Fdata2[i+1]-Fdata1[i+1])*(P-PP[P1])/(PP[P1+1]-PP
    ↪ [P1]);
Fint[3]=Fdata1[i+55665]+(Fdata2[i+55665]-Fdata1[i+55665])*(P-PP[P1])
    ↪ /(PP[P1+1]-PP[P1]);
Fint[4]=Fdata1[i+71]+(Fdata2[i+71]-Fdata1[i+71])*(P-PP[P1])/(PP[P1
    ↪ +1]-PP[P1]);
Fint[5]=Fdata1[i+55735]+(Fdata2[i+55735]-Fdata1[i+55735])*(P-PP[P1])
    ↪ /(PP[P1+1]-PP[P1]);
Fint[6]=Fdata1[i+72]+(Fdata2[i+72]-Fdata1[i+72])*(P-PP[P1])/(PP[P1
    ↪ +1]-PP[P1]);
Fint[7]=Fdata1[i+55736]+(Fdata2[i+55736]-Fdata1[i+55736])*(P-PP[P1])
    ↪ /(PP[P1+1]-PP[P1]);
Fint[8]=Fdata1[i+1988]+(Fdata2[i+1988]-Fdata1[i+1988])*(P-PP[P1])/(PP
    ↪ [P1+1]-PP[P1]);
Fint[9]=Fdata1[i+57652]+(Fdata2[i+57652]-Fdata1[i+57652])*(P-PP[P1])
    ↪ /(PP[P1+1]-PP[P1]);
Fint[10]=Fdata1[i+1989]+(Fdata2[i+1989]-Fdata1[i+1989])*(P-PP[P1])/(
    ↪ PP[P1+1]-PP[P1]);
Fint[11]=Fdata1[i+57653]+(Fdata2[i+57653]-Fdata1[i+57653])*(P-PP[P1])
    ↪ /(PP[P1+1]-PP[P1]);
Fint[12]=Fdata1[i+2059]+(Fdata2[i+2059]-Fdata1[i+2059])*(P-PP[P1])/(
    ↪ PP[P1+1]-PP[P1]);
Fint[13]=Fdata1[i+57723]+(Fdata2[i+57723]-Fdata1[i+57723])*(P-PP[P1])
    ↪ /(PP[P1+1]-PP[P1]);
Fint[14]=Fdata1[i+2060]+(Fdata2[i+2060]-Fdata1[i+2060])*(P-PP[P1])/(
    ↪ PP[P1+1]-PP[P1]);
Fint[15]=Fdata1[i+57724]+(Fdata2[i+57724]-Fdata1[i+57724])*(P-PP[P1])
    ↪ /(PP[P1+1]-PP[P1]);

Fint[0]=Fint[0]+(Fint[1]-Fint[0])*(Y-YY[j])/(YY[j+1]-YY[j]);
Fint[1]=Fint[2]+(Fint[3]-Fint[2])*(Y-YY[j])/(YY[j+1]-YY[j]);
Fint[2]=Fint[4]+(Fint[5]-Fint[4])*(Y-YY[j])/(YY[j+1]-YY[j]);
Fint[3]=Fint[6]+(Fint[7]-Fint[6])*(Y-YY[j])/(YY[j+1]-YY[j]);
Fint[4]=Fint[8]+(Fint[9]-Fint[8])*(Y-YY[j])/(YY[j+1]-YY[j]);
Fint[5]=Fint[10]+(Fint[11]-Fint[10])*(Y-YY[j])/(YY[j+1]-YY[j]);
Fint[6]=Fint[12]+(Fint[13]-Fint[12])*(Y-YY[j])/(YY[j+1]-YY[j]);
Fint[7]=Fint[14]+(Fint[15]-Fint[14])*(Y-YY[j])/(YY[j+1]-YY[j]);

Fint[0]=Fint[0]+(Fint[1]-Fint[0])*(Cabs-C[k])/(C[k+1]-C[k]);
```

```
  Fint[1]=Fint[2]+(Fint[3]-Fint[2])*(Cabs-C[k])/(C[k+1]-C[k]);
  Fint[2]=Fint[4]+(Fint[5]-Fint[4])*(Cabs-C[k])/(C[k+1]-C[k]);
  Fint[3]=Fint[6]+(Fint[7]-Fint[6])*(Cabs-C[k])/(C[k+1]-C[k]);

  Fint[0]=Fint[0]+(Fint[1]-Fint[0])*(Tb-T[l])/(T[l+1]-T[l]);
  Fint[1]=Fint[2]+(Fint[3]-Fint[2])*(Tb-T[l])/(T[l+1]-T[l]);

  F=Fint[0]+(Fint[1]-Fint[0])*(Tg-T[m])/(T[m+1]-T[m]);
  }

  if (molecule>1)
{

  i=m*1988+l*71+k;

  // Interpolate in P
  Fint[0]=Fdata1[i]+(Fdata2[i]-Fdata1[i])*(P-PP[P1])/(PP[P1+1]-PP[P1]);
  Fint[1]=Fdata1[i+1]+(Fdata2[i+1]-Fdata1[i+1])*(P-PP[P1])/(PP[P1+1]-PP
      ↪ [P1]);
  Fint[2]=Fdata1[i+71]+(Fdata2[i+71]-Fdata1[i+71])*(P-PP[P1])/(PP[P1
      ↪ +1]-PP[P1]);
  Fint[3]=Fdata1[i+72]+(Fdata2[i+72]-Fdata1[i+72])*(P-PP[P1])/(PP[P1
      ↪ +1]-PP[P1]);
  Fint[4]=Fdata1[i+1988]+(Fdata2[i+1988]-Fdata1[i+1988])*(P-PP[P1])/(PP
      ↪ [P1+1]-PP[P1]);
  Fint[5]=Fdata1[i+1989]+(Fdata2[i+1989]-Fdata1[i+1989])*(P-PP[P1])/(PP
      ↪ [P1+1]-PP[P1]);
  Fint[6]=Fdata1[i+2059]+(Fdata2[i+2059]-Fdata1[i+2059])*(P-PP[P1])/(PP
      ↪ [P1+1]-PP[P1]);
  Fint[7]=Fdata1[i+2060]+(Fdata2[i+2060]-Fdata1[i+2060])*(P-PP[P1])/(PP
      ↪ [P1+1]-PP[P1]);

  // Interpolate in C
  Fint[0]=Fint[0]+(Fint[1]-Fint[0])*(Cabs-C[k])/(C[k+1]-C[k]);
  Fint[1]=Fint[2]+(Fint[3]-Fint[2])*(Cabs-C[k])/(C[k+1]-C[k]);
  Fint[2]=Fint[4]+(Fint[5]-Fint[4])*(Cabs-C[k])/(C[k+1]-C[k]);
  Fint[3]=Fint[6]+(Fint[7]-Fint[6])*(Cabs-C[k])/(C[k+1]-C[k]);

  // Interpolate in Tb
  Fint[0]=Fint[0]+(Fint[1]-Fint[0])*(Tb-T[l])/(T[l+1]-T[l]);
  Fint[1]=Fint[2]+(Fint[3]-Fint[2])*(Tb-T[l])/(T[l+1]-T[l]);

  // Interpolate in Tg
  F=Fint[0]+(Fint[1]-Fint[0])*(Tg-T[m])/(T[m+1]-T[m]);
}

return F;

}
// General function for calling the interpolation for each component
cs_real_t FMIX(cs_real_t Cabs,
```

```
      cs_real_t Tg,
      cs_real_t Tb,
      cs_real_t Y1,
      cs_real_t Y2,
      cs_real_t P,
      int P1,
      cs_real_t C[]){

  cs_real_t F1,F2;
  cs_real_t CC1,CC2;
  cs_real_t Y;
  cs_real_t F;
  int molecule;
  if (speca == 1) // H2O
  {
      molecule =1;
      Y=Y1;
      F1=FCC(Cabs,Tg,Tb,Y,P,P1,molecule,C,Fdata1,Fdata2);
      F=F1;
  }

  if (speca==2) // CO2
  {
      molecule=2;
      Y=Y2;
      F2=FCC(Cabs,Tg,Tg,Y,P,P1,molecule,C,Fdata3,Fdata4);
      F=F2;
  }
  return F;
}

// inverse for determing Cross section from F
cs_real_t CFMIX(cs_real_t F,
                cs_real_t Tg,
                cs_real_t Tb,
                cs_real_t Y1,
                cs_real_t Y2,
                cs_real_t P,
                int P1,
                cs_real_t C[]){

  cs_real_t CFF,FMIN,FMAX,FAVE,FF1,FF2;
  unsigned long jl,jm,ju,jf;
  int ascnd;
// Determine the minimum and maximun value of F based of given value of
    ↪ C
  FMIN = FMIX(C[0],Tg,Tb,Y1,Y2,P,P1,C);
  FMAX = FMIX(C[70],Tg,Tb,Y1,Y2,P,P1,C);

  if (F < FMIN) CFF = 0.0;
  else if (F > FMAX) CFF = C[70];
```

```
  else {
    jl = 0;
    ju = 71;
    ascnd = (FMAX >= FMIN);
    while(ju-jl > 1){
      jm = (ju+jl)/2;
      FAVE = FMIX(C[jm],Tg,Tb,Y1,Y2,P,P1,C);
      if (F >= FAVE == ascnd)
        jl = jm;
      else
        ju = jm;
    }

    if (F == FMIN) jf = 0;
    else if (F == FMAX) jf = 69;
    else jf = jl;
    FF1 = FMIX(C[jf],Tg,Tb,Y1,Y2,P,P1,C);
    FF2 = FMIX(C[jf+1],Tg,Tb,Y1,Y2,P,P1,C);

    if((FF2-FF1) > 0.0)
      CFF = C[jf] + (F-FF1)/(FF2-FF1)*(C[jf+1]-C[jf]);
    else
      CFF = C[jf];
  }
  return CFF;
}
// Calculate the absorption coefficent and the weights
void SLW_RC_LBL(cs_real_t tempk[],
                cs_real_t tempbd[],
                int Ngmax,
                cs_real_t Tref,
                cs_real_t Y1REF,
                cs_real_t Y2REF,
                cs_real_t Y1LOC[],
                cs_real_t Y2LOC[],
                cs_real_t Y1FLOC[],
                cs_real_t Y2FLOC[],
                unsigned long n_cells,
                unsigned long n_faces,
                cs_real_t kgi[],
                cs_real_t agi[],
                cs_real_t agbi[]){
// Declear local variables
  cs_real_t Cmin = 1e-4;
  cs_real_t Cmax = 600.0;

  cs_real_t CTREF[Ngmax];
  cs_real_t FTREF[Ngmax];
  cs_real_t FCREF[Ngmax];

  cs_real_t *CTLOC;
```

```
  cs_real_t *CCLOC;
  cs_real_t *FTLOC;
  cs_real_t *CTLOC2;
  cs_real_t *FTLOC2;
  cs_real_t ftwg[Ngmax];
  cs_real_t Fmin = 0.0;
  cs_real_t Fmax = 1.0;

 // Allocate memory for dynamic variables
  BFT_MALLOC(CTLOC,n_cells*Ngmax,cs_real_t);
  BFT_MALLOC(CCLOC,n_cells*Ngmax,cs_real_t);
  BFT_MALLOC(FTLOC,n_cells*Ngmax,cs_real_t);
  BFT_MALLOC(CTLOC2,n_faces*Ngmax,cs_real_t);
  BFT_MALLOC(FTLOC2,n_faces*Ngmax,cs_real_t);



  for (int j = 0; j < Ngmax; j++)
  {
     ftwg[j]=0.0;
  }

  for (int j = 1; j < Ngmax; j++)
  {
    for (int i = 1; i <= j; i++)
    {
      ftwg[j]=ftwg[j]+wgs[i];
    }
  }

 // Generate F~ values based on Gaussian quadrature.
  for (int j = 0; j < Ngmax; j++)
  {
    FTREF[j]=Fmin+(Fmax-Fmin)*ftwg[j];
    CTREF[j]=CFMIX(FTREF[j],Tref,Tref,Y1REF,Y2REF,P,P1,C);
  }

  for (int j = 1; j < Ngmax; j++)
  {
    FCREF[j]=Fmin+(Fmax-Fmin)*xgs[j];
  }
//
  for (int iel = 0; iel < n_cells; iel++)
  {
    for (int j = 0; j < Ngmax; j++)
    {
      double FR=FTREF[j];
      CTLOC[iel+j*n_cells]=CFMIX(FR,tempk[iel],Tref,Y1LOC[iel],Y2LOC[iel
          ↪ ],P,P1,C);
    }
  }
```

```
 for (int iel = 0; iel < n_cells; iel++)
 {
   for (int j = 0; j < Ngmax; j++)
   {
     if (CTLOC[iel+j*n_cells]<Cmin)
     {
       CTLOC[iel+j*n_cells]=Cmin;
     }
     FTLOC[iel+j*n_cells]=FMIX(CTLOC[iel+j*n_cells],tempk[iel],tempk[
         ↪ iel],Y1LOC[iel],Y2LOC[iel],P,P1,C);
   }
 }

 for (int ifac = 0; ifac < n_faces; ifac++)
 {
   for (int j = 0; j < Ngmax; j++)
   {
     double FR=FTREF[j];
     CTLOC2[ifac+j*n_faces]=CFMIX(FR,tempbd[ifac],Tref,Y1FLOC[ifac],
         ↪ Y2FLOC[ifac],P,P1,C);
   }
 }

 for (int ifac = 0; ifac < n_faces; ifac++)
 {
   for (int j = 0; j < Ngmax; j++)
   {
     if (CTLOC2[ifac+j*n_faces]<Cmin)
     {
       CTLOC2[ifac+j*n_faces]=Cmin;
     }
     FTLOC2[ifac+j*n_faces]=FMIX(CTLOC2[ifac+j*n_faces],tempbd[ifac],
         ↪ tempbd[ifac],Y1FLOC[ifac],Y2FLOC[ifac],P,P1,C);
   }
 }

// absorption coefficent and weights for gray gases
 for (int j = 1; j < Ngmax; j++)
 {
   for (int iel = 0; iel < n_cells; iel++)
   {
   if (speca==1)
         {
               kgi[iel+j*n_cells] = P*101325/Ru/tempk[iel]*Y1LOC[iel]*
                   ↪ CCLOC[iel+j*n_cells];
         }
   if (speca==2)
    {
       kgi[iel+j*n_cells] = P*101325/Ru/tempk[iel]*Y2LOC[iel]*CCLOC[iel
           ↪ +j*n_cells];
```

```
     }
// weights at cells
      agi[iel+j*n_cells] = FTLOC[iel+j*n_cells]-FTLOC[iel+(j-1)*n_cells
          ↪ ];
    }
// weights at boundary faces
    for (int ifac = 0; ifac < n_faces; ifac++)
    {
      agbi[ifac+j*n_faces] = FTLOC2[ifac+j*n_faces]-FTLOC2[ifac+(j-1)*
          ↪ n_faces];
    }
  }

// for clear gas
  for (int iel = 0; iel < n_cells; iel++)
  {
    kgi[iel] = 0.0;
    agi[iel] = FTLOC[iel];
  }

  for (int ifac = 0; ifac < n_faces; ifac++)
  {
    agbi[ifac] = FTLOC2[ifac];
  }


  BFT_FREE(CTLOC);
  BFT_FREE(CCLOC);
  BFT_FREE(FTLOC);
  BFT_FREE(CTLOC2);
  BFT_FREE(FTLOC2);
}
```

For the purpose of the implementation of our SLW model into Code Saturne, we have modified some built-in subroutines and inserted our self developed code. This procedure are presented in the following:

- In file **cs_rad_transfer_options.c**, in function *cs_rad_transfer_options(void)*:
  set $rt\_params- > imoadf = 1$;
  $if(rt\_params- > imoadf == 1) rt\_params- > nwsgg = Nggmax$;
  and call new two function:
  $setup\_uservalue()$;
  $data\_set()$;

- In file **cs_rad_transfer_solve.c**, in function *cs_rad_transfer_solve()*, add the following code before solving the RTE:

```
                  BFT_MALLOC(ka,nwsgg,cs_real_t);
                  BFT_MALLOC(xa,n_cells_ext,cs_real_t);
                  BFT_MALLOC(xa1,n_cells_ext,cs_real_t);
                  BFT_MALLOC(xa2,n_cells_ext,cs_real_t);
```

```
cs_field_t *f_conc = NULL;
f_conc = cs_field_by_name("concentration");



for(cs_lnum_t iel = 0; iel < n_cells; iel++){
xa[iel] = f_conc->val[iel]*Ru*Tref/P/101325.0;
xa1[iel] = 0.0;
xa2[iel] = 0.0;
}

cs_real_t xa1ref = 0.0;
cs_real_t xa2ref = 0.0;

//
// calculation of weights at boundaries

cs_real_t *xabd;
cs_real_t *tempbd;
BFT_MALLOC(tempbd,n_b_faces,cs_real_t);
BFT_MALLOC(xabd1,n_b_faces,cs_real_t);
BFT_MALLOC(xabd,n_b_faces,cs_real_t);
BFT_MALLOC(xabd2,n_b_faces,cs_real_t);
cs_field_t *f_b_temp = NULL;
cs_field_t *f_b_conc = NULL;
f_b_temp = cs_field_by_name("boundary_temperature");
f_b_conc = cs_field_by_name("boundary_concentration
    ↪ ");


for (cs_lnum_t ifac = 0; ifac < n_b_faces; ifac++){
tempbd[ifac] = f_b_temp->val[ifac] ;

xabd[ifac] = f_b_conc->val[ifac]*Ru*Tref/P/101325.0;
xabd1[ifac]=0.0;
xabd2[ifac]=0.0;
}
if (speca==1) {
SLW_RC_LBL(tempk,tempbd,nwsgg,Tref,xaref,xa1ref,
    ↪ xa2ref,xa,xa1,xa2,xabd,xabd1,xabd2,n_cells,
    ↪ n_b_faces,kgi,agi,agbi);
}
else if (speca == 2) {
SLW_RC_LBL(tempk,tempbd,nwsgg,Tref,xa1ref,xaref,
    ↪ xa2ref,xa1,xa,xa2,xabd1,xabd,xabd2,n_cells,
    ↪ n_b_faces,kgi,agi,agbi);
}
SLW_RC_LBL(tempk,tempbd,nwsgg,Tref,xa1ref,xaref,
    ↪ xa2ref,xa1,xa,xa2,xabd1,xabd,xabd2,n_cells,
    ↪ n_b_faces,kgi,agi,agbi);
```

and the following lines at the end of the function:

```
BFT_FREE(ka);
BFT_FREE(xa);
BFT_FREE(xa1);
BFT_FREE(xa2);
BFT_FREE(xabd);
BFT_FREE(xabd1);
BFT_FREE(xabd2);
BFT_FREE(tempbd);.
```

Appendix C

Calculation of the Q-criterion

The tensor of velocity gradient $\nabla \mathbf{v}$ can be written as:

$$\begin{aligned}\nabla \mathbf{v} &= \frac{1}{2}(\nabla \mathbf{v} + (\nabla \mathbf{v})^T) + \frac{1}{2}(\nabla \mathbf{v} - (\nabla \mathbf{v})^T) \\ &= S + \Omega\end{aligned} \tag{C.1}$$

where $S = \frac{1}{2}(\nabla \mathbf{v} + (\nabla \mathbf{v})^T)$ is rate of strain tensor and $\Omega = \frac{1}{2}(\nabla \mathbf{v} - (\nabla \mathbf{v})^T)$ is known as vorticity tensor.
Noting that:

$$\nabla \mathbf{v} = \begin{bmatrix} \frac{\partial u}{\partial x} & \frac{\partial u}{\partial y} & \frac{\partial u}{\partial z} \\ \frac{\partial v}{\partial x} & \frac{\partial v}{\partial y} & \frac{\partial v}{\partial z} \\ \frac{\partial w}{\partial x} & \frac{\partial w}{\partial y} & \frac{\partial w}{\partial z} \end{bmatrix} \tag{C.2}$$

We further obtain:

$$S = \begin{bmatrix} \frac{\partial u}{\partial x} & \frac{1}{2}(\frac{\partial u}{\partial y} + \frac{\partial v}{\partial x}) & \frac{1}{2}(\frac{\partial u}{\partial z} + \frac{\partial w}{\partial x}) \\ \frac{1}{2}(\frac{\partial u}{\partial y} + \frac{\partial v}{\partial x}) & \frac{\partial v}{\partial y} & \frac{1}{2}(\frac{\partial v}{\partial z} + \frac{\partial w}{\partial y}) \\ \frac{1}{2}(\frac{\partial u}{\partial z} + \frac{\partial w}{\partial x}) & \frac{1}{2}(\frac{\partial v}{\partial z} + \frac{\partial w}{\partial y}) & \frac{\partial w}{\partial z} \end{bmatrix} \tag{C.3}$$

$$\Omega = \begin{bmatrix} 0 & \frac{1}{2}(\frac{\partial u}{\partial y} - \frac{\partial v}{\partial x}) & \frac{1}{2}(\frac{\partial u}{\partial z} - \frac{\partial w}{\partial x}) \\ -\frac{1}{2}(\frac{\partial u}{\partial y} - \frac{\partial v}{\partial x}) & 0 & \frac{1}{2}(\frac{\partial v}{\partial z} - \frac{\partial w}{\partial y}) \\ -\frac{1}{2}(\frac{\partial u}{\partial z} - \frac{\partial w}{\partial x}) & -\frac{1}{2}(\frac{\partial v}{\partial z} - \frac{\partial w}{\partial y}) & 0 \end{bmatrix} \tag{C.4}$$

The quantity Q is defined as second invariant of $\nabla \mathbf{v}$ (Hunt, Wray, and Moin [163]) and written as:

$$Q = \frac{1}{2}((\nabla \cdot \mathbf{v})^2 - tr((\nabla \mathbf{v})^2)) \tag{C.5}$$

For an incompressible flow, $\nabla \cdot \mathbf{v} = 0$. Thus:

$$\begin{aligned} Q &= -\frac{1}{2} tr((\nabla \mathbf{v})^2) \\ &= \frac{1}{2}(\|\Omega\|^2 - \|S\|^2) \end{aligned} \tag{C.6}$$

- If $Q > 0$, the vorticity magnitude is greater than rate of shear strain. This characterizes the presence of rotation (Jeong and Hussain [164]).
- If $Q < 0$, the shear strain rate dominates over the vorticity magnitude and this denotes stretching pattern.

The Q values are then calculated using the filter *Gradient Of Unstructured DataSet* in Paraview.

Bibliography

[1] A Yücel, S Acharya, and M L Williams. “Natural convection and radiation in a square enclosure”. In: *Numerical Heat Transfer* 15.2 (1989), pp. 261–278.

[2] Z Tan and J R Howell. “Combined radiation and natural convection in a two-dimensional participating square medium”. In: *International Journal of Heat and Mass Transfer* 34.3 (1991), pp. 785–793.

[3] G Colomer et al. “Three-dimensional numerical simulation of convection and radiation in a differentially heated cavity using the discrete ordinates method”. In: *International Journal of Heat and Mass Transfer* 47.2 (2004), pp. 257–269.

[4] G Colomer, R Consul, and A Oliva. “Coupled radiation and natural convection: Different approaches of the SLW model for a non-gray gas mixture”. In: *Journal of Quantitative Spectroscopy and Radiative Transfer* 107.1 (2007), pp. 30–46.

[5] L Soucasse et al. “Numerical study of coupled molecular gas radiation and natural convection in a differentially heated cubical cavity”. In: *Computational Thermal Sciences: An International Journal* 4.4 (2012).

[6] Y Billaud, D Saury, and D Lemonnier. “Numerical investigation of coupled natural convection and radiation in a differentially heated cubic cavity filled with humid air. Effects of the cavity size”. In: *Numerical Heat Transfer, Part A: Applications* 72.7 (2017), pp. 495–518.

[7] F Tetsu, M Itsuki, and U Haruo. “Buoyant plume above a horizontal line heat source”. In: *International Journal of Heat and Mass Transfer* 16.4 (1973), pp. 755–768.

[8] K Urakawa, I Morioka, and M Kiyota. “Swaying motion of the buoyant plume above a horizontal line heat source”. In: *Proc. 1st ASME-JSME Thermal Eng. Conf.* 1983, pp. 215–220.

[9] S Xin et al. “Numerical simulations of natural convection around a line-source”. In: *International Journal of Numerical Methods for Heat & Fluid Flow* 14.7 (2004), pp. 830–850.

[10] R H Hernandez. “Natural convection in thermal plumes emerging from a single heat source”. In: *International Journal of Thermal Sciences* 98 (2015), pp. 81–89.

[11] G V Kuznetsov and M A Sheremet. “Two-dimensional problem of natural convection in a rectangular domain with local heating and heat-conducting boundaries of finite thickness”. In: *Fluid Dynamics* 41.6 (2006), pp. 881–890.

[12] G V Kuznetsov and M A Sheremet. “Conjugate heat transfer in a closed domain with a locally lumped heat-release source”. In: *Journal of Engineering Physics and Thermophysics* 79.1 (2006), pp. 57–64.

[13] M Paroncini and F Corvaro. “Natural convection in a square enclosure with a hot source”. In: *International journal of thermal sciences* 48.9 (2009), pp. 1683–1695.

[14] G V Kuznetsov, V I Maksimov, and M A Sheremet. "Natural convection in a closed parallelepiped with a local energy source". In: *Journal of Applied Mechanics and Technical Physics* 54.4 (2013), pp. 588–595.

[15] B Souayeh et al. "Prediction of unsteady natural convection within a square cavity containing an obstacle at high Rayleigh number value". In: *International Letters of Chemistry, Physics and Astronomy* 55 (2015), p. 19.

[16] N S Gibanov and M A Sheremet. "Effect of the buoyancy force on natural convection in a cubical cavity with a heat source of triangular cross-section". In: *IOP Conference Series: Materials Science and Engineering*. Vol. 124. 1. IOP Publishing. 2016, p. 012057.

[17] D Iyi, R Hasan, and R Penlington. "Numerical simulation of 2D turbulent natural convection of humid air in a cavity filled with solid objects". In: *Procedia engineering* 56 (2013), pp. 538–543.

[18] A R Rahmati and A A Tahery. "Numerical study of nanofluid natural convection in a square cavity with a hot obstacle using lattice Boltzmann method". In: *Alexandria engineering journal* 57.3 (2018), pp. 1271–1286.

[19] M Bouafia and O Daube. "Natural convection for large temperature gradients around a square solid body within a rectangular cavity". In: *International Journal of Heat and Mass Transfer* 50.17-18 (2007), pp. 3599–3615.

[20] H Sun, E Chénier, and G Lauriat. "Effect of surface radiation on the breakdown of steady natural convection flows in a square, air-filled cavity containing a centered inner body". In: *Applied Thermal Engineering* 31.6-7 (2011), pp. 1252–1262.

[21] S G Martyushev and M A Sheremet. "Surface radiation influence on the regimes of conjugate natural convection in an enclosure with local energy source". In: *Thermophysics and Aeromechanics* 20.4 (2013), pp. 417–428.

[22] S Saravanan and C Sivaraj. "Surface radiation effect on convection in a closed enclosure driven by a discrete heater". In: *International Communications in Heat and Mass Transfer* 53 (2014), pp. 34–38.

[23] S Patil, A K Sharma, and K Velusamy. "Conjugate laminar natural convection and surface radiation in enclosures: Effects of protrusion shape and position". In: *International Communications in Heat and Mass Transfer* 76 (2016), pp. 139–146.

[24] I Miroshnichenko, M Sheremet, and A Chamkha. "Turbulent natural convection combined with surface thermal radiation in a square cavity with local heater". In: *International Journal of Numerical Methods for Heat & Fluid Flow* 28.7 (2018), pp. 1698–1715.

[25] F Archambeau, N Méchitoua, and M Sakiz. "Code Saturne: A Finite Volume Code for the Computation of Turbulent Incompressible Flows, Industrial Applications". In: *International Journal on Finite Volumes* 1 (2004).

[26] R Koch and R Becker. "Evaluation of quadrature schemes for the discrete ordinates method". In: *Journal of Quantitative Spectroscopy and Radiative Transfer* 84.4 (2004), pp. 423–435.

[27] D Balsara. "Fast and accurate discrete ordinates methods for multidimensional radiative transfer. Part I, basic methods". In: *Journal of Quantitative Spectroscopy and Radiative Transfer* 69.6 (2001), pp. 671–707.

[28] EDF. *Code_Saturne version 5.0.0 practical user's guide*. 2017.

[29] G De Vahl Davis. "Natural convection of air in a square cavity: a bench mark numerical solution". In: *International Journal for numerical methods in fluids* 3.3 (1983), pp. 249–264.

[30] G Colomer et al. "Three-dimensional numerical simulation of convection and radiation in a differentially heated cavity using the discrete ordinates method". In: *International Journal of Heat and Mass Transfer* 47.2 (2004), pp. 257–269. ISSN: 00179310. DOI: 10.1016/S0017-9310(03)00387-9.

[31] T Fusegi and J M Hyun. "Laminar and transitional natural convection in an enclosure with complex and realistic conditions". In: *International Journal of Heat and Fluid Flow* 15.4 (1994), pp. 258–268.

[32] S Laouar-Meftah. "Modélisation de la convection naturelle de double diffusion dans un mélange de gaz absorbant et émettant le rayonnement". PhD thesis. 2010.

[33] L Soucasse, P Rivière, and A Soufiani. "Natural convection in a differentially heated cubical cavity under the effects of wall and molecular gas radiation at Rayleigh numbers up to 3× 109". In: *International Journal of Heat and Fluid Flow* 61 (2016), pp. 510–530.

[34] I Sezai and A A Mohamad. "Double diffusive convection in a cubic enclosure with opposing temperature and concentration gradients". In: *Physics of Fluids* 12.9 (2000), pp. 2210–2223.

[35] M Cherifi. "Modelisasion de la convection de double diffusio en presence de rayonnement dans une cavite 3D en regime instationaire". PhD thesis. University of Boumerdes, 2017.

[36] RM Goody. "The influence of radiative transfer on cellular convection". In: *Journal of Fluid Mechanics* 1.4 (1956), pp. 424–435.

[37] F Bdéoui and A Soufiani. "The onset of Rayleigh–Bénard instability in molecular radiating gases". In: *Physics of Fluids* 9.12 (1997), pp. 3858–3872.

[38] M Behnia, J A Reizes, and G De Vahl Davis. "Combined radiation and natural convection in a rectangular cavity with a transparent wall and containing a non-participating fluid". In: *International Journal for Numerical Methods in Fluids* 10.3 (1990), pp. 305–325.

[39] H Wang, S Xin, and P Le Quéré. "Étude numérique du couplage de la convection naturelle avec le rayonnement de surfaces en cavité carrée remplie d'air". In: *Comptes Rendus Mécanique* 334.1 (2006), pp. 48–57.

[40] G Lauriat. "Combined radiation-convection in gray fluids enclosed in vertical cavities". In: *Journal of Heat Transfer* 104.4 (1982), pp. 609–615.

[41] C Y Han and S W Baek. "The effects of radiation on natural convection in a rectangular enclosure divided by two partitions". In: *Numerical Heat Transfer: Part A: Applications* 37.3 (2000), pp. 249–270.

[42] K Lari et al. "Combined heat transfer of radiation and natural convection in a square cavity containing participating gases". In: *International Journal of Heat and Mass Transfer* 54.23-24 (2011), pp. 5087–5099.

[43] K Lari et al. "Numerical study of non-gray radiation and natural convection using the full-spectrum k-distribution method". In: *Numerical Heat Transfer, Part A: Applications* 61.1 (2012), pp. 61–84.

[44] L Soucasse et al. “Transitional regimes of natural convection in a differentially heated cubical cavity under the effects of wall and molecular gas radiation”. In: *Physics of Fluids* 26.2 (2014), p. 024105.

[45] T Fusegi and B Farouk. “A computational and experimental study of natural convection and surface/gas radiation interactions in a square cavity”. In: *Journal of Heat Transfer (Transactions of the ASME (American Society of Mechanical Engineers), Series C);(United States)* 112.3 (1990).

[46] Y Clergent. “Influence du rayonnement thermique sur les écoulements de convection Naturelle en Espace Confiné”. PhD thesis. Toulouse 3, 2000.

[47] M N Borjini et al. “Effect of radiative heat transfer on the three-dimensional Boyancy flow in cubic enclosure heated from the side”. In: *International Journal of Heat and Fluid Flow* 29.1 (2008), pp. 107–118.

[48] M Rafieivand. “Etude numérique de la convection de double diffusion en présence de rayonnement en cavité rectangulaire/par Mehrdad Rafieivand”. PhD thesis. Poitiers, 1999.

[49] A Mezrhab et al. “Numerical study of double-diffusion convection coupled to radiation in a square cavity filled with a participating grey gas”. In: *Journal of Physics D: Applied Physics* 41.19 (2008), p. 195501.

[50] S Meftah et al. “Coupled radiation and double diffusive convection in nongray air-CO2 and air-H2O mixtures in cooperating situations”. In: *Numerical Heat Transfer, Part A: Applications* 56.1 (2009), pp. 1–19.

[51] S Laouar-Meftah et al. “Gas radiation effects on opposing double-diffusive convection in a non-gray air–H2O mixture”. In: *International Journal of Thermal Sciences* 77 (2014), pp. 38–46.

[52] A Ibrahim and D Lemonnier. “Numerical study of coupled double-diffusive natural convection and radiation in a square cavity filled with a N2–CO2 mixture”. In: *International Communications in Heat and Mass Transfer* 36.3 (2009), pp. 197–202.

[53] M Cherifi et al. “Interaction of radiation with double-diffusive natural convection in a three-dimensional cubic cavity filled with a non-gray gas mixture in cooperating cases”. In: *Numerical Heat Transfer, Part A: Applications* 69.5 (2016), pp. 479–496.

[54] M M Mousa. “Modeling of laminar buoyancy convection in a square cavity containing an obstacle”. In: *Bulletin of the Malaysian Mathematical Sciences Society* 39.2 (2016), pp. 483–498.

[55] A Raji et al. “Effect of the subdivision of an obstacle on the natural convection heat transfer in a square cavity”. In: *Computers & Fluids* 68 (2012), pp. 1–15.

[56] G V Kuznetsov and M A Sheremet. “On the possibility of controlling thermal conditions of a typical element of electronic equipment with a local heat source via natural convection”. In: *Russian Microelectronics* 39.6 (2010), pp. 427–442.

[57] Y Wang. “Simulations numériques de panaches thermiques dans une cavité confinée en présence de couplage convection-rayonnement volumique”. PhD thesis. La Rochelle, 2020.

[58] M K Denison and B W Webb. “An absorption-line blackbody distribution function for efficient calculation of total gas radiative transfer”. In: *Journal of Quantitative Spectroscopy and Radiative Transfer* 50.5 (1993), pp. 499–510.

[59] M F Modest. *Radiative heat transfer*. Academic press, 2013.

[60] E E Lewis and W F Miller. "Computational methods of neutron transport". In: (1984).

[61] A Schuster. "Radiation through a foggy atmosphere". In: *The astrophysical journal* 21 (1905), p. 1.

[62] K Schwarzschild. "On the equilibrium of the sun's atmosphere". In: *Nachrichten von der Königlichen Gesellschaft der Wissenschaften zu Göttingen. Math.-phys. Klasse, 195, p. 41-53* 195 (1906), pp. 41–53.

[63] L Dombrovsky, J Randrianalisoa, and D Baillis. "Modified two-flux approximation for identification of radiative properties of absorbing and scattering media from directional-hemispherical measurements". In: *JOSA A* 23.1 (2006), pp. 91–98.

[64] L A Dombrovsky, K Ganesan, and W Lipinski. "Combined two-flux approximation and Monte Carlo model for identification of radiative properties of highly scattering dispersed materials". In: *Computational Thermal Sciences: An International Journal* 4.4 (2012).

[65] W E Vargas. "Generalized four-flux radiative transfer model". In: *Applied optics* 37.13 (1998), pp. 2615–2623.

[66] B Maheu, J N Letoulouzan, and G Gouesbet. "Four-flux models to solve the scattering transfer equation in terms of Lorenz-Mie parameters". In: *Applied optics* 23.19 (1984), pp. 3353–3362.

[67] B Maheu and G Gouesbet. "Four-flux models to solve the scattering transfer equation: special cases". In: *Applied optics* 25.7 (1986), pp. 1122–1128.

[68] A Brucato et al. "Estimating radiant fields in flat heterogeneous photoreactors by the six-flux model". In: *AIChE journal* 52.11 (2006), pp. 3882–3890.

[69] G L Puma and A Brucato. "Dimensionless analysis of slurry photocatalytic reactors using two-flux and six-flux radiation absorption–scattering models". In: *Catalysis Today* 122.1-2 (2007), pp. 78–90.

[70] J H Jeans. "The Equations of Radiative Transfer of Energy". In: *Monthly Notices of the Royal Astronomical Society* 78.1 (Nov. 1917), pp. 28–36. ISSN: 0035-8711. DOI: 10.1093/mnras/78.1.28. eprint: http://oup.prod.sis.lan/mnras/article-pdf/78/1/28/4067064/mnras78-0028.pdf. URL: https://doi.org/10.1093/mnras/78.1.28.

[71] J Shen. "Efficient spectral-Galerkin method I. Direct solvers of second-and fourth-order equations using Legendre polynomials". In: *SIAM Journal on Scientific Computing* 15.6 (1994), pp. 1489–1505.

[72] Eric W Weisstein. "Legendre polynomial". In: (2002).

[73] Y Bayazitoilu and J Higenyi. "Higher-order differential equations of radiative transfer: P3 approximation". In: *AIAA Journal* 17.4 (1979), pp. 424–431.

[74] M P Mengüç and R Viskanta. "Radiative transfer in axisymmetric, finite cylindrical enclosures". In: *ASME Journal of Heat Transfer* 108 (1986), pp. 271–276.

[75] D B Olfe. "A modification of the differential approximation for radiative transfer." In: *AIAA Journal* 5.4 (1967), pp. 638–643.

[76] M F Modest. "Modified differential approximation for radiative transfer in general three-dimensional media". In: *Journal of Thermophysics and Heat Transfer* 3.3 (1989), pp. 283–288.

[77] S Chandrasekhar. "Radiative Transfer Dover Publications Inc". In: *New York* (1960).

[78] C E Lee. *The discrete Sn approximation to transport theory*. Tech. rep. Los Alamos Scientific Lab., N. Mex., 1961.

[79] K D Lathrop. "Use of discrete-ordinates methods for solution of photon transport problems". In: *Nuclear Science and Engineering* 24.4 (1966), pp. 381–388.

[80] B G Carlson. "Transport theory-the method of discrete ordinates". In: *Computing methods in reactor physics* (1968).

[81] W A Fiveland. "Discrete-ordinates solutions of the radiative transport equation for rectangular enclosures". In: *Journal of heat transfer* 106.4 (1984), pp. 699–706.

[82] W A Fiveland. "Discrete ordinate methods for radiative heat transfer in isotropically and anisotropically scattering media". In: *Journal of Heat Transfer (Transactions of the ASME (American Society of Mechanical Engineers), Series C);(United States)* 109.3 (1987).

[83] W A Fiveland. "Three-dimensional radiative heat-transfer solutions by the discrete-ordinates method". In: *Journal of Thermophysics and Heat Transfer* 2.4 (1988), pp. 309–316.

[84] J S Truelove. "Discrete-ordinate solutions of the radiation transport equation". In: *Journal of Heat Transfer (Transcations of the ASME (American Society of Mechanical Engineers), Series C);(United States)* 109.4 (1987).

[85] J S Truelove. "Three-dimensional radiation in absorbing-emitting-scattering media using the discrete-ordinates approximation". In: *Journal of quantitative spectroscopy and radiative transfer* 39.1 (1988), pp. 27–31.

[86] A S Jamaluddin and P J Smith. "Predicting radiative transfer in axisymmetric cylindrical enclosures using the discrete ordinates method". In: *Combustion Science and Technology* 62.4-6 (1988), pp. 173–186.

[87] T Y Kim and S W Baek. "Analysis of combined conductive and radiative heat transfer in a two-dimensional rectangular enclosure using the discrete ordinates method". In: *International journal of heat and mass transfer* 34.9 (1991), pp. 2265–2273.

[88] K D Lathrop and B G Carlson. *Discrete ordinates angular quadrature of the neutron transport equation*. Tech. rep. Los Alamos Scientific Lab., N. Mex., 1964.

[89] C P Thurgood. "A critical evaluation of the discrete ordinates method using HEART and T (N) quadrature." In: (1994).

[90] R Koch et al. "Discrete ordinates quadrature schemes for multidimensional radiative transfer". In: *Journal of Quantitative Spectroscopy and Radiative Transfer* 53.4 (1995), pp. 353–372.

[91] P J Coelho. "The role of ray effects and false scattering on the accuracy of the standard and modified discrete ordinates methods". In: *ICHMT DIGITAL LIBRARY ONLINE*. Begel House Inc. 2001.

[92] M A Ramankutty and A L Crosbie. "Modified discrete ordinates solution of radiative transfer in two-dimensional rectangular enclosures". In: *Journal of Quantitative Spectroscopy and Radiative Transfer* 57.1 (1997), pp. 107–140.

[93] R A Ramankutty and A L Crosbie. "Modified discrete-ordinates solution of radiative transfer in three-dimensional rectangular enclosures." In: *Journal of Quantitative Spectroscopy and Radiative Transfer* 60 (1998), pp. 103–134.

[94] H Amiri, S H Mansouri, and P J Coelho. "Application of the modified discrete ordinates method with the concept of blocked-off region to irregular geometries". In: *International Journal of Thermal Sciences* 50.4 (2011), pp. 515–524.

[95] P J Coelho. "Advances in the discrete ordinates and finite volume methods for the solution of radiative heat transfer problems in participating media". In: *Journal of Quantitative spectroscopy and Radiative transfer* 145 (2014), pp. 121–146.

[96] D Joseph et al. "Comparison of three spatial differencing schemes in discrete ordinates method using three-dimensional unstructured meshes". In: *International journal of thermal sciences* 44.9 (2005), pp. 851–864.

[97] C Aghanajafi and A Abjadpour. "Discrete ordinates method applied to radiative transfer equation in complex geometries meshed by structured and unstructured grids". In: *Journal of the Brazilian Society of Mechanical Sciences and Engineering* 38.3 (2016), pp. 1007–1019.

[98] D Le Hardy et al. "Specular reflection treatment for the 3D radiative transfer equation solved with the discrete ordinates method". In: *Journal of Computational Physics* 334 (2017), pp. 541–572.

[99] G D Raithby and E H Chui. "A finite-volume method for predicting a radiant heat transfer in enclosures with participating media". In: *Journal of heat transfer* 112.2 (1990), pp. 415–423.

[100] E H Chui, G D Raithby, and P M J Hughes. "Prediction of radiative transfer in cylindrical enclosures with the finite volume method". In: *Journal of Thermophysics and Heat transfer* 6.4 (1992), pp. 605–611.

[101] B Hunter and Z Guo. "Comparison of the discrete-ordinates method and the finite-volume method for steady-state and ultrafast radiative transfer analysis in cylindrical coordinates". In: *Numerical Heat Transfer, Part B: Fundamentals* 59.5 (2011), pp. 339–359.

[102] H C Hottel and E S Cohen. "Radiant heat exchange in a gas-filled enclosure: Allowance for nonuniformity of gas temperature". In: *AIChE Journal* 4.1 (1958), pp. 3–14.

[103] R Viskanta and M P Mengüç. "Radiation heat transfer in combustion systems". In: *Progress in Energy and Combustion Science* 13.2 (1987), pp. 97–160.

[104] H C Hottel and A F Sarofim. "Radiative Transfer". In: *New York* (1967), pp. 20–24.

[105] H Ebrahimi et al. "Zonal modeling of radiative heat transfer in industrial furnaces using simplified model for exchange area calculation". In: *Applied Mathematical Modelling* 37.16-17 (2013), pp. 8004–8015.

[106] J A Fleck Jr. *The calculation of nonlinear radiation transport by a Monte Carlo method*. Tech. rep. Lawrence Radiation Lab., Univ. of California, Livermore, 1961.

[107] J R Howell and M Perlmutter. "Monte Carlo solution of thermal transfer through radiant media between gray walls". In: *Journal of heat transfer* 86.1 (1964), pp. 116–122.

[108] D G Collins et al. "Backward Monte Carlo calculations of the polarization characteristics of the radiation emerging from spherical-shell atmospheres". In: *Applied Optics* 11.11 (1972), pp. 2684–2696.

[109] K M Case. “Transfer problems and the reciprocity principle”. In: *Reviews of modern physics* 29.4 (1957), p. 651.

[110] M F Modest. “Backward Monte Carlo simulations in radiative heat transfer”. In: *Journal of heat transfer* 125.1 (2003), pp. 57–62.

[111] R Fournier et al. “Radiative, conductive and convective heat-transfers in a single Monte Carlo algorithm”. In: *Journal of Physics: Conference Series*. Vol. 676. 1. 2016, art–012007.

[112] L Ibarrart et al. “Combined conductive-convective-radiative heat transfer in complex geometry using the Monte Carlo method”. In: 2018.

[113] C Caliot et al. “Combined conductive-radiative heat transfer analysis in complex geometry using the Monte Carlo method”. In: (2019).

[114] F C Lockwood and N G Shah. “A new radiation solution method for incorporation in general combustion prediction procedures”. In: *Symposium (international) on combustion*. Vol. 18. 1. Elsevier. 1981, pp. 1405–1414.

[115] J C Henson and W M G Malalasekera. “Comparison of the discrete transfer and Monte Carlo methods for radiative heat transfer in three-dimensional nonhomogeneous scattering media”. In: *Numerical Heat Transfer, Part A Applications* 32.1 (1997), pp. 19–36.

[116] N Selçuk and N Kayakol. “Evaluation of discrete ordinates method for radiative transfer in rectangular furnaces”. In: *International journal of heat and mass transfer* 40.2 (1997), pp. 213–222.

[117] P S Cumber. “Improvements to the discrete transfer method of calculating radiative heat transfer”. In: *International Journal of Heat and Mass Transfer* 38.12 (1995), pp. 2251–2258.

[118] P S Cumber. “Application of adaptive quadrature to fire radiation modeling”. In: *Journal of heat transfer* 121.1 (1999), pp. 203–205.

[119] P J Coelho and M G Carvalho. “A conservative formulation of the discrete transfer method”. In: *Journal of Heat Transfer* 119.1 (1997), pp. 118–128.

[120] S Heugang, H T Kamdem Tagne, and F Pelap. “A Discrete Transfer Method for Radiative Transfer through Anisotropically Scattering Media”. In: *American Journal of Heat and Mass Transfer* Vol. 3 (Nov. 2016), pp. 396–411. DOI: 10.7726/ajhmt.2016.1022.

[121] V Feldheim and P Lybaert. “Solution of radiative heat transfer problems with the discrete transfer method applied to triangular meshes”. In: *Journal of Computational and Applied Mathematics* 168.1-2 (2004), pp. 179–190.

[122] P J Coelho et al. “Modelling of radiative heat transfer in enclosures with obstacles”. In: *International Journal of Heat and Mass Transfer* 41.4-5 (1998), pp. 745–756.

[123] F Archambeau, N Méchitoua, and M Sakiz. “Code Saturne: A finite volume code for the computation of turbulent incompressible flows-Industrial applications”. In: (2004).

[124] R M Goody. “A statistical model for water-vapour absorption”. In: *Quarterly Journal of the Royal Meteorological Society* 78.338 (1952), pp. 638–640.

[125] W L Godson. “The computation of infrared transmission by atmospheric water vapor”. In: *Journal of Meteorology* 12.3 (1955), pp. 272–284.

[126] Jean Taine and Anouar Soufiani. "Gas IR Radiative Properties: From Spectroscopic Data to Approximate Models". In: ed. by J P Hartnett et al. Vol. 33. Advances in Heat Transfer. Elsevier, 1999, pp. 295 –414. DOI: https://doi.org/10.1016/S0065-2717(08)70306-X. URL: http://www.sciencedirect.com/science/article/pii/S006527170870306X.

[127] "Edited by". In: *Radiation in the Atmosphere*. Ed. by K Y Kondratyev. Vol. 12. International Geophysics. Academic Press, 1969, p. iii. DOI: https://doi.org/10.1016/S0074-6142(08)62788-6. URL: http://www.sciencedirect.com/science/article/pii/S0074614208627886.

[128] R Goody et al. "The correlated-k method for radiation calculations in nonhomogeneous atmospheres". In: *Journal of Quantitative Spectroscopy and Radiative Transfer* 42.6 (1989), pp. 539–550.

[129] A A Lacis and V Oinas. "A description of the correlated k distribution method for modeling nongray gaseous absorption, thermal emission, and multiple scattering in vertically inhomogeneous atmospheres". In: *Journal of Geophysical Research: Atmospheres* 96.D5 (1991), pp. 9027–9063.

[130] Q Fu and K N Liou. "On the correlated k-distribution method for radiative transfer in nonhomogeneous atmospheres". In: *Journal of the Atmospheric Sciences* 49.22 (1992), pp. 2139–2156.

[131] D K Edwards. "Molecular gas band radiation". In: *Advances in heat transfer*. Vol. 12. Elsevier, 1976, pp. 115–193.

[132] J Ströhle and P J Coelho. "On the application of the exponential wide band model to the calculation of radiative heat transfer in one-and two-dimensional enclosures". In: *International Journal of Heat and Mass Transfer* 45.10 (2002), pp. 2129–2139.

[133] M F Modest. "The weighted-sum-of-gray-gases model for arbitrary solution methods in radiative transfer". In: *Journal of heat transfer* 113.3 (1991), pp. 650–656.

[134] L Pierrot et al. "A fictitious-gas-based absorption distribution function global model for radiative transfer in hot gases". In: *Journal of Quantitative Spectroscopy and Radiative Transfer* 62.5 (1999), pp. 609–624.

[135] M Modest and H Zhang. "The Full-Spectrum Correlated-k Distribution for Thermal Radiation From Molecular Gas-Particulate Mixtures". In: *Journal of Heat Transfer* 124 (Feb. 2002), p. 30. DOI: 10.1115/1.1418697.

[136] M Modest and R Mehta. "Full spectrum k-distribution correlations for CO 2 from the CDSD-1000 spectroscopic databank". In: *International Journal of Heat and Mass Transfer - INT J HEAT MASS TRANSFER* 47 (May 2004), pp. 2487–2491. DOI: 10.1016/j.ijheatmasstransfer.2003.11.028.

[137] V P Solovjov and B W Webb. "Global Spectral Methods in Gas Radiation: the Exact Limit of the SLW Model and its Relationship to the ADF and FSK Methods". In: *Journal of Heat Transfer* 133 (Apr. 2011), pp. 042701–1. DOI: 10.1115/1.4002775.

[138] V P Solovjov, D Lemonnier, and B W Webb. "The SLW-1 model for efficient prediction of radiative transfer in high temperature gases". In: *Journal of Quantitative Spectroscopy and Radiative Transfer* 112 (May 2011), pp. 1205–1212. DOI: 10.1016/j.jqsrt.2010.08.009.

[139] V Goutiere, F Liu, and A Charette. “An assessment of real-gas modelling in 2D enclosures”. In: *Journal of Quantitative Spectroscopy and Radiative Transfer* 64.3 (2000), pp. 299–326.

[140] V Goutière, A Charette, and L Kiss. “Comparative performance of nongray gas modeling techniques”. In: *Numerical Heat Transfer: Part B: Fundamentals* 41.3-4 (2002), pp. 361–381.

[141] V P Solovjov et al. “The rank correlated SLW model of gas radiation in non-uniform media”. In: *Journal of Quantitative Spectroscopy and Radiative Transfer* 197 (2017), pp. 26–44.

[142] V P Solovjov et al. “The Scaled SLW model of gas radiation in non-uniform media based on Planck-weighted moments of gas absorption cross-section”. In: *Journal of Quantitative Spectroscopy and Radiative Transfer* 206 (2018), pp. 198–212.

[143] V P Solovjov et al. “Locally Correlated SLW Model for Prediction of Gas Radiation in Non-Uniform Media”. In: (June 2019).

[144] M K Denison and B W Webb. “k-distributions and Weighted-Sum-of-Gray-Gases-A hybrid model”. In: *International Heat Transfer Conference Digital Library*. Begel House Inc. 1994.

[145] J T Pearson et al. “Efficient representation of the absorption line blackbody distribution function for H2O, CO2, and CO at variable temperature, mole fraction, and total pressure”. In: *Journal of Quantitative Spectroscopy and Radiative Transfer* 138 (2014), pp. 82–96.

[146] V P Solovjov, B W Webb, and F André. “Radiative properties of gases”. In: *Handbook of Thermal Science and Engineering* (2018), pp. 1069–1141.

[147] V P Solovjov, B W Webb, and F André. “Radiative Properties of Gases”. In: *Handbook of Thermal Science and Engineering*. Cham: Springer International Publishing, 2018, pp. 1069–1141. ISBN: 978-3-319-26695-4. DOI: 10.1007/978-3-319-26695-4_59. URL: https://doi.org/10.1007/978-3-319-26695-4_59.

[148] B W Webb, V P Solovjov, and F André. “An exploration of the influence of spectral model parameters on the accuracy of the rank correlated SLW model”. In: *Journal of Quantitative Spectroscopy and Radiative Transfer* 218 (2018), pp. 161–170.

[149] C E Lee. “The discrete Sn approximation to transport theory”. In: (June 1961).

[150] W A Fiveland. “The selection of discrete ordinate quadrature sets for anisotropic scattering”. In: *Fundamentals of Radiation Heat Transfer* 160 (1991), pp. 89–96.

[151] S L Sobolev. “On mechanical quadrature formulae on the surface of a sphere”. In: *Sibirskii Matematicheskii Zhurnal* 3.5 (1962), pp. 486–496.

[152] V I Lebedev. “Quadratures on a sphere”. In: *USSR Computational Mathematics and Mathematical Physics* 16.2 (1976), pp. 10 –24. ISSN: 0041-5553. DOI: https://doi.org/10.1016/0041-5553(76)90100-2. URL: http://www.sciencedirect.com/science/article/pii/0041555376901002.

[153] A L Crosbie and R G Schrenker. “Radiative transfer in a two-dimensional rectangular medium exposed to diffuse radiation”. In: *Journal of quantitative spectroscopy and radiative transfer* 31.4 (1984), pp. 339–372.

[154] P Le Quéré. “Accurate solutions to the square thermally driven cavity at high Rayleigh number”. In: *Computers & Fluids* 20.1 (1991), pp. 29–41.

[155] E Tric, G Labrosse, and M Betrouni. “A first incursion into the 3D structure of natural convection of air in a differentially heated cubic cavity, from accurate numerical solutions”. In: *International Journal of Heat and Mass Transfer* 43.21 (2000), pp. 4043–4056.

[156] P Le Quéré and M Behnia. “From onset of unsteadiness to chaos in a differentially heated square cavity”. In: *Journal of fluid mechanics* 359 (1998), pp. 81–107.

[157] J Chang and T F Lin. “Unsteady thermosolutal opposing convection of liquid-water mixture in a square cavity—II. Flow structure and fluctuation analysis”. In: *International journal of heat and mass transfer* 36.5 (1993), pp. 1333–1345.

[158] T Nishimura, M Wakamatsu, and A M Morega. “Oscillatory double-diffusive convection in a rectangular enclosure with combined horizontal temperature and concentration gradients”. In: *International Journal of Heat and Mass Transfer* 41.11 (1998), pp. 1601–1611.

[159] A Ibrahim. “Couplage de la convection naturelle et du rayonnement dans les mélanges gazeux absorbants-émettants”. PhD thesis. 2010.

[160] Vladimir P Solovjov and Brent W Webb. “An efficient method for modeling radiative transfer in multicomponent gas mixtures with soot”. In: *J. Heat Transfer* 123.3 (2001), pp. 450–457.

[161] L Cadet. “Étude du couplage convection-rayonnement en cavité différentiellement chauffée à haut nombre de Rayleigh en ambiances habitables”. PhD thesis. La Rochelle, 2015.

[162] B E Poling, J M Prausnitz, and J O’Connell. *The properties of gases and liquids*. New York: McGraw-Hill, 2001. ISBN: 0070116822 9780070116825 0071189718 9780071189712. URL: http://www.worldcat.org/search?qt=worldcat_org_all&q=0070116822.

[163] J CR Hunt, A A Wray, and P Moin. “Eddies, streams, and convergence zones in turbulent flows”. In: (1988).

[164] J Jeong and F Hussain. “On the identification of a vortex”. In: *Journal of fluid mechanics* 285 (1995), pp. 69–94.

ÉTUDE NUMÉRIQUE DE LA CONVECTION NATURELLE COUPLÉE AU RAYONNEMENT GAZEUX DANS UN CAVITÉ CONTENANT UN OBSTACLE ACTIF

Notre objectif est d'étudier numériquement des écoulements de convection naturelle en milieu confiné, le fluide étant un mélange gazeux incluant des composants absorbants (CO_2, H_2O). On considère pour cela une cavité cubique avec une source localisée sur le plancher chauffant le fluide et diffusant un polluant participant au rayonnement. Nos calculs sont réalisés avec le code CFD Code Saturne, dans lequel nous avons implanté nos propres données pour la méthode des ordonnées discrètes (nouvelles quadratures) et pour modéliser le rayonnement des gaz (méthode SLW dans l'approche « rank-correlated »). En convection naturelle thermique pure les résultats montrent que le rayonnement du gaz modifie légèrement la structure de l'écoulement et la distribution de température. Il réduit les échanges convectifs entre le fluide et les parois de l'enceinte ainsi que l'échange radiatif entre la surface supérieure de l'obstacle et celles de la cavité. En double-diffusion, dans le cas aidant, le rayonnement du gaz tend à homogénéiser le champ thermique, accélère légèrement les couches limites pariétales, mais réduit la vitesse maximale à l'intérieur du panache. Par contre, il affecte peu le champ de concentration. Dans le cas opposant, le rayonnement intensifie le panache thermique qui se développe au-dessus de l'obstacle. Il réduit la température dans les régions proches des surfaces verticales de l'obstacle. Le champ de concentration montre les mêmes tendances d'altération que le champ thermique.

Mots clés: Analyse numérique, Chaleur–Convection, Gaz–Écoulement, Couche limite, Modélisation CFD, Rayonnement thermique, Transfert de chaleur.

NUMERICAL STUDY OF NATURAL CONVECTION COUPLED TO GAS RADIATION IN A CAVITY CONTAINING AN ACTIVE OBSTACLE

Our objective is to study numerically natural convection flows in an enclosure, the fluid being a gaseous mixture including absorbent components (CO_2, H_2O). For this purpose, we consider a cubic cavity with a source located on the floor, heating the fluid and diffusing a pollutant participating to radiation. Our calculations are performed with the CFD software Code Saturne, in which we have implemented our own data for the discrete ordinates method (new quadratures) and for modelling gas radiation (SLW method in the rank-correlated approach). In pure thermal natural convection, the results show that gas radiation slightly changes the flow structure and the temperature distribution. It reduces the convective exchanges between the fluid and the walls of the enclosure as well as the radiative exchange between the upper surface of the obstacle and the cavity boundaries. In double diffusion, in the aiding case, gas radiation tends to homogenize the thermal field and slightly accelerates the parietal boundary layers, but reduces the maximum velocity within the plume. On the other hand, it has little effect on the concentration field. In the opposing case, the radiation intensifies the thermal plume above the obstacle. It reduces the temperature in regions close to the vertical surfaces of the obstacle. The concentration field shows the same modification trends as the thermal field.

Keywords: Numerical analysis, Heat–Convection, Gas flow, Boundary layer, Computational fluid dynamics, Heat–Radiation and absorption, Heat–Transmission.